



Image-guided interactive simulation for endovascular surgery

Raffaella Trivisonne

► To cite this version:

Raffaella Trivisonne. Image-guided interactive simulation for endovascular surgery. Human health and pathology. Université de Strasbourg, 2020. English. NNT : 2020STRAD030 . tel-03855785

HAL Id: tel-03855785

<https://theses.hal.science/tel-03855785>

Submitted on 16 Nov 2022

HAL is a multi-disciplinary open access archive for the deposit and dissemination of scientific research documents, whether they are published or not. The documents may come from teaching and research institutions in France or abroad, or from public or private research centers.

L'archive ouverte pluridisciplinaire **HAL**, est destinée au dépôt et à la diffusion de documents scientifiques de niveau recherche, publiés ou non, émanant des établissements d'enseignement et de recherche français ou étrangers, des laboratoires publics ou privés.

École doctorale 269 :
Mathématiques, Sciences de l'Information et de l'Ingénieur

Laboratoire ICube (UMR 7357)
Research Team: MIMESIS - Inria Nancy Grand Est

THÈSE présentée par
Raffaella TRIVISONNE

soutenue le: **15 Octobre 2020**

pour obtenir le grade de : **Docteur de l'Université de Strasbourg**

Discipline/Specialité: Mathématiques Appliquées, Informatique

**Image-guided Interactive Simulation for
Endovascular Surgery**

THÈSE dirigée par :
M.COTIN Stéphane,
M. KERRIEN Erwan,

Directeur de Recherche, Inria, Université de Strasbourg
Chargé de Recherche, Inria

RAPPORTEURS :
Mme. ANGELINI Elsa,
M. BELLO Fernando,

Senior Data Scientist, Imperial College London
Prof. Faculty of Medicine, Imperial College London

AUTRES MEMBRES DU JURY :
M. CAZIER David,
M. NAGEOTTE Florent,

Professeur, Université de Strasbourg
Chargé de Recherche, ICube, Université de Strasbourg

*A mia madre,
a mio padre,
e a mio figlio.*

SUMMARY

Image-guided Interactive Simulation for Endovascular Surgery

Minimally invasive fluoroscopy-based procedures are the gold standard for diagnosing and treating various pathologies of the cardiovascular system. With this kind of procedures, clinicians have to infer the 3D shape of the device from 2D images. Such lack of depth perception, combined with a dense environment of overlaying anatomical structures, has been identified as one of the major factors affecting clinical performances.

Several methods have been proposed to enhance the visualization of 2D fluoroscopic images, which could improve the clinician's global insight and consequently the positive outcomes of the procedures. A widely used approach is to create a 3D reconstruction of the surgical scene to be combined with 2D fluoroscopic images, in order to have an augmented view. In general, this kind of methods aims at retrieving the 3D shape of the device (and or anatomical structures) by combining some priors on the shape and the behaviour of the device, with external observations, providing some incomplete information on its current state.

After highlighting the limitations of the existing 2D-3D reconstruction methods, our objective was to develop a method that:

1. provides a good description of both the shape and the behavior of the device; taking into account non-rigid interactions with the surrounding anatomy and non-linear phenomena (e.g. non-sliding contacts);
2. solely relies on monocular 2D fluoroscopic images, without the need to embed any external sensors onto the interventional device;
3. takes into account and compensates the uncertainties which might exist on model parameterization and the noise affecting external observations;
4. is compatible with real-time computations;

We first proposed a purely deterministic approach, where projective information from 2D fluoroscopic images is integrated to the model as mechanical constraints. Despite the good results, the proposed method is not able to take into account non-linear phenomena such as stick and slip transitions. In addition, errors on both the navigation model and external observations are not taken into account. For the above reasons, we designed a new stochastic approach. Given the ill-posedness of the 2D-3D reconstruction problem, the 3D shape of the interventional device can be seen as a random variable. Such variable is described, at the same time, through an process model, which provides a description of the variable through time and it is affected by some uncertainties, and some external

observations, which can provide some partial information on its current configuration and are affected by noise.

In particular, this thesis aims to develop a novel approach, where a Bayesian approach is used to combine a constrained physics-based simulation of the catheter navigation, with external 2D observations extracted from 2D fluoroscopic images. Whereas the physics-based model provides a prediction of the shape of the navigation device navigating the blood vessels (taking into account non-linear interactions between the catheter and the surrounding anatomy), an Unscented Kalman Filter is used to correct the navigation model using 2D features, extracted from fluoroscopic images, as external observations. The proposed method has been evaluated on both synthetic and real data.

Lastly, we present and analyse the current limitations of our method, proposing possible solutions, along with some perspectives for future works and applications.

Keywords : Computer Aided Surgery, Endovascular Intervention, Catheter Reconstruction, Physics-based Simulation, Stochastic Method, Constrained Unscented Kalman Filter

ACKNOWLEDGMENTS

First of all, I would like to express my sincere gratitude to all members of the jury. Prof. Angelini, Prof. Bello, Prof. Cazier, Dr. Nageotte. I thank you for accepting to read my work, for your insightful comments and feedback. Thank you for making your knowledge and your time available to me.

I would like to thank my supervisors, Stéphane and Erwan, for their continuous support, patience, and availability, for their motivation and immense knowledge. Each in his own way has helped me immensely to grow both on a scientific and personal level. I wish I had been a better student, this I regret. I wish I could have made you much prouder. But know that I have always tried to do my best, even in the most difficult conditions. Thank you for all that you have done for me, and for having accompanied me on this journey.

I want to thank Igor Peterlik, without whose work this thesis wouldn't have been possible. I want to thank all my fellow labmates, for the stimulating discussions, for the sleepless nights spent working together before deadlines, and for all the fun we have had in the last years. I have to thank in particular Rémi and Nico who, with their honest but ever-present friendship, have known how to stay close to me in my most difficult moments.

This PhD could not have been achieved if I had not had special people around me, who always supported and accompanied me. I, therefore, thank Stéphanie and Yves, who took care of my son and to whom I owe a lot. Thank you for your unconditional love with which you raised and welcomed him into your family. I thank with my heart full of love and gratitude, Francy, Lalla, and Michele. My family here in Strasbourg. My safe place, I have always been able to count on you, and I always will be.

I thank my siblings, Priscilla, and Federico. In my eyes, we are always little and together at the casetta of the Valli, but you have grown up strong and I am so proud of you. It's the three of us forever, thanks for all the support and love you've always shown me. Thanks for always being there.

I thank my father Raffaele, my great love, my rock. I cling to you as if I were still your little daughter because I know you will never leave me. Life hit us suddenly, but you held us tight with all your strength. Thanks, Dad. I dedicate this doctoral thesis to you, to your love for science and medicine. I hope I made you proud of me.

I thank my son Augusto. Amore di mamma, if ever one day you will read these words, I would like you to know that your mother loves you more than anything in the world and that whatever choice I have made, I made it to protect you and to guarantee you a better future. You have been my the strength in my hardest times. Life will not always be easy, my love, but you must be courageous, always walk with your head held high, and

reach your goals without being hampered by anything or anyone. I dedicate this doctoral thesis to you, to your future. May you always be free and happy.

My last words go to the person to whom I owe everything. My mother. Mom, wherever you are, know that I did all this for you. I would have liked to give up a thousand times, but you taught me that in life one must fight. I would like to see your proud and moved face among the auditorium benches. What would I pay to hear your voice again saying "Brava amore di mamma". Mom, wherever you are, thank you for everything you have done for us. I dedicate this doctoral thesis to you, who I miss you like air, and who made me the person I am today.

To my mother, my father, and my son.
My past, my present, my forever.

*Happiness can be found in the darkest of times,
if one only remembers to turn on the light.*
Albus Dumbledore



TABLE OF CONTENTS

I	General Introduction	1
1	General Introduction	3
1.1	Introduction	5
1.2	Clinical Context	6
1.2.1	Endovascular Minimally Invasive Surgery	6
1.2.1.1	Interventional Devices	8
1.2.2	Principles of Fluoroscopy	8
1.2.2.1	Equipment and Mode of Operation	9
1.2.2.2	Fluoroscopic Images	10
1.3	Problem Assessment and Contributions	10
1.3.1	Limitations of Fluoroscopic Procedures	11
1.3.2	Proposed Solution	12
1.3.3	Manuscript Outline	13
II	State Of The Art	15
2	State Of The Art	17
2.1	Introduction	19
2.2	2D Enhancement of Fluoroscopic Images	19
2.3	Enhancement of Fluoroscopic Images with 3D Anatomy Reconstruction . .	20
2.4	Enhancement of Fluoroscopic Images with 3D Instrument Reconstruction .	23
2.4.1	Interventional Device Model	23
2.4.2	Overview on Reconstruction Methods	27
2.4.2.1	Biplane Images Reconstruction	27
2.4.2.2	Monocular Images Reconstruction	28
2.4.2.3	Monocular Images Reconstruction using External Sensors	33
2.4.3	Discussion	37
2.5	Conclusion	39
III	Deterministic Simulation	41
3	Augmented 3D Catheter Navigation Using Constrained Shape From Template	43
3.1	Introduction	45
3.2	Deformable Models	45
3.2.1	Finite Element Approach	46

3.2.2	Catheter Model	47
3.3	Boundary Conditions	49
3.3.1	General Definition	49
3.3.2	Contact Model	50
3.4	Temporal Integration	51
3.4.1	Backward Euler Integration	53
3.5	Constraint-based Solution	54
3.6	2D-3D Reconstruction Constraints	56
3.6.1	Projective Constraint	57
3.6.1.1	Marker Detection and Tracking	57
3.6.1.2	Calibration and Projection Matrix	57
3.6.1.3	Projective Constraint Formalism	58
3.6.2	Entry Constraint	60
3.7	Experimentations and Results	61
3.7.1	Overview and Metrics	61
3.7.2	Synthetic Experiment on Projective Constraint and Surface Con- straint	63
3.7.3	Synthetic Experiment on Projective Constraint and Entry Constraint	67
3.7.4	Real Data Experiments on Projective Constraint and Surface Con- straint	71
3.7.5	Real Data Experiments on Projective Constraint and Entry Con- straint	75
3.8	Conclusion	78

IV Stochastic Simulation I 79

4	Preliminary Study on Stochastic State Estimation	81
4.1	Introduction	83
4.2	Bayesian Filtering	84
4.2.1	Kalman Filters	84
4.2.2	Non-linear Kalman Filters	85
4.3	State Vector Study	87
4.3.1	State Estimation	89
4.3.1.1	State vector composed of positions and velocities	90
4.3.1.2	State vector composed of only positions	91
4.3.1.3	State vector composed of only velocities	93
4.3.2	Data Assimilation	94
4.3.2.1	State vector of positions, velocities, and incorrect parameter	95
4.3.2.2	State vector of positions and incorrect parameter	96
4.3.2.3	Results	97
4.3.3	3DoF Beam	98

4.3.3.1	State vector of positions and velocities	99
4.3.3.2	State vector of only positions	100
4.3.3.3	Augmented State	101
4.3.4	2D Observations	102
4.3.4.1	State vector of positions and velocities	103
4.3.4.2	State vector of positions, velocities and model parameter .	104
4.3.5	The Modeling of Uncertainty	105
4.3.6	Conclusions	107
V	Stochastic Simulation II	109
5	Constrained State Estimation	111
5.1	Stochastic State Estimation for Catheter Navigation	113
5.1.1	State Vector	113
5.1.2	Prediction Model	113
5.1.3	Observation Model	114
5.1.4	Filter Workflow and Computation Time	115
5.1.5	Constrained State Estimation	117
5.2	Experimental Set-Up and Results	119
5.2.1	Overview and error metrics	119
5.2.2	Synthetic Experiments Set-Up	119
5.2.2.1	Ground Truth Reference	119
5.2.2.2	2D Observations	120
5.2.2.3	Stochastic Environment: Filter Parameters Tuning	120
5.2.3	Synthetic Experiments Results	122
5.2.3.1	Sensitivity to Friction Coefficient for Y-Shaped Geometry	122
5.2.3.2	Sensitivity to Generalized Model Uncertainties for Y-Shaped Geometry	124
5.2.3.3	Sensitivity to Generalized Model Uncertainties	127
5.2.4	Experiments on Real Data	129
5.2.4.1	Ground Truth Reference	129
5.2.4.2	FE model parameterization and 2D Observations	129
5.2.4.3	Stochastic Environment: Filter Parameter Tuning	130
5.2.4.4	Filter parameterization	130
5.2.4.5	Reducing the number of markers	131
5.3	Conclusion	133
VI	Conclusions and Perspectives	135
6	Problems and Solutions for Clinical Application	137
6.1	Introduction	139

6.2 Process Model 140

6.2.1 Vessel Geometry 141

6.2.2 Model Input 143

6.3 Observations Process 144

6.4 Computation Time 145

6.5 Method Validation 148

6.6 Future Applications 151

6.7 Conclusions 151

Bibliography 153

PUBLICATIONS

Journals

- [1] R. Trivisonne, E. Kerrien, S. Cotin, Constrained Stochastic State Estimation of Deformable 1D Objects: Application to Single-view 3D Reconstruction of Catheters with Radio-opaque Markers, *Computerized Medical Imaging and Graphics* 81,(2020)

Conference Paper

- [2] R. Trivisonne, E. Kerrien, S. Cotin, Augmented 3D Catheter Navigation using Constrained Shape from Template, *Hamlyn Symposium* (2017) 3–5
- [3] R. Trivisonne, I. Peterlik, S. Cotin, H. Courtecuisse, 3D Physics-Based Registration of 2D Dynamic MRI Data, in: *MMVR - Medicine Meets Virtual Reality*, Los Angeles, United States, (2016)
- [4] Y. Adagolodjo, R. Trivisonne, N. Haouchine, S. Cotin, H. Courtecuisse, Silhouette-based pose estimation for deformable organs application to surgical augmented reality, in: *2017 IEEE/RSJ International Conference on Intelligent Robots and Systems (IROS)*, (2017), pp. 539–544

Part I

General Introduction

GENERAL INTRODUCTION

Table of Contents

1.1	Introduction	5
1.2	Clinical Context	6
1.2.1	Endovascular Minimally Invasive Surgery	6
1.2.1.1	Interventional Devices	8
1.2.2	Principles of Fluoroscopy	8
1.2.2.1	Equipment and Mode of Operation	9
1.2.2.2	Fluoroscopic Images	10
1.3	Problem Assessment and Contributions	10
1.3.1	Limitations of Fluoroscopic Procedures	11
1.3.2	Proposed Solution	12
1.3.3	Manuscript Outline	13

1.1 Introduction

This PhD work is set within the domain of computer-assisted interventions (CAI). Such field of research embraces all the typologies of medical procedures planned or performed with the support of computer technologies.

In particular, we address our research towards fluoroscopy-based minimally invasive endovascular procedures, intending to enhance the visualization of X-ray fluoroscopic images. Indeed, better visualization of the fluoroscopic-guidance would improve surgical insights on all levels. This augmented view would lead to an increase in the number of positive outcomes, shorten the overall procedure and, consequently, reduce radiation exposure for both patients and operators.

In particular, this research aims to propose a new method to retrieve in real-time the three-dimensional (3D) shape of the navigating device, solely based on monocular fluoroscopic images. Combining a 3D visualization of the surgical scene with the 2D fluoroscopic images, could significantly improve the visual feedback of the ongoing procedure, allowing the surgeon to navigate inside the vascular tree relying on a three-dimensional image. Indeed three-dimensional feedback not only would facilitate navigation providing depth information, but also would allow surgeons to virtually access structures which are not visible in the fluoroscopic image.

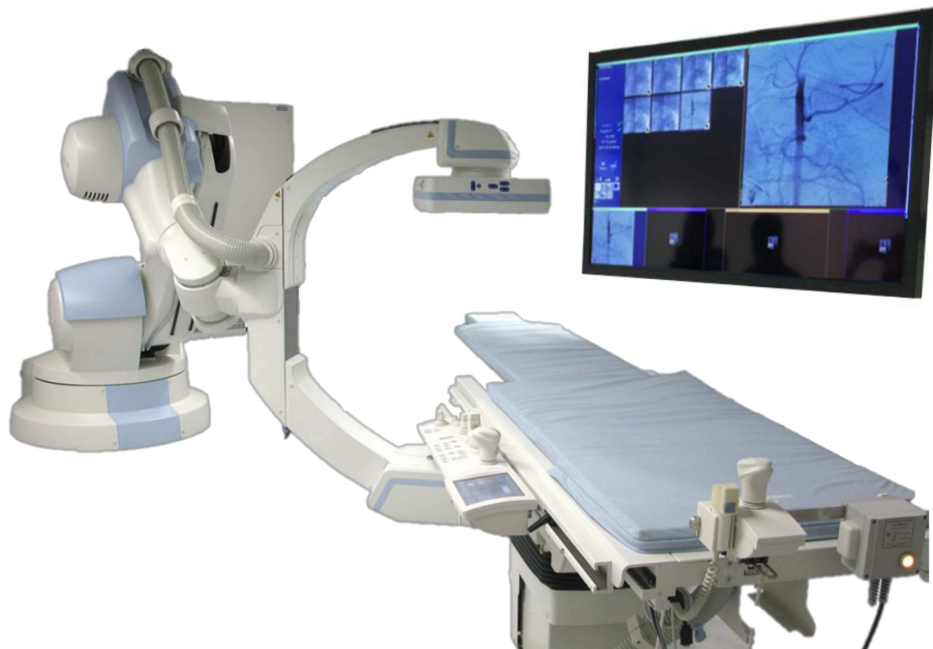


Figure 1.1: Example of Siemens C-arm Artis Zeego equipment for X-ray generation and detection, used in interventional radiology, general vascular applications and hybrid procedures.

1.2 Clinical Context

In minimally invasive surgery (MIS), target lesions are reached through small peripheral accesses, which allow surgeons to insert different kinds of surgical instruments to treat the disease without the need for large incisions. Compared to open surgery, minimally invasive procedures enable to significantly reduce the risk of complications, and the recovery time of the patients.

In the following sections, we outline a brief description of minimally invasive procedures, and the basic principles of fluoroscopy, to understand better how computer technologies, in particular a virtual simulation of the three-dimensional reconstruction of the surgical scene, could improve the visualization in such image-guided procedures.

1.2.1 Endovascular Minimally Invasive Surgery

Minimally invasive techniques are particularly useful for blood vessels and lymphatic system conditions, which can then be treated using small instruments, like catheters, guide-wires, balloons, and stents. Such procedures are known as Vascular (Endovascular) Minimally Invasive Surgery. The instruments are inserted through a distal puncture point and manipulated through the vascular tree, or other pathways, up to reach the target lesion (see Fig. 1.2).

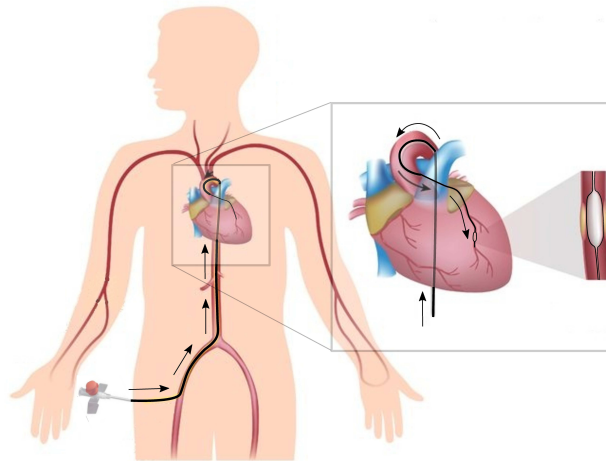


Figure 1.2: Endovascular procedure (Coronary Angioplasty) to treat coronary stenosis with a balloon catheter. The catheter is inserted through the femoral artery, and pushed through the vascular tree in order to reach the region of interest and treat the lesion.

Endovascular minimally invasive surgeries include: angiography, stent and filter placement, vascular embolization, percutaneous transluminal angioplasty (PTA), radiofre-

quency cardiac catheter ablation, thrombolytic and fibrinolytic procedures and others, for more details see [5].

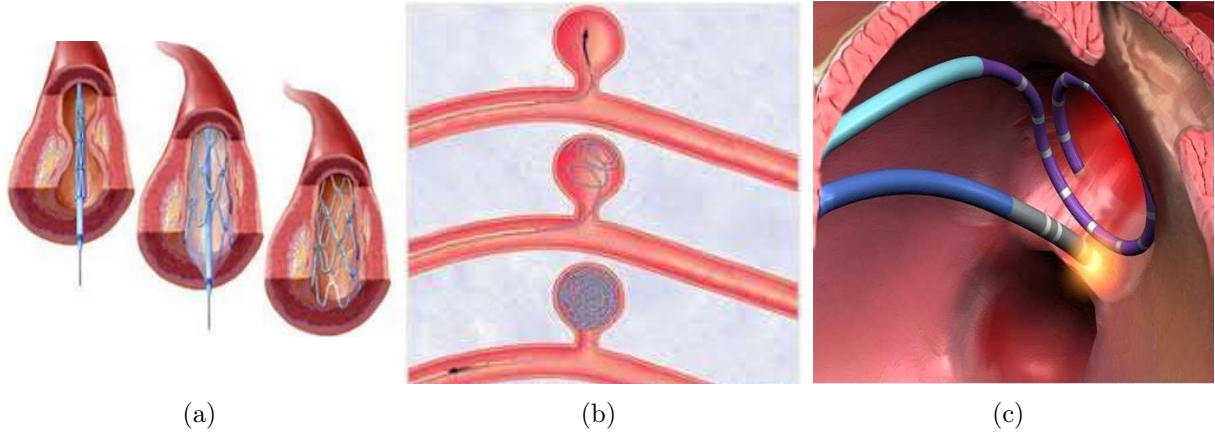


Figure 1.3: Examples of endovascular procedures performed under fluoroscopic guidance. (a) Stent placement: a wire mesh tube is placed to properly open an artery during an angioplasty. (b) Endovascular treatment of an aneurysm: several coils are placed into the aneurysm through a catheter which is subsequently detached and withdrawn. (c) Radiofrequency ablation of the cardiac wall.

Without direct access to the operative site, the entire procedure needs to be performed under medical image-guidance. Such guidance provides the operator with live feedback on the anatomy of the patient and the position and shape of the deployed interventional device. The problem is that surgeons must navigate inside the 3D vascular tree, relying only on bi-dimensional (2D) images. Also, such images may be challenging to interpret due to poor contrast or the presence of multiple overlaying structures, which prevent a clear visualization of the target lesion.

For endovascular procedures, standard imaging systems are X-ray fluoroscopy, which provides high-quality visualization of radio-opaque instruments and devices. An iodinated contrast agent is often injected to reveal the patient's vasculature, but sometimes view angles are chosen before the administration of contrast and may not demonstrate specific lesions.

Volumetric imaging systems may be used as additional support to 2D fluoroscopy to have further 3D information. For example, computed tomography angiography (CTA) and magnetic resonance angiography (MRA) allow pre-operatively acquiring three-dimensional data-sets of the vascular tree and their environment. Other techniques like 3D rotational angiography (3DRA) based on C-arm-like systems allow intra-operatively to obtain volumetric data of the vascular tree. The main problem with 3D data-sets lies in its registration to the 2D images. Indeed, tissue deformations caused by breathing motions or interaction with other organs, and different configurations between pre-operative and intra-operative acquisition, make the 2D-3D registration problem non-trivial.

The nephrotoxicity of the agent, the radiation exposure, and the loss of depth perception in X-ray images, are reasons why improved means of visualization have been investigated.

1.2.1.1 Interventional Devices

The interventional devices typically used in endovascular procedures are catheter and guide-wires. A catheter is a hollow flexible tube that can be inserted in duct or vessels. Thereby, catheters either allow the injection or drainage of fluids or provide a passage-way and access for other surgical instruments, such as stents, balloons, or micro-coils. Catheters are normally composed of different polymers which present good properties in terms of strength, flexibility, torque control, low resistance of the internal surface, and radio-opacity. Their configuration (fig.1.4(a)) presents a hub, a body, and a proximal tip, available in different designs according to the specific application (fig.1.4(b)).

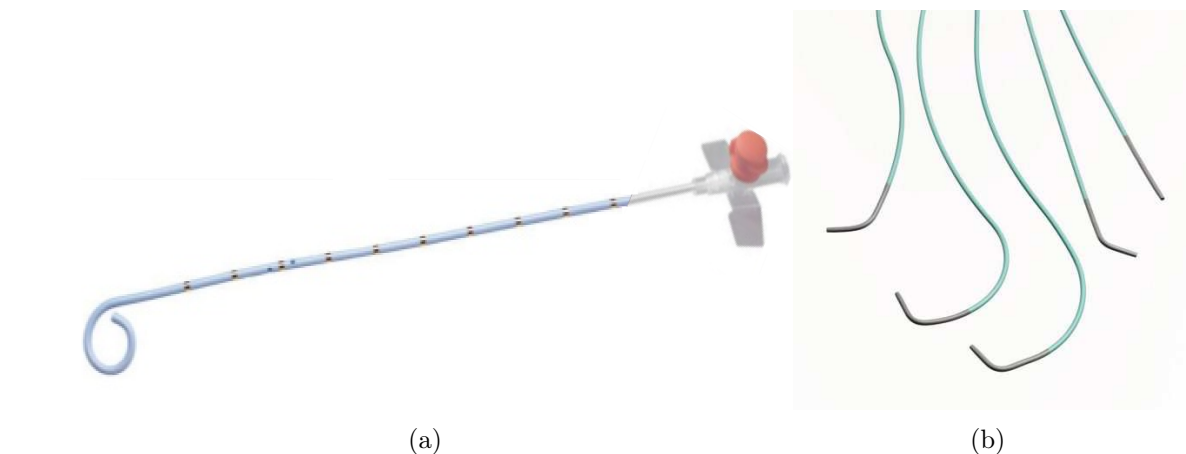


Figure 1.4: (a) The hub is a threaded plastic connection at the end of the catheter, which allows the injection of fluids or the insertion of coaxial instrument. The body can reach length of 80-120cm according to the specific application (b) The design of the tip (straight, pigtail, cobra tail, sheperd,...) Depends on the application and the anatomical target © Boston Scientific.

Catheters may be pushed towards placement, through a stainless steel metallic structure, known as the guide-wire. Guide-wires are used to facilitate the insertion of the catheter by increasing its rigidity. Thereby, the clinician first inserts the guide-wire, and then the coaxial catheter slides around the guide, following its path.

1.2.2 Principles of Fluoroscopy

Fluoroscopy is a real-time imaging technique based on X-rays. It is principally used for guidance in interventional radiology and image-guided surgery, due to its ability to

show the dynamic anatomical process. An overview of fluoroscopy based procedures is presented in [6]. In particular, fluoroscopic techniques enable clinicians to visualize in real-time, and simultaneously, the contrast-enhanced internal anatomical structures, their motion, as well as the dynamics of the interventional devices which are being deployed.

1.2.2.1 Equipment and Mode of Operation

A fluoroscope consists of an X-ray source and a detector, and the patient is positioned in between. Modern fluoroscopic systems are typically mounted on a C-arm machine (see Fig. 1.1). The X-ray source and the detector are on the opposite extremities of the C-arm. Such configuration allows effortless rotations around the operating table, providing posteroanterior, lateral, and oblique angles of view. Typical C-arm equipment may be floor mounted (Fig. 1.1), ceiling mounted (Fig. 1.5(a)), or mobile in order to be displaced within the operating room (Fig. 1.5(b)). Biplane systems include two C-arms (Fig. 1.5(c)) and enable clinicians to visualize simultaneously two different projections of the patient. Such systems are used for specific applications in cardiac and neuroangiography procedures.

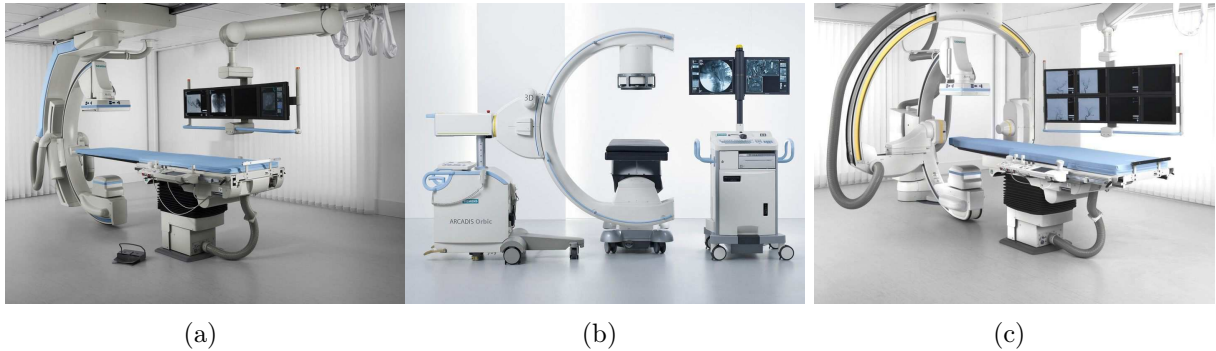


Figure 1.5: (a) Ceiling mounted, (b) Mobile C-arm, (c) Biplane System. All right reserved © Siemens

Different modes of operation may be used according to the specific application. In classic continuous fluoroscopy, the X-ray beam continuously hits the patient providing high time resolution; this is particularly useful to examine processes which require at least 30 frames/s to be adequately visualized. On the other hand, such modality entails a higher amount of emitted ionizing radiation. For that, both the patient dose and the fluoroscopy time needs to be lowered. An alternative to continuous fluoroscopy is pulsed fluoroscopy, in which a series of short X-ray pulses (i.e. 10ms/pulse) is emitted at different selectable frame rates (30, 15, 7.5 frame/s). Pulsed fluoroscopy images appear sharper with lower motion blur. Low pulses rates enable a spare of X-ray dose, but that may not be suitable for rapidly moving organs or advancing instruments. Higher acquisition rates provide better images for dynamic phenomena, to the detriment of X-ray dose reduction. An interesting comparison between continuous and pulsed fluoroscopy can be found in [7]

and [8].

1.2.2.2 Fluoroscopic Images

Typically, in fluoroscopic images, all the radio-opaque structures appear overlaid on a grey-scale projected image. The grey level of each structure depends on the proper X-ray absorption coefficient (see fig. 1.6(a)). Image processing is therefore employed to improve the quality of the fluoroscopic flow. Commonly, to reduce image noise, a frame averaging on consecutive images, with a user-selectable number of frames, may be performed ([9]). Such temporal averaging combines the most recent frame with the previous ones, allowing to eliminate the temporally uncorrelated noise. This processing technique allows the reduction of quantum noise and works optimally whenever changes between two consecutive images are small.

In endovascular procedures, Digital Subtraction Angiography (DSA) is a type of fluoroscopic technique used to visualize vasculature in a dense environment clearly (see Fig. 1.6(b)). In particular, sequential images acquired after injection of a contrast agent are subtracted from a mask image that includes only the anatomical background (previous injection). DSA images eliminate static structures and enhance contrast. A further imaging mode, is the road-map (see Fig. 1.6(c)) that enables to create a map of the vasculature, generated by using a stored image of a contrast-filled vessel (similar to Fig. 1.6(a)) subtracted in real-time to a contrast-free fluoroscopic image. Such road-map image can be either displayed alongside the live fluoroscopy or overlaid to it, so that clinicians may have an idea of both the path to follow and the live motion of a deployed instrument. References or further information about fluoroscopy and its principles can be found in [10], [11], [12].

1.3 Problem Assessment and Contributions

The use of fluoroscopy as intra-operative guidance facilitated the development of several minimally invasive techniques. Nevertheless, this type of medical imaging technique presents some drawbacks, related to several factors. Study researches in different domains have been carried out to overcome some of these disadvantages.

In the following sections, we illustrate the main shortcomings of fluoroscopy, and how our own proposed solution can overcome some of the limitations. The chapter ends with our contributions to the state of the art.

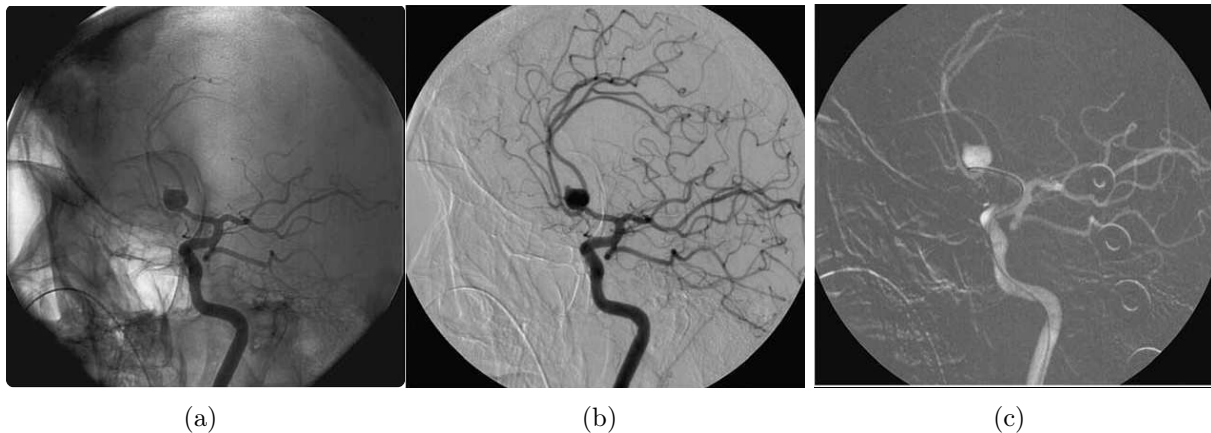


Figure 1.6: (a) Original fluoroscopic unsubtracted image-head, bone structures are superimposed to contrast-enhanced vasculature. (b) DSA image (here at the end of contrast medium injection) where the vasculature is enhanced with respect to the background, online subtraction of a constant, contrast-free mask image, during contrast medium injection. (c) Road-map in which both the vessel path and the radio-opaque instrument are visible, online subtraction of a constant, contrast-enhanced image, during tool navigation under fluoroscopic guidance.

1.3.1 Limitations of Fluoroscopic Procedures

Like other X-ray based procedures, fluoroscopy carries some risks linked to radiation exposure. Such risks may include biological effects, such as injuries to the skin and the underlying tissues, and radiation-induced cancer. These effects may affect both the patient and the operators, and extensive studies have been carried out to evaluate radiation exposure ([13], [14]).

Risks related to radiation exposure are mainly due to the ability of fluoroscopy to display dynamic processes: a fluoroscopic flow is, in fact, provided by a series of images, produced at a maximum rate of 30 frames per second. Whereas the radiation exposure needed to generate one fluoroscopic image is low, higher exposures can result from the overall procedure time given the large series of acquired images. Thus, the total fluoroscopic time is one of the significant factors that determine the dose. Staff and operators are usually protected by lead aprons and lead glass shielding. For both the patients and the operators several dose reduction techniques may be applied: pulsed fluoroscopy at low image rate, last image hold, intermittent exposures, grid removal and others ([15], [16]).

Another minor disadvantage is related to the need for nephrotoxic contrast agents used to enhance the visualization of internal structures. Iodine-based or Gadolinium-based solutions are usually injected in the navigated artery through a catheter, for techniques such as DSA or road mapping, to highlight blood vessels changing the absorption of X-ray. Despite being safe drugs, an adverse allergic reaction may occur. In their work, [17] summarize current knowledge for safe use of contrast media.

The second main drawback related to the intrinsic properties of X-ray images is the lack of spatial information. In particular, projective 2D fluoroscopic images cannot provide depth

information. Such lack of depth perception is further complicated by the environment of overlaid dense multiple anatomical structures (see Fig. 1.7), and it has been identified as one of the most important factors affecting clinical performance [18]. By solely relying

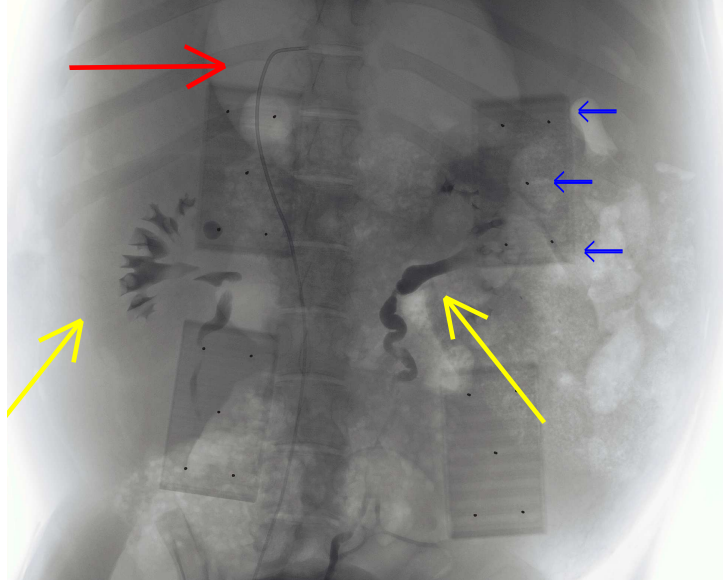


Figure 1.7: Fluoroscopic image of porcine abdomen acquired during experimental trials. A contrast medium has been injected and, for that, renal arteries appear more visible (yellow arrows). Other anatomical structures appear overlaid in the background more or less visible according to their properties. The radio-opaque catheter is pointed out with a red arrow, whereas blue arrows show some radio-opaque markers which we used in our experiences to calibrate the C-arm. In this figure, black dots are radio-opaque calibration markers.

on bi-dimensional images, it is often arduous for the clinicians to mentally reconstruct the 3D spatial configuration of the interventional device, the tortuous anatomy, the bifurcations, or the precise location of the target lesion. Therefore, to better reconstruct the three-dimensional configuration, clinicians often rely on other imaging techniques, like ultrasound, or acquire other fluoroscopic images along different projective angles of view. This reconstruction implicates increasing procedure time, with a consequent increase of radiation exposure.

1.3.2 Proposed Solution

The main objective of the work is to enhance the visual feedback of procedures based on fluoroscopic images. Therefore, we propose to retrieve the 3D shape of the device from a monocular fluoroscopic view and combine the 3D reconstruction with the 2D fluoroscopic images. A better 3D visualization of the device within the patient anatomy would eventually allow to decrease the global procedure time and, as a result, the overall radiation exposure.

2D fluoroscopic images provide just partial information about the current configuration of the device. Such projective information could still be combined with a 3D model of the device to find an optimal estimation of the real 3D catheter shape. Retrieving a 3D shape from 2D information is not straightforward. 2D-3D reconstruction is an extremely ill-posed problem. Given the missing information on depth direction, several 3D configurations may correspond to the same projection, and a unique solution does not exist. To reduce the ambiguities deriving from the absence of depth information, some additional constraints need to be applied. Such constraints may be of different kinds. For example: regularization criteria applied to the 3D model (geometrical or physical properties), a boundary volume defined by the surrounding vessel or the use of multiple images acquired under different angles of view.

Compared to the existing methods, this work proposes a novel stochastic approach that combines a 3D navigation model of the device with 2D information from fluoroscopic images through an Unscented Kalman Filter (UKF). We focused our research on the reconstruction of flexible and inextensible devices like catheters and guide-wires.

We defined an advanced navigation model, where the interventional device is described through a physics-based finite element (FE) model. Indeed, taking into account the tool's physical properties enables achieving a better description of its dynamic behavior. The navigation of the device inside the vasculature is performed through a non-linear collision model, which takes into account complex phenomena, like non-rigid non-slip contacts, providing a more realistic description of the interactions between the catheter and the surrounding vessel. An optimized implementation allows achieving real-time computation and performing FE simulation at frame-rates compatible with fluoroscopy ones. Although the advanced model provides a realistic description of the catheter dynamics, a perfect characterization of the navigation model is practically not feasible. Some errors may affect the mechanical parameterization of the catheter's model, and some uncertainty related to the interaction model (friction coefficient of the vessels surface, the vessel geometry, etc.).

An Unscented Kalman Filter is used to merge the catheter navigation model with the detected image features. In practice: we correct the predicted 3D shape of the device (provided by the navigation model) using the information provided by external measurements about its current state (the projected shape of the device in the fluoroscopic image). The use of such Bayesian formalism allows considering and tackling errors and uncertainties in model parameterization and implementation, and noise in external measurements (i.e. error detection in fluoroscopic images).

In conclusion, we propose a novel method to reconstruct the 3D shape of an interventional device, which can handle and tackle several challenges.

- The type of external measurements: we use one-view projective observations, that only provide partial information on the current state of the estimated object.

- The nature of the shape to reconstruct: a catheter is a threadlike object, different from reconstructing than an entire surface.
- The interaction between devices and surrounding vessel: for the stochastic filter, this is a problem of constrained state estimation.
- The real-time computation to achieve: the aim is to be compatible with typical fluoroscopy acquisition frame rates.

These aspects will be examined in detail in the following chapters, highlighting why such subjects are challenging and how our approach can overcome them.

1.3.3 Manuscript Outline

This manuscript is structured as follows:

1. The current chapter introduces the clinical context, the current problems and limitations, and our proposed solution.
2. Chapter II includes the state of the art of the related works. Besides a more detailed review on 3D reconstruction method from 2D views, we also present some literature on the different scientific topics covered by our approach. We provide a full description of different models used for interventional devices, and we present a brief state of the art on image segmentation methods, although this subject is out of the scope of our work, and no research has been performed in this field.
3. Chapter III presents an initial approach for 3D catheter reconstruction from 2D monocular images. The method can be defined as a constrained Shape-from-Template approach, in which image information is taken into account within the simulation as mechanical constraints computed through Lagrange multipliers. This work has been the object of the publication [2].
4. Chapter IV introduces stochastic simulation, presenting a preliminary study on the state vector and the identification of model uncertainties.
5. Chapter V, the core of our work, details the stochastic simulation for catheter navigation, also defined as a constrained Unscented Kalman Filter approach. The physics-based catheter model and 2D fluoroscopic image features are redefined within the Bayesian framework of an Unscented Kalman Filter. This work has been the object of the publication [1].
6. Chapter VI presents a final overview of our work. We highlight possible solutions to enhance and generalize our approach, along with some perspective for future works.

Part II

State Of The Art

STATE OF THE ART

Table of Contents

2.1	Introduction	19
2.2	2D Enhancement of Fluoroscopic Images	19
2.3	Enhancement of Fluoroscopic Images with 3D Anatomy Reconstruction	20
2.4	Enhancement of Fluoroscopic Images with 3D Instrument Reconstruction	23
2.4.1	Interventional Device Model	23
2.4.2	Overview on Reconstruction Methods	27
2.4.2.1	Biplane Images Reconstruction	27
2.4.2.2	Monocular Images Reconstruction	28
2.4.2.3	Monocular Images Reconstruction using External Sensors	33
2.4.3	Discussion	37
2.5	Conclusion	39

2.1 Introduction

Fluoroscopic guidance provides essential information about the current configuration of both the patient’s anatomy and the deployed interventional device. Nevertheless, X-ray images’ projective nature entails a loss of information in terms of 3D perception.

For the last twenty years, computer-aided image guidance has enabled us to process 2D fluoroscopic images, combine them with other medical data, enhance their visualization, or provide more realistic feedback of the surgical scene. In particular, it is possible to augment the fluoroscopic view by merging the 2D X-ray images with 3D models of the anatomical environment and or the interventional device.

In general, existing approaches, which enable to enhance the visualization of fluoroscopic images, can be classified into two main classes: methods purely operating in the 2D domain, where the interventional device is segmented within fluoroscopic; and approaches using 3D priors to add 3D information to the surgical scene.

In this chapter, we provide a quick overview of methods proposing a 2D enhancement fluoroscopic images (Sec. 2.2), whereas in Sec. 2.3 we expose the different solutions currently used to enhance the visualization of X-ray fluoroscopic images through the visualization of 3D anatomical structures. A more detailed state of the art of methods proposing a 3D reconstruction of the surgical device is presented in Sec. 2.4, being the main objective of this thesis.

2.2 2D Enhancement of Fluoroscopic Images

Over the last years, several approaches have been proposed to detect and track the interventional device in X-ray images. Catheter and guide-wires are deformable structures, with average contrast, in a noisy and dense background. Therefore, their visualization is often impractical without subtracted images, as in Fig. 1.6(a).

The segmentation of the device within the image can be performed with different purposes: to purely enhance the visualization of the tool, to exploit the extracted shape to compensate for respiratory motion ([19], [20]), or to use the segmented shape to perform 2D-3D registration of anatomical models. In particular, vessel registration can be performed by aligning the vessel center-line with the extracted device shape ([21], [22]).

For general curved shapes, one of the first works on guide-wire extraction and tracking in fluoroscopic images was presented by [23], based on researches on enhancement and extraction of curved line structures ([24]). The method relies on the use of Hessian-based filters, to enhance the instrument in images with a low signal-to-noise ratio (SNR) and then interpolate the extracted points with a B-spline model. Other methods have been then proposed, based on the same principles ([25], [26], [27]).

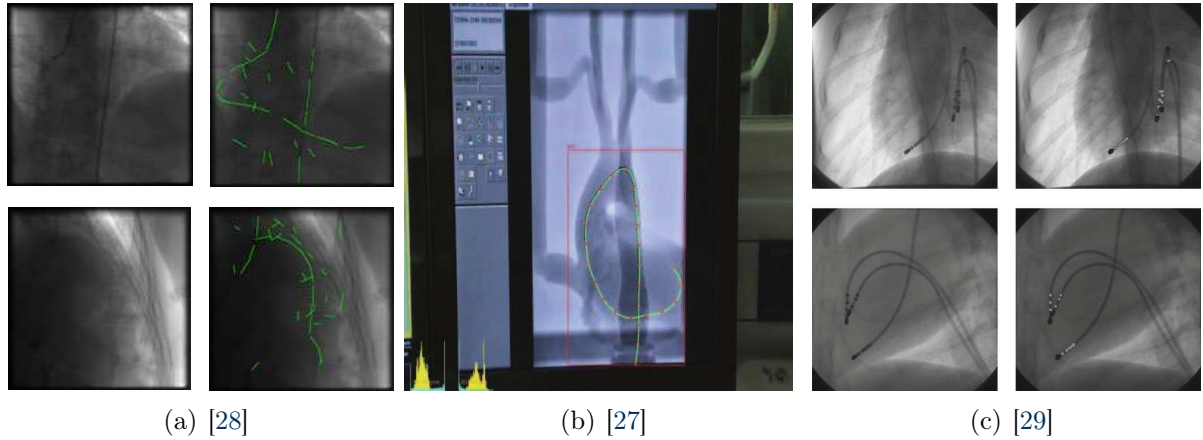


Figure 2.1: [28] Input image and detected segments. [27] Optimal B-Spline (yellow) which allows to track the catheter even in presence of self-intersections. [29] Electrode detection: input image on the left and results of detection with overlaid extracted features.

Machine learning, [28],[30], and convolutional neural networks (CNNs) [31] are different approaches that allows segmenting curved structures within fluoroscopic images.

Specific methods exist for ablation catheters, embedded with metallic electrodes ([32],[33],[29]) that are easy to detect and track in fluoroscopic images.

A recent method by [34] proposes to improve depth perception without employing virtual or augmented reality, but rather by predicting depth information from a single view X-ray image. In particular, the depth model is learned through a label-consistent deep learning method incorporating atlas, prior spatial constraints, and patient-specific pre-operative CT models. The work is an initial proof of concept on simulated X-ray images.

Although such methods can significantly improve the quality of the visualization, they solely provide 2D information that does not overcome the lack of depth perception. 3D knowledge may be included by merging the fluoroscopic image of either 3D models of the vascular anatomy, or 3D representations of the inserted device. Such approaches are respectively discussed in detail in sections 2.3 and 2.4.

2.3 Enhancement of Fluoroscopic Images with 3D Anatomy Reconstruction

The intrinsic nature of 2D projective images often forces clinicians to infer a 3D surgical scene from theoretical knowledge of the anatomical structures. In general, such priors can not always be reliable due to substantial anatomical variability. For that, whenever using C-arm like equipment, several acquisitions along different angles may be performed before starting the procedure, to conceive a better virtual reconstruction of the anatom-

ical configuration. Nevertheless, this multiple-acquisitions inspection can be extremely time consuming and not always feasible in a clinical room. Usually, only one optimal fluoroscopic view is generally chosen according to the specific pathology. Besides that, this view can not be valid and useful during the whole procedure.

As presented in [35], image-guided surgery (IGS) extensively exploits mixed reality to combine the real environment with pre-operative or intra-operative models of the patient anatomy. Such augmented visualization provides the surgeon with a more extensive view beyond the anatomy that is actually visible, which entails a better understanding of the overall anatomical configuration. Pre-operative 3D volumetric data may be acquired through different technologies and then registered to 2D X-ray images. 3D imaging technologies include: Computed Tomography Angiography (CTA), as done in [36] and [37], or 3D Rotational Angiography (3DRA) as presented by [38] (Fig. 2.2). In fluoroscopy-based procedures, enhanced views, where different kinds of images are fused to 2D X-ray images, enable globally reducing the radiation time, the overall procedure time, and the injected contrast medium. This has been shown by [39], who compare classic thoracic endovascular aortic repair procedures (TEVAR) with hybrid TEVAR procedures performed with 2D-3D of image fusion (IF) (Fig. 2.3(a)).

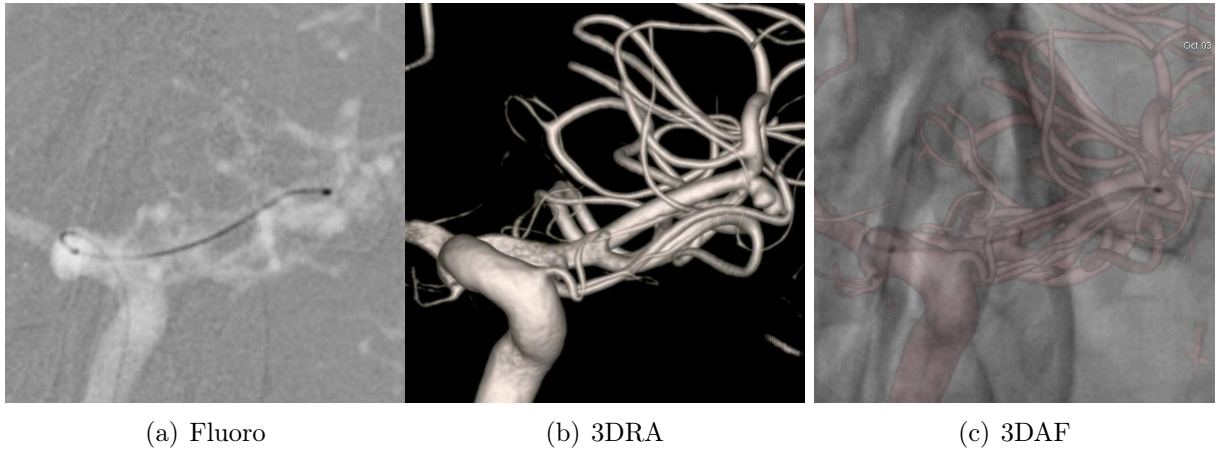


Figure 2.2: [38] (a) Fluoroscopic Image. (b) 3D Model of the Vasculature (DRA). (c) 3D Augmented Fluoroscopy (3DAF) with transparent 3D model and 2D image. It is possible to notice how the 3D model allows visualizing an aneurysm, otherwise not detectable within the 2D image

In general, to register a 3D model to a 2D image, a calibration of the C-arm must be performed to find the projection matrix relating the 2D space of the fluoroscopic image with the 3D world. Several methods have been proposed. In [40], authors use a rigid phantom embedded with radio-opaque markers: minimizing the reprojection mean quadratic error of such reference points, they retrieve the projection matrix. In [41], a calibration method has been developed, specific for a clinical context, exploiting a mechanical model of the C-arm. Using a planar calibration target, they measure the variation of the intrinsic

parameters on a vascular C-arm. Other approaches are based on 2D-3D registration. [42] propose a review of the main methods used in image-guided interventions: feature-based strategies iteratively minimize the distance between corresponding points or contours, intensity-based or gradient-based approaches iteratively optimize the similarities between images or gradient vectors.

An important aspect lies in the fact that vascular structures are soft tissues which may undergo large deformations due to external forces or physiological phenomena; also significant changes may occur between the pre-operative and the intra-operative configurations. For that non-rigid 2D-3D registration techniques have been developed. Some methods in an one view scenario have been proposed by [43] (see Fig.2.3(b)), [44] or [45]. Non-rigid registration requires additional constraints beyond iterative minimizations or optimizations, such as: geometry preservation constraints [43], center-line matching between the real vessel and the virtual surface [44] or center-line matching between the real vessel and the 2D catheter shape extracted in fluoroscopic images in [46].

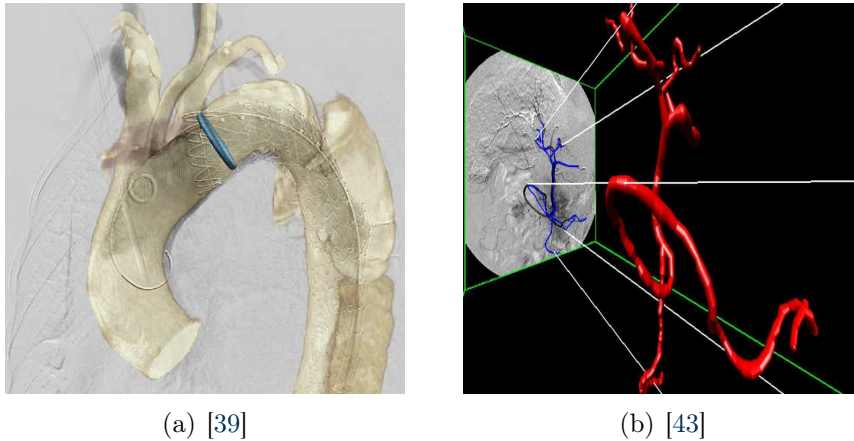


Figure 2.3: Example of 2D-3D overlaid images: [39] Complete angiogram after TEVAR procedure with IF of a 3D model of descending aorta. [43] Visualization of the 2D-3D C-arm/ patient scenario

Multi-modal imaging techniques above presented would allow reducing the ambiguities by providing an augmented view. Intra-operative live reconstructions could be performed with a C-arm like equipment, to check, whenever needed throughout the procedure, the precision of the 2D-3D registration. Unfortunately, temporal constraints (related to the acquisition time and the processing and reconstruction of medical images) and a substantial amount of additional radiation exposure make the use of real-time intra-operative 3D reconstructions not feasible in practice. Another minor disadvantage is that regardless of the registration method, the benefits of using 3D overlays on 2D images are limited by the visualization choice. The high opacity of the 3D structures makes the background X-ray image not visible but enhances the virtual 3D model. Besides, low transparencies keep the X-ray image visible but reduce the actual usefulness of the 3D render.

2.4 Enhancement of Fluoroscopic Images with 3D Instrument Reconstruction

Besides the 3D visualization of anatomical models, it is possible to reconstruct the 3D shape of the interventional device. Combining the current 2D fluoroscopic image with a 3D reconstruction of the interventional device, plus the 3D visualization of the anatomical structures, could greatly improve the surgical insight.

To retrieve the shape of the interventional device, information on its current state must be provided. In general, such information may consist of visual data extracted from fluoroscopic images (monocular images or obtained from biplane system), measurements provided by external sensors embedded onto the device (such as electromagnetic sensor, or optical fibers based sensors), or a combination of both. In any case, to retrieve the 3D shape of the device, this kind of data must be interpolated or regularized by a model providing some priors on the shape of the device and or its behavior. Such models can include but are not limited to: geometric models, FEM models, kinematic or dynamic navigation models. Several approaches have been developed to retrieve the 3D reconstruction of the device, combining priors on the device and information about its current state, according different strategies.

Although different types of interventional devices exist, we focused the state of the art of this thesis on methods like ours, conceived for devices like catheters and guide-wires. Generally speaking, this type of instruments undergoes rigid motion (due to i.e. respiratory motions) and non-rigid deformations, caused by interaction with surrounding anatomy or manipulations by the operators. The time-varying shape of the device can generally be seen as a 3D open non-planar curve.

2.4.1 Interventional Device Model

As stated above, information about the current configuration of the device, provided by fluoroscopic images or external sensors, is not sufficient to retrieve the whole 3D reconstruction of the instrument. For that, it must be combined with a model describing the shape and or the behavior of the device. Generally speaking, such models can be either geometric, purely describing the shape, or physics-based and kinematic, providing a description of the behavior of the device.

Parametric models, such as splines, have been widely used to model the shape of catheter-like devices. A spline is a polynomial piecewise-defined function (see Fig. 2.4(a)) and different types of splines may be used according to the specific modeling needs. For surgical thread simulations, authors in [47] combine the use of Catmull-Rom splines and uniform cubic B-Spline respectively for their property of interpolation and their better continuity. Given that splines are purely geometric models that do not provide any information about the behavior of the device, authors defined a constraint to control the model; in partic-

ular, they constrain the curve to slide through known fixed locations. Indeed, given the properties of spline functions, a good estimation of the device shape is only possible when combining spline models with additional information coming from other sources: biplane images ([48], [49], [50]), external sensors ([51], [52]) or applying multiple regularization constraints ([53], [54]).

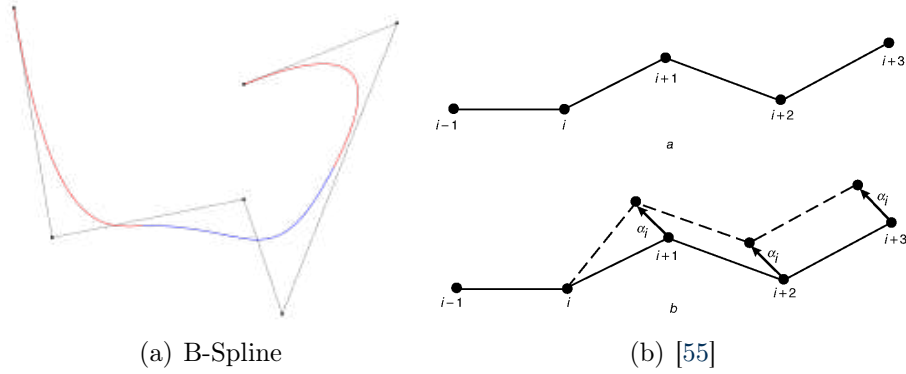


Figure 2.4: (a) Example of a B-spline as a piece-wise polynomial function. (b) [55] Schematic representation of guide-wire at rest and under rigid translation after one joint changes configuration.

A geometric approach, where the catheter is represented as a multi-body system composed of connected links, enables users to have a description of the device behavior. Researches presented in [56] and [57] propose to model endoscopic devices as rigid-links connected through joints, which allow the bending of the instrument. In [58], where authors propose a training system for interventional radiology, three different forces can be applied to the multi-body object: contact forces, injection forces for the device, and forces applied by the user at the proximal end of the instrument. This discrete model enables a good approximation of a catheter, but it requires many small links to represent a high degree of flexibility, thus leading to increased computational cost. In [55], a guide-wire is modeled as a series of connected small incompressible rigid rods. A further constraint of length preservation is imposed so that the movement of any joint is restricted to a 2D surface in the 3D space. The method operates in the quasi-static domain, to provide a good propagation of the device without precise knowledge of friction forces. Authors in [59] model the guide-wire as a series of rigid segments whose behavior is modeled according to Hooke's law. In their work, a quasi-static approach is adopted, and static friction forces are taken into account, under the hypothesis that the device is inserted slowly without any acceleration. The proposed approach does not fulfill real-time requirements. In [60], authors propose a mass-spring model in which the device is modeled as a series of particles connected by rigid springs of equal length, where rotation and translation movements are handled separately. The proposed strategy presents some instabilities when the instrument collides with a vessel bifurcation during the insertion. Both [60] and [59] solely model bending deformations. The method presented in [61] proposes a geometric approach for VR simulations of catheter navigation within a heart chamber. The device is modeled as

a series of rigid links which undergo different motions, depending on the segment of the catheter represented (tip, shaft, proximal part). According to the interaction with the heart wall (non-slip, pseudo-slip, slip contacts), the catheter model undergoes a different type of deformations. The method of [62] relies on a quasi-static approach for the propagation of the guide-wire, which is modeled as a linked rigid rod undergoing bending and translations. To take into account the mechanical properties of the device, they define a function of angular spring, constant for each joint. Collision response between the device and the surrounding anatomy is performed with a force correction strategy, instead of performing a time-consuming collision detection at every iteration of the algorithm. (Fig. 2.5(b)).

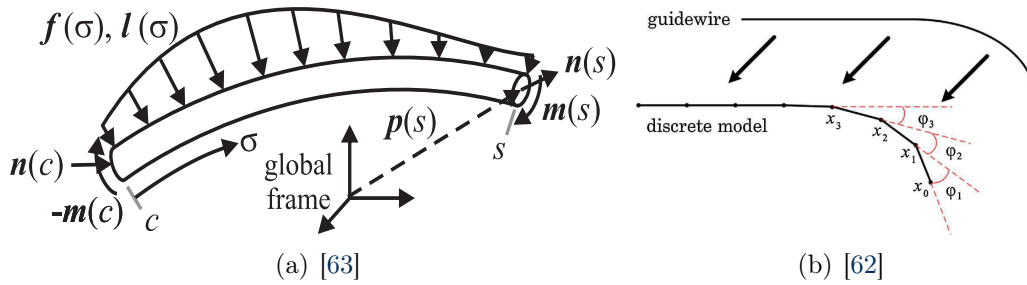


Figure 2.5: (a) [63] Section of a rod from c to s , subject to distributed and internal forces and moments. (b) [62] The guide-wire is separated into linked rigid rods and the tip portion is intrinsically curved.

The main advantage of geometric approaches lies in the low computational cost. Nevertheless, such methods require explicit modeling of contact forces and do not provide an accurate prediction of the device's behavior. For example, they do not allow any physical modeling of motions like torsions, or significant bending.

In that sense, physics-based approaches can provide a better prediction of the behavior of the device. Cosserat rod theory has been widely used to model one-dimensional elastic objects. Such a theory involves equilibrium relationships relating internal and external forces and moments along the length of a rod (Fig. 2.5(a)). The popularity of Cosserat models in computer graphics arose with [64], who proposed an expensive Newton iterative static approach to model thin elastic objects. [65] proposed a physically-based deformation model of Cosserat rod theory, based Finite Element Methods (FEM), to take into account effects like torsion. In medical applications, a hybrid approach is presented by [66] where they simulate guide-wire insertions, combining the body of the device (modeled as a series of non-linear elastic Cosserat rods) and the tip, modeled using a more efficient generalized bending model. Cosserat theory has also been used to compute the statics of a magnetically actuated catheter [67]. However, contact handling with such a model is difficult. For catheter navigation, where collisions occur continuously along the device's length, this is indeed a critical issue. Other physics-based approaches relying on a finite element representation have been proposed. Authors in [68] propose a new method based on three-dimensional beam theory which enables to handle geometric non-linearities

while having a real-time computation, through an incremental approach to handle large deformations. Based on this approach, [69] proposes a composite model of catheter/guide-wire taking into account complex interactions between the devices and the surrounding vessels. Similarly, [70] models an embolization coil as a set of deformable linked beams (see Fig. 2.6(a)), and interactions are modeled with non-holonomic constraints applied through Lagrange multipliers. More in general, this FE based approach, relying on three-dimensional beam theory, allows modeling bending, twist, and other deformations, plus the interactions with the surrounding anatomy in real-time.

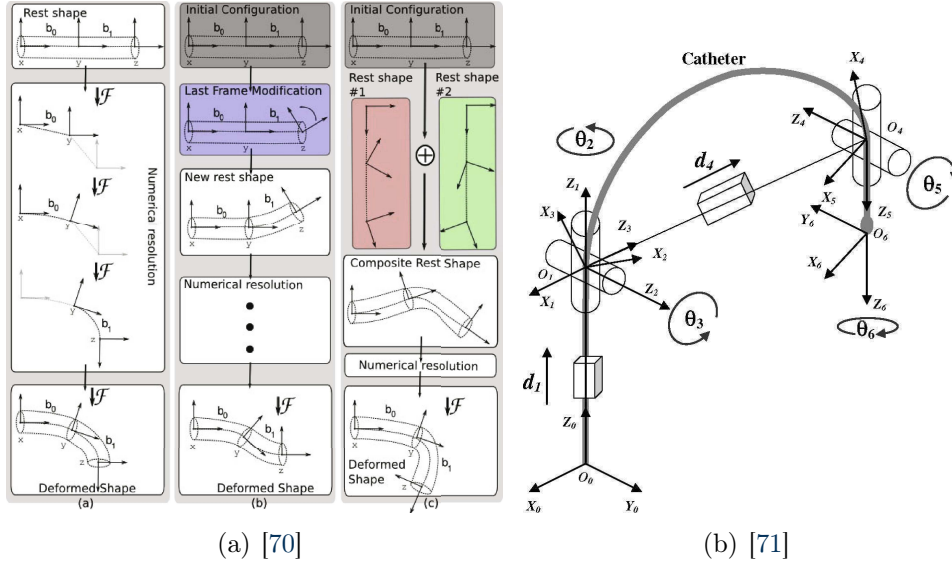


Figure 2.6: (a) [70] Modeling of a wire using linked beam element, internal forces are computed using a local reference frame to handle large deformations. (b) [71] Catheter model and the assigned Denavit-Hartenberg (D-H) coordinate frames.

Continuous robot theory is a third approach to model catheter-like devices. An exhaustive survey is presented in [63]. This is particularly useful for steerable robots, where the tip deflection is activated through a pull-wires mechanism. A first kinematic model has been proposed by [71], in which the tip position is predicted based on the configuration of the shaft and the manipulations performed on the catheter handle (see Fig. 2.6(b)). Interactions with surrounding anatomy are not taken into account. In [72], the authors model the tip of a steerable catheter through the beam theory to describe large deflections. Such approaches are valid only for devices actuated with a pull-wires like mechanisms.

The choice of the most appropriate model for catheter-like structures depends on the trade-off among model complexity, computational expense, and accuracy. Geometric approaches are more computationally efficient to solve, but they lack physical realism and precision for large deformations. On the other hand, physics-based approaches assure a better description of the object's behavior, but they are more computationally expensive.

2.4.2 Overview on Reconstruction Methods

Two are the sources of information that must be combined to reconstruct the shape of the device: information on the current configuration of the device and priors on its shape or behavior. For that, we decided to classify the reconstruction methods classified according to three main categories: reconstruction methods based on the use of biplane images (sec. 2.4.2.1), monocular reconstruction solely relying on visual data (sec. 2.4.2.2), and methods of monocular reconstruction based on the use of external sensors (sec. 2.4.2.3),

2.4.2.1 Biplane Images Reconstruction

As in Fig.1.5(c), biplane angiographic systems allow the simultaneous acquisition of images in two quasi-orthogonal planes. This setup improves the operator's perception of space for both the anatomical structures and the deployed devices. In this context, the 3D reconstruction of the device shape can be described as a classic stereoscopic reconstruction problem, in which the two calibrated cameras are the X-rays sources of the biplane system (see Fig. 2.7).

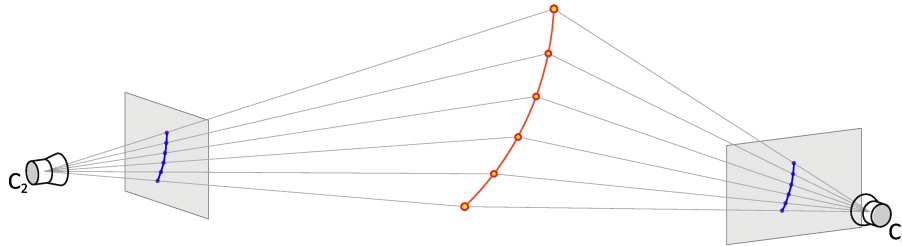


Figure 2.7: Schematic description of biplane reconstruction.

A common practice is to extract the projected shape of the device as a 2D curve and find the corresponding 3D shape under the hypothesis of uniqueness¹, regularity², and monotony of pairing³.

In [48], the authors use some B-spline models to fit the 2D projections. By enforcing the above-mentioned constraints, they retrieve a 3D B-spline from the two views. The quality of the reconstruction is dependent on the precision of the 2D B-spline extracted in the fluoroscopic images. Unfortunately, it is not always possible to have an accurate analytic parameterization of such 2D curves, given the image segmentation quality. In [73], the authors model the 3D shape as a set of connected 3D points. Constraints of monotony and uniqueness are applied by estimating, in 3D, a specific catheter direction and consequently defining a new 3D point along the predicted direction. Yet, they require a pre-processing step in which the position and the orientation of one of the 3D points must be initialized.

¹ A single 3D curve is projected on a unique 2D curve within the image.

² Enforce the smoothness of the curve, preventing from large curvatures.

³ The function which interpolates corresponding points has to be monotonic.

Additionally, the linear estimation of a new catheter path leads to some problems during the reconstruction algorithm. Alternatively, [74] proposes to reconstruct the 3D shape from non-structured 2D points. In particular, they back-project the 2D points first, then through clustering methods, they obtain a set of representative 3D points, reduced to a unique curve, thanks to a moving least-squares approach. Nevertheless, an additional third view is necessary to reconstruct more complex shapes. Another type of constraint exploits the temporal coherence of the catheter path. In [49], where the biplane system is employed asynchronously, a 3D B-spline curve is regularized so that its projections are consistent with the image features extracted in two views, where the information from the missing image (caused by the asynchronous acquisition) is created from the interpolation of its sequence neighbor. Nevertheless, a temporal constraint is not always suitable since abrupt movements may occur between two consecutive images. Also, the initialization step may be affected by some problems. In [50], the authors use epipolar geometry to segment images and create correspondences between 2D segments, rather than set 2D points. Then, when enforcing monotony and regularity constraints, they identify an optimal 3D shape using a B-spline function. A thorough state of the art of the main approaches relying on biplane systems is presented in Chapter III of [75], in which methods are classified according to both the type image-features detected within the images (e.g. set of disconnected points, fragments and segments, and parameters lines), and the constraints applied to retrieve the optimal 3D shape.

Although biplane systems facilitate the navigation providing two different angles of view, such equipment is not widely used in clinical routine (mostly due to their relatively high cost). Instead, they are used for specific applications where, in any case, solely one view is actually followed by surgeons. Other disadvantages are due to the necessary synchronization of the images. Also, the manipulation of biplane systems is not straightforward. For example, it is not possible for surgeons to indiscriminately change the orientations of C-arms during the procedure.

2.4.2.2 Monocular Images Reconstruction

Unlike biplane systems, mono-plane fluoroscopic systems (see Fig. 1.1) are extensively used in clinical practice and provide X-rays images along a single angle of view. The reconstruction of the 3D catheter using only a single 2D projection is an intrinsically ill-posed problem: several 3D configurations may correspond to the same 2D image, which entails an infinity of possible solutions (see Fig. 2.8).

In general, the information extracted from fluoroscopic images consists of the projected shape of the interventional device. Such projected shape is generally represented as a parametric curve, connected segments, or sets of points. The precision of the segmentation depends mainly on the quality of the image, in particular on the contrast to noise ratio of the instrument. In [76], a guide-wire is segmented as a parametric curve, and its

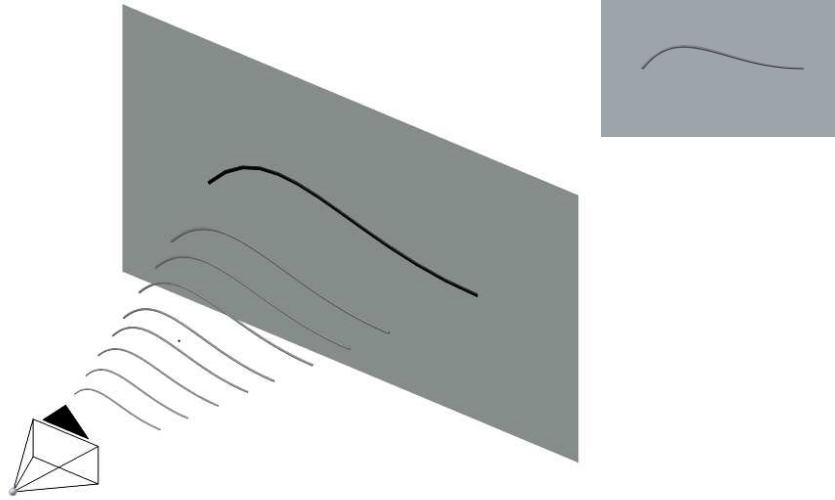


Figure 2.8: Several 3D configurations may correspond to the same 2D projection.

shape is detected within fluoroscopic images. Authors provide a segmentation error of 1.5 pixel (see Fig. 2.9(a)), for a guide-wire presenting in the image width of 3-5 pixels. The segmentation error increased with an increment in noise in images. Other approaches, such as [32], aim at detecting in fluoroscopic images specific features such as electrodes of ablation catheter (see Fig. 2.9(b)), gathering 2D detection errors of 0.50 ± 0.29 mm.

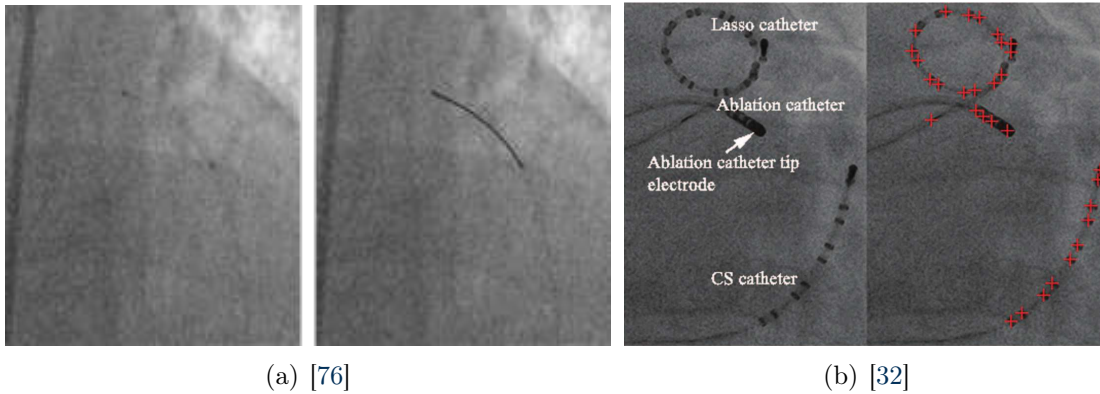
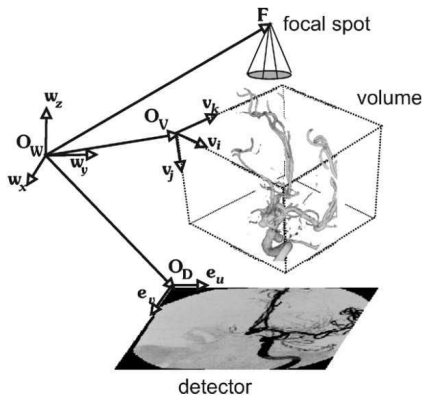


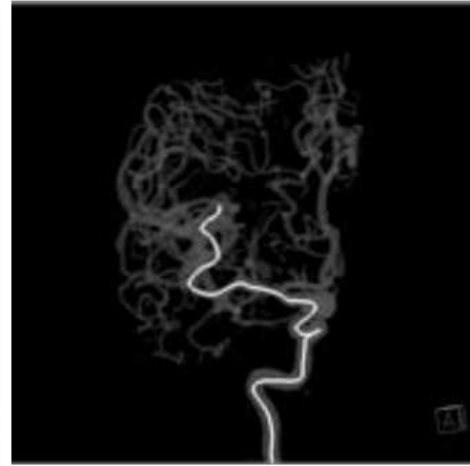
Figure 2.9: Two examples of what kind of observation can be extracted from fluoroscopic images

Once visual information has been extracted from monocular images, it must be interpolated or regularized by a device model. The first work proposing the reconstruction of an interventional device from one-view images is [77], where authors retrieve the 3D position and orientation of the catheter through a rigid transformation. In particular, a known rigid 3D model of the catheter is projected into the image plane. The reprojection

error (between the projected positions and the measured image positions) is iteratively minimized until finding the best rigid transformation. In this case, the catheter was equipped with radio-opaque markers, making image-features detection, and 2D-3D correspondences less arduous. Their rigid registration method has been proved to be robust to noisy images, but sensitive to changes in catheter's tip shape (i.e. deformation). In [53], authors present the reconstruction of a guide-wire within a cerebral artery, where a pre-operative model of the vascular branch is registered on the fluoroscopic image and used as a further constraint (Fig. 2.10(a)). Since, in reality, the device navigates inside the blood vessel, the reconstructed device shape must lay within the restrictive volume defined by the vessel surface. The 2D guide-wire is segmented within the images, and it is parameterized as a B-spline. Then, points are back-projected, and a 3D shape is found enforcing criteria of continuity and spacial coherence. In practice, a 3D model of B-spline is found, inside the vessel surface's restrictive volume, as the minimum cost 3D continuous path that respects the 2D parameterization. The precision of the method is limited by the accuracy of the B-spline segmented within fluoroscopic images. In their work, the segmentation is done manually, defining some points along the guide-wire and, subsequently, performing a B-spline interpolation and re-sampling. Another limitation of such methods is related to computation time, which is not compatible with the 10-20 frames/second of the imaging system.



(a) [53]



(b) [54]

Figure 2.10: [53] Global setup and coordinate systems involved in the 3-D reconstruction. [54] 3D visualization of the estimated wire after subtraction.

Since fluoroscopic procedures rely on a flow of images, another constraint exploited by [54] takes into account the temporal coherence of the catheter path. Using a particle filter, the authors combine a known 3D geometric model of the vessels with the back-projection of 2D features, creating a 3D probability distribution of the wire position, which is recursively propagated. For each distribution, the probability density is mainly

composed of three terms: the likelihood between the observations and the points (related to the intensity of the point projected into the image), the knowledge of the last time step, and the update providing a prediction where the points could go given the current position. A B-spline model with maximum probability, maximum length, and minimum curvature priors is set to regularize the maximum a posterior solution (Fig. 2.10(b)). This method mainly relies on the hypothesis of temporal continuity. In practice, the device position can drastically change between two images due to operators' movements or contacts with surrounding anatomy. Despite good results, such a purely geometric model would not ensure a correct reconstruction when dealing with ambiguous views of the surgical scene (i.e. whenever the catheter moves along the direction of the X-ray detector optical axis or the image is not clear due to multiple overlapping vessels). In [78], the 3D reconstructed shape is defined as a smooth curve lying inside the blood vessels and matching the projection of the guide-wire segmented in the images. Smoothness and continuity are ensured with a set of priors, including a constraint of matching the vessel center-line. Such regularization criteria lead to shapes that do not perfectly match reality. Center-line alignment precludes from reproducing any contacts between the device and the vessel surface, while they frequently occur. Ambiguous cases are not handled and left for the clinician to interpret. Also, their approach does not provide a unique curve but rather a combination of possible reconstructions (Fig. 2.11(a)). Authors in [79], propose a Hidden Markov Model (HMM) to reconstruct the catheter's tip within a 3DRA surface. (Fig. 2.11(c)). The catheter is segmented within the fluoroscopic images, and a 2D-3D registration is performed by aligning the vessel center-line with the extracted catheter. The probability distribution of the 3D tip position is computed using an HMM and updated based on the previous distribution and the 2D-3D registration results.

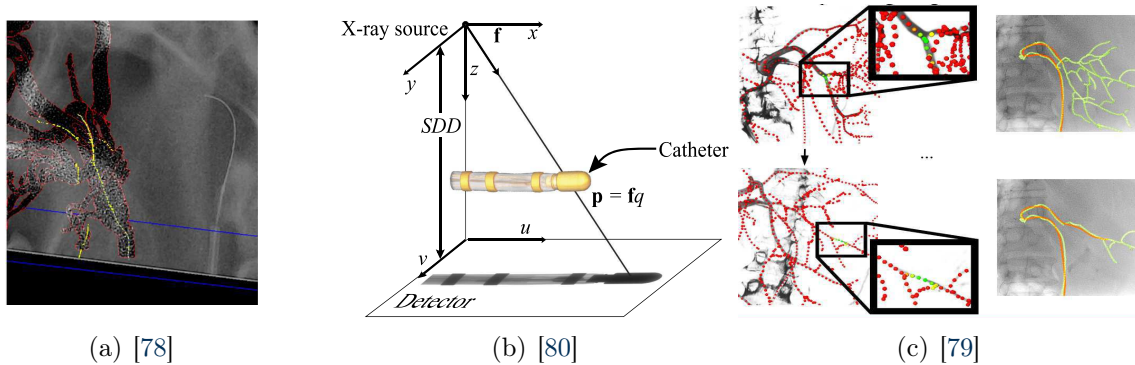
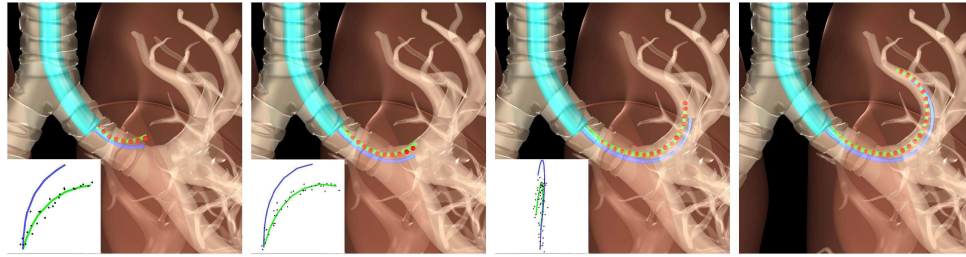


Figure 2.11: (a) [78] 3D view with all possible reconstructions (yellow). (b) [80] magnification associated with a cone beam acquisition geometry. (c) [31] 3D tip tracking using Hidden Markov Model.

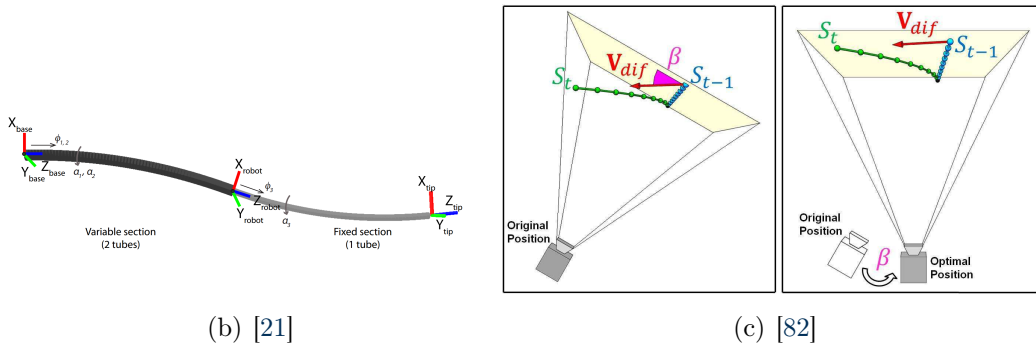
Electrophysiology catheters are embedded with metallic electrodes, that easily detectable in fluoroscopic images. In fact, their projection in fluoroscopic images presents different characteristics than a simple navigation device. Based on this assumption, detecting changes in object magnifications enables to retrieve the original position and the

orientation of the object with respect to the X-rays sources. Authors in [80] compare the fluoroscopic projection of the object with DRR images of a model of the same object while varying its pose. Template matching is used to obtain a measure of similarity between the template image and the segmented feature in the X-ray image. Once a preliminary estimate has been found, it is refined via multivariate function minimization. In [29], authors present a method to detect and predict the depth of catheter electrodes from single-view images, employing a full convolution neural network. The robustness in the depth direction needs to be improved (6.08 ± 4.66 for tip electrodes in a lateral view). More in general, such methods rely on magnification changes requiring high accuracy in image segmentation, at sub-pixel level, which is easier for such catheters due to the electrodes. Given that catheter-like devices are not easily detectable in fluoroscopic images, it is not possible to assimilate an X-ray projection to an orthographic projection. Approaches relying on different magnification effects do not apply to standard catheters.

Robotic steerable catheters can be seen as a series of rigid links connected and an a prior knowledge on the controls, along with schematic parameterizations of the joints, allows defining a unique kinematic model. Based on multi- views fluoroscopic images,



(a) [81]



(b) [21]

(c) [82]

Figure 2.12: (a) [81] Concentric tube robot shape reconstruction. (b) [21] Kinematic parameters of a concentric tube robot (c) [82] C-arm rotation towards optimal position where V_{dif} is on the image plane.

[83] propose a method to reconstruct the 3D shape of an ablation catheter for cardiac diseases, based on Non-Rigid Structure-from-Motion⁴ combined with robotic modeling. In

⁴A well known problem in Computer Vision of reconstructing a non-rigid object from a moving camera.

particular, the method uses a low-dimensional parameterization of catheter deformation and does not require the use of 3D vessel geometry as further constraints. In [81], the shape of the continuous robot is estimated through a kinematic model, which is refined with X-rays image-features (Fig. 2.12(a)). The images are acquired under an optimal positioning of the C-arm, which allows users to extract robust features. This method relies on the hypothesis of varying, multiple times during the procedure, the C-arm orientation. This is not always acceptable during the clinical work-flow. The work of [82] presents a technique to reconstruct the 3D shape of a Hansen artisan robotic catheter, without the need for external hardware for shape sensing, based on adaptive C-arm positioning and offline appearance priors. The shape of the device is modeled using a graph representation, where each 3D edge corresponds to the center-line of each 3D segment of the catheter, and the nodes their connections. First, they extract the 2D center-line of the catheter in the image. Then, they estimate the 3D shape using appearance priors. Lastly, they calculate the optimal positioning of the C-arms. The C-arm is iteratively rotated until the difference between the current 3D shape, and the previous one has been minimized. This method relies on the hypothesis of varying C-arm orientation multiple times during the procedures, which is not always acceptable during the clinical work-flow. Also, the orientation of the 3D catheter is based on 2D detected features, typical of concentric tubes. The same authors, in [21], overcame the problem of multiple C-arm acquisitions, by taking into account a kinematic model of the robotic catheter (Fig. 2.12(b)). They perform a 2D-3D registration combining the 2D features extracted from fluoroscopic images, with a 3D shape estimation calculated from forward kinematics. The kinematic model is typical of concentric tube robots. The shape is calculated through a boundary value problem (BVP) for the relative twist angle (between concentric tubes) and for bending and torsional curvature as functions of arc length. The integration of such values provides the shape of the robot as a function of arc length.

2.4.2.3 Monocular Images Reconstruction using External Sensors

In case of monocular images, given the absence of further information (such as the second image of biplane systems) additional constraints must be defined. In particular, another possible solution is to embed external sensors onto the catheter. While fluoroscopic images only enable the gathering of the current projected shape of the device, external sensors would allow retrieving some 3D information about its configuration and location. For catheter-like devices, two categories of sensors can be used: fiber optic sensors (FOS) based and electromagnetic (EM) tracking.

Fiber Bragg Grating (FBG) is a particular category of optical fiber sensors that act as a wavelength selective mirror. This feature arises when a light produced by a broadband source is transmitted through the fiber. In FBG sensors, only the light centered on the Bragg wavelength is reflected by the grating: other components will continue their path all along the fiber with no signal loss. Whenever an external load is applied to the optical

fiber, the induced deformation produces a mechanical strain, resulting in a wavelength shift for the reflected light. When analyzing the wavelength shift, it is possible to retrieve the strain and estimate the curvature to reconstruct the shape (see Fig. 2.13(a)). The main advantages of such sensors are related to their size and their miniaturized design, which makes them easy to integrate onto the instrument. Also, presenting high elasticity and flexibility, they do not significantly modify the device's properties. In the medical context, FBG sensors are typically used to perform surgical needle shape tracking, and achieved precision can reach ranges of 0.74 – 1.2 mm ([84], [85], [86]), using different needles length and different numbers of FBG sensors spaced out at various distances along the fibers.

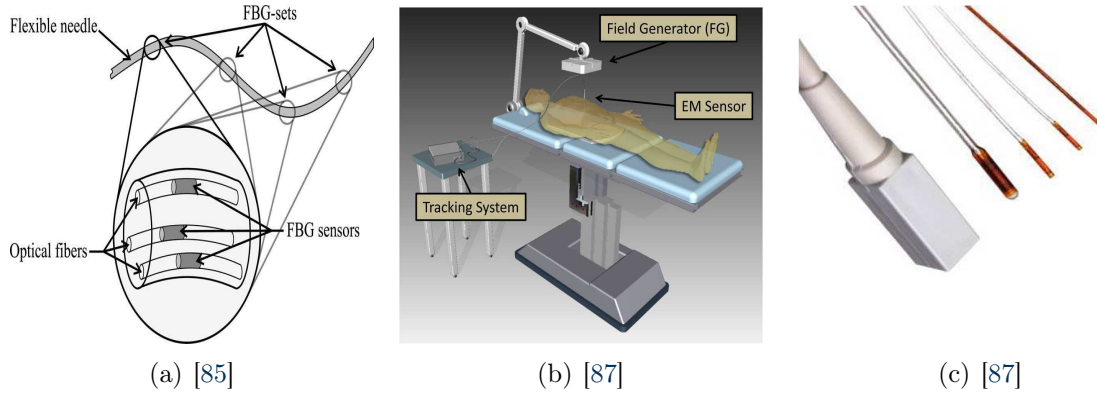


Figure 2.13: (a) [88] Demonstration of the curvature-strain model for helically-wrapped FBG sensors. (b) [87] Principle of intra-operative EM tracking, (c) examples of sensor from Ascension Technology Corporation.

It has been demonstrated that FBG sensors present reasonable performances for shape sensing of devices with high stiffness (i.e. needles), where the strain is perfectly transferred from the deformed device to the sensor. For catheter-like devices, authors in [51] propose a simultaneous catheter and environment modeling (SCEM) for trans-femoral Transcatheter Aortic Valve Implantation procedures (TAVI). They replace classic fluoroscopic images with a virtual reconstruction of the 3D anatomy and the inserted device. Whereas the reconstruction of the vasculature is based on data fusion between intravascular ultrasound (IVUS) and electromagnetic (EM) tracking, shape sensing based on FBG sensors is performed to retrieve the catheter shape; an overview of the hardware and software set-up is presented in Fig. 2.14(b). In this work, the clinical procedure is not fluoroscopy-based, but to the best of our knowledge, this is the only method to propose an FBG sensor to reconstruct the catheter shape. FOS-based sensing does not suite the large deformations and the low stiffness of interventional devices like catheters.

Another technology widely adopted in medicine is electromagnetic (EM) tracking. Thorough reviews of electromagnetic tracking in clinical environment have been presented in [89] and [87]). The working principle of EM sensors relies on Faraday's Law. Whenever

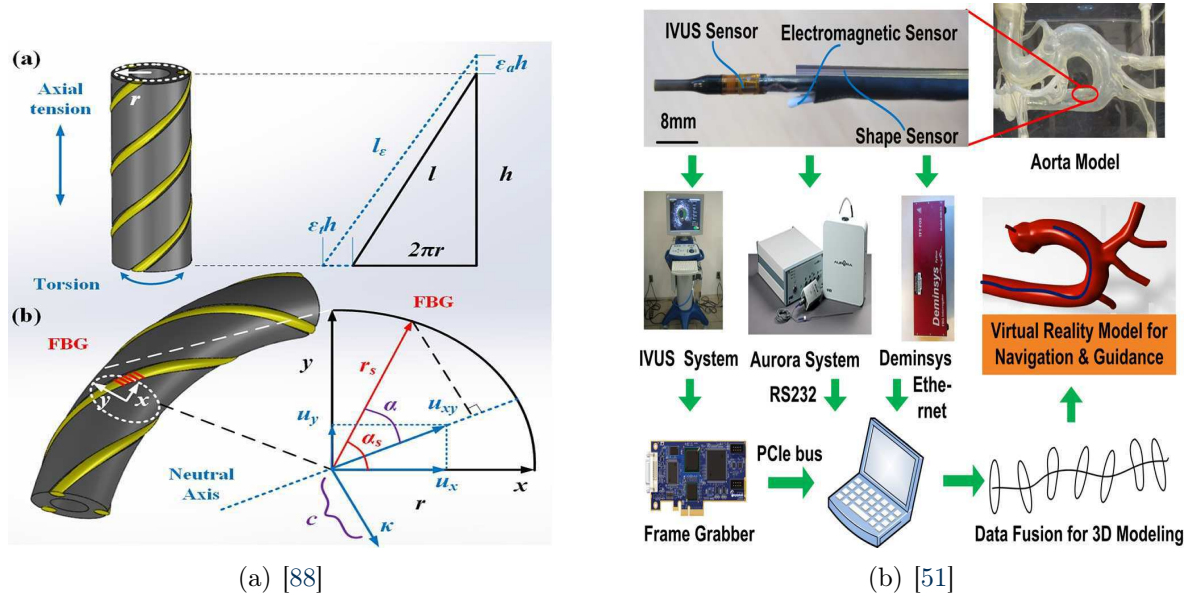
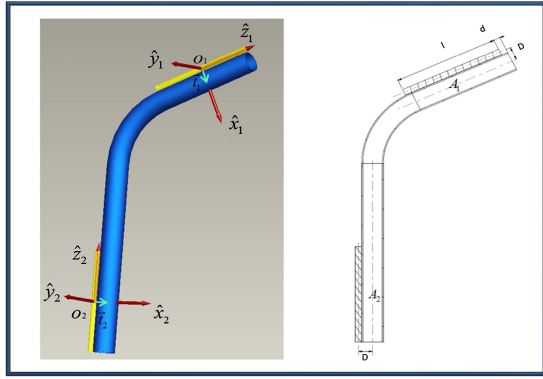


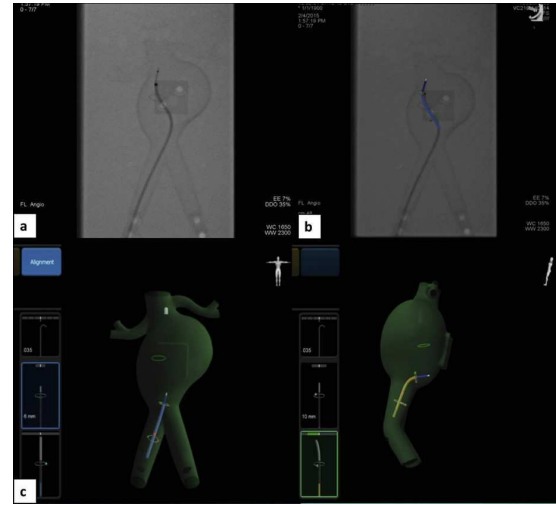
Figure 2.14: (a) [88] Demonstration of the curvature-strain model for helically-wrapped FBG sensors. (b) Sensor fusion framework and hardware configuration for the system presented in [51].

a receiver moves within a magnetic field, a voltage, proportional to the intensity of the magnetic field, is induced in the receiver. Such induced voltage gives the measurement of the orientation and the position of the receiver with respect to the emitter. EM technology is mainly used to localize and track the 3D location and orientation of surgical tools, by embedding the device with an EM sensor. The sensor is tracked within the working volume of an EM field generator (see Fig. 2.13(b)). Magnetic sensors can present different sizes and different detected degrees-of-freedom (DoFs), usually: 3 DoFs for position and 2 / 3 DoFs for orientation (see Fig. 2.13(c)); similarly, different field generators can create a working volume of different sizes. Various configurations may be adopted in the operating room, according to the chosen equipment. Generally speaking concerning precision, most assessments show promising results below 1.0 mm (see [87]). For catheter-based procedures, the general idea is to embed an external sensor into the instrument, to have a 3D knowledge on the position of the tip or other parts of the device.

Compared to FBG sensors, EM tracking is more adaptable to deformable devices like catheters. In [90], authors propose to use EM tracking in combination with occasional intra-operative CTA, within a navigator where a virtual 3D reconstruction of the surgical scene is introduced. In particular, they developed a general EM navigation framework in which the catheter is embedded with 2 EM sensors (5 DoFs) at the distal part. The mutual information provided by the two sensors allows the reconstruction of the curvature of the tip. The sensor can be attached to the instrument or inserted into a customized multi-lumen catheter (see Fig. 2.15(a)). Authors in [22] propose a method to reconstruct the shape of the device based on a probabilistic fusion of the real-time EM tracking with a



(a) [90]



(b) [91]

Figure 2.15: (a) [90] Representation of a traditional catheter with two sensor coils (yellow cylinder). (b) [91] Comparison between classic fluoroscopic images against 3D virtual reality images generated with 3D EM sensors for catheter position and model of the anatomy.

simulation of catheter navigation, based on a kinematic model. Their framework is overall composed of 7 sensors (one 6DoF and the rest 5DoF) distributed along the catheter. A Kalman filter is used to combine the pose information provided by the sensors, with the kinematic model of catheter navigation. Such a probabilistic approach allows taking into account measurement errors from EM sensors and inaccuracies associated with the kinematic model. In this case, an algorithm simulating the insertion used to provide a prediction of the catheter dynamic consequent to a certain insertion length. The catheter model is defined through a given number of oriented nodes. The shape is computed minimizing the bending and the elastic energy of the device inside the vasculature, based on the approach proposed by [55]. In particular, following a known insertion length, total energy is minimized to find the consequent displacement of each node. A first-order iterative analytic solution is proposed to efficiently obtain the vector of the displacement of each segment. Another probabilistic approach is proposed by [52]. In this case, the 2D information extracted from fluoroscopic images is combined with the pose information of EM sensors to retrieve a 3D reconstruction of the entire catheter shape. The catheter is modeled as a 3D B-spline and multiple EM sensors are embedded onto the instrument, to retrieve the position and orientation of several segments of the device. The reconstruction of the 3D catheter shape is achieved by optimizing the B-spline model's probability density, given the EM information and the 2D image-features. As before, a probabilistic approach allows taking several errors into account: noise and distortion in fluoroscopic images, errors from EM sensors, and registration errors between EM data and fluoroscopic images. EM trackers were also combined in [91] with a robotic catheterization system, providing a 3D instrument position and orientation visualization instead of the classic 2D fluoroscopic

view (see Fig. 2.15(b)).

Although embedded trackers can give a rather precise location of the catheter, they allow only for a very partial reconstruction of the device, and a full shape cannot be retrieved. Only when combined with other information, such as a kinematic model of the device [22] or image features [52]), it is possible to reconstruct the whole shape. Also, their embedding on the interventional device implies significant work-flow changes, hence restricting the possible clinical applications. EM tracker limitations are associated with the sensitivity to ferromagnetic materials. In particular, ferromagnetic and conductive objects may create distortions of the magnetic field. EM localization errors may further increase in an operating room's environment, where interactions with ferromagnetic materials cannot be neglected. The majority of sensor intends to replace classic fluoroscopy guidance to reduce radiation exposure. Nevertheless, existing technology is not mature enough, and fluoroscopy remains the only reliable method for accurate information on the ongoing procedure status.

2.4.3 Discussion

Given the presented state of the art, it is clear that multiple sources of information need to be combined to retrieve a reliable 3D reconstruction of the device: a model (physics-based or geometric, including motions and deformations), constraints (contacts with surrounding vessels, regularization criteria on the shape, temporal coherence), and information on the current state of the device (projective 2D from image features, 3D from position or shape sensors).

Reconstruction methods based on geometric priors of the shape of the catheter (mainly B-splines) cannot guarantee a reliable reconstruction, especially under ambiguous views. Moreover, in this case, the device motion is not modeled. For that, 2D-3D data association is more arduous, and the thereafter reconstruction may fail, especially after sudden modifications of the catheter's shape (e.g. following a contact with the surrounding anatomy or an abrupt movement). Reconstruction methods defining a kinematic or physics-based model of the device provide a better description of the device's behavior within blood vessels. On the other hand, they may be computationally expensive, thus incompatible with frame-rates of acquisition images (7.5-15 fps). Reconstruction methods exploiting embedded external sensors entail significant modifications of the clinical work-flows. Also, EM tracking, which is the most suitable for catheter-like devices, presents important limitations related to ferromagnetic interactions in a clinical environment.

In table 2.1, we summarize all the above-listed methods according to different criteria.

Information on the device's current state can be provided by biplane images, monocular images and or external sensors. 2D information extracted from images can be either

	Information on Current Configuration			Device Model		Method Requirements				
	Biplane	Monoplane	Sensor	Geometric	Advanced	3D Anatomy	Feature-based Image Detection	Feature-less Image Detection	Deterministic	Probabilistic
[31]		X		3D Tip		X		2D B-Spline		HMM
[29]		X		3D tip			Projected Electrodes		CNN	
[48]	X			3D B-Spline				2D B-Spline	X	
[73]	X			3D Connected Points				2D Unstructured Points	X	
[54]		X		3D B-Spline		X		2D Unstructured Points		Particle Filter
[90]			2 EM sensors 5DoF		Kinematic Model	X			X	
[50]	X			3D B-Spline				2D Line Segment	X	
[22]			7 EM Sensors (5-6 DoFs)		Physics-Based Model	X				Kalman Filter
[77]		X			Rigid Body Model		2D Radio-opaque Markers		X	
[81]		X			Robot Kinematic Model	X	Robotic Catheter Features		X	
[83]		X			Robot Kinematic Model		Robotic Catheter Features		Non Rigid Structure from Motion	
[74]	X			3D Point Cloud				2D Unstructured Points	X	
[78]		X		3D B-Spline and Arc Length		X		2D Unstructured Points	X	
[80]		X		Rigid Model			Projected Electrodes		X	
[49]	X			3D B-Spline				2D B-Spline	X	
[51]			3 Fibers with 8 FBG + 1 EM 6DoFs	3D B-Spline		X			X	
[52]		X	4 EM Sensors 5DoFs	3D B-Spline	X	X		2D Line		Maximum Likelihood Estimation and
[82]		X		3D Graph Representation			Robotic Catheter Features		X	
[21]		X		3D B-Spline			Robotic Catheter Features		X	
[53]		X		3D B-Spline		X		2D B-Spline	X	

Table 2.1: Classification of reviewed approaches according to: observations used, chosen model for the device and its navigation, and methods characteristics

feature-based (i.e. markers detection or detection specific features such electrodes) or without any specific features. The model of the device can be purely geometric (i.e. B-spline) or take into account its behavior through a kinematic or physics-based approach. Specific methods take into account the surrounding 3D anatomy as a further constraint to the 3D space, considering as well the interactions with the blood vessels. All of the above-mentioned methods are prone to be tainted with errors, either related to the obser-

variations or inaccuracies in the model. Whereas deterministic methods either don't mention uncertainties nor take them into account through empiric parameters, probabilistic approaches can handle various sources of error. For example, [22] proposed a Kalman Filter formalism to fuse data from multiple EM sensors with the physics-based model, taking into account uncertainties on both the models and the external measurements. In [52], authors retrieve the 3D shape of the device, optimizing a posterior probability function. This is defined as the probability of the spline model given the data originating from the EM sensors and the fluoroscopic images. In practice, they perform a maximum likelihood estimation. To take into account the uncertainty on the 3D configuration of the catheter, authors in [54] describes the 3D position of the device as a probability function, where both the representation and the temporal update are performed using a particle filter. Particle filters are particularly useful for describing multi-modal probability distributions, but they may be extremely computationally expensive due to the number of generated particles. In [31], the 3D tip location is represented through a Hidden Markov Model. The probability that the catheter is at a specific location is the probability that the HMM is in the corresponding state. Each state changes at each discrete time step, according to the probabilities associated with the current 2D observation. Despite the good results, they apply their method only to the tip of the device.

In a more general computer vision context, some methods have been proposed to recover the 3D shape of a deforming non-rigid surface from a monocular sequence based on Finite Element (FE) models. FE models enable to implement sophisticated priors on the shape to capture realistic deformations while being robust to occlusions [92, 93]. Under a probabilistic approach, it has been recently shown how a FE model could be leveraged in an EKF framework to achieve online reconstruction [94]. Two hypotheses are necessary for this method: they assume to know the deformation modes of the surface, and they suppose to detect and track some 2D features, whose correspondences with 3D points of the FE model are assumed to be known. The FE model, driven by the 2D detected features, captures elastic deformations of the surface, but it does not provide any information about the dynamic behavior of the object. Contacts and collisions are not taken into account, whereas only fixed physical constraints can be included in the model. Also, such a framework could not directly fit our specific problem of catheter reconstruction, as a surface FE model cannot be applied to a curved shape like the interventional device.

2.5 Conclusion

The main aim of our work is to reconstruct the 3D shape of the interventional device from 2D single-view fluoroscopic images, without the need of any additional hardware. To this end, the final proposed result of this thesis is a finite element (FE) simulation reproducing the navigation within blood vessels through a constrained physics-based simulation. Similarly to the physics-based model presented in sec. 2.4.2.2, our model aims

at having a better prediction of the device physical behavior, in particular taking into account contacts with the surrounding blood vessels while guaranteeing real-time computation. Information on the current state of the catheter is solely provided by 2D fluoroscopic images where we detect and extract the projection of radio-opaque markers the catheter is embedded with.

We first proposed a deterministic approach (Chapter III), where the 2D features extracted from fluoroscopic images are integrated into the navigation model as mechanical constraints. Despite the good results, this purely deterministic method needs some specific hypothesis making it restrictive for a straightforward application. In addition, uncertainties on the navigation model and errors on extracted features are not taken into account.

We then evaluated a probabilistic approach (Chapter V). Through a Bayesian filter, the predicted shape of the device is corrected with the 2D monocular images. Such stochastic formulation allows us not only to take into account inaccuracies in the navigation model (such as mechanical characterization of the catheter model, uncertainties on applied constraints, etc.), but it also allows interpreting the missing depth information of 2D image-features as a further source of uncertainty of the stochastic state. Given the non-linearity of both the model and the observation processes, we propose to use an Unscented Kalman Filter [95].

One of the major contributions of this work is a solution to the constrained state estimation problem raised by contacts. In stochastic, a constrained estimation occurs when not all the values of the random variable are acceptable samples. In our case, as the device is constrained to stay inside the vessel, the estimated positions cannot assume all the possible values within their probability distribution (e.g. outside the vessel surface). The proposed method casts such constrained estimation as a Non-linear Complementarity Problem (NLCP) solved using a Gauss-Seidel Method.

Part III

Deterministic Simulation

AUGMENTED 3D CATHETER NAVIGATION USING CONSTRAINED SHAPE FROM TEM- PLATE

Table of Contents

3.1	Introduction	45
3.2	Deformable Models	45
3.2.1	Finite Element Approach	46
3.2.2	Catheter Model	47
3.3	Boundary Conditions	49
3.3.1	General Definition	49
3.3.2	Contact Model	50
3.4	Temporal Integration	51
3.4.1	Backward Euler Integration	53
3.5	Constraint-based Solution	54
3.6	2D-3D Reconstruction Constraints	56
3.6.1	Projective Constraint	57
3.6.1.1	Marker Detection and Tracking	57
3.6.1.2	Calibration and Projection Matrix	57
3.6.1.3	Projective Constraint Formalism	58
3.6.2	Entry Constraint	60
3.7	Experimentations and Results	61
3.7.1	Overview and Metrics	61
3.7.2	Synthetic Experiment on Projective Constraint and Surface Constraint	63

3.7.3	Synthetic Experiment on Projective Constraint and Entry Constraint	67
3.7.4	Real Data Experiments on Projective Constraint and Surface Constraint	71
3.7.5	Real Data Experiments on Projective Constraint and Entry Constraint	75
3.8	Conclusion	78

3.1 Introduction

In this chapter, we present a deterministic approach to retrieve the 3D shape of the catheter from 2D monocular X-rays images. We model the navigating device through a Finite Element approach, where the information collected through 2D image-features is integrated into the model as mechanical constraints. Given the ill-posedness of the problem, further constraints providing additional 3D knowledge have to be identified to retrieve an optimal 3D shape. In the following sections, we present the FE model of the surgical device in detail, the constraints formalism used to integrate the 2D image features, and the different types of constraints that can be defined to add 3D knowledge to the problem.

3.2 Deformable Models

When simulating catheter-like devices, two parameters have to be taken into account to define an efficient model: the different motions the device can undergo and the resulting deformations. Devices such as catheters, or guide-wires, are flexible but inextensible non-linear elastic objects. When pushed inside blood vessels, they show high non-linearities. This is due to contacts with the surrounding anatomy, high tensile strength, and low resistance to bending. The motion of such devices is induced by the manual movement performed by clinicians at their proximal end. Indeed, by pushing, pulling, or twisting this extremity, operators can navigate the device through the vascular tree and reach the target lesion.

In section 2.4.1, we presented the existing approaches used to model catheter-like devices. Mass-spring models or multi-body dynamics present limitations related to the fact that the physical parameters like Young's modulus cannot entirely be translated with a spring stiffness. Also, torsional energy terms and geometric non-linearities are not taken into account. If geometric non-linearities, such as contacts and friction phenomena, are taken into account, they are however incompatible with real-time requirements ([59]). To provide an efficient biomechanical characterization of the instrument, while handling non-linearities within a real-time computation, we exploit the FE approach presented by [68] and [96]. Such an approach is based on the three-dimensional beam theory introduced by [97]. Combining such FE model with a co-rotational approach allows us to represent highly non-linear behaviour while guaranteeing a fast computation.

3.2.1 Finite Element Approach

The finite element method is a numerical technique used to analyze any physical phenomenon that can be described using partial differential equations (PDEs). FEM belongs to variational methods that, in a general manner, aim at energy minimization. In particular, whenever a boundary condition (like a displacement or a force) is applied, only the configuration with minimum total energy is chosen among all possible. First, in FE approaches, infinite DoFs of a continuum object are sampled into finite discrete elements connected with each other at nodes. By joining such elements, the field quantity becomes interpolated over the entire structure through a piecewise polynomial interpolation. The governing equations at partial derivatives (plus the boundary conditions) are then approximated to algebraic equations (eq. 3.1) and solved simultaneously for each node.

$$\underbrace{\mathcal{F}}_{\text{Property}} \underbrace{\mathbf{u}}_{\text{Behaviour}} = \underbrace{\mathbf{f}}_{\text{Action}} \rightarrow \mathbf{u} = \mathcal{F}^{-1}\mathbf{f} \quad (3.1)$$

\mathcal{F} is a non-linear function describing the mechanical characterization of the material, providing as well as information on the discretization of the surface; the vector \mathbf{f} expresses the internal forces on all the nodes; the vector \mathbf{u} , unknown of the equation, expresses the displacement of each node between its initial and deformed position ($\mathbf{u}_f - \mathbf{u}_0$).

Different types of FEM may be defined according to the object to be modeled and the deformations it undergoes. Linear FE models describe the elastic behavior of the object through Hooke's law, characterized basically by Young's modulus and Poisson ratio. In this case, \mathcal{F} is replaced by its first order approximation $\mathcal{F}(\mathbf{u}_f - \mathbf{u}_0) = \mathbf{K}(\mathbf{u}_f - \mathbf{u}_0) + O(\|\mathbf{u}_f - \mathbf{u}_0\|^2)$, where \mathbf{K} becomes a constant matrix, computed as the Jacobian of \mathcal{F} evaluated in \mathbf{u}_0 : $\mathbf{K} = \frac{\partial \mathcal{F}}{\partial \mathbf{u}}$, which can be pre-computed at the beginning of the simulation. Several works have been presented relying on linear FEM ([98], [99], [100]). Although their robustness and computational speed make them suitable for real-time computations, the linear approach does not perfectly describe large deformations and non-linearities, which may typically occur in medical simulation.

Instead, large deformations can be accurately described by hyperelastic (non-linear) models; most common models, among others, are St-Venant-Kirchoff, Neo-Hookean, and Mooney-Rivlin. Hyperelastic materials can be described through a strain-energy density function, which is used to derive a non-linear constitutive model. More in general, the stress \mathbf{S} depends on the tensor strain \mathbf{E} and the energy function \mathbf{W} , through the expression $\mathbf{S} = \frac{\partial \mathbf{W}}{\partial \mathbf{E}}$. Despite the large range of deformations described, hyperelastic FE models are computationally expensive (given the non-linearity of the internal forces, the stiffness matrices are not constant thus not pre-computable). Also, they cannot guarantee the numerical stability of the simulations. To be compatible with the real-time requirements of medical simulations, [101] proposed an approach based on an implicit integration scheme, leading to a faster stiffness matrix assembly for isotropic and anisotropic materi-

als. Another FE method, which allows modeling large deformations, is the co-rotational approach. Initially proposed by [102], such a method assumes that occurring rotations are the main cause of geometrical non-linearities. The method has been then adapted to real-time computations for volumetric objects by [103] or [104], where the rotations of each element are independently computed. In particular, assuming that linear elastic forces are invariant under translations but not under rotations, they propose to work with a constant linear stiffness matrix \mathbf{K} and extract the rotational part \mathbf{R} of the deformation. Let \mathbf{q}_{i0} be the position of the i^{th} element before its displacement, the function \mathcal{F} can be written as:

$$\mathcal{F}_i = \mathbf{R}_i \mathbf{K}_i (\mathbf{R}_i^{-1} \mathbf{q}_i - \mathbf{q}_{i0}) \quad (3.2)$$

For a tetrahedral element, the matrix $\mathbf{R}_i \in \mathbb{R}^{12 \times 12}$ is a diagonal matrix, where each $\mathbf{R}_x \in \mathbb{R}^{3 \times 3}$ represents a global rotational component of the rigid body transformation of the element.

$$\mathbf{R}_i = \begin{bmatrix} \mathbf{R}_x & & & 0 \\ & \mathbf{R}_x & & \\ & & \mathbf{R}_x & \\ 0 & & & \mathbf{R}_x \end{bmatrix} \quad (3.3)$$

They first rotate the deformed positions \mathbf{q}_i back to the initial frame using the inverse matrix \mathbf{R}_i^{-1} ; then, the forces are computed as $\mathbf{K}_i (\mathbf{R}_i^{-1} \mathbf{q}_i - \mathbf{q}_{i0})$ and rotated back as in equation 3.2. Finally, the new stiffness matrix is estimated through the derivative $\mathbf{K}'_i = \frac{\partial \mathcal{F}_i}{\partial \mathbf{q}_i} = \mathbf{R}_i \mathbf{K}_i \mathbf{R}_i^{-1}$

3.2.2 Catheter Model

To model large deformations while being compatible with real-time computations, we use a combination of a FE model of the three-dimensional beams with a co-rotational approach.

A beam is an element composed of two linked nodes, each one described by 6 DoFs. The elementary beam is characterized by a stiffness matrix $\mathbf{K}_e \in \mathbb{R}^{12 \times 12}$, which is a symmetric matrix relating forces and torques (applied to the e^{th} element) with the corresponding spatial and angular displacement. Such a matrix can be formalized as follows:

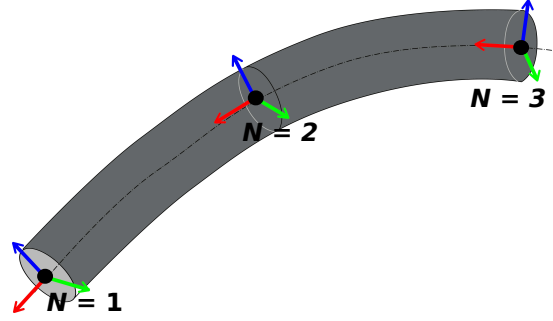


Figure 3.1: 6DoFs beam obtained as a series of N connected nodes

$$\mathbf{K}_e = \frac{E}{l} \begin{array}{c|c} \begin{array}{cccccc} \text{A} \\ 0 & \frac{12I_z}{l^2(1+\Phi_y)} & & & & \\ 0 & 0 & \frac{12I_y}{l^2(1+\Phi_z)} & & & \\ 0 & 0 & 0 & \frac{GJ}{E} & & \\ 0 & 0 & -\frac{6I_y}{l(1+\Phi_z)} & 0 & \frac{6I_y}{l(1+\Phi_z)} & \\ 0 & \frac{6I_z}{l(1+\Phi_y)} & 0 & 0 & 0 & \frac{4+\Phi_y I_z}{1+\Phi_y} \\ -\text{A} & 0 & 0 & 0 & 0 & 0 \end{array} & \begin{array}{c} \text{Symmetric} \\ \text{A} \\ 0 & \frac{12I_z}{l^2(1+\Phi_y)} & & & & \\ 0 & 0 & \frac{12I_y}{l^2(1+\Phi_z)} & & & \\ 0 & 0 & 0 & \frac{GJ}{E} & & \\ 0 & 0 & \frac{6I_y}{l(1+\Phi_z)} & 0 & \frac{4+\Phi_z I_y}{1+\Phi_z} & \\ 0 & \frac{6I_z}{l(1+\Phi_y)} & 0 & 0 & 0 & \frac{4+\Phi_y I_z}{1+\Phi_y} \end{array} \end{array} \quad (3.4)$$

where the different parameters are summarized in the following table:

E	Young's Modulus	I	cross-section moment of inertia
ν	Poisson's ratio	$\Phi = \frac{12EI}{GA l^2}$	shear deformation parameters
A	beam cross section	J	polar moment
l	beam length	$G = \frac{E}{2 \cdot (1+\nu)}$	

Table 3.1: Mechanical parameters to describe a three-dimensional beam model.

All the beam elements are then linked to each other through a finite element model expressed with a co-rotational formulation. Therefore, the local forces for each element can be expressed as in equation 3.2 where the local rotations are now associated to the two nodes of the beam. The rotation matrix \mathbf{R}_e of the e^{th} element of the beam is $\mathbf{R}_e = \text{diag}(\mathbf{R}_e^1 \ \mathbf{R}_e^1 \ \mathbf{R}_e^2 \ \mathbf{R}_e^2)$, where \mathbf{R}_e^1 and \mathbf{R}_e^2 are the rotations of the node 1 and 2 of the beam. The total co-rotational elastic forces may be expressed as:

$$\mathcal{F}_e = \mathbf{R}_e \ \mathbf{K}_e \ (\mathbf{R}_e^{-1} \mathbf{q}_e - \mathbf{q}_{e0}) \quad (3.5)$$

where the stiffness matrix \mathbf{K}_e is computed as in equation 3.4, the vectors $\mathbf{q}_e, \mathbf{q}_{e0} \in \mathbb{R}^{12 \times 1}$ represent the positions and orientations of each beam (for the deformed state and the initial one), and the matrix \mathbf{R}_e describes the elementary rotations associated with the two nodes of each beam. Such a co-rotational FE approach allows taking into account non-linearities occurring in large deformations, while assuring a fast and stable computation. This last advantage is also due to the particular structure of beams, which can be numerically described as a Block Tridiagonal system (BTD), whose inversion can be performed more rapidly than a full matrix.

3.3 Boundary Conditions

The linear system resulting from the FE method is singular. Therefore, boundary conditions need to be defined to make it invertible. The choice of appropriate boundary conditions is fundamental for the correct resolution of the computational problem. In a medical simulation, such boundary conditions are generally represented by two objects interacting together (i.e. two anatomical structures in contact, a surgical instrument in contact with an organ or an object constrained within a specific area). In our case, boundary conditions are provided by the blood vessel the catheter interacts with during the navigation. In the following sections, we provide a general definition of the mechanical constraints, along with the formalism describing the interactions between the catheter and the surrounding anatomy.

3.3.1 General Definition

In classic mechanics, constraints can be mainly classified as *holonomic* and *non-holonomic* constraints.

Holonomic constraints, also known as *equality* constraints, can be formalized as:

$$\mathcal{W}(\mathbf{q}_1, \mathbf{q}_2) = 0 \quad (3.6)$$

where \mathbf{q}_1 and \mathbf{q}_2 are generalized coordinates of the nodes that represent the two objects in contact. Such kind of constraints operate on the position of an object, constraining it to lay e.g. on a surface (fig. 3.2(a)), a line (fig. 3.2(b)) or a to match specific point according to the DoFs of the constraint (fig. 3.2(c)).

Non-holonomic constraints, also known as *inequality* constraints, express all the differential constraints which can be formalized as:

$$\mathcal{W}(\mathbf{q}_1, \mathbf{q}_2) \leq 0 \quad (3.7)$$

A practical example can be the case of a 3 DoFs particle trapped inside a sphere of radius R , the non-holonomic constraint can be described as $\sqrt{x^2 + y^2 + z^2} < R$.

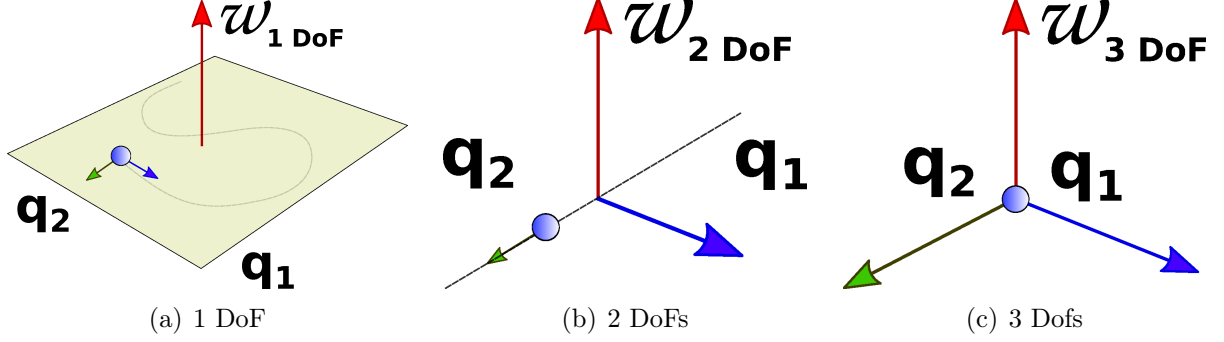


Figure 3.2: **Holonomic constraints on position:** (a) 1 DoF constraints operate on only on one DoF of the object (\mathbf{q}_1), which is hence enforced to slide on a surface (\mathbf{q}_2). (b) 2 DoFs constraints operate on two DoFs of the object, which is hence enforced to slide on a line (\mathbf{q}_2). (c) 3 DoFs constraint, constrain three Dofs of the object whose position is fixed at \mathbf{q}_1 .

3.3.2 Contact Model

The interventional device is bound to remain inside the blood vessels, and some interactions may occur between the catheter and the vessel wall. Such boundary condition, plus the collisions that may occur between the device and the vessel wall, can be expressed as non-holonomic constraints which enforce the catheter to stay inside the blood vessel. Looking at eq. 3.7, the formulation $\mathcal{W}(\mathbf{q}_{cat}, \mathbf{q}_{ves}) < 0$ bounds the catheter inside the surface, and the equality $\mathcal{W}(\mathbf{q}_{cat}, \mathbf{q}_{ves}) = 0$ is used to formalize the situation where the two objects are in contact. This kind of constraints are applied through Lagrange multipliers ([98, 105]) in a prediction-correction approach. First, an unconstrained motion is performed, then, if an interpenetration occurs $\mathcal{W}(\mathbf{q}_{cat}, \mathbf{q}_{ves}) > 0$ (i.e. the catheter is outside the vessel), contact forces are applied to all the positions violating the boundary constraints, to correct them and bring them inside the vessel surface. Lagrange multipliers represent the intensity of such contact forces, which must be applied to respect the defined constraints. Physical laws defining contacts are expressed here above, while the temporal integration will be detailed in Sec. 3.4.

Contact conditions can be assessed by the interpenetration $\delta_{\mathbf{n}}$, and the amplitude of the contact force $\lambda_{\mathbf{n}}$ that needs to be applied to correct a potential constraint violation. Both of these quantities are expressed along the normal \mathbf{n} of the surface of contact. The collision response is governed by Signorini's law (eq. 3.8):

$$\begin{cases} \delta_{\mathbf{n}} \geq 0 \\ \lambda_{\mathbf{n}} \geq 0 \\ \delta_{\mathbf{n}} \cdot \lambda_{\mathbf{n}} = 0 \end{cases} \quad (3.8)$$

expressing that at any time, the interpenetration $\delta_{\mathbf{n}}$ is non-negative (null if contact), the contact force $\lambda_{\mathbf{n}}$ is non-negative (null if no contact), and either $\delta_{\mathbf{n}}$ or $\lambda_{\mathbf{n}}$ is null at any moment of time (see [106, 107] for details). In practice, if there is no interpenetration ($\delta_{\mathbf{n}} > 0$) no force needs to be applied ($\lambda_{\mathbf{n}} = 0$); otherwise, if $\delta_{\mathbf{n}} < 0$ a contact force $\lambda_{\mathbf{n}} > 0$ must be applied to bring the position back to the contact point ($\delta_{\mathbf{n}} = 0$).

Coulomb's friction law states that the reaction force has a non-null component in the tangential direction (see [106]). Considering the dynamic friction of a single contact point, the direction of the friction force must lay in the direction of the tangential motion. In particular, such reaction force belongs to a pyramid cone whose height and directions are defined by the normal force $\lambda_{\mathbf{n}}$ and the cone angle is defined by a parameter μ that models the friction amplitude. Combining Coulomb's law with Signorini's law expresses conditions that govern stick and slip phenomenon in friction:

$$\delta_{\mathbf{T}} = 0 \rightarrow \|\lambda_{\mathbf{T}}\| < \mu \|\lambda_{\mathbf{n}}\| \quad (\text{stick}) \quad (3.9)$$

$$\delta_{\mathbf{T}} \neq 0 \rightarrow \|\lambda_{\mathbf{T}}\| = -\mu \|\lambda_{\mathbf{n}}\| \quad (\text{slip}) \quad (3.10)$$

where $\delta_{\mathbf{T}}$ represents the tangential component of the interpenetration $\delta = \delta_{\mathbf{n}} + \delta_{\mathbf{T}}$. In this case, contacts can be analyzed in two orthogonal directions, given by the surface of contact: collision is assessed along its normal \mathbf{n} , whereas the friction acts in the tangential plane \mathbf{T} . As stated above, such interactions can be expressed by a non-linear function $\mathcal{W}(\mathbf{q}_1, \mathbf{q}_2)$ depending on the positions of both objects in contact. Given the linearized problem, the transpose of the Jacobian $\mathbf{J} = \frac{\partial \mathcal{W}}{\partial \mathbf{q}}$ expresses the directions along which all the contact forces λ , for all points in contact, are applied.

3.4 Temporal Integration

Once the mechanical model has been defined, and the boundary conditions have been set, a method of temporal integration must be chosen to describe the process through time. The dynamics of the interventional device can be generally described by Newton's second law of motion (here expressed as second order differential equation):

$$\mathbb{M}(\mathbf{x})\ddot{\mathbf{x}} = \mathbb{F}(t) - \mathcal{F}(\mathbf{x}, \dot{\mathbf{x}}) + \mathcal{W}(\mathbf{x}, \dot{\mathbf{x}}) \quad (3.11)$$

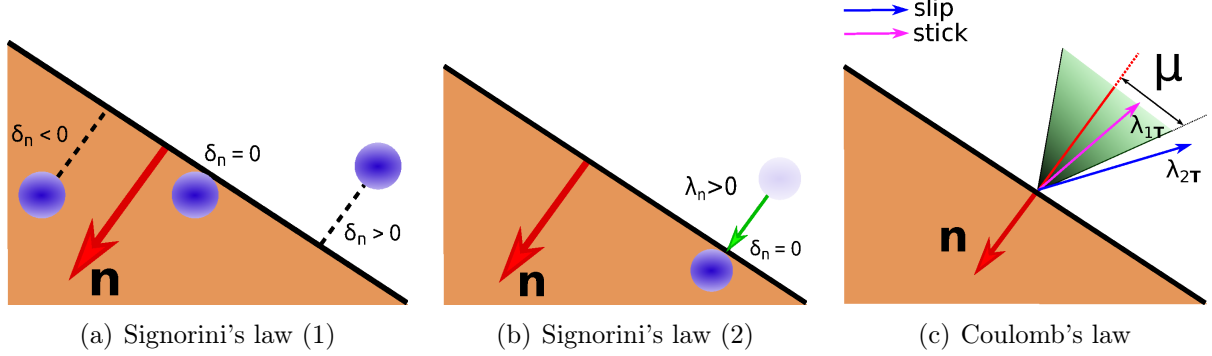


Figure 3.3: \mathbf{n} represent the normal to the surface discriminating the boundary condition. (a) The first step in collision response is to verify whether, under unconstrained motion, interpenetration may occur along the normal \mathbf{n} ($\delta_n > 0$). (b) If a violation is detected, a correction contact force $\lambda_n > 0$ needs to be applied to correct the interpenetration $\delta_n = 0$. (c) Whenever friction must be taken into account, the contact force will lay inside a cone defined by the normal \mathbf{n} and the parameter μ . If eq. 3.9 is verified, λ_{1T} will lay inside the cone and a stick contact will occur, otherwise, according to eq. 3.10, λ_{2T} will be applied for a slip contact.

Where $(\mathbf{x}, \dot{\mathbf{x}}, \ddot{\mathbf{x}})$ express respectively position, velocity and acceleration of a catheter's node; $\mathbb{M}(\mathbf{x})$ and $\mathcal{F}(\mathbf{x}, \dot{\mathbf{x}})$ represent respectively the inertia matrix and the internal forces, both derived from the co-rotational FE model, $\mathbb{F}(t)$ expresses the external forces while $\mathcal{W}(\mathbf{x}, \dot{\mathbf{x}})$ formalizes the boundary conditions applied to the model.

A method is explicit if the step displacement \mathbf{x}_k , at time k , is determined using the equation of motion at the previous step $\ddot{\mathbf{x}}_{k-1}$:

$$\begin{aligned}\ddot{\mathbf{x}}_{k-1} &= m^{-1}\mathbf{f} \\ \dot{\mathbf{x}}_k &= \dot{\mathbf{x}}_{k-1} + \ddot{\mathbf{x}}_{k-1}T \\ \mathbf{x}_k &= \mathbf{x}_{k-1} + \dot{\mathbf{x}}_{k-1}T\end{aligned}\tag{3.12}$$

These methods, also known as *Forward Euler* methods, are simple, fast, but unstable for real-time computations. In fact, the conditional stability of the central difference method requires using very small time-steps, which is an issue for real-time or fast simulations. On the other hand, implicit methods such as *Backward Euler* solve the system using the equation of motion $\ddot{\mathbf{x}}_k$, of the current step k , to determine the current step displacement \mathbf{x}_k :

$$\begin{aligned}\dot{\mathbf{x}}_k &= \dot{\mathbf{x}}_{k-1} + \ddot{\mathbf{x}}_kT \\ \mathbf{x}_k &= \mathbf{x}_{k-1} + \dot{\mathbf{x}}_kT\end{aligned}\tag{3.13}$$

Implicit time integration algorithms require additional computations but have the benefit of being unconditionally stable. This is due to the fact that a linear system must be solved at each time-step, where global equilibrium is verified at each time increment.

3.4.1 Backward Euler Integration

In the case of interventional device navigation, we have a relatively stiff object whose boundary conditions are represented by the vessel wall and the contacts that occur with the surrounding surface. Non-rigid contacts are non-linear phenomena, varying through time, and collision response on mechanical objects leads to discontinuities in velocities. This problem belongs to the domain of non-smooth mechanics, for which accelerations are not defined. To handle non-smooth dynamics while enabling fast computations, we use a *time-stepping* method [108] based on an Implicit Integration scheme.

Considering the discrete time-step $T = [k - 1 \rightarrow k]$, Eq. 3.11 may be rewritten as:

$$\begin{aligned} \mathbb{M}(\mathbf{x})(\dot{\mathbf{x}}_k - \dot{\mathbf{x}}_{k-1}) &= T(\mathbb{F}_k - \mathcal{F}(\mathbf{x}_k, \dot{\mathbf{x}}_k)) + T\mathcal{W}(\mathbf{x}_k, \dot{\mathbf{x}}_k) \\ \dot{\mathbf{x}}_k &= \dot{\mathbf{x}}_{k-1} + (\dot{\mathbf{x}}_k - \dot{\mathbf{x}}_{k-1})T \\ \mathbf{x}_k &= \mathbf{x}_{k-1} + \dot{\mathbf{x}}_k T \end{aligned} \quad (3.14)$$

In this case, the acceleration is defined as a difference of velocities. Non-linear terms, such as $\mathcal{F}(\mathbf{x}_k, \dot{\mathbf{x}}_k)$, are linearized using a first order Taylor series expansion:

$$\mathcal{F}(\mathbf{x}_{k-1} + d\mathbf{x}, \dot{\mathbf{x}}_{k-1} + d\dot{\mathbf{x}}) = \mathbf{f}_{k-1} + \frac{\partial \mathcal{F}}{\partial \mathbf{x}} d\mathbf{x} + \frac{\partial \mathcal{F}}{\partial \dot{\mathbf{x}}} d\dot{\mathbf{x}} \quad (3.15)$$

The implicit velocity update is then computed as:

$$(\mathbf{M} - T \frac{\partial \mathcal{F}}{\partial \dot{\mathbf{x}}} - T^2 \frac{\partial \mathcal{F}}{\partial \mathbf{x}}) d\dot{\mathbf{x}} = T(\mathbf{f}_{k-1} + T \frac{\partial \mathcal{F}}{\partial \mathbf{x}} \dot{\mathbf{x}}_{k-1}) + T \mathbf{J}^T \boldsymbol{\lambda}_k \quad (3.16)$$

where $d\mathbf{x} = (\mathbf{x}_k - \mathbf{x}_{k-1})$ and $d\dot{\mathbf{x}} = (\dot{\mathbf{x}}_k - \dot{\mathbf{x}}_{k-1})$. After discretization, the matrix \mathbf{M} expresses the mass and it can be considered as constant and lumped, leading to a diagonal matrix $\mathbf{M} \in \mathbb{R}^{12N \times 12N}$. The partial derivatives of elastic forces can be defined as $\mathbf{K} = \frac{\partial \mathcal{F}}{\partial \mathbf{x}} \in \mathbb{R}^{12N \times 12N}$ and the $\mathbf{B} = \frac{\partial \mathcal{F}}{\partial \dot{\mathbf{x}}} \in \mathbb{R}^{12N \times 12N}$, respectively approximating the stiffness of all the vertices and damping of the model. The term $\mathbf{J}^T \boldsymbol{\lambda}_k$ expresses the linearized contacts. A more detailed explanation will be provided in following sections.

Last equation, rewritten as a linear system ¹, becomes:

$$\underbrace{(\mathbf{M} - T\mathbf{B} - T^2\mathbf{K})}_{\mathbf{A}} \underbrace{\mathbf{q}}_{d\dot{\mathbf{x}}} = \underbrace{T(\mathbf{f}_{k-1} + T\mathbf{K}\dot{\mathbf{x}})}_{\mathbf{b}} + T\mathbf{J}^T \boldsymbol{\lambda} \quad (3.17)$$

Matrices $\mathbf{M}, \mathbf{B}, \mathbf{K}$ are computed by summing up each element's contributions to its vertices. This operation is called the assembly and, for elastic deformations, matrix $\mathbf{A} \in \mathbb{R}^{12N \times 12N}$ is symmetric definite positive. The vector $\mathbf{b} \in \mathbb{R}^{12N}$ expresses applied external forces.

¹discrete-time index is dropped for sake of simplicity.

3.5 Constraint-based Solution

To integrate the dynamics of the non-rigid objects (Eq. (3.17)) with contact's law and friction's law (Equations (3.8)-(3.10)), we use a Lagrange multiplier approach with a single linearization per time-step. Penalty methods, such as spring-like forces, which try to keep the object inside the surface (i.e. enforcing the boundary conditions) are neither suitable nor stable solutions for our problem. Instead, we use Lagrange multipliers, ensuring that at the end of each time-step we have a valid configuration (every point of the catheter lies inside the vessel) while reducing the computational cost.

Based on Eq.(3.8) and (3.17), the overall dynamic behavior of two interacting objects may be described as a Karush-Kuhn-Tucker system (KKT) as follows:

$$\begin{cases} \mathbf{A}\mathbf{q} = \mathbf{b} + \mathbf{J}^T\boldsymbol{\lambda} \\ \mathbf{J}^T\mathbf{q} = \boldsymbol{\delta} \end{cases} \quad (3.18)$$

The aim is to compute, for each node, $\boldsymbol{\lambda}$ deriving from contact's law and the current state \mathbf{q} . Such resolution is performed through iterative steps:

1. **Free Motion:** we solve the linear system $\mathbf{A}\mathbf{q} = \mathbf{b}$, which will provide \mathbf{q}^{free} at the end of the time-step, as if no interaction constraints were applied ($\boldsymbol{\lambda} = 0$ in Eq.(3.17), see Fig. 3.4(b)).

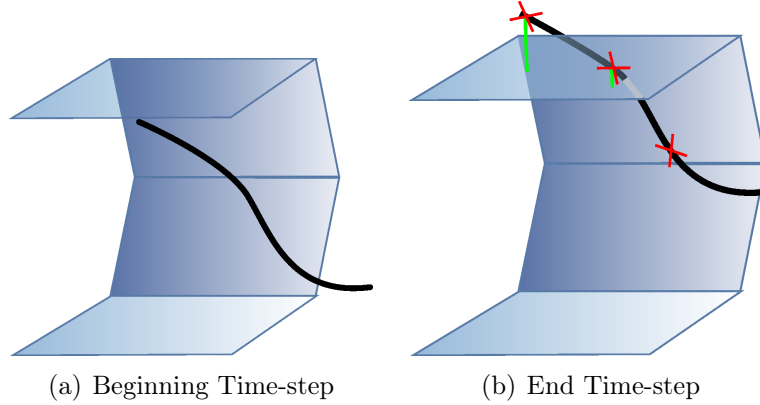


Figure 3.4: Example of free motion. At the beginning of the time-step, the catheter enforces the boundary conditions lying inside the surface. After the free motion, the catheter advanced exiting the vessel. Green segments in (b) shows the interpenetration δ that has occurred.

This step may be expensive given that it requires the inversion of a large matrix: $\mathbf{q}^{free} = \mathbf{A}^{-1}\mathbf{b}$. We use direct solvers to decompose matrix \mathbf{A} in smaller sub-matrices (LU decomposition, LDL^T decomposition, Block Tridiagonal (BTD) inversion, Cholesky decomposition). Iterative solvers also exist, but they are not well designed for ill-conditioned scenarios, such as stiff and light objects as the

catheter.

2. **Constraint definition:** we perform proximity detection (as described in sec. 3.3.2) and we compute the Jacobian of the constraints $\mathbf{J}^T = \frac{\partial \mathcal{W}}{\partial \mathbf{x}}$. In practice, this matrix gathers the directions \mathbf{n} (see Fig. 3.5(b)) along which the correction forces $\boldsymbol{\lambda}$ will be applied.

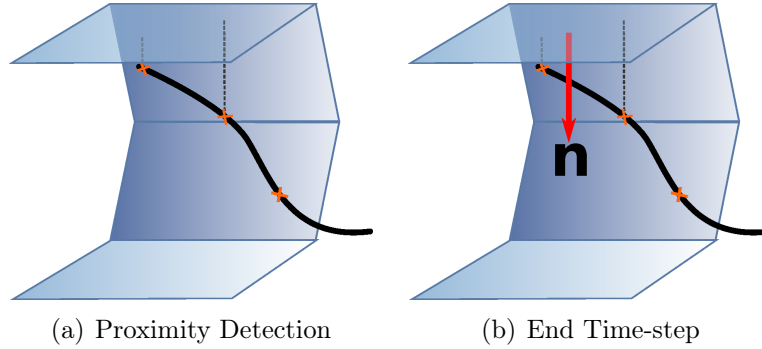


Figure 3.5: For each node of the catheter, the closest surface is detected and its normal \mathbf{n} (pointing inside the surface) is identified.

The proximity detection is performed using the positions at the beginning of the time-step (Fig. 3.5(a)), supposing the matrix \mathbf{J} to be constant during the time-step.

3. **Compliance Computation:** once both the directions of the constraints (expressed through \mathbf{J}) and the free motion \mathbf{q}^{free} (without constraints) are known, we can define $\boldsymbol{\delta}$, being the violation of the constraint. In practice, it is the distance the interpenetration, projected along the constraint directions n gathered in \mathbf{J} .

From Eq.(3.17): $\mathbf{q} = \mathbf{q}^{free} - \mathbf{A}^{-1}\mathbf{J}^T\boldsymbol{\lambda}$, we can rewrite the second term of Eq. (3.18) as:

$$\underbrace{(\mathbf{J}\mathbf{A}^{-1}\mathbf{J}^T)}_{\mathbf{W}}\boldsymbol{\lambda} = \mathbf{J}\mathbf{q}^{free} - \boldsymbol{\delta} \quad (3.19)$$

The *Delassus Operator* \mathbf{W} represents the mechanical coupling between the constraints and it is the most expensive step of the simulation as it requires to explicitly multiply the inverse of the mechanical matrix \mathbf{A} with the Jacobian of the contacts.

4. **Constraint Resolution:** the above expression provides a Non-linear Complementarity Problem (NLCP) where two are the unknowns: the applied forces $\boldsymbol{\lambda}$ and the violation $\boldsymbol{\delta}$. This is solved through an iterative Gauss-Seidel Method, where each constraint is treated singularly independently from other current constraints. More details on this step are presented in [96] and [107].
5. **Final Correction:** once contact forces $\boldsymbol{\lambda}$ are known, it is possible to compute the final position and velocity of each node of the model:

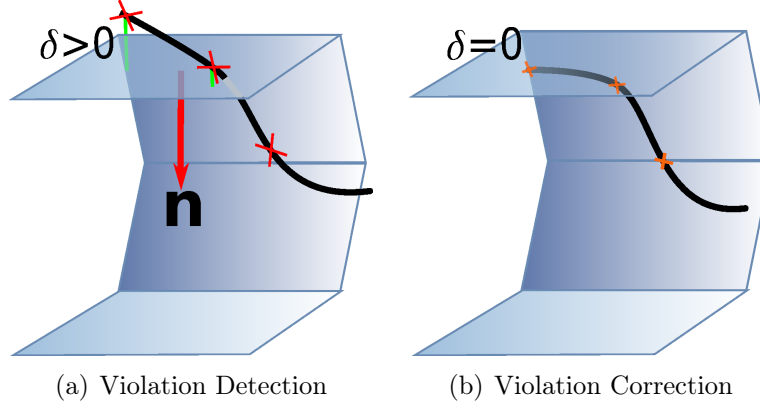


Figure 3.6: Whenever an interpenetration has occurred ($\delta > 0$) along the direction \mathbf{n} , contact forces $\lambda > 0$ are applied in order to correct the positions ($\delta = 0$).

$$\begin{aligned} \mathbf{q} &= \mathbf{q}^{free} - \mathbf{A}^{-1} \mathbf{J}^T \lambda \\ \dot{\mathbf{x}}_k &= \dot{\mathbf{x}}_{k-1} + \mathbf{q} T \\ \mathbf{x}_k &= \mathbf{x}_{k-1} + \dot{\mathbf{x}}_k T \end{aligned} \tag{3.20}$$

3.6 2D-3D Reconstruction Constraints

The navigation model described in the previous sections provides an estimate of the catheter shape by simulation. When synchronization is made with actual X-ray image sequences, it is pretty straightforward to see that the simulation rapidly deviates from the real data. To retrieve the catheter's real shape, the model needs to be combined with external observations about the current state of the device. The approach we first followed in our thesis consisted of expressing such information as mechanical constraints. We report in this section on the various constraints we investigated, and both their impact and limitations.

The 2D projected shape of the catheter is detected in the X-ray images. Hence, the first hypothesis we made is to enforce the simulated device's projected shape to match the detected 2D projection. To have information on the catheter configuration, we use radio-opaque markers placed on the catheter length and automatically detected and tracked in fluoroscopic images. This gives rise to a set of 2DoFs holonomic constraints, as described in section 3.3.1. A common problem with 2D-3D matching is the uncertainty of the depth of the object in 3D, especially with deformable objects. The second set of constraints is provided by the contact conditions that force the catheter to remain inside the blood vessels. The lack of constraint on the proximal part of the catheter, outside the blood vessel, can have a definite impact on its distal shape. Therefore, we investigated a third and last set of constraints placed at the proximal part of the catheter, which is why we

called them entry constraints.

3.6.1 Projective Constraint

In general, the projected shape of the device, extracted from fluoroscopic images, can be represented as: unstructured points, segments of curves, or ordered points (or curves), which can define a complete parameterization of a projected 3D curve. Different techniques are adopted to match the detected 2D features with the corresponding parts on the 3D model, according to the type of extracted information.

The focus of this thesis is on data/simulation fusion. Segmentation of interventional devices in fluoroscopic images, along with new contributions in this field, is not attempted in this work. To simplify image processing, we make the assumption extensively used in monocular reconstruction to detect and track 2D features corresponding to known 3D points. In particular, we used a catheter tagged with radio-opaque markers, easy to detect and track. Furthermore, X-ray images were calibrated, i.e. a projection matrix \mathbf{C} was determined for each image sequence. Thus, the image constraint is mainly based on 2D-3D point correspondences.

3.6.1.1 Marker Detection and Tracking

As above stated, the catheter is assumed to be tagged with M radio-opaque markers $\{\mathbf{m}_i = (x_i, y_i, z_i)\}_{i \in [1, M]}$, equally distributed along the catheter length (Fig. 1.4(a)). Each marker \mathbf{m}_i is related to the catheter nodes through a constant linear mapping \mathcal{M}_i . In the X-ray image (Fig. 3.27(a)) (acquired in this case on a rigid phantom), the catheter's markers appear clearly visible inside the vessel. Given their shape, size, and grey-scale intensity, they are easily distinguishable from other structures, such as the calibration markers used to retrieve the projection matrix. Fluoroscopic images are treated in real-time to detect the markers. In particular, linear and non-linear filtering operations are applied to extract the markers.

3.6.1.2 Calibration and Projection Matrix

In the image, each marker is detected at pixel coordinates $p_i = (u_i, v_i)$ which are related to the 3D marker coordinates through the $[3 \times 4]$ projection matrix \mathbf{C} , such that

$$\underline{\mathbf{p}}_i = \mathbf{C} \underline{\mathbf{m}}_i \quad (3.21)$$

where the underline notation expresses homogeneous coordinates. The calibration matrix

\mathbf{C} only depends on the X-ray view incidence, which is assumed constant during the acquisition of a fluoroscopic sequence. A calibration procedure is performed to retrieve \mathbf{C} . For our work, 3D markers are glued at the surface of the phantom and detected in the X-ray image, as well as in a 3D CT scan of the phantom, which enables us to build 2D-3D point correspondences. The 3x4 projection matrix is computed by solving the linear system built from those 2D-3D correspondences [109].

In general, a 3D point $P(x, y, z)$ can be expressed either in the world reference frame \mathcal{R}_w , or within the camera reference frame \mathcal{R}_c . This entails that the projection matrix \mathbf{C} can be decomposed in intrinsic parameters $\mathcal{K} \in \mathbb{R}^{3 \times 3}$ ([110]) and extrinsic parameters $\mathbf{E} \in \mathbb{R}^{3 \times 4}$ so that:

$$\mathbf{C} = \mathcal{K} \times \mathbf{E}$$

$$\begin{pmatrix} m_{11} & m_{12} & m_{13} & m_{14} \\ m_{21} & m_{22} & m_{23} & m_{24} \\ m_{31} & m_{32} & m_{33} & m_{34} \end{pmatrix} = \begin{pmatrix} f_x & s & x_0 \\ 0 & f_y & y_0 \\ 0 & 0 & 1 \end{pmatrix} \times \begin{bmatrix} r_{11} & r_{12} & r_{13} & t_1 \\ r_{21} & r_{22} & r_{23} & t_2 \\ r_{31} & r_{32} & r_{33} & t_3 \end{bmatrix} \quad (3.22)$$

The extrinsic matrix \mathbf{E} is defined by a rigid rotation \mathbf{R} and a translation T , with $\mathbf{E} = [\mathbf{R}|T]$ allowing the transformation between the two reference frames \mathcal{R}_w and \mathcal{R}_c .

Let P_c be the point expressed in the camera reference frame and P_w its correspondent in the world reference frame, we can hence express:

$$P_c = \mathbf{R}P + T \quad (3.23)$$

$$P_w = \mathbf{R}^t P_c - \mathbf{R}^t T \quad (3.24)$$

Concerning the intrinsic matrix \mathcal{K} , it transforms 3D camera coordinates to 2D homogeneous image coordinates expressing the focal length in terms of pixels f_x, f_y , the principal point of the camera x_0, y_0 and the skew s between the axes. \mathcal{K} is invertible, and given the $p(u, v)$ pixel coordinates of the projected point P (expressed in homogeneous coordinates) we can easily express the line of sight associated to p , as the line going (through the origin of the camera frame \mathcal{R}_c and along vector \mathbf{n}_p given in \mathcal{R}_c by::

$$n_p = \mathcal{K}^{-1} \underline{p} \quad (3.25)$$

3.6.1.3 Projective Constraint Formalism

Each detected marker \mathbf{m}_i defines a line of sight with the optical center of the camera (origin of \mathcal{R}_c), along vector $\mathbf{n}_i = \mathcal{K}^{-1} \underline{\mathbf{m}_i}$. If P is a 3D point, a Cartesian equation of this

line in \mathcal{R}_c is thus given by:

$$\Delta_i : \begin{cases} \mathbf{v}_1^t P = 0 \\ \mathbf{v}_2^t P = 0 \end{cases} \quad (3.26)$$

which expresses that Δ_i is the intersection of two planes normal to respectively \mathbf{v}_1 and \mathbf{v}_2 . Both vectors must be orthogonal to \mathbf{n}_i and we chose (see Fig. 3.7(b)):

$$\begin{cases} \mathbf{v}_1 = (\mathbf{n}_{i+1} - \mathbf{n}_i) \times \mathbf{n}_i \\ \mathbf{v}_2 = \mathbf{v}_1 \times \mathbf{n}_i \end{cases} \quad (3.27)$$

Assuming the all linear mappings between the markers and the catheter's nodes are the identity mapping, the hypothesis that the projected shape of the device have to match the shape extracted withing the image can be geometrically translated by enforcing the nodes of the catheter to slide along the markers' lines of sight in 3D. This can be translated, for each node \mathbf{x}_i , by:

$$\mathbf{v}_1^t(\mathbf{R}P_i + T) = 0 \quad \text{and} \quad \mathbf{v}_2^t(\mathbf{R}P_i + T) = 0 \quad (3.28)$$

where P denotes the position component of the generalized coordinate \mathbf{x} , in \mathcal{R}_w . This constraint takes the general form $\mathcal{P}(\mathbf{x}_i) = 0$, and is therefore holonomic.

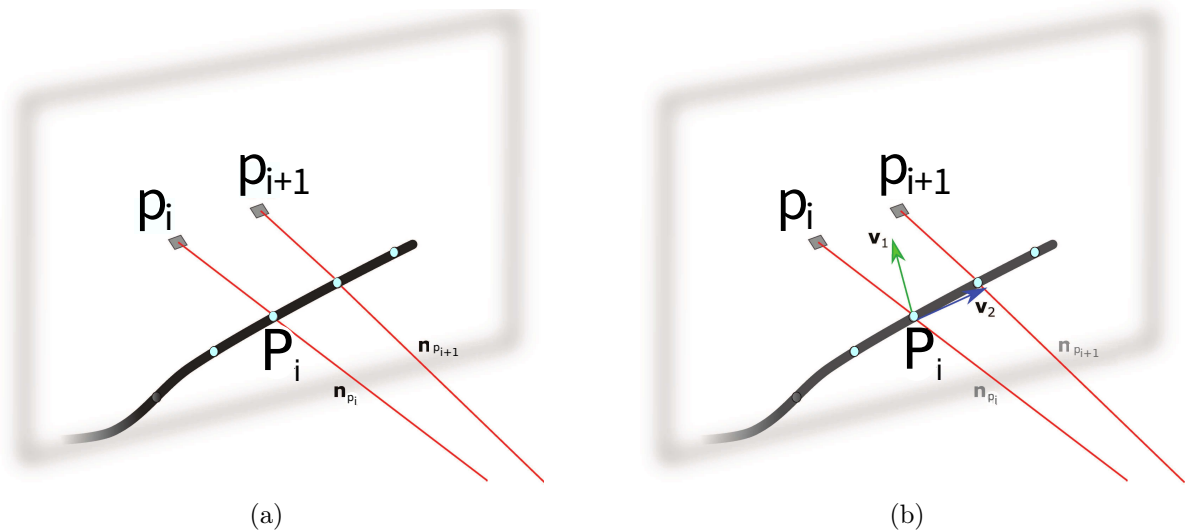


Figure 3.7: The line of sight for each 3D catheter's node is defined from its corresponding 2D point detected onto the image and the camera center. Normals \mathbf{v}_1 and \mathbf{v}_2 are calculated from eq.3.27.

Forces are applied on each node, along the associated vectors \mathbf{v}_1 and \mathbf{v}_2 . The formalism adopted to choose \mathbf{v}_1 and \mathbf{v}_2 makes that both plane constraints are adapted to the projected shape of the catheter: assuming $\mathbf{n}_{i+1} - \mathbf{n}_i$ is approximately tangent to this shape, and that \mathbf{n}_i is approximately orthogonal to the image plane, then \mathbf{v}_1 is orthogonal to the projected catheter shape and parallel to the image plane and \mathbf{v}_2 is also parallel to the image plane and tangent to the projected catheter shape.

3.6.2 Entry Constraint

Another constraint we defined, to have additional 3D knowledge on the insertion point of the device, is called *Entry Constraint* since it applies to the proximal portion of the catheter. To define such constraint, we exploited the fact that instruments are usually inserted through a rigid valve, of whom we can retrieve position and orientation (Fig. 3.8). Through this constraint, we want to fix a third dimension for the registration, and an orientation through which the insertion will be initialized. Similarly to the Projection Constraint, it is a holonomic constraint at 2DoFs, authorizing the sliding of the catheter along a certain line defined by the intersection of the planes whose normals are \mathbf{v}_1 and \mathbf{v}_2 .

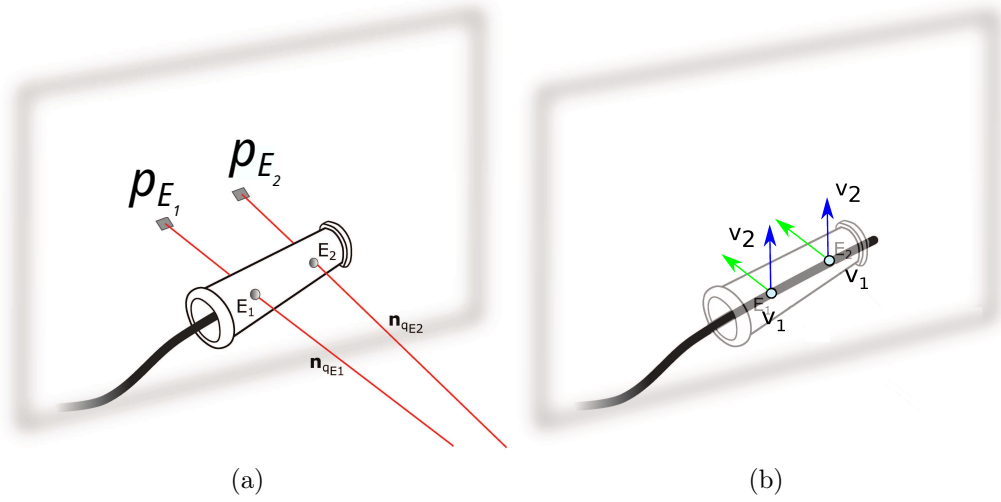


Figure 3.8: Two points of the valve are identified both in 2D and 3D in order to define the normals of the bilateral constraint. The constraint is then applied to the catheter nodes closest to the entry markers.

E_1 and E_2 are the two 3D points on the valve, and p_{E_1} and p_{E_2} their corresponding 2D points detected on the image (Fig. 3.8(a)), the sliding line Δ_E can be defined as:

$$\Delta_E : \begin{cases} \mathbf{v}_1^t P = 0 \\ \mathbf{v}_2^t P = 0 \end{cases} \quad (3.29)$$

where the normals (Fig. 3.8(b)) can be defined as:

$$\begin{cases} \mathbf{v}_1 = \mathbf{n}_{p_{E_1}} \\ \mathbf{v}_2 = \mathbf{v}_1 \times (\mathbf{n}_{p_{E_2}} - \mathbf{n}_{p_{E_1}}) \end{cases} \quad (3.30)$$

For both the projection constraint and the entry constraint, given their linear formulation, the elements of the Jacobian matrix corresponding to each applied boundary conditions will be the coefficients a, b, c and a', b', c' of a generic line f expressed in the Euclidean three-dimensional space through two linearly independent Cartesian equations, identifying the intersection of two non parallel planes:

$$f : \begin{cases} ax + by + cz + d = 0 \\ a'x + b'y + c'z + d' = 0 \end{cases} \quad (3.31)$$

In particular given (3.28), for a given constraint we can write the above coefficients as $(a, b, c) = \mathbf{v}_1^t \mathbf{R}$ and $(a', b', c') = \mathbf{v}_2^t \mathbf{R}$, whereas the vector $\tilde{\mathbf{x}}$ will be composed of $d = \mathbf{v}_1^t T$ and $d' = \mathbf{v}_2^t T$, where \mathbf{v}_1 and \mathbf{v}_2 are normalized.

3.7 Experimentations and Results

In this section, we evaluate the accuracy of the proposed method on both synthetic and real data. In particular, we want to test the method relying solely on *Surface Constraint* or *Entry Constraint* formalism, each one combined with the *Projective Constraint*. The general approach is to compare the achieved reconstruction to a known ground-truth, and evaluate its quality based on some evaluation metrics.

3.7.1 Overview and Metrics

In the synthetic experiments, a simple Y-shape geometry (mimicking a vessel bifurcation) is chosen to generate a ground-truth simulation of catheter navigation. The tagged device is assumed to be inserted through a rigid insertion valve. 2D synthetic observations are generated by projecting the 3D radio-opaque markers according to a chosen view and adding some Gaussian noise. In this case, two orthogonal views have been chosen. Combining the obtained 2D observations, with a catheter navigation model that presents different parameterization from the ground-truth's, we tried to retrieve the real 3D shape of the device. This particular type of geometry has been chosen to evaluate the performances when using different observation angles of view. In particular, we wanted to test the robustness of the reconstruction if the device path is not deductible from the image

(i.e. the plane containing vessel bifurcation is orthogonal the view).

The first real data-set was acquired using the test-bed described in [111], where two different stereoscopic cameras provide a ground-truth reconstruction of the shape of the navigating catheter. These data provided no information on the insertion valve location. Therefore, we only evaluated our method relying on the surface and projective constraints. We generated 2D observations by projecting the reconstructed reference shape according to one of the stereoscopic views and adding some Gaussian noise. Combining such 2D information with the constrained navigation model, we evaluate the quality of the reconstruction in the presence of different parameterization of the catheter navigation model. The second real data-set aims at evaluating the quality of the reconstruction when solely relying on 2D information and the entry constraint. The aim is to establish whether it is possible to perform a correct 3D reconstruction of the catheter shape, without the need of the surrounding anatomy. In this case, we used a catheter equipped with actual markers visible in the X-ray images. The ground-truth catheter insertion has been performed under fluoroscopic guidance and 2D images of the procedure have been acquired. 2D image features are detected and tracked within the recorded images. Additional 3D acquisitions have been performed on some significant points of the insertion, to validate our reconstruction.

The quality of the reconstruction has been evaluated by comparing the 3D shape of the reconstructed catheter with the known ground-truth. Comparison metrics have been evaluated on B-spline interpolations, computed starting from the tip, of both the reference shape $\mathbf{g}_M = (g_1, \dots, g_M)$ and the catheter's $\mathbf{c}_M = (c_1, \dots, c_M)$, (with $M = 10N$ against the N nodes of the FE model). This allows to have a finer discretization of the shapes. Concerning the metrics we evaluated:

- The Euclidean distance between the reference tip and the reconstructed tip:

$$\mathbf{d}(\mathbf{g}_M, \mathbf{c}_M) = \sqrt{(g_1 - c_1)^2}$$

- The mean distance between the distal segment of the reference shape and the distal segment of the reconstructed shape:

$$\mathbf{m}(\mathbf{g}_M, \mathbf{c}_M) = \frac{1}{L} \left(\sqrt{\sum_{i=1}^L (g_i - c_i)^2} \right)$$

with $i \in [1, L]$ covering the 1cm distal part of the device;

- The 3D Hausdorff distance between the whole ground-truth shape and the reconstructed shape:

$$\mathbf{h}(\mathbf{g}_M, \mathbf{c}_M) = \max_{g \in \mathbf{g}_M} (\min_{c \in \mathbf{c}_M} (\mathbf{d}(g, c)))$$

We focused on the tip and distal segment of the device, because it is the part most subject to variations during the insertion and of the highest importance for clinicians.

3.7.2 Synthetic Experiment on Projective Constraint and Surface Constraint

In order to generate the ground-truth scenario, the simulation is based both onto the vessel geometry constraint and the passage of the catheter through an insertion valve. The Y-shaped vessel geometry has been generated by connecting three cylinders of 1 cm of diameter, whereas the catheter is modeled as a series of $N = 30$ connected beams for a total length of 10cm. Once the reference shape has been acquired, 2D observations are generated. First, two orthogonal views are chosen (see Fig. 3.9), then the 3D nodes, corresponding to the markers, are projected according to the selected view and some Gaussian noise (with $\sigma = 0.25$ pixels) is added to the projected positions, to be consistent with the level of noise occurring in image-feature detection. Three different instances of 2D noisy measurements have been generated for each view. Thereby, six different data-sets of 2D observations were generated.

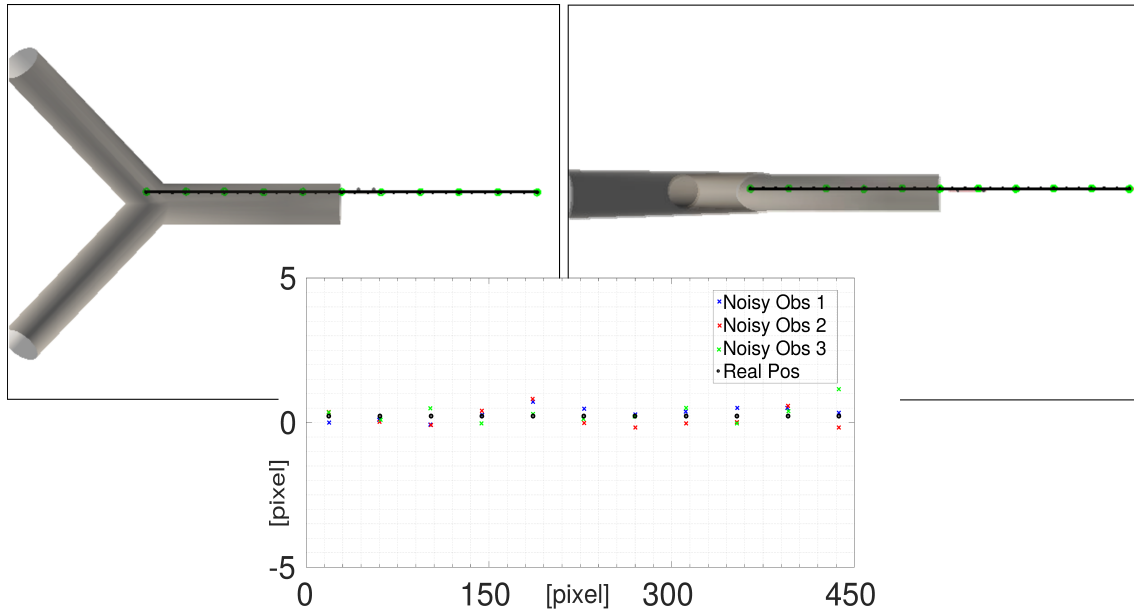


Figure 3.9: Top view and side view. According these views, three different instances of noisy observations are generated to strengthen the statistical significance of the results.

The 2D-3D reconstruction is then performed by relying on the projective and surface constraints (see Fig. 3.10-(b)). No information is provided on the entry of the catheter. Different parameterizations of the catheter navigation model have been tested to mimic different kinds of misknowledge affecting the physics-based model. The objective is to evaluate the robustness of the reconstruction. In general, the primary sources of uncertainty consist of physical parameters (such as Young's modulus), the insertion force, the initial configuration of the catheter, and parameters concerning the applied constraints (such as the friction coefficient or the vessel geometry). For that, three different scenarios

have been evaluated. Model parameters for ground-truth and registration scenarios have been summarized in tab. 3.2.

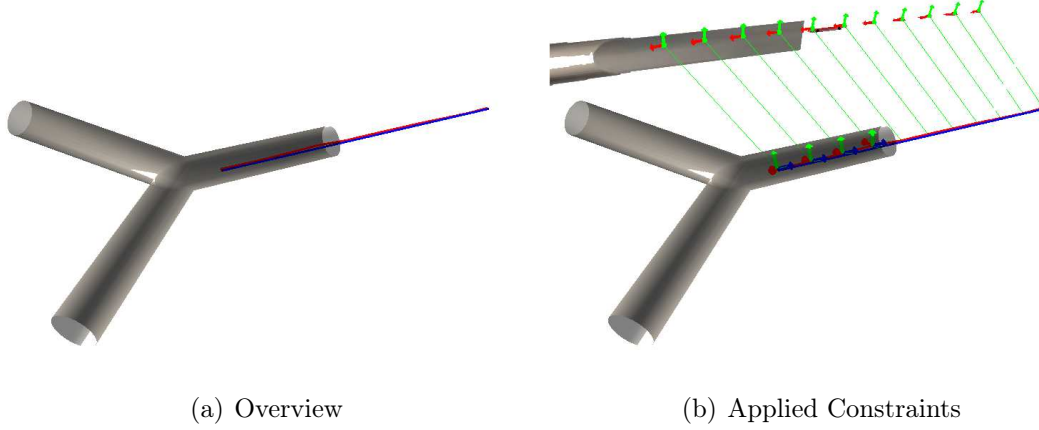


Figure 3.10: (a) The blue shape represents the reference shape, whereas the red shape is the achieved reconstruction. (b) We apply projective constraints and surface constraints. Constraint normals are represented as green and red arrows. Green lines represent line of sight between the camera and the detected markers (in this case, according to a side view).

	Ground Truth	Case 1	Case 2	Case 3	unit
<i>Young's Modulus</i>	750	500	1000	1500	MPa
<i>Outer Radius - Inner Radius</i>	0.35-0.02				mm
<i>Mass</i>	0.48				g
<i>Insertion Force</i>	1.7e-03	1.7e-04		1.7e-02	N/s
<i>Time-step</i>	0.001				s
<i>Total Length</i>	10				cm
<i>Nodes</i>	30	10			
<i>Friction Coefficient</i>	0.01			0.5	
<i>Initial Configuration</i>	c_0		$\mathbf{c}_0 \cdot [\mathbf{R} \mathbf{T}_c]$	c_0	
<i>Surface Constraint</i>	s_0			$\mathbf{s}_0 \cdot [\mathbf{R} \mathbf{T}_s]$	

Table 3.2: Simulation parameters for synthetic evaluation considering the vessel information. See Fig. 3.10 for reference configuration c_0 (blue shape) and Fig. 3.14-(a) for the real vessel geometry here noted as s_0 .

Case 1. In this case, both Young's modulus and insertion force were incorrect with respect to the reference values. A coarser discretization of the beam is adopted. As shown in Fig. 3.11, the reconstruction provided good results. In particular, we obtained an average 3D Hausdorff distance of $h = 3.5 \pm 1.4$ [mm] when using side observations, and $h = 2.4 \pm 0.6$ [mm] for observations from a top view. The average mean error at the distal segment of the tip is $m = 1.5 \pm 0.8$ [mm] for side observations and $m = 0.6 \pm 0.5$ [mm] for top observations. Concerning the average error at the tip, we obtained $d = 0.4 \pm 0.4$

[mm] when using side observations and $d = 0.3 \pm 0.3$ [mm] for a top view.

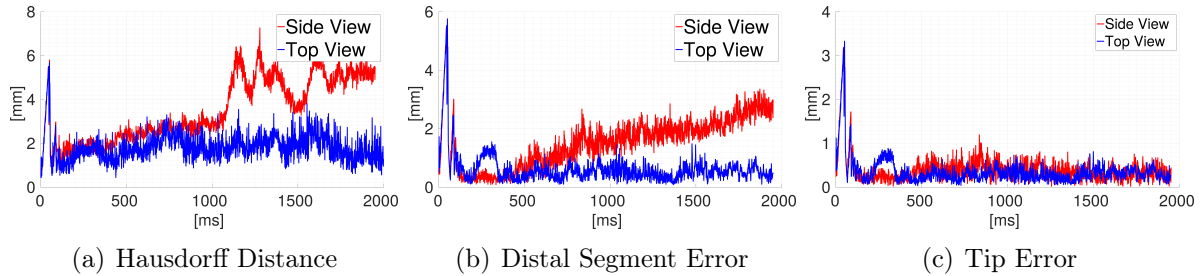


Figure 3.11: Evaluation metrics to compare reconstructed shape with ground truth. Red and blue curves represent respectively the reconstruction error when using side and top view observations. The error is evaluated on the whole 3D reconstruction (a), on the distal segment (b), and on the tip location (c). Both top and side view observations allow retrieving an accurate reconstruction, especially for the distal part.

For the Hausdorff distance, the main errors occurred at the entry point, on the part of the catheter not yet in the phantom. The tip error was always very good, as well as the error on the distal segment in the top view. This error slowly deteriorates in the side view, due to the ambiguity on the bifurcation, remaining within acceptable ranges (2.5 mm, compared to the 1 cm vessel diameter). Results appeared to be more accurate when using observations from a top view (blue graph in Fig. 3.11), due to the fact that there is no ambiguity in the depth direction, showing the geometry of the bifurcation along with the catheter path.

Case 2. A further uncertainty on the initial configuration is taken into account.

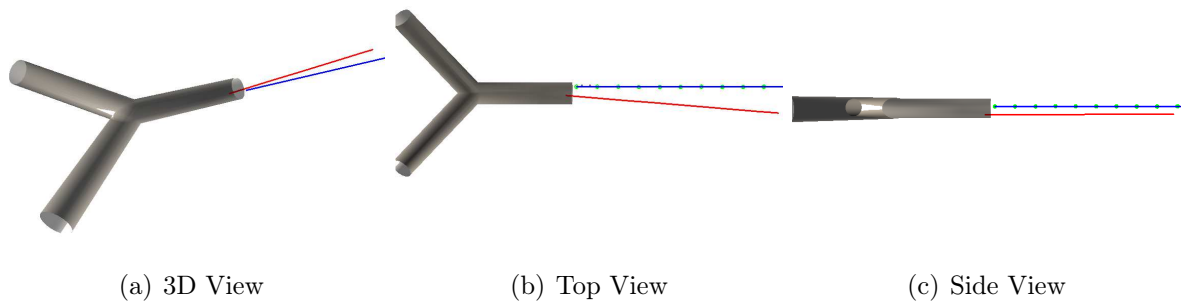


Figure 3.12: Insight on initial configuration error. Real shape (blue) against erroneous (red).

Again, in both cases of side and top observations, we were able to retrieve the catheter's correct position. In particular, we obtained an average 3D Hausdorff distance of $h = 4.3 \pm 0.8$ [mm] for side observations and $h = 3.1 \pm 0.6$ [mm] for observations from a top view. Concerning the average mean error at the distal segment of the tip, we had

$m = 1.7 \pm 0.8$ [mm] for side observations and $m = 0.6 \pm 0.6$ [mm] for top observations. The average error at the tip is $d = 0.4 \pm 0.4$ [mm] when using side observations and $d = 0.4 \pm 0.3$ [mm] for observations from a top view. In this case, errors appear greater (especially for Hausdorff distance) due to the initial wrong configuration where, on the whole length, the distance between the real shape and the reconstructed one is more important. Nevertheless, the tip presents accurate reconstruction results.

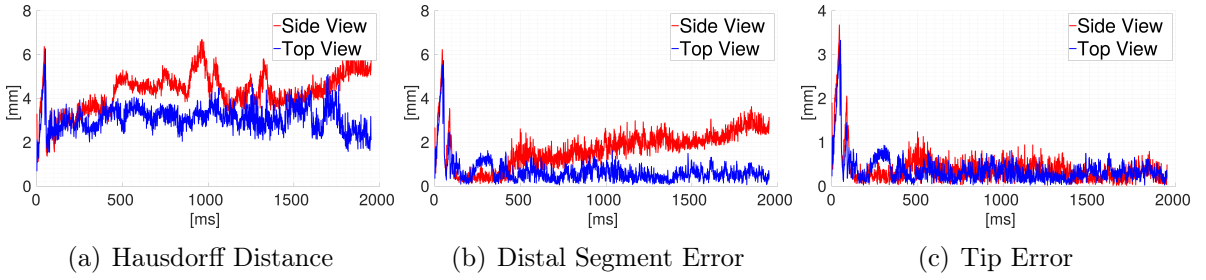


Figure 3.13: Reconstruction errors for Case 2 scenario. Similarly to previous case, both reconstructions performed with top (blue) and side (red) view observations allow retrieving an accurate reconstruction (i.e. the error between the ground truth shape and the reconstructed one remains acceptable).

Case 3. In this case, we wanted to test the accuracy of the reconstruction when having errors on the surface constraint. In particular, we supposed to have an erroneous geometry (see Fig. 3.14-(a)), and an incorrect friction coefficient. Results are presented in Fig. 3.15.

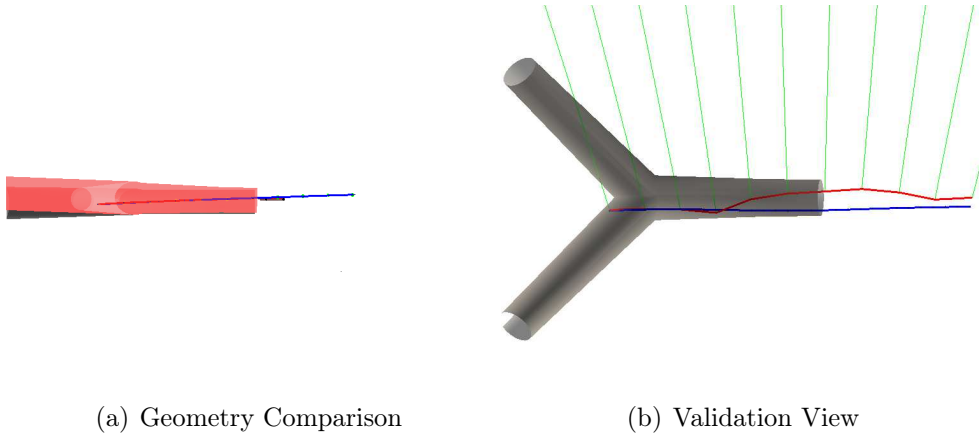


Figure 3.14: (a) The red geometry presents some differences from the real one (here shown from a lateral angle). (b) Looking at the validation view (when using side observations) error appears to be mainly on the bottom on the catheter and in the depth direction.

The average 3D Hausdorff distance is $h = 5.7 \pm 0.9$ [mm] for side observations and $h = 3.8 \pm 0.7$ [mm] for observations from a top view. The average mean distance at the distal segment of the tip is $m = 1.7 \pm 0.8$ [mm] for side observations and $m = 2.2 \pm 0.6$ [mm] for top observations; and average error at the tip is $d = 0.7 \pm 0.4$ [mm] when using

side observations and $d = 1.2 \pm 0.3$ [mm] for observations from a top view. Given the error on the geometry, errors appeared to be higher compared to previous cases. Nevertheless, they mainly occurred on the distal end of the catheter, which is in general less constrained within the vessel geometry.

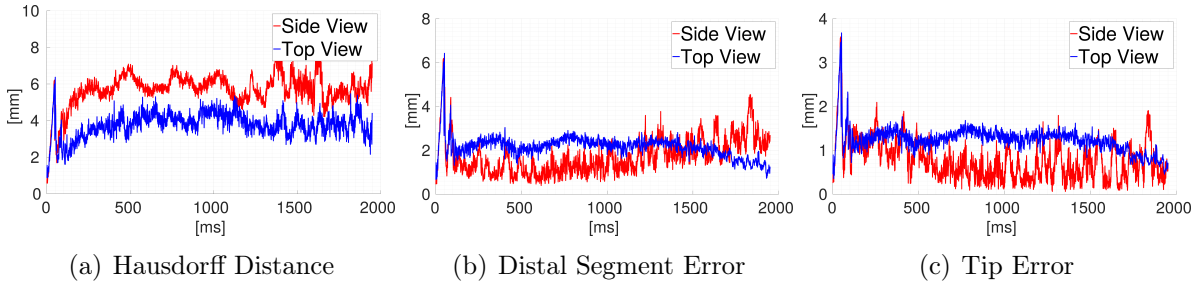


Figure 3.15: Reconstruction errors for Case 3 scenario. In this case, the reconstruction is less accurate than previous cases and the distance from the ground truth (computed on the whole shape (a), the distal segment (b), and the tip location (c)) appears more important. This is due to the error on the vessel geometry initialization which impacts the reconstruction.

As expected, for all the three scenarios, observations from side view (where there is no knowledge of the bifurcation) provide less accurate results. Nevertheless, the reconstruction of the distal segment, whose accuracy is essential for a successful procedure, is always achieved within acceptable ranges of error.

3.7.3 Synthetic Experiment on Projective Constraint and Entry Constraint

Within this second set, we wanted to evaluate whether it is possible to retrieve the correct 3D shape of the device without any knowledge of the surrounding vessels. Indeed, as we have seen above, it is difficult to accurately model vessel segmentation noise. In this sense, it could be interesting to be relieved from considering contacts with the vessel walls, in the case of deformable blood vessels, which is a very complex matter to tackle. However, initial tests rapidly confirmed that 2D markers did not sufficiently constrain the catheter. Therefore, the reconstruction method only relies on the entry constraint and the projective information (see Fig. 3.16).

As in previous cases, in the ground-truth scenario, we supposed the catheter to be inserted through a rigid valve embedded with two radio-opaque markers. These markers are detected and are used to define the entry constraint as presented in Sec. 3.6.2. Analogously to the previous experience, three different scenarios have been set up, where the model parameters differ from the real values to simulate potential misknowledge on the navigation model (see Tab. 3.3). Multiple sources of error have been taken into account simultaneously, to evaluate the quality of the reconstruct when dealing with more or less incorrect models.

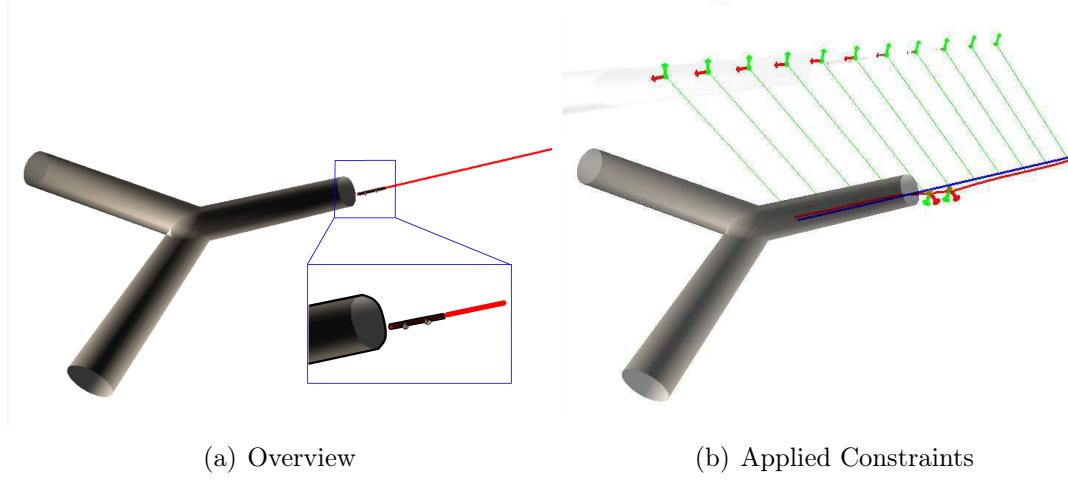


Figure 3.16: (a) The catheter is inserted through a rigid valve embedded with two radio-opaque markers. (b) Detected markers are used to define the entry constraint, which is applied along with the projective constraints. Normals are represented as green and red arrows. Green lines represent line of sight between the camera and the detected point (in this case, according to a side view).

	Ground Truth	Case 1	Case 2	Case 3	unit
<i>Young's Modulus</i>	750	500	1000	1500	MPa
<i>Radius</i>	0.35-0.02				mm
<i>Mass</i>	0.48				g
<i>Insertion Force</i>	3e-03	3e-04		3e-02	N/s
<i>Time-step</i>	0.001				s
<i>Total Length</i>	10				cm
<i>Nodes</i>	30	10			
<i>Initial Configuration</i>	c_0		$\mathbf{c}_0 \cdot [\mathbf{R} \mathbf{T}_c]$	c_0	
<i>Entry Constraint</i>	e_0			$\mathbf{e}_0 \cdot [\mathbf{R} \mathbf{T}_c]$	

Table 3.3: Simulation parameters for synthetic evaluation considering the vessel information. See Fig. 3.10 for reference configuration c_0 (blue shape) and Fig. 3.14-(a) for the real vessel geometry here noted as s_0 .

Case 1. In the first scenario, we supposed to have an incorrect Young's modulus initialization and an erroneous insertion force. As noticeable in Fig. 3.17, only when using observations from the top view (blue graph), it was possible to retrieve the correct shape of the device. In particular, we obtained an average Hausdorff distance of $h = 2.1 \pm 0.4$ [mm], an average mean distance at the distal segment of $m = 1.3 \pm 0.4$ [mm] and an average error at the tip of $d = 0.70.2 \pm$ [mm]. However, we observed a drift after the bifurcation was taken in the side view. This is because the lateral view does not allow us to discern the path of the catheter, and there is no knowledge about the bifurcation, in the model. As a result, the 3D reconstructed catheter enforced the projective constraint (Fig. 3.18-(a)), but it is free to move in the depth direction (Fig. 3.18-(b)). The absence of

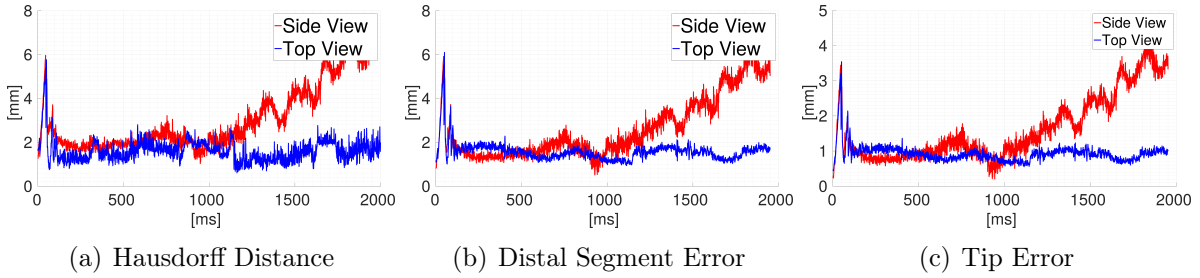


Figure 3.17: Reconstruction errors for Case 1 scenario. Curves, computed between the ground-truth shape and the 3D reconstruction, are the Hausdorff distance (a), the mean distance at the distal segment (b), and the distance at the tip location (c). Red curve represents the reconstructions error when using observations from a lateral view, blue curve refers to top observations. Observations acquired along lateral angle (i.e. where the bifurcation is not visible) do not allow retrieving the correct shape of the catheter.

space constraints (such as the vessel), combined with the lack of 2D information, generates 3D configurations which are physically coherent (i.e., they enforce the applied constraints) but may appear outside of the vessel surface. Instead, observations from a superior view (orthogonal to the bifurcation's principal axis) provide information about the catheter's path. For that, it is possible to retrieve the correct shape of the device, even without any knowledge of the surrounding geometry.

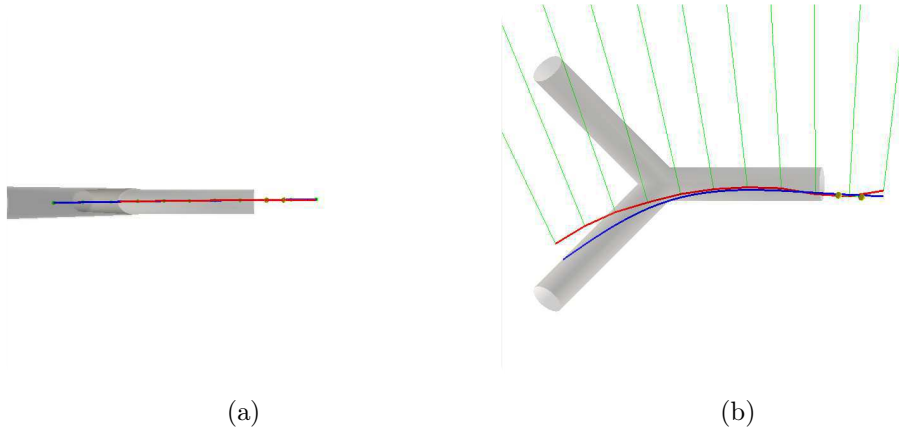


Figure 3.18: (a) Reconstructed matches the projective reference shape. (b) In 3D, the reconstructed catheter assumes a configuration falling outside the vessel surface.

Case 2. In this second scenario, we additionally supposed to have an erroneous initial configuration of the catheter, as in Fig. 3.12. Like previously, only when using observations that provide information about the path of the catheter (i.e. top view), it is possible to retrieve the correct 3D shape (blue shape in Fig. 3.19). We obtained an average 3D Hausdorff distance of $h = 2.4 \pm 0.4$ [mm], an average mean distance at the distal segment of $m = 1.6 \pm 0.4$ [mm] and an average error at the tip of $d = 0.9 \pm 0.2$ [mm].

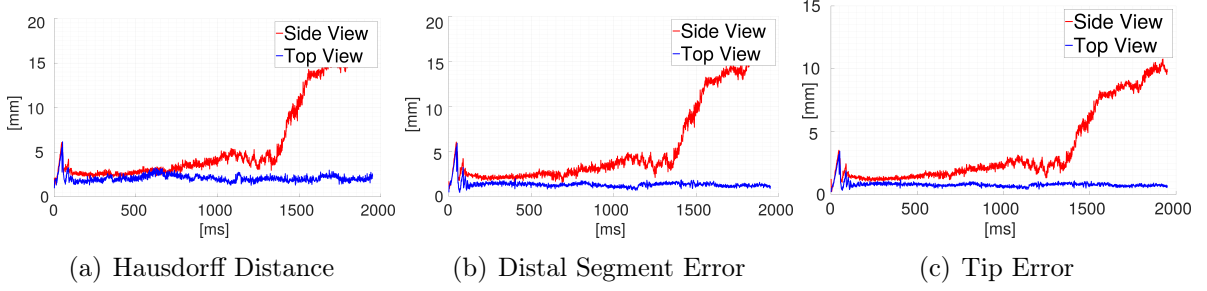


Figure 3.19: Reconstruction errors for Case 2, representing the distance between the ground-truth shape and the 3D reconstruction. As previously, side view observations prevent from an exact reconstruction (red curve diverging). In this case, errors are more important due to the difference on the initial configuration of the catheter.

Case 3. In this last scenario, we further supposed to have an error on the initialization on the entry constraint. To mimic a segmentation error on the radio-opaque markers embedded on the insertion valve, we assumed the entry constraint to be misplaced compared to the real markers position (see Fig. 3.20).

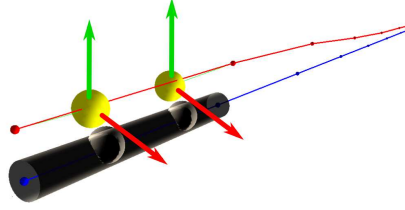


Figure 3.20: Misplaced entry constraint (yellow spheres) enforces the reconstructed catheter (red shape) to diverge from the ground-truth shape (blue) which lies inside the insertion valve.

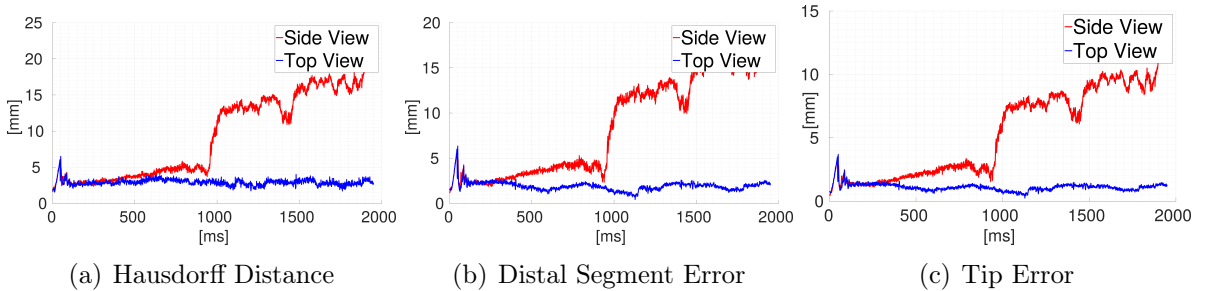


Figure 3.21: Reconstruction errors for Case 3 scenario. As shown by the red curve, representing the reconstruction performed with observations acquired along lateral angle (i.e. where the bifurcation is not visible), side observations do not allow retrieving the correct shape of the catheter. Reconstruction errors from lateral observation appears greater due to the uncertainty on the entry constraint initialization.

As in previous cases, only the top view allows to retrieve the correct shape of the

catheter (blue shape in Fig. 3.21). We obtained an average 3D Hausdorff distance of $h = 2.9 \pm 0.4$ [mm], an average error at the distal segment of $m = 1.9 \pm 0.5$ [mm] and an average error at the tip of $d = 1.1 \pm 0.2$ [mm].

3.7.4 Real Data Experiments on Projective Constraint and Surface Constraint

In this experiments on real data, we evaluated the method relying on the projective and surface constraints. As performed in [111], a 1.7F micro-catheter (Headway TM 17, MicroVention Inc.) was inserted in a rigid phantom made of a silicone mold of an internal carotid artery (H+N-R-A-003 model, Elastrat). The navigation within the transparent phantom was captured at 198 fps by a pair of two high speed cameras (TM-6740CL, JAI/Pulnix), synchronized using a trigger (C320 Machine Vision Trigger Timing Controller, Gardasoft). The stereovision camera setup was calibrated using a chessboard target and OpenCV algorithms. One camera was placed above the phantom to provide a top view, and the other one provided the side view. In particular, the calibration measured the projection matrices for each view (matrix \mathbf{C} in Eq. (3.21)).

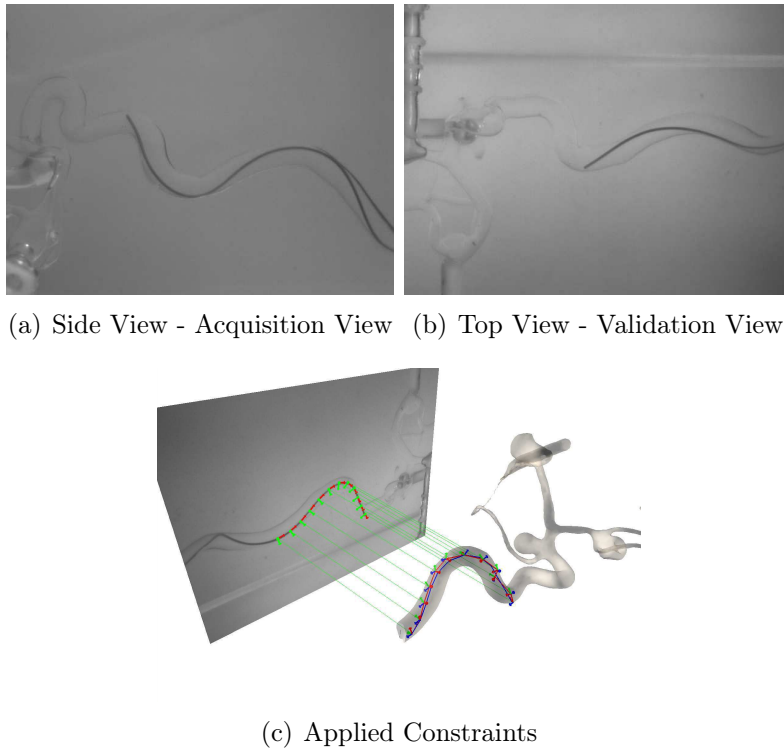


Figure 3.22: Two orthogonal views are acquired (a)-(b). Reconstruction is performed applying projective constraint and surface constraints, whose normals are represented as green and red arrows. Green lines represent line of sight, blue shape is the real catheter, and in red is the reconstructed catheter.

A sequence of 2130 images (640 x 480 pixels, with a pixel size of 0.13 mm), of a total duration of 10 s, was acquired: the catheter was automatically segmented and reconstructed in 3D by triangulation in each frame. This setup provided the ground-truth reconstruction. It is worthwhile noting that this data-set is particularly interesting due to a stick-slip motion, which occurs around $T = 1200$. The velocity profile suddenly changes due to the accumulative effect of friction phenomena. At each time step of the simulated insertion, virtual markers placed on the catheter are projected through the known projection matrix so that their 2D positions are automatically computed according to two different orthogonal views (Fig. 3.22). Each data-set has markers projected in a view called hereafter *the acquisition view*, while the other orthogonal view will be referred to as *the validation view*. This latter view is not involved in the reconstruction process, and therefore enables an objective assessment of the capacity of our algorithm to retrieve the correct shape, even in the depth direction of the acquisition view. Three different observations sets were generated by adding a random Gaussian 2D noise to such projected 2D positions. A standard deviation of 0.1 pixels was chosen to be consistent with the level of detection error encountered in actual images. Thereby, six different data-sets of 2D observations were generated. Without further knowledge of the physics-based model of the catheter, we decided to evaluate the reconstruction for three different scenarios, presenting each a different value of Young's Modulus, insertion force, and friction coefficient. Models parameterizations are summarized in Tab. 3.4, where parameters have been initialized with different values, all included within a range of physically coherent values.

	Case 1	Case 2	Case 3	unit
<i>Young's Modulus</i>	500	250	750	MPa
<i>Radius</i>	0.4-0.02			mm
<i>Mass</i>	0.2			g
<i>Insertion Force</i>	2.5e-03	2.5e-04	2.5e-02	N/s
<i>Time-step</i>	0.001			s
<i>Total Length</i>	6			cm
<i>Nodes</i>	12			
<i>Friction Coefficient</i>	0.01	0	0.5	

Table 3.4: Simulation parameters for real data-set experience, using surface and projective constraints.

As we show in Fig. 3.24, the catheter perfectly enforced the projective constraint. Observing from the acquisition view, the projection of the reconstructed catheter (in green) perfectly matches the 2D shape in the images. Instead, when considering the whole 3D shape, it is possible to notice that: 1) at the beginning of the insertion, we were able to reconstruct the correct 3D shape, 2) the reconstruction method failed when the stick-slip transition occurred. On average, among the three scenarios, we obtained a 3D Hausdorff distance $h = 5.2 \pm 2.5$ [mm]; an average error at the distal segment of the device $m = 2 \pm 1.3$ [mm]; and an average error at the tip $d = 1.4 \pm 0.8$ [mm].

In Fig. 3.25, we present qualitative reconstruction results: whereas side view was used as observations view, the reconstructed catheter is here superimposed (in yellow)

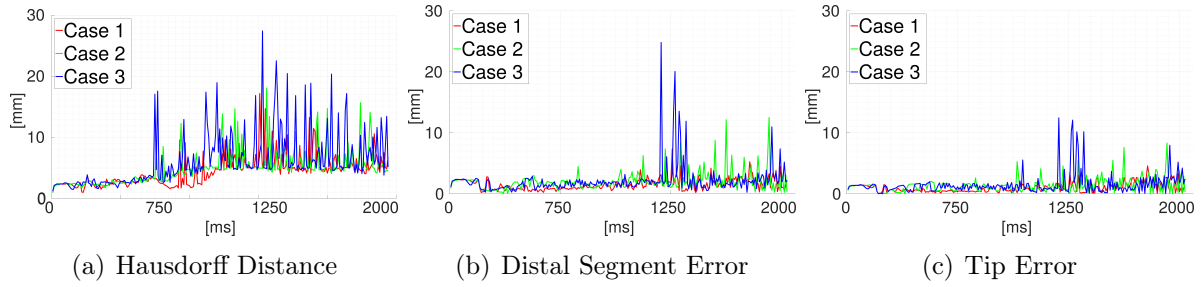


Figure 3.23: The Hausdorff distance (a), the mean distance at the distal segment (b), and the error at the tip (c), have been computed between ground-truth shape and 3D reconstruction. Curves represent reconstruction errors when using different sets of model parameters initializations. The method is unable to compensate stick-slip transition occurring around $T = 1300$, as shown by appearing peaks.

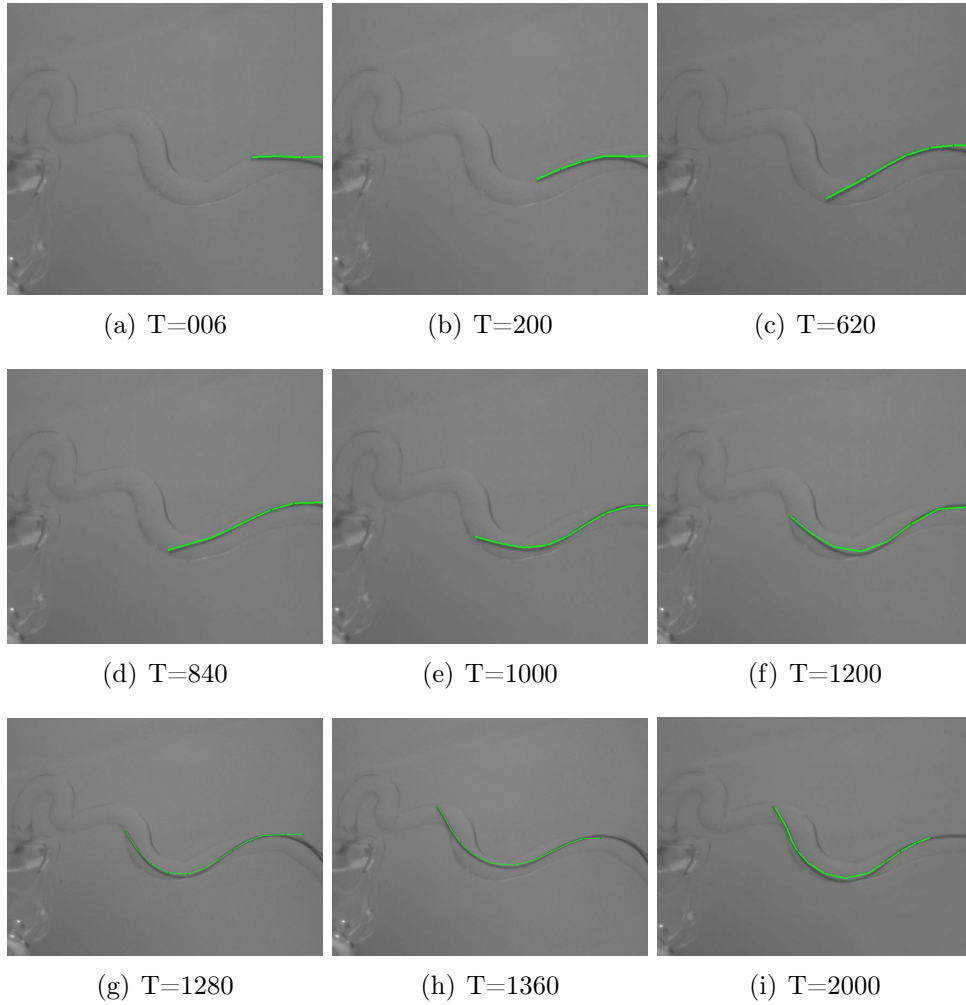


Figure 3.24: Reconstruction along acquisition view. In fig. (f), (g), (h) it is possible to observe the stick and slip transition, with an abrupt movement occurring within a short interval (for details see [111]).

over the validation view. As soon as accumulative phenomena occur (around $T = 1000$, Fig. 3.25-(e)), the method is no more able to retrieve the correct 3D configuration. The problem, which is already over-constrained and ill-conditioned, presents a further complication consisting of the abrupt variation of the velocity profile. This phenomenon causes an important discrepancy between the observed 2D positions and what is provided by the navigation model. To compensate for such variation while enforcing all the applied constraints, the reconstructed device assumes 3D configurations non-physically coherent.

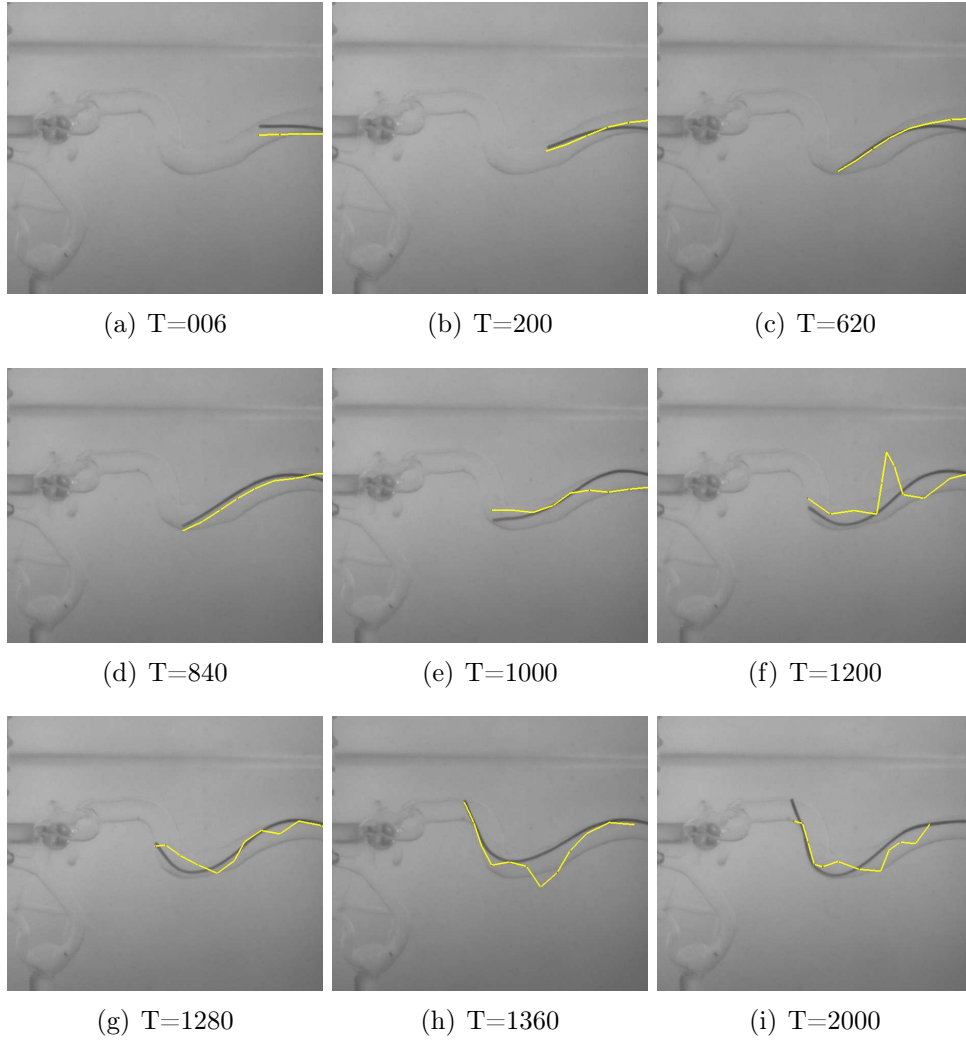


Figure 3.25: The reconstructed shapes are superimposed in the validation view (view orthogonal to the observation view).

3.7.5 Real Data Experiments on Projective Constraint and Entry Constraint

The last evaluation on real data has been performed on a rigid phantom simulating a vascular branch of 1.8 cm of diameter. Indeed, the above experiment demonstrates that projective and surface constraints are not sufficient to retrieve the correct 3D shape of the catheter in the presence of non-linear phenomena. Unfortunately, in the previous setup, we had no means of capturing the position of the insertion valve to test for the impact of the entry constraint. We therefore designed and experimented on a new phantom-based setup. In particular, we wanted to test the method solely relying on the Entry Constraint and the Projective Constraints. As for the synthetic scenario, we tried to evaluate whether it is possible to retrieve the correct 3D shape of the device, without any knowledge of the surrounding vessels.

Medical images have been acquired through a 3D capable angiography C-arm (Artis Zeego, Siemens Healthcare, Erlangen). We chose a large vessel on purpose so that the shape of the catheter could not be directly determined from the shape of the vessel. Calibration markers, both visible in 3D CT-scan and 2D X-ray images, were embedded onto the phantom so that a 3D CT/2D X-ray marker-based registration could provide the projection matrix (Fig. 3.26) as described in Sec. 3.6.1.2. Two additional markers were positioned on the entry valve, to retrieve the catheter entrance's coordinates.

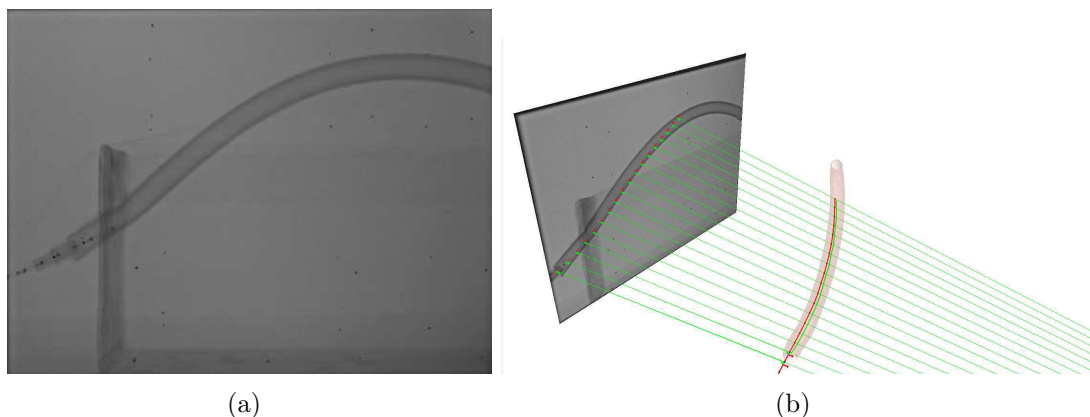


Figure 3.26: (a) 2D fluoroscopic images showing both calibration markers embedded onto the phantom and radio-opaque markers of the partially inserted catheter. (b) Green lines represent the line of sight of the camera; red shape represents the reconstructed catheter whereas the green catheter shape represents the ground-truth.

The instrument is a flexible catheter with radio-opaque tags every 1cm; no contrast medium was needed. The catheter insertion is performed under 2D fluoroscopy; during the insertion some 3D scans were taken to retrieve the real 3D position of the catheter and validate our reconstruction. A simple tracking algorithm, based on thresholds on gray levels and blob detection, was used to extract and track image features automatically.

We exploited the temporal coherence of the detected markers to bind the 2D markers with the corresponding 3D nodes of the catheter (see Fig. 3.27). 3D coordinates of calibration markers and ground-truth catheter needed for the validation were manually extracted through segmentation of medical data. The catheter is modeled as a series of 30

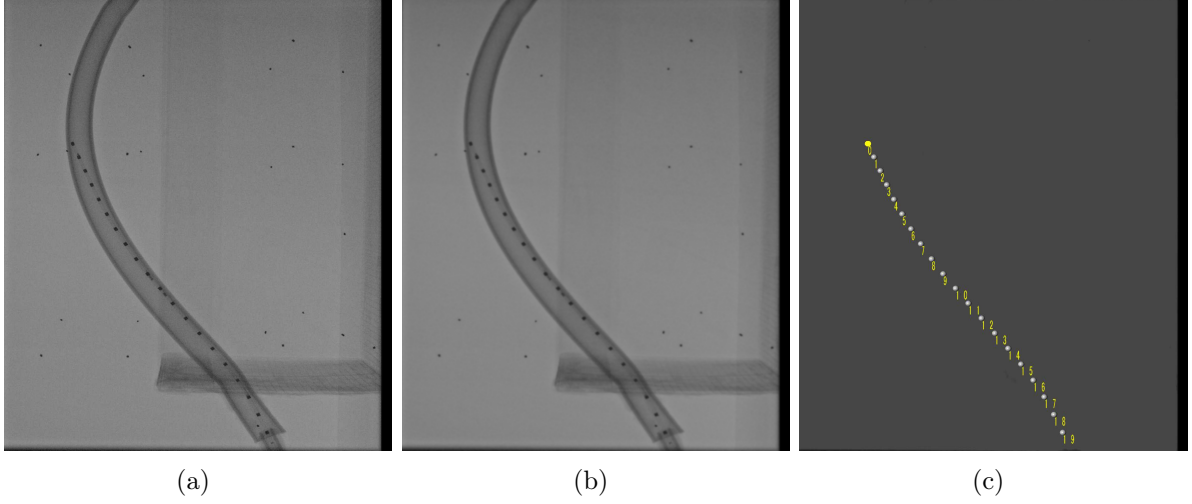


Figure 3.27: Typical work-flow from the original image (a) to the extracted markers with the corresponding indices(d). First a Gaussian filter is applied to smooth the image (b), then a threshold on gray levels and a blob detection allow to extract the markers (c).

connected beams, each one 1 cm long. Given the absence of any knowledge of the devices' physical parameters, we tested the method for three different scenarios presenting different model parameterizations, all coherent with typical values from the literature. Values are summarized in Tab. 3.5.

	Case 1	Case 2	Case 3	unit
<i>Young's Modulus</i>	750	500	1000	MPa
<i>Radius</i>	0.85-0.7			mm
<i>Mass</i>	1			g
<i>Insertion Force</i>	3e-03	3e-04	3e-02	N/s
<i>Time-step</i>	0.001			s
<i>Total Length</i>	30			cm
<i>Nodes</i>	30			

Table 3.5: Simulation parameters for real data-set experiments, using entry and projective constraints.

In this case, given the single-arm fluoroscopic equipment, we did not have a second validation view (orthogonal to the acquisition view) to validate the method. Instead, we performed some 3D acquisitions at some key points of the insertion, that we denoted as

v_1, v_2, v_3 . The extracted 3D shapes represent the ground-truth values, and the evaluation metrics are computed between these configurations and the catheter reconstruction.

In Fig. 3.28, we present the numerical results. At the first validation step ν_1 , performed shortly after the beginning of the insertion, the average 3D Hausdorff distance is $h = 4.6 \pm 0.12$ [mm], which represents about 25% of the total vessel diameter; the mean distance at the segment is $m = 4.6 \pm 0.11$ [mm] and the error at the tip is $e = 2.8 \pm 0.14$ [mm]. At the second validation step ν_2 , performed at the half of the insertion path, the overall error between the ground-truth and the reconstructed shape decreases: the average 3D Hausdorff distance is $h = 2.6 \pm 0.4$ [mm], which represents about the 14% of the total vessel diameter; the mean distance at the segment is $m = 1.7 \pm 0.1$ [mm] and the error at the tip is $e = 0.8 \pm 0.3$ [mm]. This is because more markers are detected, therefore, the projective information better allows us to reconstruct the shape. At the third validation step ν_3 , performed at the end of the insertion, we compute an average 3D Hausdorff distance of $h = 5.9 \pm 0.5$ [mm], a mean distance at the distal segment of $m = 4.6 \pm 0.4$ [mm] and an error at the tip of $e = 3.2 \pm 0.64$ [mm]. Contrarily to the previous step, the reconstructed shape diverges from the ground-truth; we attributed this behavior to the fact that the entry constraint, providing 3D information, is now more distant from the distal part of the catheter, hence his influence is lower.

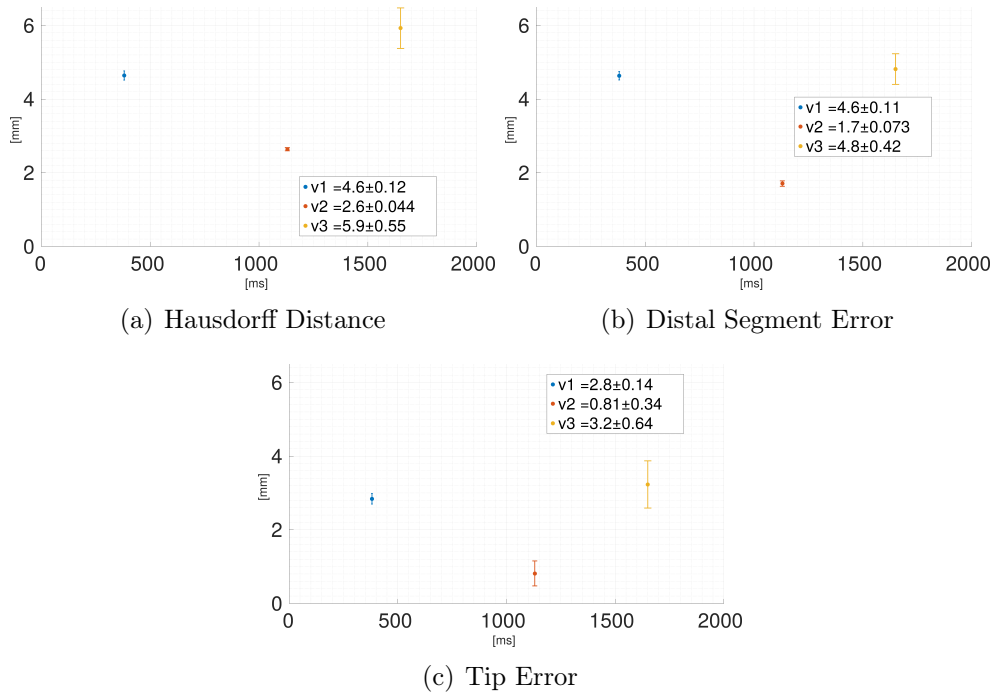


Figure 3.28: Reconstruction errors are computed at the three validation steps ν_1, ν_2, ν_3 , comparing the ground-truth 3D acquisition with the 3D reconstruction. Best results are achieved in the middle of the insertion where the markers provide more 2D information and the entry constraint is not too far to influence the orientation of the catheter.

Qualitative results are presented in Fig. 3.29, where we assess the 3D view augmented with the virtual vessel (displayed along an angle orthogonal to the acquisition view), and compare it with the projective view of the fluoroscopic images.

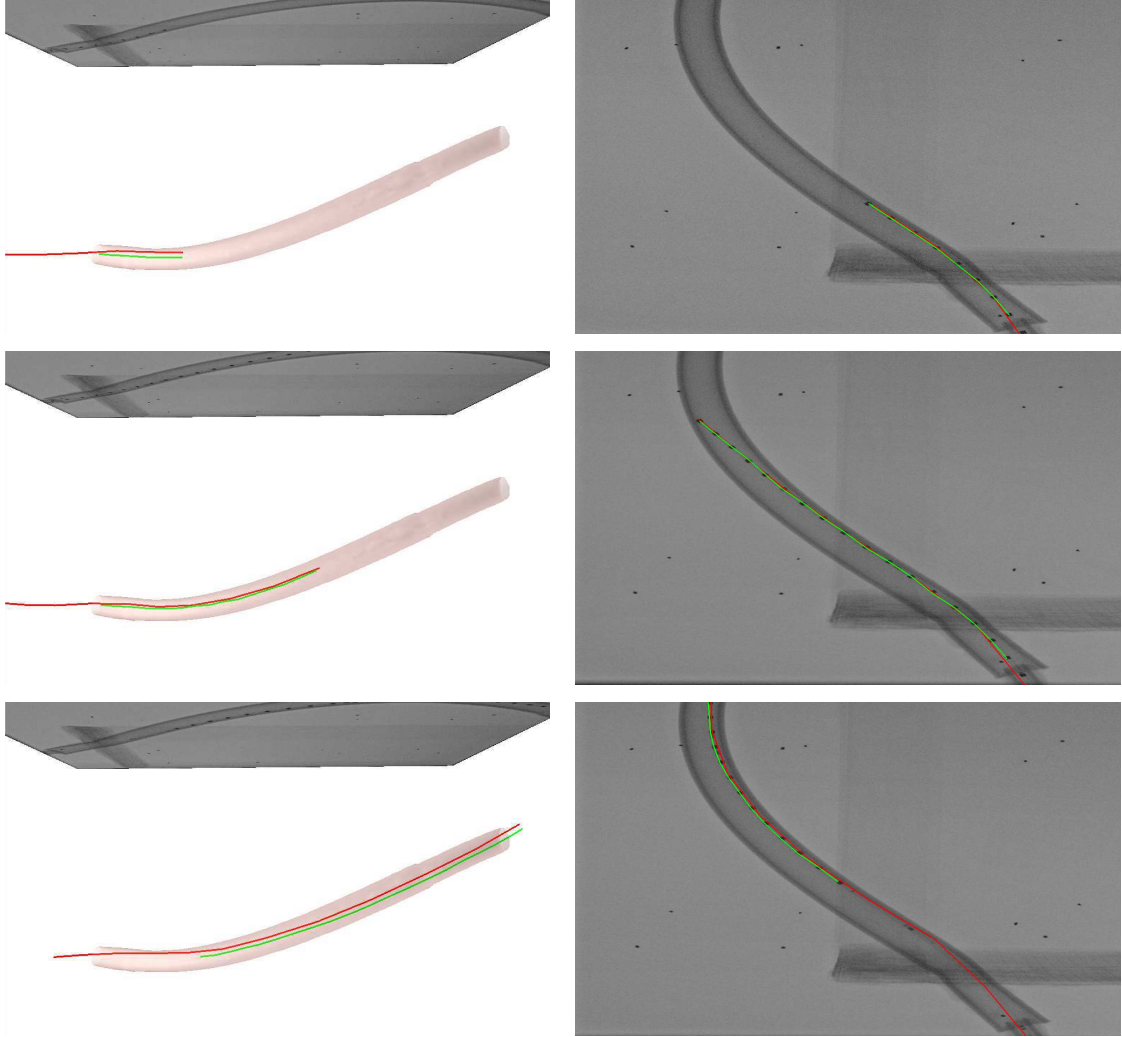


Figure 3.29: 3D augmented view and projective view for the three validations of the first data-set. Real catheter is represented through red points, while the green line is the virtual catheter resulting from our simulation

3.8 Conclusion

In this chapter, we presented a deterministic method to retrieve the 3D shape of the device from 2D monocular fluoroscopic images. In particular, we focused our approach on a constrained physics-based simulation where the chosen constraints do not require to embed an external sensor onto the catheter to have 3D information. The *Projective Constraint* allows us to integrate the 2D information extracted from fluoroscopic images. In particular, it enforces the projected 2D shape of the real catheter to correspond to the 2D features detected and tracked within the images. The *Surface Constraint* bounds the catheter within the volume of the vessel geometry; this aims at reducing the number of possible solutions, defining a boundary volume where the 3D configurations may exist. The *Entry Constraint* provides a 3D information about the orientation of the catheter at distal the insertion point. The *Projective Constraint* is always enforced. In all of our scenarios the projected shape of the reconstructed , catheter always corresponds to the 2D information extracted from the fluoroscopic images. As might have been expected, the evaluation experiments carried out outlined some limitations of the proposed method. For example, relying solely on the *Entry Constraint* enables to achieve reliable results only whenever the path of the catheter is deductible from the 2D images. In Fig. 3.18, we show how the method is unable the reconstruct the correct shape of the device when the catheter is heading towards a vessel branch, which is not observable from the fluoroscopic images. The *Surface Constraint* appears to be fundamental to compensate for the ill-posedness of the 2D-3D registration problem. Nevertheless, whenever geometry is affected by segmentation errors, the quality of the reconstruction deteriorates. In addition, we have shown how this deterministic method is unable to compensate for non-linear phenomena occurring in real life, such as stick and slip transition due to friction effects. Lastly, this method does not take into account errors in the parameterization of the physics-based model of the catheter. In reality, it is impossible to have a perfect knowledge of the parameter of the model and such errors must be taken into account.

For the above reasons, we started investigating stochastic methods which allow taking into account the uncertainties associated the mathematical model, as well as the noise which may affect the external measurements describing the current configuration of the catheter.

Part IV

Stochastic Simulation I

PRELIMINARY STUDY ON STOCHASTIC STATE ESTIMATION

Table of Contents

4.1	Introduction	83
4.2	Bayesian Filtering	84
4.2.1	Kalman Filters	84
4.2.2	Non-linear Kalman Filters	85
4.3	State Vector Study	87
4.3.1	State Estimation	89
4.3.1.1	State vector composed of positions and velocities . .	90
4.3.1.2	State vector composed of only positions	91
4.3.1.3	State vector composed of only velocities	93
4.3.2	Data Assimilation	94
4.3.2.1	State vector of positions, velocities, and incorrect parameter	95
4.3.2.2	State vector of positions and incorrect parameter . .	96
4.3.2.3	Results	97
4.3.3	3DoF Beam	98
4.3.3.1	State vector of positions and velocities	99
4.3.3.2	State vector of only positions	100
4.3.3.3	Augmented State	101
4.3.4	2D Observations	102
4.3.4.1	State vector of positions and velocities	103
4.3.4.2	State vector of positions, velocities and model parameter	104

4.3.5	The Modeling of Uncertainty	105
4.3.6	Conclusions	107

4.1 Introduction

In general, all of the methods developed to reconstruct the 3D shape of the device are prone to be affected by errors. Such errors may be related to the external measurements, intrinsically affected by noise, or to inaccuracies of the process model, due to parameterization errors and inexact mathematical modeling, as shown in the previous chapter. Recursive Bayesian estimation methods have been investigated to handle various sources of error. In practice, these methods allow retrieving the most likely state of a system, described by a process model affected by inaccuracies and observed through noisy external measurements.

In Chapter II, we introduced some of the methods that rely on a probabilistic approach to retrieve the 3D shape of the device. For [54], the 3D shape of the device is described through a probability function, where the optimal estimation is retrieved through a particle filter. Particle filters (for more details see [112]) are particularly useful to describe multi-modal probability distributions. Still, they may be exceptionally computationally expensive due to the number of particles that are generated. In our case, each particle requires to perform a simulation step to be propagated, which is not currently compatible with real-time computations. In [22], a catheter insertion model is combined with 3D positions measured of external EM sensors through an Extended Kalman Filter (EKF). The filter enables to manage some level of non-linearities in the dynamics of the system, as well as noisy measurements from EM trackers. In this case, the method still relies on the use of external EM sensors and the navigation model of the device does not take into account the mechanical properties of the catheter. It has been recently shown how a FE model could be leveraged in an EKF framework to achieve online surface reconstruction [94],[113]. Two hypotheses are necessary for this method: they assume to know the deformation modes of the surface and they suppose to detect and track some 2D features, whose correspondences with 3D points of the FE model are assumed to be known. In such an approach, the FE model, driven by the 2D detected features, captures the elastic deformations of the surface, but it does not provide any information about the dynamic behavior of the object; contacts and collision are not taken into account, whereas only fixed physical constraints can be included in the model. Such a framework could not directly fit our specific problem of catheter reconstruction, as a surface FE model cannot be applied to a curved shape like the interventional device.

In this chapter, first, we are going to introduce the Bayesian filtering formalism; then, we present a preliminary study on the state vector and analyze the inaccuracies of the process model.

4.2 Bayesian Filtering

Bayes filters recursively estimate the probability density function associated with a random state ([114]). In the discrete domain, such a state can be represented as a random variable X_k , with k being the discrete time-step, assumed to evolve according to a given process model. The process model can be expressed as a collection of functions $g_k(\cdot)$ such that:

$$\mathbf{X}_k = g_k(\mathbf{X}_{k-1}, \mathbf{u}_k, \omega_k) \quad (4.1)$$

Other external data may also be available at each time-step, providing partial measurements \mathbf{Z}_k of the current state of the system. Such observations are related to the state through a known observation function $h_k(\cdot)$:

$$\mathbf{Z}_k = h_k(\mathbf{X}_k, \mathbf{u}_k, \nu_k) \quad (4.2)$$

where the control input \mathbf{u}_k is a known non-random vector and both state and observations are affected by random noise processes, respectively ν_k and ω_k whose probability density function is known.

Bayes filters are based on a general prediction-update scheme of the posterior probability $P(\mathbf{X}_k|\mathbf{Z}_k)$. Given the previous estimation $P(\mathbf{X}_{k-1}|\mathbf{Z}_{k-1})$ at time $k-1$, the first step consists of computing a prediction of the probability density function, by propagation through the process model g_k : $P(\mathbf{X}_k|\mathbf{Z}_{k-1})$. The predicted estimate is then updated using the current observation, to provide the posterior estimate: $P(\mathbf{X}_k|\mathbf{Z}_k)$. The final state of the system \mathbf{X}_k is thereafter selected according to some optimality criterion (e.g. Maximum A Posteriori or expected value).

4.2.1 Kalman Filters

Kalman filters [115] are a particular case of Bayes filters where noise processes are assumed to be Gaussian, and both process and observation models are linear and can be expressed by matrices:

$$\begin{aligned} \mathbf{X}_k &= A\mathbf{X}_{k-1} + B\mathbf{u}_k + \omega_k \\ \mathbf{Z}_k &= C\mathbf{X}_k + D\mathbf{u}_k + \nu_k \end{aligned} \quad (4.3)$$

where ω_k is the process noise, assumed to be a multivariate normal distribution with zero mean and covariance \mathbf{Q} : $\omega \sim \mathcal{N}(0, \mathbf{Q})$. and ν_k is the observation noise, assumed to be a multivariate normal distribution with covariance \mathbf{R} : $\nu \sim \mathcal{N}(0, \mathbf{R})$. usually

elements A, B, C, D, ω , and ν are indexed by k since they are allowed to vary with time¹. The main steps of a Kalman filter are:

Prediction

$$\text{Predicted State: } \hat{\mathbf{X}}_k = A\mathbf{X}_{k-1} + B\mathbf{u}_k$$

$$\text{Predicted Covariance: } \hat{\mathbf{P}}_k = A\mathbf{P}_{k-1}A^T + \mathbf{Q}$$

Correction

$$\text{Predicted Observation: } \hat{\mathbf{Z}}_k = C\hat{\mathbf{X}}_k + D\mathbf{u}_k$$

$$\text{Innovation: } \mathbf{Y}_k = \mathbf{Z}_k - \hat{\mathbf{Z}}_k$$

$$\text{Innovation Covariance: } \mathbf{P}_{\mathbf{Y}_k} = C\hat{\mathbf{P}}_kC^T + \mathbf{R}$$

$$\text{Optimal Kalman Gain: } \mathbf{K}_k = \hat{\mathbf{P}}_kC^T\mathbf{P}_{\mathbf{Y}_k}^{-1}$$

$$\text{Final State: } \mathbf{X}_k = \hat{\mathbf{X}}_k + \mathbf{K}_k\mathbf{Y}_k$$

$$\text{Final Covariance: } \mathbf{P}_k = (\mathbf{I} - \mathbf{K}_kC)\hat{\mathbf{P}}_k$$

The final state is a linear combination of the prediction and the innovation, where the weight between the two is the Kalman Gain.

4.2.2 Non-linear Kalman Filters

The linear Kalman filter relies on linear models for both the state prediction and the observation function, as well as on the hypothesis of Gaussian noises. Whenever these assumptions are not valid, the Kalman filter formalism may still be used, but some approximations are necessary. For example, the Extended Kalman Filter (EKF) can handle non-linear process and observation models, propagating the system covariance thanks to their first order approximations. In this case, A and C are the Jacobian matrices of g_k and h_k ([116]), which are usually computed as numerical derivatives.

A linear approximation cannot fully capture the behavior of a non-linear system, in particular in the case of abrupt state changes and discontinuities. In our context, the boundary conditions represented by the vessel wall and the non-rigid contacts occurring between the device and the surrounding surface are non-linear phenomena, varying through time, which lead to discontinuities in velocity profiles of the objects in contact. In this work, we decided to use an Unscented Kalman Filter (UKF) (see [95, 116] for more

¹here the index is dropped for the sake of simplicity; in addition, many problems can be modeled with constant matrices.

details) that applies a sampling-based approach to handle the non-linearities of the prediction and observation models (Eq.(4.1)-(4.2)), with potentially stronger non-linearities than EKF can manage. Instead of approximating the non-linear state model, the idea behind a UKF is to draw r deterministic samples from the current estimate of the state in such a way that these samples, called *sigma-points* (red points in Fig. 4.1), capture the first two moments of the state probability distribution, with minimum distortion on the third moment ([95]). Each sigma-point realization σ_j is propagated through the involved non-linearities, which enables to compute the transformed mean and covariance of the state (see Fig. 4.1).

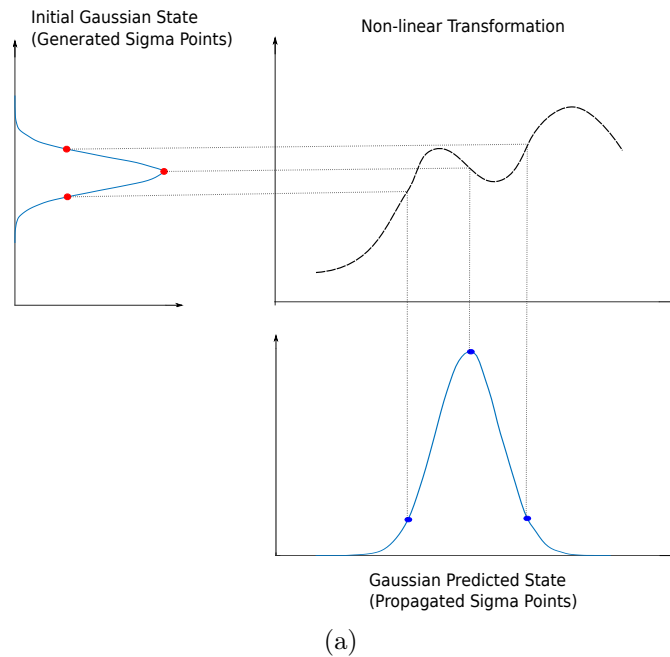


Figure 4.1: **Unscented Transform.** Forecasting a Gaussian variable through a non-linear process provides a non-Gaussian prediction. In the Unscented Transform, the probability distribution is characterized only in terms of a finite set of statistics (mean and covariance, expressed through the sigma-points sampling the distribution). Forecasting only the samples through the non-linear function allows to retrieve a Gaussian prediction, given as the mean and the covariance of the propagated sigma-points.

The by-design preservation of the first moments of the probability density function makes a UKF a better choice than EKF whenever such kind of non-linearities occur [95, 117]. The implementation of an EKF, where the computation of derivatives of both the state transition and the observation matrix is needed, is not straightforward or computationally efficient in our context of collision response and projective observations. The *sigma-points* can be chosen according to different heuristics (see [117]). In particular, being p the size of the state vector $\mathbf{X} \in \mathbb{R}^p$, it is possible to choose: *canonical sigma-points* ($r = 2p$), *star sigma-points* ($r = 2p + 1$), and *simplex sigma-points* ($r = p + 1$). In our work, we opted for the simplex method which provides the smallest amount of deterministic realizations and hence is more suitable for faster computations. Table 4.1

Table 4.1: **Notations : discrete time index k was dropped for simplicity**

\mathbf{X} state vector	\mathbf{P} model covariance matrix
σ_j j^{th} sigma-point	$\mathbf{I}^{(j)}$ unit vector to generate σ_j
\mathbf{Q} model noise covariance matrix	\mathbf{Z} observations vector
$\mathbf{P}^{\hat{Z}}$ observations covariance	\mathbf{R} obs. noise covariance matrix
$\mathbf{P}^{\hat{X}\hat{Z}}$ state-observations cross-covariance	\mathbf{K} Kalman gain
g prediction function	h observation function

and algorithm 1 summarize the notations used throughout the chapter and recall the main steps of a UKF.

Initialization: set $\mathbf{X}_0, \mathbf{P}_0, \mathbf{Q}_0, \mathbf{R}_0$

```

1 for new discrete step  $k + 1$  do
    Prediction:
2     for  $j = 1 : r$  do
3          $\sigma_{jk} = \mathbf{X}_{k-1} \pm \sqrt{\mathbf{P}_{k-1}} \mathbf{I}^{(j)}$  generate sigma-point
4          $\hat{\sigma}_{jk} = g(\sigma_{jk-1}, \mathbf{0})$  propagatesigma-point
5     end
6      $\hat{\mathbf{X}}_k = \mathbb{E}[\hat{\sigma}_k^*]$  compute predicted state = sigma-points mean
7      $\hat{\mathbf{P}}_k = \text{cov}[\hat{\sigma}_k^*, \hat{\sigma}_k^*] + \mathbf{Q}_k$  predicted covariance = sigma-points covariance
    Correction:
8     for  $j = 1 : r$  do
9          $\hat{\mathbf{Z}}_{jk} = h(\hat{\sigma}_{jk})$  compute predicted observations
10    end
11     $\mathbf{P}_k^{\hat{X}\hat{Z}} = \text{cov}[\hat{\sigma}_k^*, \hat{\mathbf{Z}}_k^*]$  compute state-observations cross-covariance
12     $\mathbf{P}_k^{\hat{Z}} = \text{cov}[\hat{\mathbf{Z}}_k^*, \hat{\mathbf{Z}}_k^*] + \mathbf{R}_k$  compute observations covariance
13     $\mathbf{K}_k = \mathbf{P}_k^{\hat{X}\hat{Z}} (\mathbf{P}_k^{\hat{Z}})^{-1}$  compute Kalman gain
14     $\mathbf{X}_k = \hat{\mathbf{X}}_k + \mathbf{K}_k (\mathbf{Z}_k - \mathbb{E}[\hat{\mathbf{Z}}_k^*])$  compute final state
15     $\mathbf{P}_k = \hat{\mathbf{P}}_k - \mathbf{P}_k^{\hat{X}\hat{Z}} (\mathbf{P}_k^{\hat{Z}})^{-1} (\mathbf{P}_k^{\hat{X}\hat{Z}})^t$  compute final covariance
16 end
```

Algorithm 1: Unscented Kalman Filter algorithm. See Table 4.1 for notations. The symbol $*$ stands for the whole set of sigma-points, whereas the subscript j indicates a single sample.

4.3 State Vector Study

The state vector \mathbf{X}_k includes the variables describing the current state of the system in question. In order to choose which variables must be considered, we carried out a series of tests of increasing complexity: starting with a simple scenario, we gradually moved towards a more complex system, similar to the catheter model.

First, we considered a 3DoFs point, assuming that the mechanical parameters are known, to estimate its position and velocity. Secondly, some uncertainty is introduced on the mechanical parameters, in order to see to what extent they can be estimated by data assimilation. Then, we considered a 3DoFs beam, where the mechanical parameters are assumed to be known. Lastly, we are interested in modeling the observations in our projective X-ray imaging framework.

The quantity that interests us, in the end, is the position, which allows us to visualize the object in 3D at each time-step. However, to be mechanically coherent with the object's dynamics, the speed must also be estimated. We thus explored three hypotheses for the state vector: only the positions, only the speeds, and positions and speeds. The objective is to find the best compromise between the filter's performances and the size of the state vector. Considering these simple scenarios, we wanted to identify which variable must be taken into account into the state vector, in order to retrieve the current state of the object, given an incorrect process model and noisy measurements of its position.

The three state vector configurations are tested under different filter parameters tuning $(\mathbf{P}_0, \mathbf{Q}, \mathbf{R})$. In order to properly initialize filter parameters, it is important to quantify both model and observations uncertainty. In general, the observations noise may be easily deduced from the specifications of the used sensor. In this synthetic case, it corresponds to the standard deviation of the Gaussian noise added to the object's real position.

On the other hand, model uncertainty σ_{mod} is not straightforward to initialize. Model uncertainties may be due either to an incorrect formulation of the equations modeling the system or incorrect parameterization of such a model. In our synthetic scenario, model errors are due to a known incorrect parameterization of the acceleration. In practice, it is not always possible to quantify the existing uncertainty. For that, we have taken into account different ranges of parameter tuning. First, we define a nominal configuration $\mathcal{P} = [\mathbf{P}_0, \mathbf{Q}, \mathbf{R}]$ where: where $\mathbf{P}_0 = \mathbf{Q}$, and \mathbf{Q} and \mathbf{R} are set according to the known standard deviations σ_a and σ_{obs} . Besides such nominal configuration \mathcal{P} , we take into account an overestimation and an underestimation of the model uncertainty. Overestimating model uncertainty implies intrinsically relying more on the external observations, which are hence assumed to be more trustful than the model. Such a set of filter parameters will be noted as \mathcal{P}_{obs} . Consequently, the filter parameters set, expressing the underestimation of model uncertainty, will be indicated as \mathcal{P}_{mod} .

$$\mathcal{P}_{obs} = [2^2 \mathbf{P}_0, 2^2 \mathbf{Q}, \mathbf{R}] \quad \mathcal{P}_{mod} = [0.5^2 \mathbf{P}_0, 0.5^2 \mathbf{Q}, \mathbf{R}]$$

To evaluate the accuracy of the filter estimation, we compare the ground truth with the reconstructed state, computing the Euclidean distance between the reference trajectory and the estimated trajectory, as well as the error between the estimated velocity and the real velocity.

4.3.1 State Estimation

As above stated, we first considered a 3DoFs point submitted to a constant force. Initially, we generated a ground truth scenario, where the acceleration is set with a given value \mathbf{a}_{real} . Then, we simulate an incorrect process model, with an uncertainty on the acceleration $\mathbf{a}_{mod} = \boldsymbol{\mu}_a \pm \boldsymbol{\sigma}_a \neq \mathbf{a}_{real}$. External observations are generated by adding some Gaussian noise (with standard deviation σ_{obs}), to the known ground truth 3D positions of the point. Model parameterization is summarized in Table 4.2.

	Parameter	Unit
\mathbf{a}_{real}	$[2.5 \ 0 \ 0]$	m/s^2
$\boldsymbol{\mu}_a$	$[0.25 \ 0 \ 0]$	m/s^2
σ_a	2	m/s^2
$\boldsymbol{\sigma}_{obs}$	$[1e-3 \ 1e-3 \ 1e-3]$	m
T	0.001	s

Table 4.2: Simulation parameters for 3DoF point state vector study experiments.

In order to have an insight into differences between the ground truth, the incorrect model and the external observations, in Fig. 4.2, we compare the real trajectory (green), with the measured positions (blue) and the trajectory obtained with the incorrect model (red).

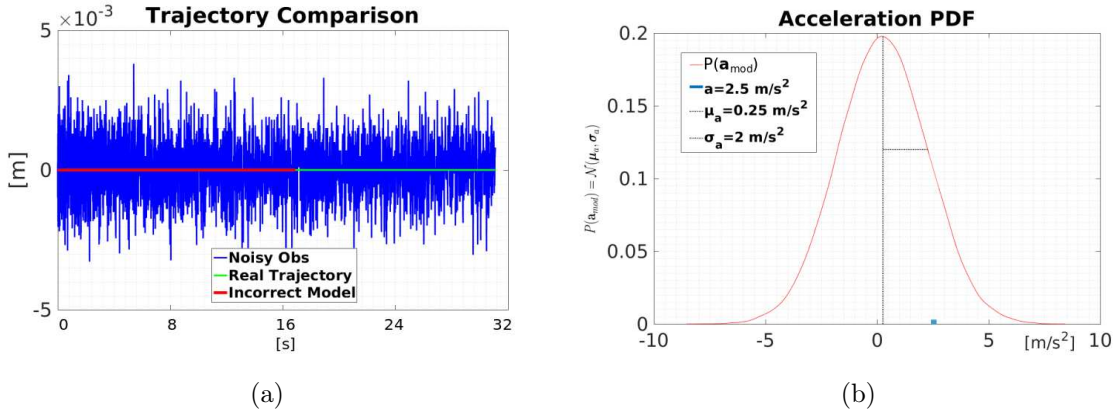


Figure 4.2: **Trajectory comparison.** (a) The 3DoFs point moves along one directions: an incorrect acceleration (red trajectory) as well as noisy measurements (blue trajectory), provide different behaviors from the ground truth. (b) The incorrect model is characterized by a misknown acceleration, described as a Gaussian variable.

The aim of the study is to retrieve the dynamics of the object, notably its trajectory positions \mathbf{x}_k and velocities \mathbf{v}_k . Usually, in Bayesian filters for trajectory estimation, the

state vector is composed of position, velocity and acceleration of the object [95]. In our case, we evaluate the estimation of positions and/or velocities given that using the time integration scheme presented in Eq. (3.17), the acceleration is in fact expressed as a difference of velocities. In general, we assumed an uncertainty on the acceleration $\mathbf{a}_k = \boldsymbol{\mu}_a + \boldsymbol{\sigma}_a$, characterized by an additive Gaussian noise:

$$\begin{aligned}\boldsymbol{\sigma}_a &= \mathcal{N}(\mathbf{0}, \sigma_a^2 \mathbf{I}_3) \quad \text{with} \\ \mathbf{E}(\boldsymbol{\sigma}_a) &= \mathbf{0} \\ \mathbf{E}(\boldsymbol{\sigma}_a \boldsymbol{\sigma}_a^T) &= \sigma_a^2 \mathbf{I}_3\end{aligned}$$

4.3.1.1 State vector composed of positions and velocities

According to Eq. 3.14, we can formalize the dynamic behavior of the 3DoFs point as:

$$\begin{aligned}\mathbf{a}_k &= \frac{\mathbf{f}}{m} + \boldsymbol{\sigma}_a \\ \mathbf{v}_k &= \mathbf{v}_{k-1} + \mathbf{a}_k T \\ \mathbf{x}_k &= \mathbf{x}_{k-1} + \mathbf{v}_k T\end{aligned}\tag{4.4}$$

where T is the discrete time-step. The object's dynamics is retrieved based on external noisy measurements on the 3D location of the object.

The state vector can be written as $\mathbf{X}_k = [\mathbf{x}_k, \mathbf{v}_k]^T$. In the state vector space, Eq. 4.3.1.1 can be rewritten as:

$$\begin{pmatrix} \mathbf{x}_k \\ \mathbf{v}_k \end{pmatrix} = \underbrace{\begin{bmatrix} \mathbf{I}_3 & T \mathbf{I}_3 \\ \mathbf{0}_3 & \mathbf{I}_3 \end{bmatrix}}_A \begin{pmatrix} \mathbf{x}_{k-1} \\ \mathbf{v}_{k-1} \end{pmatrix} + \underbrace{\begin{bmatrix} T^2 \mathbf{I}_3 \\ T \mathbf{I}_3 \end{bmatrix} \boldsymbol{\mu}_a}_{B \boldsymbol{\mu}_k} + \underbrace{\begin{bmatrix} T^2 \mathbf{I}_3 \\ T \mathbf{I}_3 \end{bmatrix} \boldsymbol{\sigma}_a}_{\boldsymbol{\omega}}\tag{4.5}$$

In this case, the observations are related to the state vector through:

$$\mathbf{Z}_k = \underbrace{\begin{bmatrix} \mathbf{I}_3 & \mathbf{0}_3 \end{bmatrix}}_C \mathbf{X}_k + \boldsymbol{\nu}_k\tag{4.6}$$

where $\boldsymbol{\nu}_k = \mathcal{N}(\mathbf{0}_3, \sigma_{obs}^2 \mathbf{I}_3)$ is the noise associated to the external observations. The model uncertainty covariance matrix and the observation noise covariance matrix are given by:

$$\mathbf{Q} = E[\boldsymbol{\omega} \boldsymbol{\omega}^T] = \sigma_a^2 \begin{bmatrix} T^4 \mathbf{I}_3 & T^3 \mathbf{I}_3 \\ T^3 \mathbf{I}_3 & T^2 \mathbf{I}_3 \end{bmatrix} \quad \mathbf{R} = E[\boldsymbol{\nu} \boldsymbol{\nu}^T] = \sigma_{obs}^2 \mathbf{I}_3\tag{4.7}$$

Results

Eq. 4.7 (combined with Tab. 4.2) allows initializing \mathbf{Q} with $\mathbf{P}_0 = \mathbf{Q}$, and $\mathbf{R} = 10^{-6}\mathbf{I}_3$:

$$\mathbf{Q} = (2)^2 \begin{pmatrix} 10^{-12}\mathbf{I}_3 & 10^{-9}\mathbf{I}_3 \\ 10^{-9}\mathbf{I}_3 & 10^{-6}\mathbf{I}_3 \end{pmatrix} \sim \begin{pmatrix} \mathbf{0}_3 & \mathbf{0}_3 \\ \mathbf{0}_3 & 4 \cdot 10^{-6}\mathbf{I}_3 \end{pmatrix} \quad (4.8)$$

The results are shown in Fig.4.3, where we present the Euclidean distance between the reference trajectory and the retrieved one (Fig.4.3-(a)), and the error between the real and the estimated velocity (Fig.4.3-(b)). Filter performances have been evaluated for three different parameters configurations: \mathcal{P} , \mathcal{P}_{mod} , \mathcal{P}_{obs} . All the filter parameters configurations allow us to retrieve the correct behavior of the object (mean Euclidean distance with ground truth $d = 3.6e - 3$ [m] and mean error on velocity estimation $e = 2e - 3$ [m/s]). The least precise reconstruction is obtained with \mathcal{P}_{mod} (blue graph), which corresponds to having more confidence in the model than the external observations.

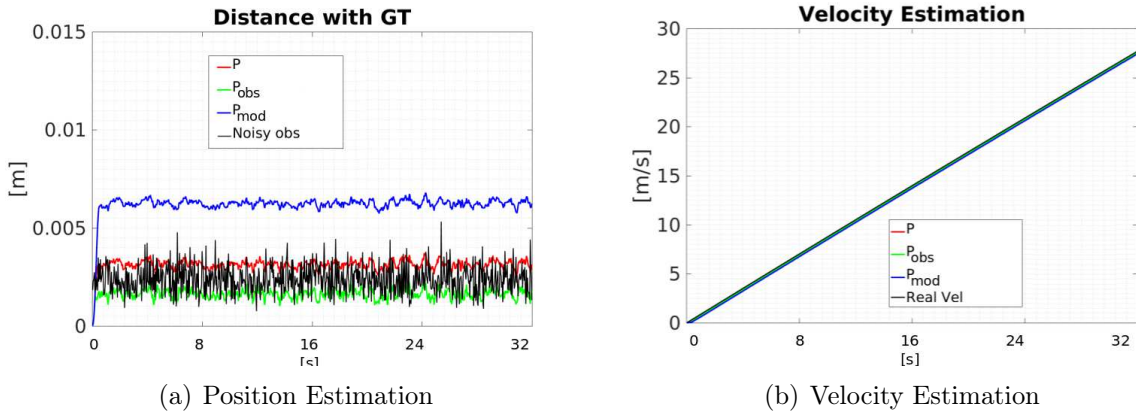


Figure 4.3: $\mathbf{X}_k = [\mathbf{x}_k, \mathbf{v}_k]^T$ Estimating both positions and velocities allows retrieving the correct state of the 3DoFs points for all filter parameter tunings. (a) The retrieved position shows the same behavior as the ground truth, presenting an average mean distance of 0.0036 m. More or less accurate reconstructions depends on the parameters tuning: overestimating model uncertainty (\mathcal{P}_{obs} (green)) provides a noisy reconstruction but closer to the reference trajectory, in terms of Euclidean distance; underestimating model uncertainty (\mathcal{P}_{mod} (blue)) provides a smoother reconstruction, but less precise. (b) Instead, we retrieve the correct velocity profile for all filter parameters tuning.

4.3.1.2 State vector composed of only positions

In this case, the dynamic behavior can be expressed as:

$$\mathbf{x}_k = \mathbf{x}_{k-1} + \mathbf{v}_{k-1}T + \mathbf{a}_kT^2 \quad (4.9)$$

Given that the velocity is not included within the state vector, at the end of the filter algorithm, we deterministically updated the velocity as $\mathbf{v}_k = (\mathbf{x}_k - \mathbf{x}_{k-1})/T$. Hence, the

state vector becomes $\mathbf{X}_k = [\mathbf{x}_k, \mathbf{x}_{k-1}]^T$ with:

$$\begin{cases} \mathbf{x}_k = 2\mathbf{x}_{k-1} - \mathbf{x}_{k-2} + \mathbf{a}_k T^2 \\ \mathbf{x}_{k-1} = \mathbf{x}_{k-1}. \end{cases} \quad (4.10)$$

In the state space, the state update can be written as:

$$\mathbf{X}_k = \underbrace{\begin{bmatrix} 2\mathbf{I}_3 & -\mathbf{I}_3 \\ \mathbf{I}_3 & \mathbf{0}_3 \end{bmatrix}}_A \mathbf{X}_{k-1} + \underbrace{\begin{pmatrix} \mu_a T^2 \\ 0 \end{pmatrix}}_{B\mathbf{u}_k} + \underbrace{\begin{pmatrix} \sigma_a T^2 \\ 0 \end{pmatrix}}_{\omega} \quad (4.11)$$

while the observation function may be expressed as:

$$\mathbf{Z}_k = \underbrace{\begin{bmatrix} \mathbf{I}_3 & \mathbf{0}_3 \end{bmatrix}}_C \mathbf{X}_k + \nu_k \quad (4.12)$$

Whereas the observation noise covariance matrix remains the same as in the previous case, the model uncertainty is given by:

$$\mathbf{Q} = E[\omega\omega^T] = \sigma_a^2 \begin{bmatrix} T^4 & 0 \\ 0 & 0 \end{bmatrix} \quad (4.13)$$

Results

Taking into account only the positions within the state vector shows different behavior according to the observations error covariance value.

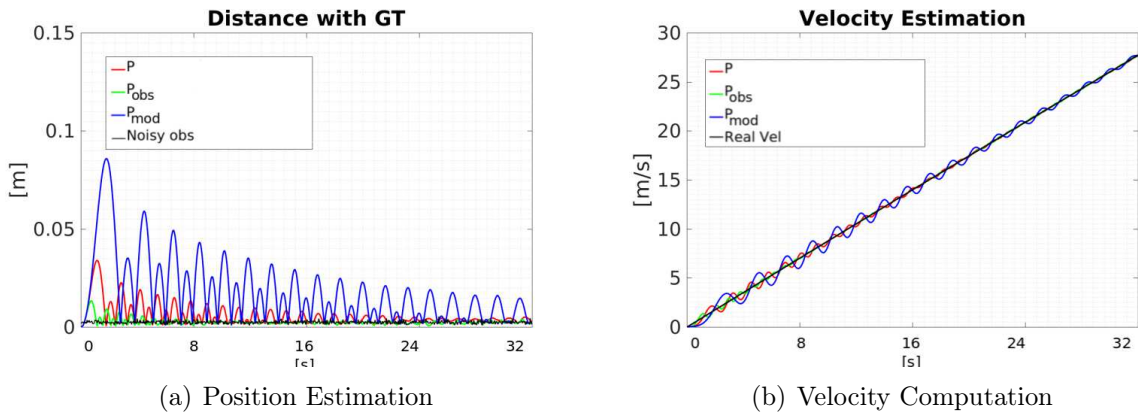


Figure 4.4: State Vector with positions only and with $\sigma_{obs} = 10^{-3}$ [m]. (a) The filter is unable to retrieve the correct trajectory. (b) The computed velocity, does not correspond to the ground truth profile.

When considering $\sigma_{obs} = 10^{-3}$, the filter is unable to retrieve neither the trajectory nor the velocity profile (see 4.4). This may be due to several reasons: the velocity is not well

computed, and therefore positions are not well estimated, the second order estimation, numerical instability, etc.

Instead, if we increase the confidence in the observations assuming $\sigma_{obs} = 10^{-4}$, the filter can provide a more accurate trajectory and velocity profile (mean distance with ground truth $d = 1.7e - 3$ [m])(see Fig. 4.5). Nevertheless, trajectory reconstruction (and therefore the computed velocity) appears to be noisier. Indeed, including velocity into the state vector allows dampening the observations noise. A state vector including only positions provides the same results as deterministically taking into account the external measurements information (in Fig.4.5-(a) curves have the same behavior as the black graph obtained from external observations).

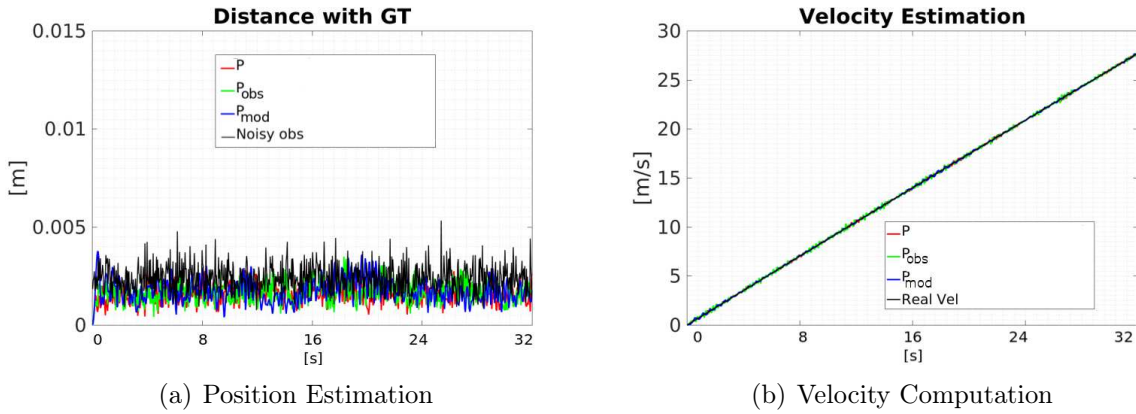


Figure 4.5: Increasing the confidence into external observations, the filter is able to retrieve the correct position; computed velocity corresponds to the real profile. Strongly relying on external measurements, the estimated state is sensibly affected by observations noise.

4.3.1.3 State vector composed of only velocities

The discrete equation of the the state update and the observation function are:

$$\underbrace{\begin{pmatrix} v_{x_k} \\ v_{y_k} \\ v_{z_k} \end{pmatrix}}_{\mathbf{X}_k} = \underbrace{\mathbf{I}_3}_A \underbrace{\begin{pmatrix} v_{x_{k-1}} \\ v_{y_{k-1}} \\ v_{z_{k-1}} \end{pmatrix}}_{\mathbf{X}_{k-1}} + \underbrace{\boldsymbol{\mu}_a T}_{B\mathbf{u}_k} + \underbrace{\boldsymbol{\sigma}_a T}_{\boldsymbol{\omega}_k} \quad (4.14)$$

$$\mathbf{Z}_k = \underbrace{T\mathbf{I}_3}_C \mathbf{X}_k + \underbrace{\mathbf{x}_{k-1}}_{D\mathbf{u}_k} + \boldsymbol{\nu}_k \quad (4.15)$$

At the end each time-step, we recompute positions according to the estimated velocity $\mathbf{x}_k = \mathbf{x}_{k-1} + \mathbf{v}_k T$.

Results

Given that there is no direct relation between the estimated variable and the observed variable, the filter is unable to estimate the correct velocity and therefore to retrieve the correct trajectory (see Fig. 4.6). All the filter parameter combinations provide the same, erroneous estimate.

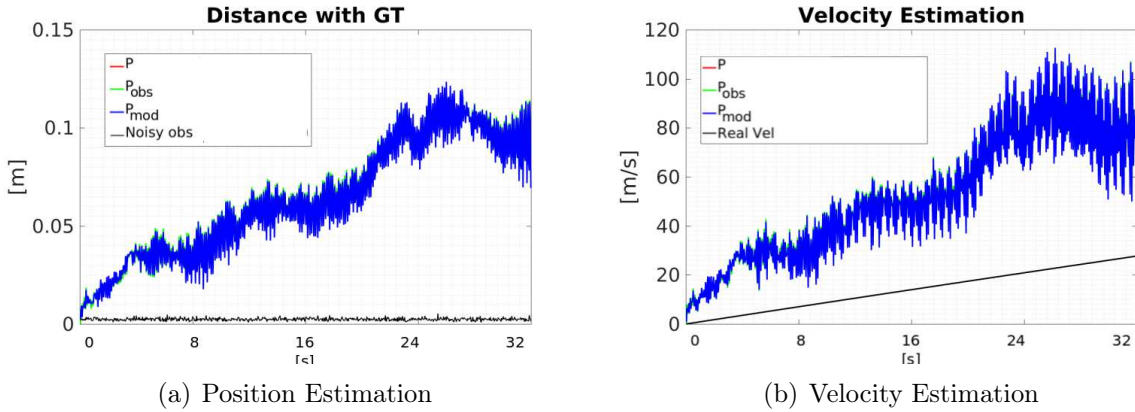


Figure 4.6: $\mathbf{X} = [\mathbf{v}]^T \in \mathbb{R}^3$ with $x_{k+1} = x_k + v_{k+1}T$ Including only velocities into the state vector, does not allow retrieving the good trajectory nor the exact velocity profile.

Perhaps, the estimation of only velocities would be useful when also some external observations about the velocity itself are available.

4.3.2 Data Assimilation

We previously assumed a global uncertainty on the acceleration, without any knowledge of the specific incorrect parameter. In the second set of experiments, we experimented with the data assimilation capability of Bayes filters to cope with imprecise knowledge of mechanical parameters.

In general, inverse modeling allows us to estimate the input parameters p of the model, besides the dynamic variables (such as positions and velocities). The aim is to improve the model's predictive power by fine-tuning the parameters' value and the other state variables. Similarly to other methods, Kalman filters may be used to estimate parameters. In this case, the filter presents a so-called augmented state:

$$\widetilde{\mathbf{X}}_k = \begin{bmatrix} \mathbf{X}_k \\ p \end{bmatrix} \quad (4.16)$$

The state equation reads:

$$\begin{bmatrix} \mathbf{X}_k \\ p \end{bmatrix} = \begin{bmatrix} g(\mathbf{X}_{k-1}, p) \\ p \end{bmatrix} \quad (4.17)$$

The error variances are augmented as well:

$$\mathbf{P}_0 = \begin{pmatrix} \mathbf{P}_{0x} & \mathbf{0} \\ \mathbf{0} & P_{0p} \end{pmatrix} \quad \mathbf{Q} = \begin{pmatrix} \mathbf{Q}_x & \mathbf{0} \\ \mathbf{0} & 0 \end{pmatrix} \quad (4.18)$$

An insight on data assimilation theories may be found in [118, 119], which provides an overview of different approaches (such as Kalman filters or variational methods) for data assimilation, with an application on meteorology and oceanography.

Considering the same 3DoFs point, subject to a constant force, we decided to model the acceleration as $\mathbf{a}_k = c_k \frac{\mathbf{f}}{m}$, where c_k is an unknown parameter. In particular, we assume it to be constant, $c_k = c + \sigma_c$, and characterized by Gaussian noise.² Similarly to the previous section, we first generated a ground truth scenario, where we considered the parameter $c = 1$. Then, in the incorrect model, we initially set $c = 0.1$ assuming an associated standard deviation $\sigma_c = 0.8$. Filter performances have been tested for different configurations of filter parameters; we set a nominal configuration \mathcal{P} (values for $\mathbf{X}_k = [\mathbf{x}_k, \mathbf{v}_k, c]^T$ are summarized in tab. 4.3), along with an overestimation of model uncertainty $\mathcal{P}_{obs} = 2^2 \mathcal{P}$ and an underestimation of model uncertainty: $\mathcal{P}_{mod} = 0.5^2 \mathcal{P}$.

		\mathcal{P}
\mathbf{Q}	eq. 4.19	$\begin{pmatrix} \mathbf{0}_{3 \times 3} & \mathbf{0}_{3 \times 3} & \mathbf{0}_{6 \times 1} \\ \mathbf{0}_{3 \times 3} & (2 \cdot 10^{-3})^2 \mathbf{I}_{3 \times 3} & \\ \mathbf{0}_{1 \times 6} & & 0 \end{pmatrix}$
\mathbf{P}_0		$\begin{pmatrix} \mathbf{0}_{3 \times 3} & \mathbf{0}_{3 \times 3} & \mathbf{0}_{6 \times 1} \\ \mathbf{0}_{3 \times 3} & (2 \cdot 10^{-3})^2 \mathbf{I}_{3 \times 3} & \\ \mathbf{0}_{1 \times 6} & & 0.8^2 \end{pmatrix}$
\mathbf{R}	eq. 4.20	$10^{-3} \mathbf{I}_{3 \times 3}$

Table 4.3: Filter parameters for $\mathbf{X}_k = [\mathbf{x}_k, \mathbf{v}_k, c]^T$

4.3.2.1 State vector of positions, velocities, and incorrect parameter

The dynamic process is described as:

$$\begin{cases} c_k = c + \sigma_c \\ \mathbf{v}_k = \mathbf{v}_{k-1} + c \frac{\mathbf{f}}{m} T + \sigma_c \frac{\mathbf{f}}{m} T \\ \mathbf{x}_k = \mathbf{x}_{k-1} + \mathbf{v}_{k-1} T + c \frac{\mathbf{f}}{m} T^2 + \sigma_c \frac{\mathbf{f}}{m} T^2 \end{cases}$$

²Similarly to Sec. 4.3.1, it is characterized by an additive Gaussian noise, where $\sigma_c = \mathcal{N}(0, \sigma_c^2)$, with $\mathbf{E}(\sigma_c) = 0$ and $\mathbf{E}(\sigma_c, \sigma_c) = \sigma_c^2$.

Considering the augmented state vector including the parameter c , the state vector becomes: $\mathbf{X}_k = [\mathbf{x}_k, \mathbf{v}_k, c]^T$. In the state vector space, Eq. 4.19 can be written as follows:

$$\underbrace{\begin{pmatrix} x_k \\ y_k \\ z_k \\ v_{x_k} \\ v_{y_k} \\ v_{z_k} \\ c \end{pmatrix}}_{\mathbf{X}_k} = \underbrace{\begin{bmatrix} \mathbf{I}_{3 \times 3} & T \mathbf{I}_{3 \times 3} & \frac{\mathbf{f}}{m} T^2 \\ \mathbf{0}_{3 \times 3} & \mathbf{I}_{3 \times 3} & \frac{\mathbf{f}}{m} T \\ \mathbf{0}_{1 \times 6} & & 1 \end{bmatrix}}_A \underbrace{\begin{pmatrix} x_{k-1} \\ y_{k-1} \\ z_{k-1} \\ v_{x_{k-1}} \\ v_{y_{k-1}} \\ v_{z_{k-1}} \\ c \end{pmatrix}}_{\mathbf{X}_{k-1}} + \underbrace{\begin{bmatrix} \frac{\mathbf{f}}{m} T^2 \\ \frac{\mathbf{f}}{m} T \\ 1 \end{bmatrix}}_{\omega_k} \sigma_c \quad (4.19)$$

In this case, the observations are related to the state vector through:

$$\underbrace{\begin{pmatrix} x_k \\ y_k \\ z_k \end{pmatrix}}_{\mathbf{Z}_k} = \underbrace{\begin{bmatrix} \mathbf{I}_3 & \mathbf{0}_{3 \times 4} \end{bmatrix}}_C \mathbf{X}_k + \boldsymbol{\nu}_k \quad (4.20)$$

4.3.2.2 State vector of positions and incorrect parameter

For the state vector composed of **positions only and parameter**: $\mathbf{X}_k = [\mathbf{x}_k, \mathbf{x}_{k-1}, c]$, the discrete-time equations are:

$$\begin{cases} c_k = c + \sigma_c \\ \mathbf{x}_k = 2\mathbf{x}_{k-1} - \mathbf{x}_{k-2} + \mathbf{c} \frac{\mathbf{f}}{m} T^2 + \boldsymbol{\sigma}_c \frac{\mathbf{f}}{m} T^2 \\ \mathbf{x}_{k-1} = \mathbf{x}_{k-1} \end{cases}$$

In the state space, the state update can be written as:

$$\mathbf{X}_k = \underbrace{\begin{bmatrix} 2\mathbf{I}_3 & -\mathbf{I}_3 & \frac{\mathbf{f}}{m} T^2 \\ \mathbf{I}_3 & \mathbf{0}_3 & 0 \\ \mathbf{0}_{1 \times 3} & \mathbf{0}_{1 \times 3} & 1 \end{bmatrix}}_A \mathbf{X}_{k-1} + \underbrace{\begin{bmatrix} \frac{\mathbf{f}}{m} T^2 \\ \mathbf{0}_{3 \times 1} \\ 1 \end{bmatrix}}_{\omega} \sigma_c \quad (4.21)$$

The observation function may be expressed as:

$$\underbrace{\begin{pmatrix} x_k \\ y_k \\ z_k \end{pmatrix}}_{\mathbf{Z}_k} = \underbrace{\begin{bmatrix} \mathbf{I}_3 & \mathbf{0}_{3 \times 4} \end{bmatrix}}_C \mathbf{X}_k + \boldsymbol{\nu}_k \quad (4.22)$$

4.3.2.3 Results

In case of $\mathbf{X}_k = [\mathbf{x}_k, \mathbf{v}_k, c]^T$, including the incorrect parameter in the state vector globally improves the accuracy of the reconstruction (compare Fig. 4.7-(a) where the mean distance is $d = 5e - 4$ [m] with Fig. 4.3-(a) where $d = 3.6e - 3$ [m]).

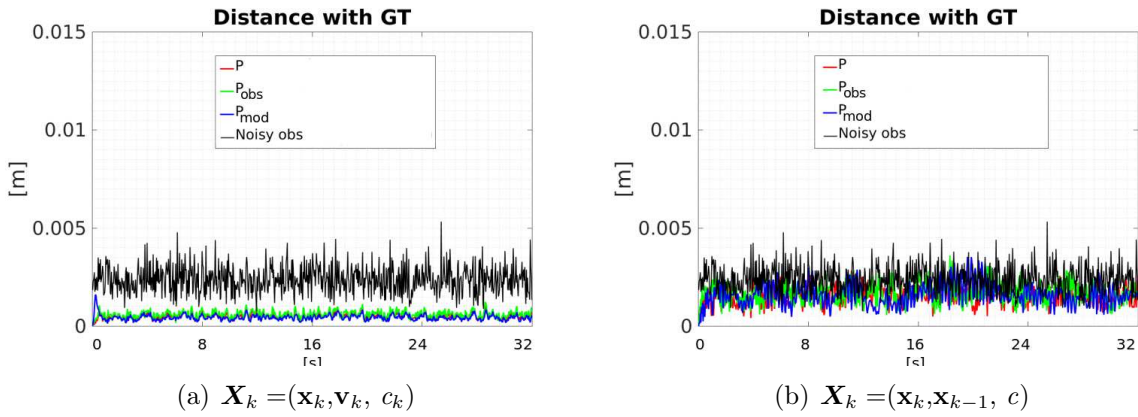


Figure 4.7: An augmented state vector, with parameter estimations, allows improving the results only when the state vector take into account both positions and velocities.

Instead, when only positions are estimated $\mathbf{X}_k = [\mathbf{x}_k, \mathbf{x}_{k-1}, c]^T$, performing the parameter estimation does not globally improve the results (compare Fig. 4.7-(b) and Fig. 4.4-(a), where in both cases the mean Euclidean distance from ground truth is $d = 1.7e - 3$ [m]). Nevertheless, in both cases it is possible to retrieve the real value of the mechanical parameter (see Fig. 4.8).

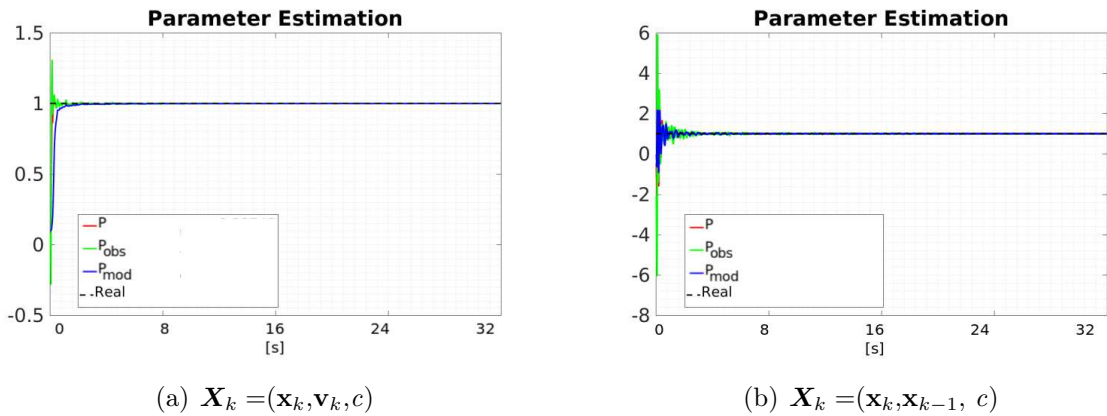


Figure 4.8: Both state vectors allows retrieving the real value of the parameter $c = 1$.

4.3.3 3DoF Beam

Let's now consider a 3D beam, where each node is described through 6DoFs (3DoFs for position and 3DoFs for orientation). We suppose to have a pendulum-like behavior, where an extremity of the beam is fixed and the other one is subject to a given force (as Fig. 4.9). The discrete-time equation describing the dynamics of the object will be:

$$\begin{aligned} \mathbf{a}_k &= c\mathbf{A}_k^{-1}\mathbf{b}_k \\ \mathbf{v}_k &= \mathbf{v}_{k-1} + \mathbf{a}_k T \\ \mathbf{x}_k &= \mathbf{x}_{k-1} + \mathbf{v}_{k-1}T + \mathbf{a}_k T^2 \end{aligned} \tag{4.23}$$

where the matrices $\mathbf{A}_k, \mathbf{b}_k$ are computed as in Eq. 3.17.

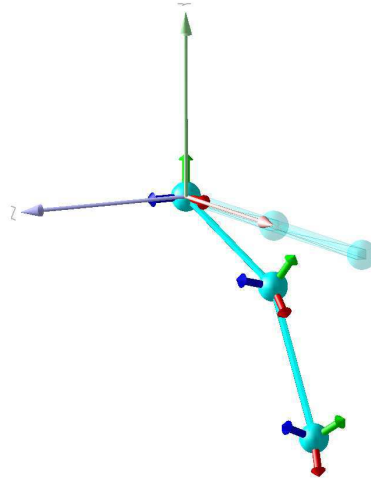


Figure 4.9: Set up for the 3DoFs beam experiment.

The reference scenario has been generated according to Eq. 4.23, where the matrices \mathbf{A}_k and \mathbf{b}_k depends essentially on physical parameters: mass $m = 3$ [kg], Young's modulus $E = 400$ [MPa], radius of the beam $r = 3$ [mm] and external force $\mathbf{f} = [0, -10, 0, 0, 0.1, 0]^T$. In the ground truth scenario, we initialized the parameter $c = 1$, whereas in the incorrect model, we supposed to have $c = 0.1$ with $\sigma_c = 0.8$, in order to mimic potential uncertainties on the acceleration knowledge. Synthetic observations of the positions of the nodes have been generated by adding some Gaussian noise, with $\sigma_{obs} = 0.001$, to the 3D locations of the reference beam's nodes. As previously performed, we tested filter performances for different sets of filter parameters tuning: $\mathcal{P}, \mathcal{P}_{mod}, \mathcal{P}_{obs}$. In order to quantify the accuracy of our reconstruction, we compute the maximal distance between the estimated positions and the real one, as well as the mean error between the real velocity and the estimated one.

4.3.3.1 State vector of positions and velocities

Positions and velocities of each node are obtained as Eq.4.3.1.1, where the acceleration is affected by some uncertainty, $\mathbf{a}_k = \boldsymbol{\mu}_a \pm \boldsymbol{\sigma}_a$. In this case, the state vector is expressed as:

$$\mathbf{X}_k = [x_{k_i}, y_{k_i}, z_{k_i}, \psi_{k_i}, \theta_{k_i}, \phi_{k_i}, v_{x_{k_i}}, v_{y_{k_i}}, v_{z_{k_i}}, v_{\psi_{k_i}}, v_{\theta_{k_i}}, v_{\phi_{k_i}}]_{i=1:3}^T$$

while the state update can be written as:

$$\mathbf{X}_k = \underbrace{\mathbf{I}_3 \otimes \begin{bmatrix} \mathbf{I}_6 & T \mathbf{I}_6 \\ \mathbf{0}_6 & \mathbf{I}_6 \end{bmatrix}}_A \mathbf{X}_{k-1} + \underbrace{\mathbf{I}_3 \otimes \begin{bmatrix} T^2 \mathbf{I}_6 \\ T \mathbf{I}_6 \end{bmatrix}}_{B \mathbf{u}_k} \boldsymbol{\mu}_a + \underbrace{\mathbf{I}_3 \otimes \begin{bmatrix} T^2 \mathbf{I}_6 \\ T \mathbf{I}_6 \end{bmatrix}}_{\boldsymbol{\omega}_k} \boldsymbol{\sigma}_a \quad (4.24)$$

and the observations are related to the state vector through:

$$\mathbf{Z}_k = \mathbf{I}_3 \otimes \underbrace{\begin{bmatrix} \mathbf{I}_3 & \mathbf{0}_{3 \times 9} \end{bmatrix}}_C \mathbf{X}_k + \mathbf{I}_3 \otimes \underbrace{\sigma_{obs} \mathbf{I}_3}_{\boldsymbol{\nu}_k} \quad (4.25)$$

Results

In case of $\mathbf{X}_k = [\mathbf{x}_{k_i}, \mathbf{v}_{k_i}]_{i=1:3}^T$, the filter is able to retrieve the correct trajectory and velocity (see Fig. 4.10). All filter parameters configurations provided good results. The maximum distance between the real trajectory and the retrieved one was on average of $d = 1.1e - 3$ [m] for all filter parameters combination (see Fig. 4.10-(a)). Concerning the error between the real velocity and the estimated profile, we obtained an average error of $e = 1e - 3$ [m/s] (see Fig. 4.10-(b)).

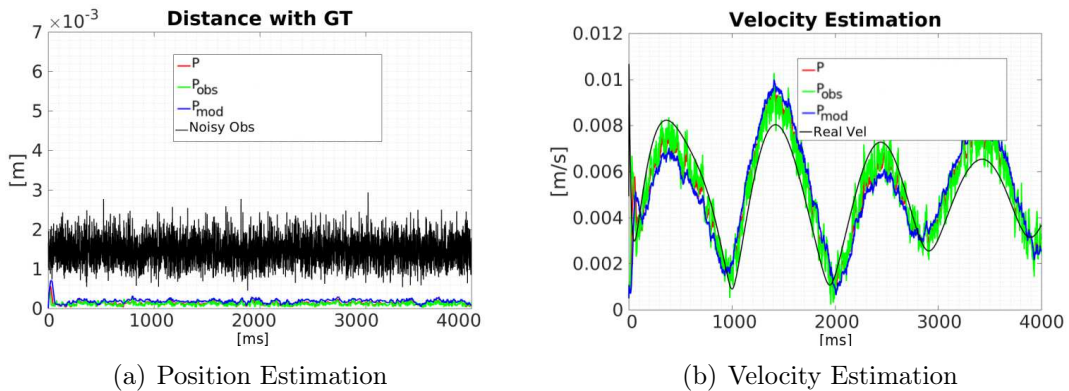


Figure 4.10: $\mathbf{X}_k = [\mathbf{x}_{k_i}, \mathbf{v}_{k_i}]_{i=1:3}^T$. All filter parameters allow retrieving the correct trajectory and an accurate profile of velocities.

4.3.3.2 State vector of only positions

For each node of the beam, the positions are obtained through Eq. 4.9. The state vector can hence be written as:

$$\mathbf{X}_k = [x_{k_i}, y_{k_i}, z_{k_i}, \psi_{k_i}, \theta_{k_i}, \phi_{k_i}, x_{k-1_i}, y_{k-1_i}, z_{k-1_i}, \psi_{k-1_i}, \theta_{k-1_i}, \phi_{k-1_i}]_{i=1:3}^T$$

where the state update is:

$$\mathbf{X}_k = \underbrace{\mathbf{I}_3 \otimes \begin{bmatrix} 2\mathbf{I}_6 & -\mathbf{I}_6 \\ \mathbf{I}_6 & \mathbf{0}_6 \end{bmatrix}}_A \mathbf{X}_{k-1} + \underbrace{\mathbf{I}_3 \otimes \begin{pmatrix} \mu_a T^2 \\ 0 \end{pmatrix}}_{B\mathbf{u}_k} + \underbrace{\mathbf{I}_3 \otimes \begin{pmatrix} \sigma_a T^2 \\ 0 \end{pmatrix}}_{\boldsymbol{\omega}_k} \quad (4.26)$$

and the observation function may be expressed as:

$$\mathbf{Z}_k = \mathbf{I}_3 \otimes \underbrace{\begin{bmatrix} \mathbf{I}_3 & \mathbf{0}_3 \end{bmatrix}}_C \mathbf{X}_k + \boldsymbol{\nu}_k \quad (4.27)$$

Results

When considering only positions in the state vector $\mathbf{X}_k = [\mathbf{x}_{k_i}, \mathbf{x}_{k-1_i}]_{i=1:3}^T$, the position estimation has the same quality as a deterministic integration of the external observations (see Fig. 4.11-(a)), where the average max distance from the ground truth trajectory is $d = 1.1e - 2$ [m]. In addition, neither the velocity (Fig. 4.11-(b)) nor the orientations (Fig. 4.12-(c)) are well retrieved.

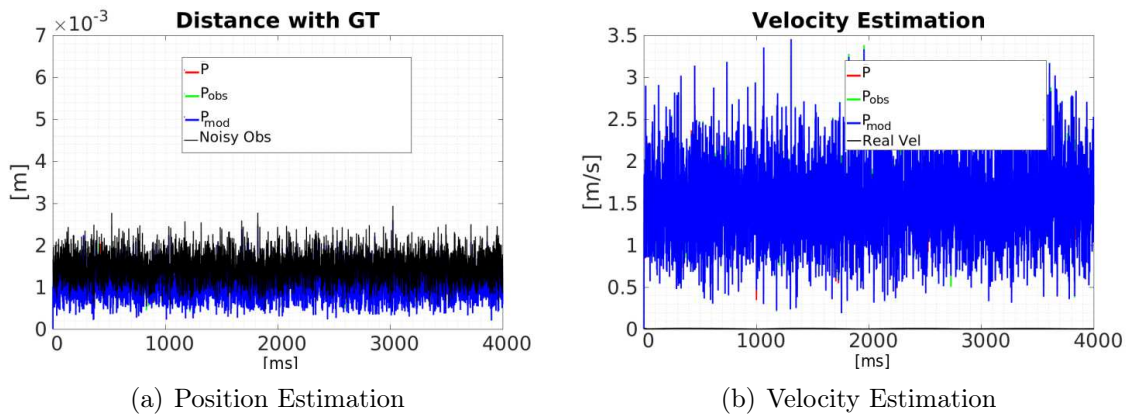


Figure 4.11: State vector with positions only. The estimated positions are strictly related to the external observations. Velocity cannot be properly retrieved: all filter parameter configurations provide the same noisy profile (blue, red and green curves overlaps on the graph).

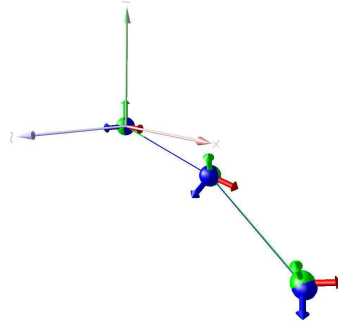


Figure 4.12: Blue spheres represent the real positions while green spheres represent the filter estimate. Whereas the 3D positions are accurately retrieved, the estimated orientations of each node are not coherent with the configuration of the beam.

4.3.3.3 Augmented State

In this case, we augmented the state vector with the incorrect parameter $c_k = c + \sigma_c$. The state vector including both positions and velocities is:

$$\mathbf{X}_{k_i} = [x_{k_i}, y_{k_i}, z_{k_i}, \psi_{k_i}, \theta_{k_i}, \phi_{k_i}, v_{x_{k_i}}, v_{y_{k_i}}, v_{z_{k_i}}, v_{\psi_{k_i}}, v_{\theta_{k_i}}, v_{\phi_{k_i}}, c]_{i=1:3}^T$$

whereas when considering only the positions in the state vector we have:

$$\mathbf{X}_k = [x_{k_i}, y_{k_i}, z_{k_i}, \psi_{k_i}, \theta_{k_i}, \phi_{k_i}, x_{k-1_i}, y_{k-1_i}, z_{k-1_i}, \psi_{k-1_i}, \theta_{k-1_i}, \phi_{k-1_i}, c]_{i=1:3}^T$$

Results

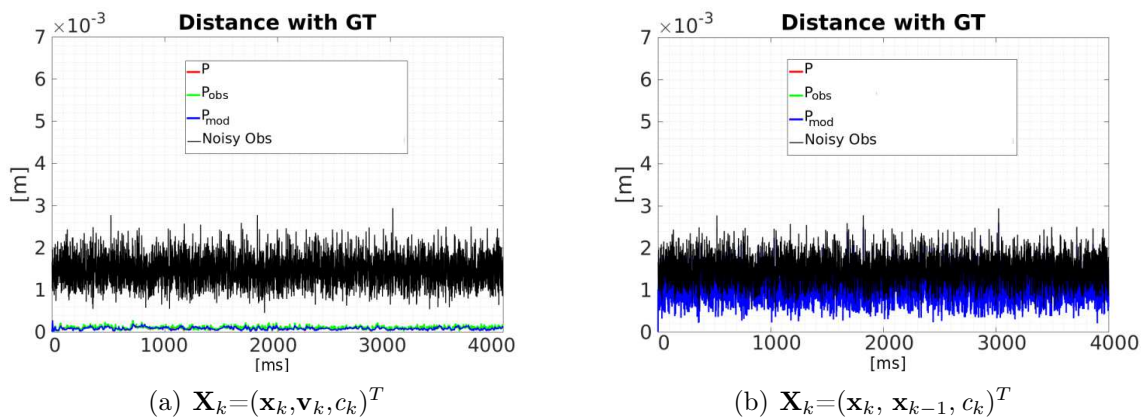


Figure 4.13: Only when estimating positions, velocities and the incorrect parameter, the filter is able to retrieve the correct positions and the retrieve the correct trajectory (a). Whenever considering positions only with parameter estimation, trajectory estimation presents the same results as positions only estimation (b).

When considering an augmented state with positions, velocities, the incorrect parameter c , it is possible to see that not only did we retrieve the correct parameter (Fig. 4.14-(a)), but also the state estimation is improved compared to the previous one (max distance from ground truth is on average $d = 9e - 5$ [m]).

Instead, when estimating the incorrect parameter with positions only, we are unable to retrieve the real value (Fig. 4.13-(d)) and the augmented state does not show any improvement compared to estimating only positions (mean max distance from ground truth $d = 1.1e - 2$ [m]).

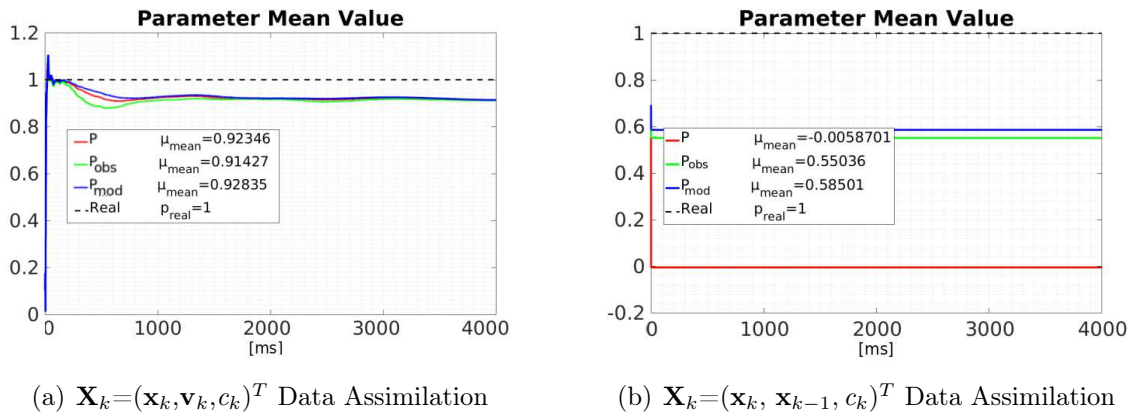


Figure 4.14: Only when estimating positions, velocities and the incorrect parameter it is possible to retrieve the real value of the parameter (a). Whenever considering positions only with parameter estimation, it is not possible to retrieve the real value of the estimated parameter (b).

4.3.4 2D Observations

In the previous cases, the external observations consisted of the 3D positions of the object. In a clinical scenario, the external measurements consist of the image-features extracted from fluoroscopic images. For that, in this last study, we supposed we observed the 2D projection of the nodes of the beam. The observation vector is $\mathbf{Z}_k = (u_{k_i}, v_{k_i})_{i=1:N}^t$ such that $u_k = u'_k/s'_k$ and $v_k = v'_k/s'_k$. Hence the observation function can be expressed, in homogeneous coordinates as:

$$\begin{pmatrix} u'_k \\ v'_k \\ s'_k \end{pmatrix} = \mathbf{I}_3 \otimes \underbrace{\begin{pmatrix} m_{11} & m_{12} & m_{13} & m_{14} \\ m_{21} & m_{22} & m_{23} & m_{24} & \mathbf{0}_6 \\ m_{31} & m_{32} & m_{33} & m_{34} \end{pmatrix}}_{\mathbf{C}} \mathbf{X}_k + \mathbf{I}_3 \otimes \boldsymbol{\nu}_k \quad (4.28)$$

In this case, the external observations are related to the state vector through a function including the projection matrix $\mathbf{C} \in \mathbb{R}^{3 \times 4}$ defined through the coefficients m_{ij} obtained

through a calibration process as described in Sec. 3.6.1. In particular, we considered a frontal view of the beam (see Fig. 4.15-(a)), whereas the object has a movement out of the projective plane (see Fig. 4.15-(b)).

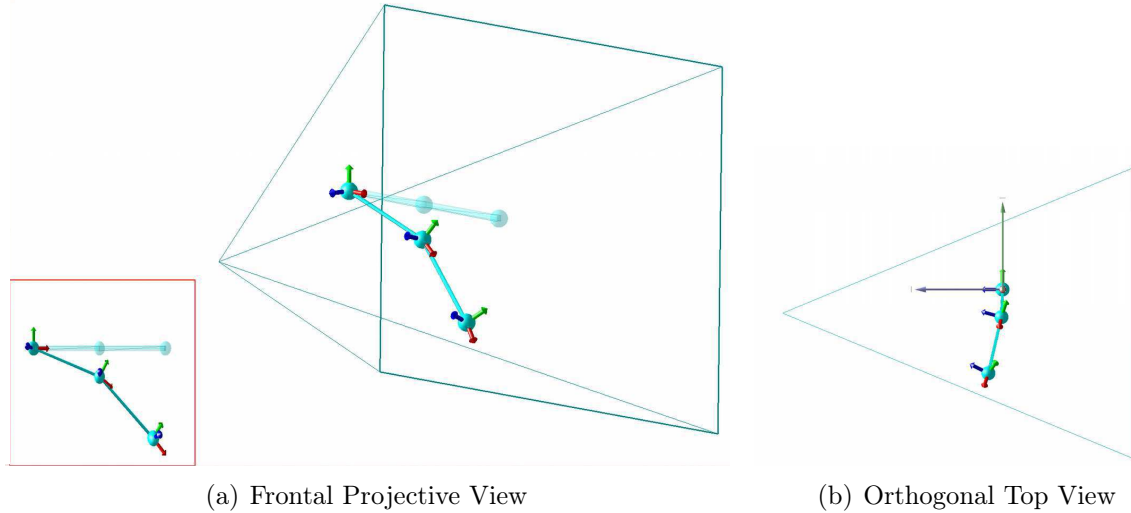


Figure 4.15: (a) Red square is the observed frontal view from which 2D external observations are retrieved. (b) The orthogonal top view is presented as well to show the existing out of plane motion.

First, we generated a ground truth scenario where the dynamics of the model follow the same equations as the previous section, with the same parameter initialization. In order to generate synthetic 2D observations, we projected the 3D positions of the beam's nodes along a chosen 2D view and random Gaussian noise, with standard deviation $\sigma_{obs} = 0.05$, has been added to the projected positions. Filter performances have been tested for different filter parameters configurations $\mathcal{P}, \mathcal{P}_{mod}, \mathcal{P}_{obs}$ defined as previously. To quantify the quality of the estimation, we evaluated the 3D maximal distance between the reference beam and the reconstructed one, and the mean error between the real velocity and the estimated velocity.

4.3.4.1 State vector of positions and velocities

When considering only positions and velocities $\mathbf{X}_k = [\mathbf{x}_{k_i}, \mathbf{v}_{k_i}]_{i=1:3}^T$, we were able to retrieve the correct 3D trajectory of the beam, as well as the correct velocity. The accuracy of the results depends on the filter parameter tuning. On average, we obtained a max distance of $e = 2.4e - 4$ [m] and an average mean error between real and estimated velocity of $d = 5.4e - 4$ [m/s]. In particular, for \mathcal{P}_{obs} results appear degraded. This is because, in such configuration, we trusted more the observations than the model. Nevertheless, 2D observations have an intrinsic uncertainty in the depth direction, which is the cause of a higher deviation from the ground truth (see Fig. 4.16).

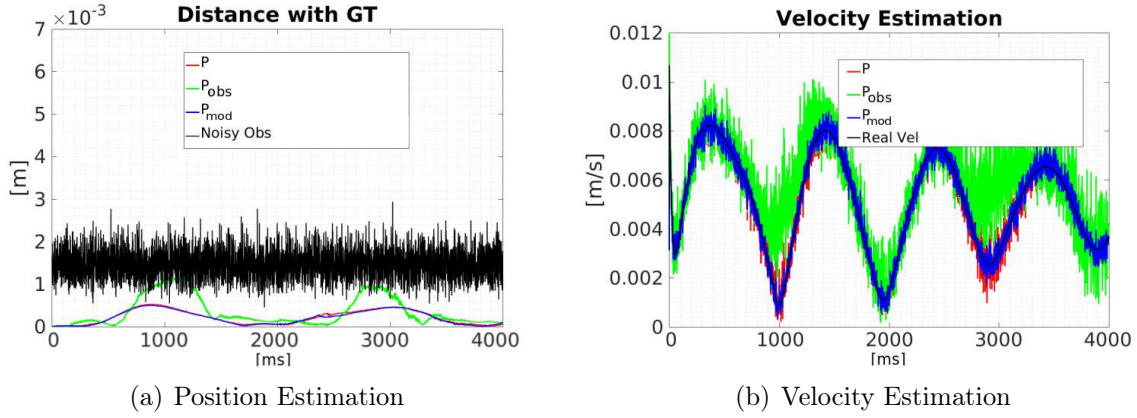


Figure 4.16: $\mathbf{X}_k = [\mathbf{x}_{k_i}, \mathbf{v}_{k_i}]_{i=1:3}^T$ and 2D observations. The filter is able to retrieve the correct 3D positions as well as the velocities profile.

4.3.4.2 State vector of positions, velocities and model parameter

When considering positions, velocities and the incorrect parameter $\mathbf{X}_k = [\mathbf{x}_{k_i}, \mathbf{v}_{k_i}, c]_{i=1:3}^T$, results presented an improvement (see Fig. 4.17) compared to the previous case (on average $d = 1.5e - 4$ [m] and $e = 5.2e - 4$ [m/s]). Again, the quality of the results depended on the filter parameters tuning and \mathcal{P}_{obs} provided the less accurate reconstruction.

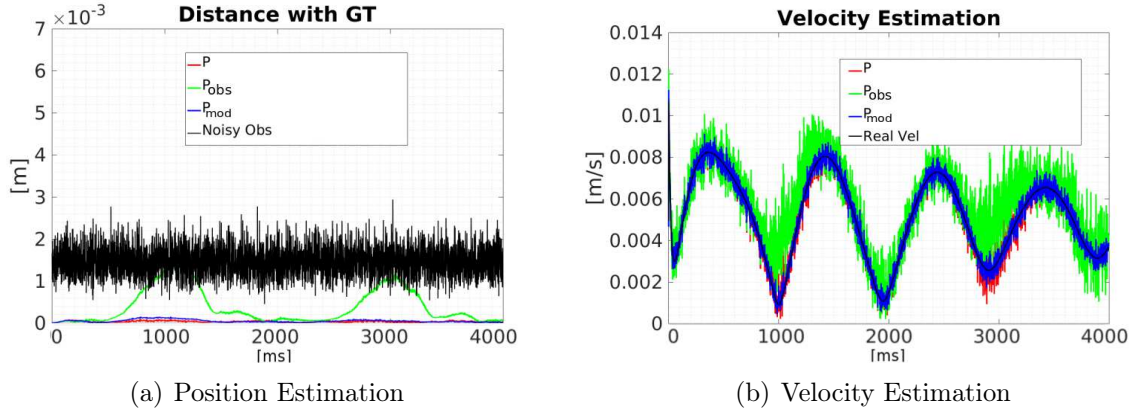
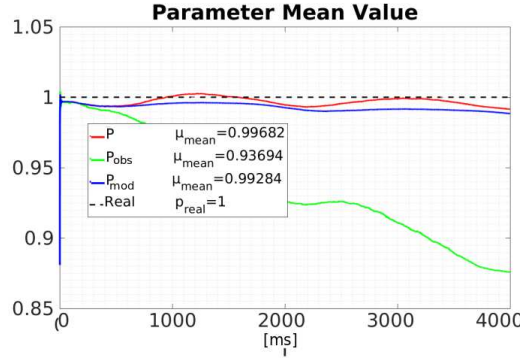


Figure 4.17: $\mathbf{X}_k = [\mathbf{x}_{k_i}, \mathbf{v}_{k_i}, c]_{i=1:3}^T$. Including the parameter into the state vector allows overall improving the results, except when tuning the filter with a higher confidence into external observations (green curve).

Parameter estimation depends as well on filter parameters tuning (see Fig. 4.18). In general, it is possible to retrieve the real value of the incorrect parameter. Filter parameter set \mathcal{P}_{obs} presents the less accurate results ($c = 0.93 \pm 0.06$).



(a) Parameter Estimation

Figure 4.18: $\mathbf{X}_k = [\mathbf{x}_{k_i}, \mathbf{v}_{k_i}, c]_{i=1:3}^T$ Incorrect parameter is well estimated, in particular we obtain for $\mathcal{P}, c = 0.99 \pm 0.04$, $\mathcal{P}_{mod}, c = 0.99 \pm 0.03$ and $\mathcal{P}_{obs}, c = 0.93 \pm 0.06$.

4.3.5 The Modeling of Uncertainty

As can be seen from the results above presented, filter parameters tuning represents a fundamental part of the proper use of Kalman filters. Indeed, an inappropriate initialization of matrices $\mathbf{P}_0, \mathbf{Q}, \mathbf{R}$ may significantly impact the results of the estimation.

Whereas the observations error covariance \mathbf{R} may be easily initialized from the specifications of the sensor used to retrieve external observations (i.e. the pixel detection error, or the precision of the sensor providing 3D positions), the model error covariance \mathbf{Q} can be harder to initialize. First of all, it is necessary to identify the sources of uncertainty that may affect the model. In general, they may be due to: 1) inappropriate approximations and simplifications of the mathematical model, 2) an incorrect initial setting of the model parameters. As presented in Sec. 3.4, we use a FE model of the beam, whose dynamic behavior is described through an Implicit Integration scheme. This model has been widely validated in literature (see 3.2). For that, we assume that the model choice (i.e. the mathematical formalization of the physical problem) does not represent a source of error. Instead, uncertainties may exist on the physical parameter characterizing such model. In particular, the FE model can diverge from the real behavior of the device due to: 1) errors on intrinsic parameters (such as the mass, stiffness and radius of the device), 2) the chosen discretization of the beam model.

In Fig. 4.19, we present a simple experiment showing the accuracy of our beam model. In practice, given a segment of catheter fixed at one extremity and undergoing simple gravity, we reproduced its behavior through simulation and we evaluated whether the beam model provides a final configuration similar to the original layout. We used a Headway Duo device has been used and its mechanical parameters, retrieved from manufacturer specifications or empirical experiences, have been used for the FE model characterization.

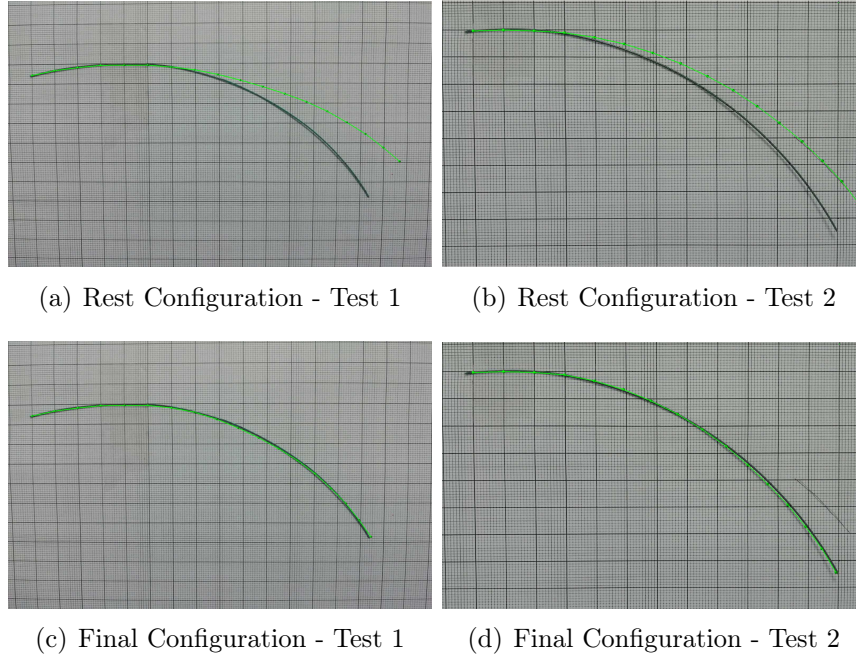


Figure 4.19: **Beam FE Model.** Starting from an initial configuration (green shape in (a) and (b) slightly curved due to the usage of the catheter) we reproduce with the simulation the behavior of the device, fixed at one extremity and subject to gravity. Using the real mechanical parameter, we retrieve an accurate shape

The diameter has been retrieved from device specifications, and no error is associated with such parameter: outer diameter 0.7 [mm], inner diameter 0.424 [mm]. Concerning the mass, it has been estimated through multiple weighing on a precision scale. We obtained a linear density $\rho = 0.036 \pm 0.011$ [mg/cm]. A higher uncertainty exists on the Young's modulus value, which was not given by the manufacturer. Using known values from literature, the simulation provided coherent results for an interval of 710 ± 110 [MPa]. In particular, we showed the ability of the co-rotational FE model to retrieve an accurate configuration (mean 2D Hausdorff distance from real catheter 3.8 ± 2.1 [pixel]). Another parameter that could influence the simulation's behavior is the discretization of the beam (i.e. the number $N - 1$ of serially linked elements). In Fig. 4.20, we show how differently discretized models, under the same mechanical parameters, led to the same behavior (mean 2D Hausdorff distance from real catheter 3.5 ± 2.2 [pixel]), except for the coarse model ($N=8$) which cannot retrieve the correct final configuration (mean 2D Hausdorff distance from real catheter 15.4 ± 1.8 [pixel]). Other potential sources of uncertainty are represented by the forces applied to the device. Indeed, they are difficult to know with precision, and they are likely to vary all along the path of the device. Contact forces hinge on the friction coefficient μ , which depends on several factors, such as patient anatomy, type of catheter, blood flow, etc. and cannot be known accurately. Concerning the insertion force, we assume it to be constant through time: in real cases the insertion force depends on the clinician gesture and its intensity may therefore vary through time.

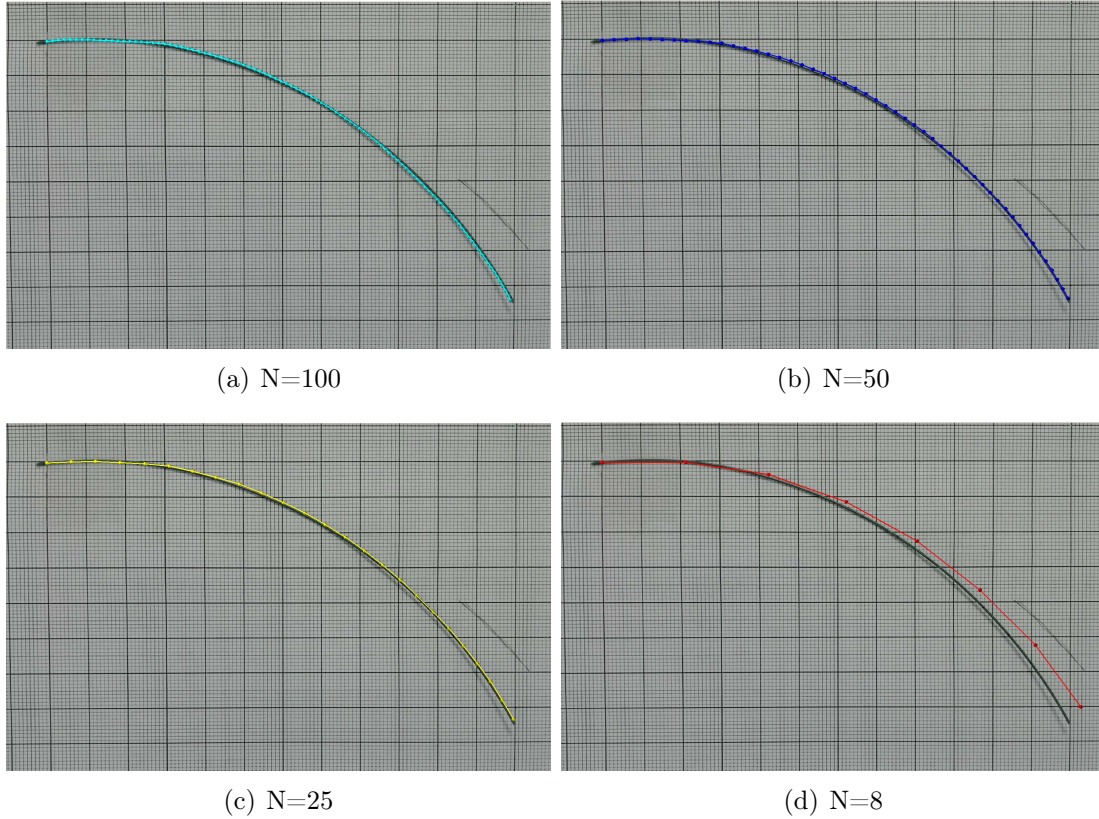


Figure 4.20: **Beam FE Model Discretization.** Coarser models deteriorate the mechanical behavior. Results for $N = 10$ are shown in Fig. 4.20(c)-(d).

4.3.6 Conclusions

This study allowed us to define which variables must be included in the state vector. In conclusion, both positions and velocities must be taken into account in order to have a correct reconstruction of the dynamics. Furthermore, an augmented state, including incorrect parameters, allows us to globally improve the results. In our case, uncertainties on physical parameters, model discretization, etc. can be wrapped up in some uncertainty on the forces, or, equivalently, on the acceleration.

In the case of our synthetic study, we supposed to have $\mathbf{a}_k = c_k \mathbf{A}_k \mathbf{b}_k$ where the unknown parameter $c_k = c + \sigma_k$ mimics the potential uncertainty with may affect model parameterization. In real cases, multiple sources of error can coexist at the same time, without precise knowledge of the specific incorrect parameter. Therefore, it is possible to model the acceleration through an equivalent formalism:

$$\mathbf{a}_k = \mathbf{A}_k^{-1} \mathbf{b}_k + \mathbf{c}_k \quad (4.29)$$

where \mathbf{c}_k is still a Gaussian variable $P(\mathbf{c}_k) = \mathcal{N}(\boldsymbol{\mu}_c, \boldsymbol{\sigma}_c)$ whose uncertainty gathers the

uncertainty on the mechanical parameterization $\sigma_c \propto \sigma_A^{-1} \sigma_b$. In practice, the parameter \mathbf{c}_k translates the noise on the acceleration, which from the mechanical point of view can be seen as a fictive corrective force compensating for the errors on the misknown terms.

In the next chapter, we will present the Bayesian framework for the catheter navigation simulation.

Part V

Stochastic Simulation II

CONSTRAINED STATE ESTIMATION

Table of Contents

5.1	Stochastic State Estimation for Catheter Navigation	113
5.1.1	State Vector	113
5.1.2	Prediction Model	113
5.1.3	Observation Model	114
5.1.4	Filter Workflow and Computation Time	115
5.1.5	Constrained State Estimation	117
5.2	Experimental Set-Up and Results	119
5.2.1	Overview and error metrics	119
5.2.2	Synthetic Experiments Set-Up	119
5.2.2.1	Ground Truth Reference	119
5.2.2.2	2D Observations	120
5.2.2.3	Stochastic Environment: Filter Parameters Tuning	120
5.2.3	Synthetic Experiments Results	122
5.2.3.1	Sensitivity to Friction Coefficient for Y-Shaped Geometry	122
5.2.3.2	Sensitivity to Generalized Model Uncertainties for Y-Shaped Geometry	124
5.2.3.3	Sensitivity to Generalized Model Uncertainties	127
5.2.4	Experiments on Real Data	129
5.2.4.1	Ground Truth Reference	129
5.2.4.2	FE model parameterization and 2D Observations	129
5.2.4.3	Stochastic Environment: Filter Parameter Tuning	130
5.2.4.4	Filter parameterization	130
5.2.4.5	Reducing the number of markers	131

5.3	Conclusion	133
-----	----------------------	------------

5.1 Stochastic State Estimation for Catheter Navigation

Compared to the previous study, the specific context of catheter simulation for endovascular surgery needs, in addition, to take into account the fact that the catheter is bounded within the vessel surface.

In this section, we present the formalism for a physics-based model of catheter navigation that handles constraints from both contacts, through a Lagrange multipliers approach (see Chapter III), and external 2D observations, through a UKF (see Chapter II). In the following notation, the index i specifies the catheter nodes, k indicates the discrete time-step, and j refers to sigma-points.

5.1.1 State Vector

Following the study on the state vector (Sec. 4.3), we need to estimate both positions and velocities of each node of the beam. Considering the i^{th} node, the state vector can be expressed as:

$$\mathbf{X}(i) = \underbrace{[x_i, y_i, z_i, \psi_i, \theta_i, \phi_i]}_{\text{position } \mathbf{x}_i^t} \underbrace{[v_{x_i}, v_{y_i}, v_{z_i}, v_{\psi_i}, v_{\theta_i}, v_{\phi_i}]}_{\text{velocity } \mathbf{v}_i^t}^T \quad (5.1)$$

with $i \in (1, N)$ and N being the number of serially linked beams. Given that positions and velocities are expressed taking into account 6DoFs, the whole state will be $\mathbf{X} \in \mathbb{R}^{12N}$.

5.1.2 Prediction Model

In Chapter III, we introduced the equation describing the dynamics of our process and its time integration. At the discrete time k , the temporal evolution of the state results from a two-step process: first solve Eq. (3.18) (recalled as Eq. 5.2 below) for $\Delta \mathbf{v}$ to compute the velocity variation, and then update the positions \mathbf{x}_k and velocities \mathbf{v}_k through Eq. (3.20) (recalled as Eq. 5.1.2 below). The problem belongs to the domain of non-smooth mechanics. In this case, accelerations are not defined but instead considered as a difference of velocities (at the end and the beginning of the time-step $\Delta \mathbf{v} = (\mathbf{v}_k - \mathbf{v}_{k-1})$). We assume the uncertainty affecting the process model to mainly come from an uncertain characterization of the FE model, that it is propagated to the estimated $\Delta \mathbf{v}$, solution of Eq. (5.2). The resultant noise is modeled as a Gaussian additive random term $\boldsymbol{\sigma}_{mod}$, Eq. (5.3). As a result, our process model is given by:

- Velocity variation is computed according mechanics and applied constraints:

$$\begin{cases} \mathbf{A}_k \Delta \mathbf{v} = \mathbf{b}_k + \mathbf{J}_k^T \boldsymbol{\lambda}_k \\ \mathbf{J}_k^T \Delta \mathbf{v} = \boldsymbol{\delta}_k \end{cases} \quad (5.2)$$

- Due to uncertainty on model parameterization, we supposed the acceleration to be affected by Gaussian noise:

$$\Delta \hat{\mathbf{v}} = \Delta \mathbf{v} + \boldsymbol{\sigma}_{mod} \quad (5.3)$$

- The uncertainty on the acceleration is propagated, through time integration, to positions and velocities:

$$\begin{aligned} \mathbf{v}_k &= \mathbf{v}_{k-1} + T \Delta \hat{\mathbf{v}} \\ \mathbf{x}_k &= \mathbf{x}_{k-1} + T \mathbf{v}_k \end{aligned} \quad (5.4)$$

The model noise covariance, quantifying the uncertainty of the process model, is computed according to eq. 4.7. After approximation (as presented in eq. 4.8) it can be expressed as:

$$\mathbf{Q} = \mathbf{I}_N \otimes \begin{pmatrix} \mathbf{0}_{6 \times 6} & \mathbf{0}_{6 \times 6} \\ \mathbf{0}_{6 \times 6} & \sigma_{mod}^2 T^2 \mathbf{I}_6 \end{pmatrix} \quad (5.5)$$

where the initial state covariance matrix, which expresses the uncertainty on the initial configuration, can be written as:

$$\mathbf{P}_0 = \mathbf{I}_N \otimes \begin{pmatrix} \sigma_{mod}^2 T^4 \mathbf{I}_6 & \mathbf{0}_{6 \times 6} \\ \mathbf{0}_{6 \times 6} & \sigma_{mod}^2 T^2 \mathbf{I}_6 \end{pmatrix} \quad (5.6)$$

where \otimes is the Kronecker product and \mathbf{I}_N is the $N \times N$ identity matrix, with N the number of nodes of the beam model.

5.1.3 Observation Model

External observations are provided by the projection of the radio-opaque markers detected in the images. For the i^{th} marker the observation vector is:

$$\mathbf{Z}(i) = q_i = [u_i, v_i]^t \quad \forall i \in [1, M] \quad (5.7)$$

According to our observation model, the i^{th} detected feature will depend on the corresponding 3D marker, through the calibrated projection matrix $\mathbf{C}_{[3 \times 4]}$:

$$\underline{\mathbf{Z}}(i)_k = [\mathbf{C} \quad \mathbf{0}_{3 \times 9}] \begin{pmatrix} x_{k+1} \\ y_{k+1} \\ z_{k+1} \\ 1 \\ \psi_{k+1} \\ \theta_{k+1} \\ \phi_{k+1} \\ v_{x_{k+1}} \\ v_{y_{k+1}} \\ v_{z_{k+1}} \\ v_{\psi_{k+1}} \\ v_{\theta_{k+1}} \\ v_{\phi_{k+1}} \end{pmatrix} + \boldsymbol{\nu} = \mathbf{C}_+ \underline{\mathbf{X}}(i)_k + \boldsymbol{\nu}_k \quad (5.8)$$

The observation function $h_k(\cdot)$ (in eq. 4.2) is therefore constant : $h_k = h$. As previously done, we assumed that an identity mapping relates the radio-opaque markers to nodes of the FE model such that: a node is defined at each tag location, and M (the number of markers) equals N (the number of nodes). The observations vector $\mathbf{Z}_k \in \mathbb{R}^{2N}$ concatenates the locations of all the 2D markers detected in the image at the new time-step. We assumed that all observations are independent and that the noise $\boldsymbol{\nu}$ on the observations does not depend on the acquisition time. Therefore, its covariance matrix is constant and diagonal: $\mathbf{R} = \sigma_{obs}^2 \mathbf{I}_{2N}$.

5.1.4 Filter Workflow and Computation Time

The *simplex method* [117] was used to generate the sigma-points with a minimum computation cost: it requires only $r = p + 1$ sigma-points, where $p = 12N$ is the state vector size. A generic sigma-points is expressed as:

$$\boldsymbol{\sigma}_j = [(\boldsymbol{\sigma}_{\mathbf{x}_1}, \boldsymbol{\sigma}_{\mathbf{v}_1}), \dots, (\boldsymbol{\sigma}_{\mathbf{x}_N}, \boldsymbol{\sigma}_{\mathbf{v}_N})]_j^t \quad \text{with } j \in [1, r] \quad (5.9)$$

Alg. (2) summarizes a UKF estimation, modified to take into account our specific process and observation model. Fig. 5.1 summarizes the global pipeline in which filter and simulation are combined.

In the prediction phase, an entire simulation step is run for every sigma-point $\boldsymbol{\sigma}_j$. From each propagated $\hat{\boldsymbol{\sigma}}_j$ we can compute the predicted observations $\hat{\mathbf{Z}}_j$, through the observation function $h(\cdot)$. A major challenge of our method lies in achieving high computation

Initialization: set $\mathbf{X}_0, \mathbf{P}_0, \mathbf{Q}, \mathbf{R}$

```

1  for each simulation step  $k$  do
    Prediction:
2    for  $j = 1 : r$  do
3      generate sigma-points
4       $[\boldsymbol{\sigma}_x, \boldsymbol{\sigma}_v]_{j_k} = [\mathbf{x}_{k-1}, \mathbf{v}_{k-1}] + \sqrt{\mathbf{P}_{k-1}} \mathbf{I}^{(j)}$ 
5      propagate sigma-points (eqs. (5.2)- (5.4))
6       $\mathbf{A} \Delta \boldsymbol{\sigma}_{\mathbf{v}_{j_k}} = \mathbf{b} + \mathbf{J}^T \boldsymbol{\lambda}$ 
7       $\mathbf{J}^T \Delta \boldsymbol{\sigma}_{\mathbf{v}_{j_k}} = \boldsymbol{\delta}$ 
8       $\hat{\boldsymbol{\sigma}}_{\mathbf{v}_{j_k}} = \boldsymbol{\sigma}_{\mathbf{v}_{j_{k-1}}} + \Delta \boldsymbol{\sigma}_{\mathbf{v}_{j_k}}$ 
9       $\hat{\boldsymbol{\sigma}}_{\mathbf{x}_{j_k}} = \boldsymbol{\sigma}_{\mathbf{x}_{j_{k-1}}} + T \hat{\boldsymbol{\sigma}}_{\mathbf{v}_{j_k}}$ 
10    end
11     $\hat{\mathbf{X}}_k = \mathbb{E}[\hat{\boldsymbol{\sigma}}_k^*]$ 
12     $\hat{\mathbf{P}}_k = \text{cov}[\hat{\boldsymbol{\sigma}}_k^*] + \mathbf{Q}$ ;
    Correction:
13    for  $j = 1 : r$  do
14       $\hat{\mathbf{Z}}_{j_k} = \mathbf{C}_+ \hat{\boldsymbol{\sigma}}_{j_k}$  compute predicted observations see eq. (5.8)
15    end
16     $\mathbf{P}_k^{\hat{\mathbf{X}}\hat{\mathbf{Z}}} = \text{cov}[\hat{\boldsymbol{\sigma}}_k^*, \hat{\mathbf{Z}}_k^*]$ 
17     $\mathbf{P}_k^{\hat{\mathbf{Z}}\hat{\mathbf{Z}}} = \text{cov}[\hat{\mathbf{Z}}_k^*, \hat{\mathbf{Z}}_k^*] + \mathbf{R}$ 
18     $\mathbf{K}_k = \mathbf{P}_k^{\hat{\mathbf{X}}\hat{\mathbf{Z}}} (\mathbf{P}_k^{\hat{\mathbf{Z}}\hat{\mathbf{Z}}})^{-1}$ 
19     $\mathbf{X}_k = \hat{\mathbf{X}}_k + \mathbf{K}_k (\mathbf{Z}_k - \mathbb{E}[\hat{\mathbf{Z}}_k^*])$ 
20     $\mathbf{P}_k = \hat{\mathbf{P}}_k - \mathbf{P}_k^{\hat{\mathbf{X}}\hat{\mathbf{Z}}} (\mathbf{P}_k^{\hat{\mathbf{Z}}\hat{\mathbf{Z}}})^{-1} (\mathbf{P}_k^{\hat{\mathbf{X}}\hat{\mathbf{Z}}})^t$ 
21  end

```

Algorithm 2: UKF for catheter navigation physics-based simulation. Index i is omitted in the notation. r is the number of sigma-points and $\boldsymbol{\sigma}_k^*$ is a matrix $[12N \times r]$ gathering all the sigma-points.

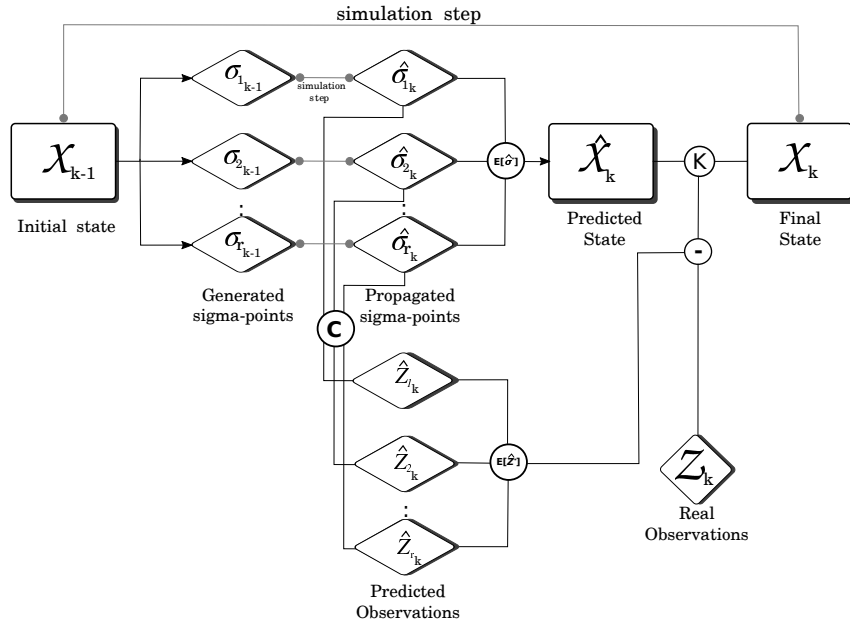


Figure 5.1: One single simulation-step is composed of several filter-steps. Filter final state will provide the mechanical state of the catheter to be used in the following simulation step.

time. Whereas a classic physics-based constrained simulation may be performed in real-time (over 25 FPS), such a combined approach entails higher computation times due to the multiple simulations performed during each time-step ($r = 12N + 1$).

5.1.5 Constrained State Estimation

The catheter bounded within the vessel surface and the non-rigid contacts represent, from the filter point of view, a problem known as Constrained State Estimation (see [120]).

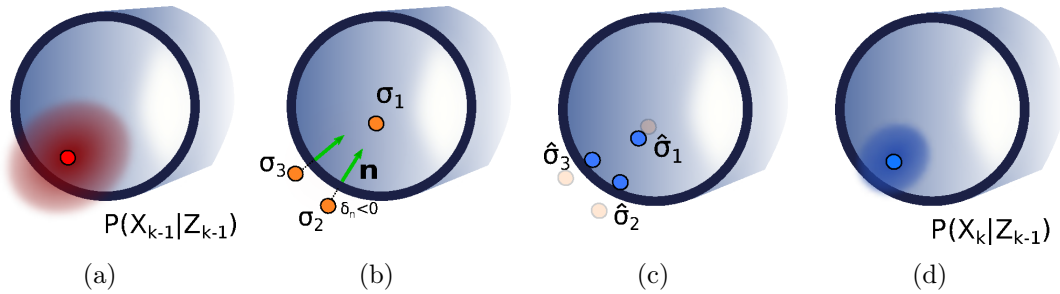


Figure 5.2: (a) Red dot represents a node at time $k - 1$, described as a state vector and its covariance. (b) Generated sigma-points may fall outside the geometry, behaving as interpenetrated objects $\delta_n \leq 0$ (c) Their position is then corrected during propagation through collision response. (d) Predicted mean and covariance are hence computed from propagated samples.

More generally, one talks about *Constrained State Estimation* when some physical limitations exist in the estimated state. For example, physical parameters cannot have negative values or, as in our case, positions must enforce a boundary condition. Such existing boundary conditions represent a problem especially during the prediction phase, where random sampling of the Gaussian distribution may generate some sigma-points σ_j whose positions fall outside the vessel surface (Fig. 5.2(b)), hence representing configurations not physically coherent.

From the simulation point of view, such a scenario corresponds to a configuration of the catheter not respecting the constraint ($\delta_n < 0$ in Fig. 5.2(b)). The collision response model presented in Sec. 3.5 allows us to solve this problem. During the propagation step, nodes detected as crossing the vessel wall are corrected through contact forces and projected back into the space of physically acceptable states (i.e. with positions inside the vessel) (see Fig. 5.2). Furthermore, non-linear interactions with the surrounding surface, taking into account non-sliding contacts (see Eq. (3.18)), enables us to improve the prediction of the catheter shape further.

Our proposed Bayesian filter enables the fusion of mechanical constraints with the geometric constraints provided by 2D image features. The number of possible solutions to the ill-posed 2D-3D reconstruction problem is thereby reduced down to a single high probability, and correct, hypothesis in the vast majority of cases. Analyzing the covariance of the position of the catheter's nodes allows us to back up this assertion. The covariance of the position (i.e. its uncertainty) is greatly reduced when the first contact occurs (see Fig. 5.3).

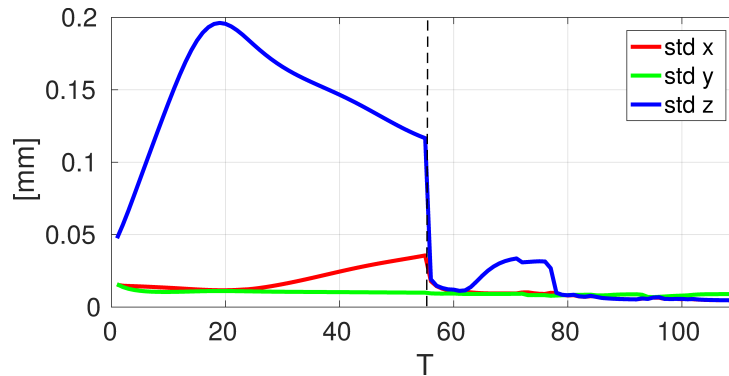


Figure 5.3: These results refer to the synthetic scenario performed in Sec. 5.2.2. The contact occurring around $T \sim 55$ considerably reduces the standard deviation of the tip position. Also, it is possible to notice how the uncertainty on Z-axis, i.e. the depth direction of the projective view, is greater than the uncertainty on X-axis and Y-axis before any contact has occurred

5.2 Experimental Set-Up and Results

5.2.1 Overview and error metrics

We tested the method to retrieve the 3D shape of a navigating device from 2D images, both in a synthetic environment and with real data. Tests have been carried out to estimate the filter's performance in the presence of different model uncertainty sources, observation noise, and different parameter tuning. In particular, our experiments aimed at demonstrating how our approach can naturally handle uncertainties related to model parameterization as well as observations obtained from different angles of view.

As in Chapter III, the quality of the reconstruction has been evaluated comparing the 3D shape of the reconstructed catheter with a known ground-truth. Comparison metrics have been evaluated on B-spline interpolations, computed starting from the tip, of both the reference shape $\mathbf{g}_M = (g_1, \dots, g_M)$ and the catheter's $\mathbf{c}_M = (c_1, \dots, c_M)$, (with $M = 10N$ against the N nodes of the FE model). Such interpolation allows having a finer discretization of the shapes. We focused on the tip and distal segment of the device because it is the part most subject to variations during the insertion and of the highest importance for clinicians.

5.2.2 Synthetic Experiments Set-Up

The synthetic set-up provided a fully controlled ground-truth and allowed us to evaluate the robustness of the method to inaccuracies in the process model and filter parameters tuning.

5.2.2.1 Ground Truth Reference

We simulated catheter insertion on two different geometries. First, a Y-shaped surface, mimicking a vessel bifurcation, was generated by connecting 3 cylinders of 1 cm in diameter. A second geometry, extracted from an anatomical vascular phantom (see Sec. 5.2.3.3), has been used to simulate a more realistic scenario. In both cases, we generated a sequence of ground-truth 3D shapes using the deterministic model of physics-based simulation (presented in Chap. III) with known model parameters.

Overall, we set three different reference scenarios: two performed with the Y-shaped geometry and one with the anatomical vessel. Model parameterizations used to generate the three different ground-truth scenarios are respectively summarized in tables 5.1, 5.2 and 5.3. The ground-truth navigation was simulated by mimicking a full insertion of the catheter along the vessel's total length (10 cm).

5.2.2.2 2D Observations

2D image-features were generated by projecting the ground-truth positions under two different view incidences (816 x 600 pixels, with a pixel size of 0.24 mm), (see Fig. 5.4 for the set-up in the Y-shaped geometry): one from the side where the view of the bifurcation is ambiguous (a catheter viewed in the vessels could be in any bifurcating branch), and one from the top with a clear view of the bifurcation.

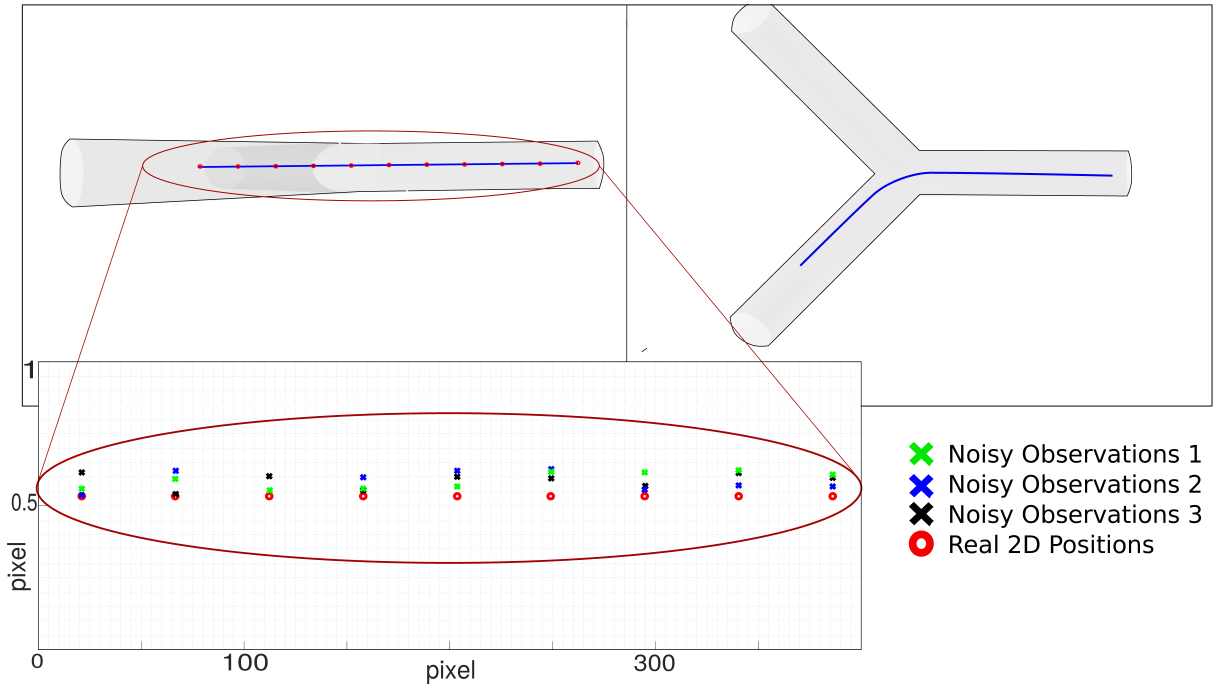


Figure 5.4: Two different views for 2D observations, side and top views. 2D observations were created by rendering the virtual catheter, equipped with markers, in each view, detecting the markers, and adding Gaussian noise to their locations. Three instances of noisy observations were created for each view, adding Gaussian noise of 0.1 pixels to Real 2D Positions.

At each time step of the simulated insertion, virtual markers placed on the catheter are projected through the known projection matrix and their 2D positions were automatically computed. 3 different observations sets were generated by adding random Gaussian 2D noise to the projected 2D position. A standard deviation of 0.1 pixels was chosen to be consistent with the level of detection error encountered in actual images. Thereby, six different data-sets of 2D observations were generated.

5.2.2.3 Stochastic Environment: Filter Parameters Tuning

Filters parameters P_0 , Q and R should be initialized to fit the actual level of noise tainting both the process and the observations, which is usually very difficult to set in

practice. In our synthetic, fully controlled, environment, these parameters are known (\mathbf{R}), or can be evaluated (\mathbf{P}_0 and \mathbf{Q}). Indeed, our experiments apply known perturbations on the input mechanical parameters, which are propagated to the computed velocity $\Delta \mathbf{v}$ through the dynamic system resolution process. \mathbf{P} and \mathbf{Q} are related to the noise on $\Delta \mathbf{v}$ and must therefore be evaluated. The covariance matrices \mathbf{P}_0 and \mathbf{Q} have been estimated following a Monte Carlo approach based on multiple process configurations, each characterized by a certain model inaccuracy (see Fig. 5.5).

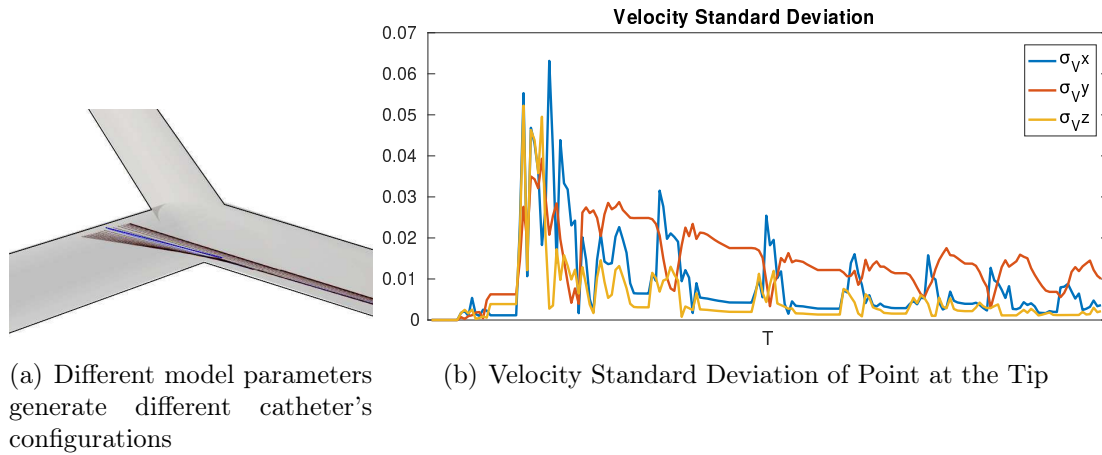


Figure 5.5: Initial values of \mathbf{P}_0 and \mathbf{Q} are set through a Monte Carlo forecasting multiple simulations affected by different model parameterizations. (a) Different configurations due to errors in Young's Modulus. (b) Standard deviation of tip velocity, computed among different configurations obtained with different Young's Modulus.

In practice, we forecast multiple simulations characterized by a specific model parameterization which is incorrect compared to the known ground-truth (red shape in Fig. 5.5). These differences in model parameterization generate different catheter configurations (blue shapes in Fig. 5.5). Computing the standard deviation of all the configurations positions and velocities, we initialize the uncertainty associated with the model (ν_k in Eq. (5.3)). In practice, we used the computed values to initialize \mathbf{P}_0 and \mathbf{Q} according to Eq. (5.3), in a nominal configuration that we will call \mathcal{P}_0 . The statistics on the positions and velocities were only computed on the catheter's distal segment, since they represent the part we want to characterize. To evaluate filter performance against its parameterization, we ran it with \mathcal{P}_0 along with two additional parameters configurations: an overestimation $\mathcal{P}_{sup} = 1.75^2 \mathcal{P}_0$ an underestimation $\mathcal{P}_{inf} = 0.25^2 \mathcal{P}_0$. Besides, two further observation noise covariance values were also considered: \mathbf{R}_1 and \mathbf{R}_2 . As a consequence, the filter was run with 6 different parameterizations: $[\mathcal{P}_0, \mathbf{R}_1]$, $[\mathcal{P}_0, \mathbf{R}_2]$, $[\mathcal{P}_{sup}, \mathbf{R}_1]$, $[\mathcal{P}_{sup}, \mathbf{R}_2]$, $[\mathcal{P}_{inf}, \mathbf{R}_1]$, $[\mathcal{P}_{inf}, \mathbf{R}_2]$. Numerical values will be provided in the following sections for each experiment.

5.2.3 Synthetic Experiments Results

The evaluation aimed at testing the sensitivity of the reconstruction to an ample range of model uncertainty, while providing valid results within a reasonable range of filter parameters tuning. For that, we supposed to have uncertainties on different parameters: the friction coefficient, Young's modulus, initial configuration, and applied forces.

5.2.3.1 Sensitivity to Friction Coefficient for Y-Shaped Geometry

The friction coefficient μ is an impacting parameter in the case of simulations taking account collisions between objects whose value is hard to measure in practice. In order to evaluate the impact of the misknowledge in practice exists on such parameter, we generated a ground-truth scenario, where the friction coefficient was set as $\mu = 0.04$ according to the literature [121]. Then, we tested our filter with 20 different process model configurations, each corresponding to a different value for μ , ranging from 0 (i.e. no friction) to 0.08 (i.e. twice the ground-truth value, and excluding the ground-truth value 0.04) by steps of 0.004 (see Fig. 5.5). It is noteworthy that usually acceptable uncertainty lies in a range of 10-20%, but we wanted to test the filter capacity to deal with larger errors. Other parameters were the same as the reference model (Tab. 5.1).

	Ground Truth	Incorrect Model	unit
<i>Young's Modulus</i>	10		MPa
<i>Inner Outer Radius</i>	0.4		mm
<i>Mass</i>	0.5		g
<i>Insertion Force</i>	0.5e-03		N/s
<i>Total Length</i>	9		cm
<i>Time-step</i>	0.001		s
<i>Nodes</i>	10		
<i>Friction Coefficient</i>	0.04	0.04 \pm 0.04	

Table 5.1: Simulation parameters for friction coefficient sensitivity.

Filter parameter \mathbf{P}_0 and \mathbf{P} have been initialized, according to Eq. (5.5), with the empirical variance values found in Sec. 5.2.2.3. Thus, \mathbf{Q} was initialized as follows:

$$\mathbf{Q} = \mathbf{I}_N \otimes \begin{pmatrix} \mathbf{0}_{6 \times 6} & \mathbf{0}_{6 \times 6} \\ \mathbf{0}_{6 \times 6} & \begin{pmatrix} 10^{-4} & 0 & 0 & 0 & 0 & 0 \\ 0 & 10^{-4} & 0 & 0 & 0 & 0 \\ 0 & 0 & 10^{-4} & 0 & 0 & 0 \\ 0 & 0 & 0 & 10^{-6} & 0 & 0 \\ 0 & 0 & 0 & 0 & 10^{-6} & 0 \\ 0 & 0 & 0 & 0 & 0 & 10^{-6} \end{pmatrix} \end{pmatrix} \quad (5.10)$$

Concerning the nominal observations noise covariance, we tested for two different instances: $\mathbf{R}_1 = (0.1)^2 \mathbf{I}_{2N}$ and $\mathbf{R}_2 = (0.01)^2 \mathbf{I}_{2N}$; both observation noise levels provided similar results. Results with R_1 are depicted in Fig. 5.6. The filter provided an accurate

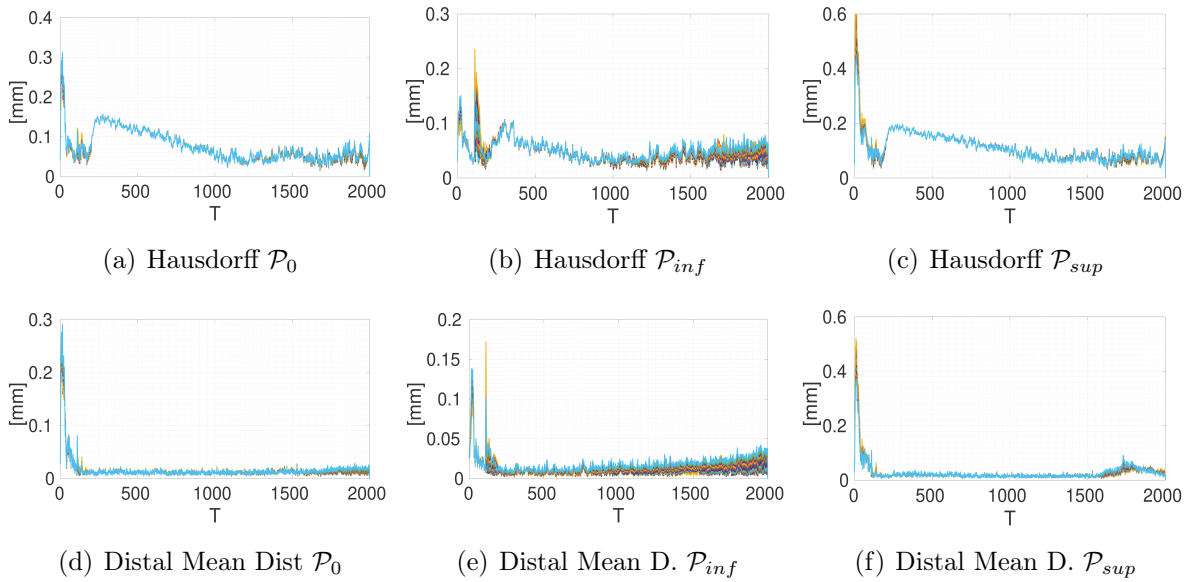


Figure 5.6: Comparing reconstruction errors for different process model parameterizations (21 curves on each plot). Observations from the side view were used, and measurement noise covariance was \mathbf{R}_1 . All reconstructions lay within the same range of accuracy, showing the same trends, independent of the uncertainty on the model (error on μ).

estimate of the 3D catheter shape, even for important model uncertainties (i.e. $\mu = 0$, or $\mu = 0.08$). Errors were mainly noticeable in the depth direction and on the proximal part of the catheter, (Fig. 5.6 (a-c)), meaning that the distal segment was always accurately reconstructed (Fig. 5.6 (b-d)) due to the contact with the vessel surface. For a given observation data set and filter configuration, all the reconstructions presented the same error trend, indicating a behavior independent from model uncertainty. Nevertheless, the filter parameters \mathcal{P}_{inf} provided the best results (see Fig. 5.6). The initial peak, common to all the graphs, is due to the filter starting-up. The effect of mechanical constraints on the quality of the reconstruction is particularly noticeable on the Hausdorff distance, which improves and stabilizes after the first contact (around $T = 250$). On average, for filter

parameters \mathcal{P}_{inf} , we measured a 3D Hausdorff distance of 0.07 ± 0.037 mm; a 3D distance at the tip equal to 0.021 ± 0.009 mm and a 3D mean distance on the distal segment of the catheter of 0.02 ± 0.008 mm. Such accurate results derive from the fact that this sensitivity analysis has been carried out assuming a limited uncertainty on the model. In fact, solely the friction coefficient is unknown compared to the real model. Also, friction phenomena are mainly accumulative phenomena whose effect expresses through time. This means that higher deviations from the reference shape occur through time. Within the filter algorithm, a correction step is performed at each time-step. Hence, such divergence is iteratively minimized.

5.2.3.2 Sensitivity to Generalized Model Uncertainties for Y-Shaped Geometry

In reality, models may present multiple sources of uncertainty. In this section, we evaluate our filter performances when multiple incorrect parameters are taken into account simultaneously. A ground-truth simulation of catheter navigation has been run on the Y-shaped geometry. Mass and diameters for catheter's models have been set according to manufacturer specifications for Headway Duo catheter (MicroVention Inc). Variations from ground-truth have been taken into account: Young's modulus, insertion force, friction coefficient, and initial shape. Three different cases have been investigated, where we systematically used 10 catheter nodes (against 31 in the ground-truth) to experiment with reasonable filter computation speed. Models parameterizations are summarized in Tab. 5.2.

	Ground Truth	Case 1	Case 2	Case 3	unit
<i>Young's Modulus</i>	750	250	500	1500	MPa
<i>Inner Outer Radius</i>	0.35-0.02	0.35-0.02	0.35-0.02	0.35-0.02	mm
<i>Mass</i>	0.48	0.48	0.48	0.48	g
<i>Insertion Force</i>	1.7e-03	1.7e-03	1.7e-04	1.7e-02	N/s
<i>Time-step</i>	0.001	0.001	0.001	0.001	s
<i>Total Length</i>	10	10	10	10	cm
<i>Nodes</i>	31	10	10	10	
<i>Friction Coefficient</i>	0.01	0.1	0	0.01	
<i>Initial Configuration</i>	c_0	c_0	$c_0 \cdot [R T_c]$	$c_0 + T_c$	

Table 5.2: Simulation parameters for sensitivity test to multiple model uncertainties. See Fig. 5.8 for reference configuration c_0 (blue shape).

Observations have been acquired from the side and top view. The nominal configuration \mathcal{P}_0 was initialized with:

$$\mathbf{Q} = \mathbf{I}_N \otimes \begin{pmatrix} \mathbf{0}_{6 \times 6} & \mathbf{0}_{6 \times 6} \\ \mathbf{0}_{6 \times 6} & \begin{pmatrix} 10^{-4} & 0 & 0 & 0 & 0 & 0 \\ 0 & 10^{-4} & 0 & 0 & 0 & 0 \\ 0 & 0 & 10^{-4} & 0 & 0 & 0 \\ 0 & 0 & 0 & 10^{-4} & 0 & 0 \\ 0 & 0 & 0 & 0 & 10^{-4} & 0 \\ 0 & 0 & 0 & 0 & 0 & 10^{-4} \end{pmatrix} \end{pmatrix} \quad (5.11)$$

In this case, the model error covariance on the velocity has higher values, due to the more significant amount of model uncertainty. Concerning the nominal observations noise covariance, we tested for three different instances: $\mathbf{R}_1 = (0.1)^2 \mathbf{I}_{2N}$, $\mathbf{R}_2 = (0.01)^2 \mathbf{I}_{2N}$ and $\mathbf{R}_3 = (0.001)^2 \mathbf{I}_{2N}$.

Case 1 (Tab.5.2): we considered uncertainties on Young's modulus and friction coefficient. Averaging results for all filter parameterization and both top and side observations, we obtained a 3D Hausdorff distance of 1.15 ± 0.15 mm; a 3D distance at the tip equal to 0.07 ± 0.05 mm and a 3D mean distance on the distal segment of the catheter of 0.13 ± 0.09 mm.

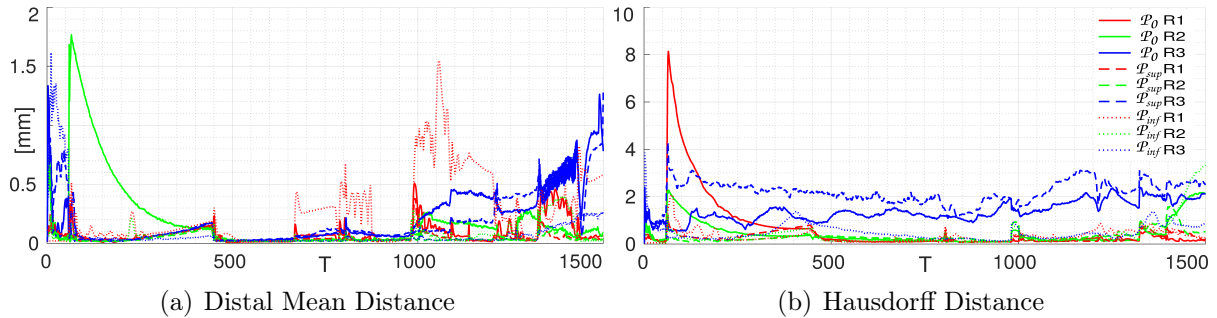


Figure 5.7: Metrics evaluated between ground-truth shape and reconstructed shape. Each color is associated to a shape reconstruction obtained with a different set of filter parameters (see legend). All filter parameterizations provide good results. Whenever \mathbf{R} is small and \mathbf{Q} is higher, a more important error appears at the tail of the catheter, in the depth direction (blue graphs).

All filter parameterizations allowed retrieving an accurate 3D shape. Whenever a small \mathbf{R} is combined with higher \mathbf{Q} , a larger error appears at the tail of the catheter (Fig. 5.7-(b) blue graphs); this is due to a greater trust in 2D observations (small \mathbf{R}) which intrinsically have an uncertainty in the depth direction.

Case 2 : besides erroneous model parameterization, we considered a different initial configuration (Fig. 5.8-(b), real blue shape against incorrect red shape). On average (for all filter parameterizations and views), the 3D Hausdorff distance was 2.29 ± 1.27 mm, the 3D mean distance on the distal segment of 0.26 ± 0.25 mm and the 3D error at the tip of 0.13 ± 0.15 mm. The initial peak is due to the mismatch of the initial configuration, which is compensated by the filter after a few time steps.

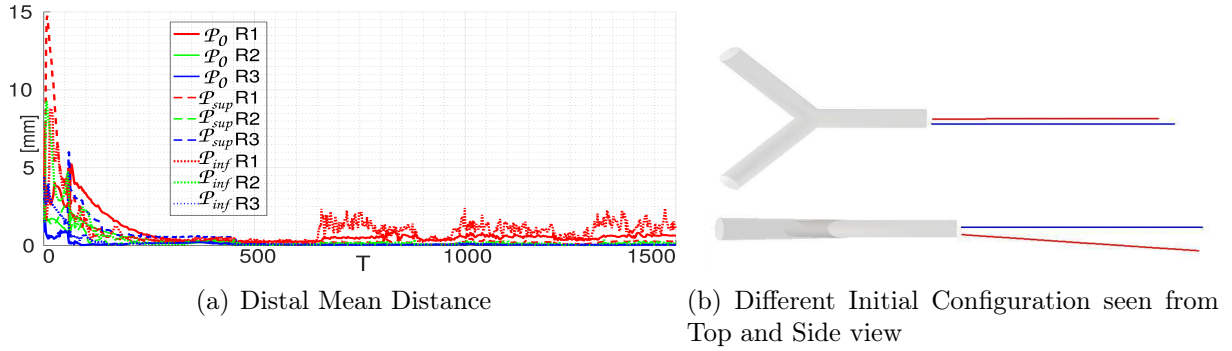


Figure 5.8: Distal mean distance between ground-truth distal segment and reconstructed catheter distal segment. Each color is associated to a shape reconstruction obtained with a different set of filter parameters (see legend). Blue shape c_0 , red shape $c_0 \cdot [R|T_c]$.

Case 3: we considered model parameters errors plus an initial configuration that only differed from the ground-truth by a translation such that the erroneous position can be observed in the top view, but not in the side view. This new initial configuration would naturally lead the catheter (represented in red in Fig. (Fig. 5.9)) to go towards the opposite branch.

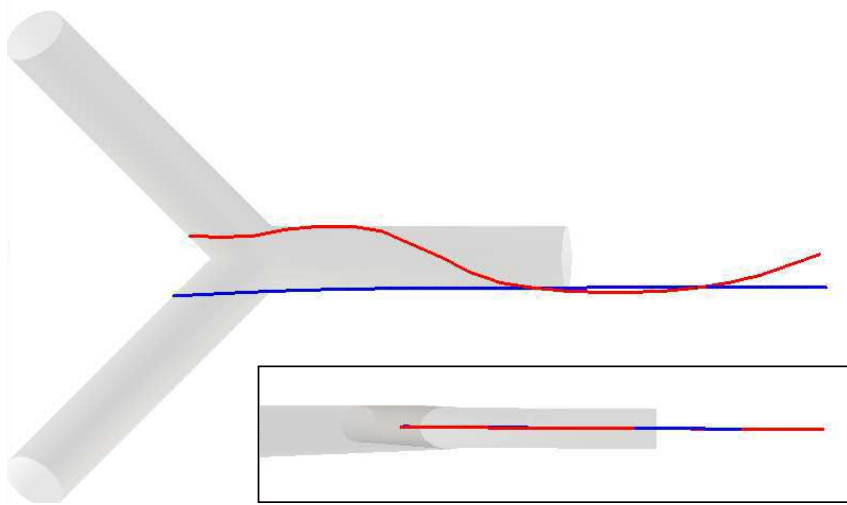


Figure 5.9: A perfectly horizontal view, does not allow solving the ambiguity, whenever the model would naturally go towards the wrong branch.

In the case of 2D observations from a top view, the filter can compensate for model uncertainties and retrieve the correct shape because external measurements gather the right amount of information about the catheter's motion. Instead, in case of perfectly horizontal observations, it is not possible to solve the ambiguity: the filter would not be able to reconstruct the catheter in the right direction, and the reconstructed shape will diverge from the ground-truth (Fig. 5.9). Nevertheless, a slight rotation of the camera

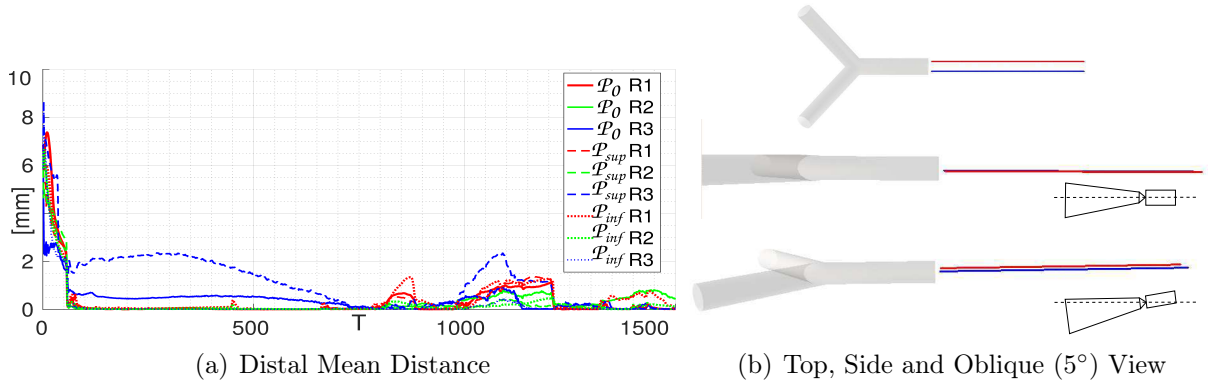


Figure 5.10: Each curve represents the distance between the ground-truth distal segment and the reconstructed one, obtained with different filter parameters combinations (see legend). The ambiguity is easily solved by having an angle of view slightly rotated with respect to the horizontal axis

around the horizontal axis ($\sim 5^\circ$ as shown in Fig. 5.10-(b)) allows us to solve the ambiguity and retrieve the correct 3D shapes, obtaining on average a 3D Hausdorff distance of 1.14 ± 1.25 mm; a 3D distance at the tip equal to 0.23 ± 0.15 mm and a 3D mean distance on the distal segment of the catheter of 0.40 ± 0.29 mm.

5.2.3.3 Sensitivity to Generalized Model Uncertainties

Lastly, we performed a similar synthetic evaluation, taking into account a more complex geometry extracted from real anatomy (Fig. 5.11-(a)). The vessel is 13 cm long with an average diameter of 7 mm, and it represents a section of the internal carotid artery (H+N-R-A-003 model, Elastrat). A more complex geometry entails more occurring contacts between the instrument and the vessel. A mechanical characterization of catheter model has been set according to manufacturer specifics for Headway TM 17 catheter (MicroVention Inc.), which is the same device used for the experiences in Chap. III. Parameters are summarized in Table 5.3.

	Ground Truth	Incorrect Model	unit
<i>Young's Modulus</i>	300	400	MPa
<i>Inner Outer Radius</i>	0.4 - 0.215		mm
<i>Mass</i>	0.1		g
<i>Insertion Force</i>	0.01	0.0001	N/s
<i>Total Length</i>	6		cm
<i>Time-step</i>	0.001		s
<i>Nodes</i>	21	11	
<i>Friction Coefficient</i>	0.1	0.2	

Table 5.3: Simulation parameters for sensitivity test on synthetic vessel geometry.

In this testbed, we simulated a clinical scenario where the real insertion force is unknown, unless embedding the device with an external sensor. In order to take into account such uncertainty and improve the estimation, we added the insertion force to the state vector estimating its value:

$$\mathbf{X} = [\mathbf{x}_1^t, \mathbf{v}_1^t, \dots, \mathbf{x}_N^t, \mathbf{v}_N^t, \mathbf{f}^t] \quad (5.12)$$

The constant 6DoFs force \mathbf{f} is assumed to be applied at the bottom of the device. We modeled the force as constant through time except for a Gaussian error $\mathbf{f}_k = \mathbf{f}_{k-1} + \boldsymbol{\nu}_{\mathbf{f}}$ with $P(\boldsymbol{\nu}_{\mathbf{f}}) = \mathcal{N}(\mathbf{0}, \boldsymbol{\sigma}_{\mathbf{f}})$. Thus, the initial state covariance matrix \mathbf{P}_0 and the model covariance matrix \mathbf{Q} are modified as follows:

$$\mathbf{P}_0 = \begin{pmatrix} \mathbf{I}_N \otimes \begin{pmatrix} \mathbf{0}_{6 \times 6} & \mathbf{0}_{6 \times 6} \\ \mathbf{0}_{6 \times 6} & \mathbf{I}_6 \boldsymbol{\sigma}_{mod}^2 T^2 \end{pmatrix} & \mathbf{0}_{12N \times 6} \\ \mathbf{0}_{6 \times 12N} & \mathbf{0}_{6 \times 6} \end{pmatrix} \quad (5.13)$$

$$\mathbf{Q} = \begin{pmatrix} \mathbf{I}_N \otimes \begin{pmatrix} \mathbf{I}_6 \boldsymbol{\sigma}_{mod}^2 T^4 & \mathbf{0}_{6 \times 6} \\ \mathbf{0}_{6 \times 6} & \mathbf{I}_6 \boldsymbol{\sigma}_{mod}^2 T^2 \end{pmatrix} & \mathbf{0}_{12N \times 6} \\ \mathbf{0}_{6 \times 12N} & \boldsymbol{\sigma}_{\mathbf{f}_{6 \times 1}}^2 \end{pmatrix} \quad (5.14)$$

Observations have been acquired along the projective view from Fig. 5.11 and, as previously, Gaussian noise has been added to the projected position.



Figure 5.11: Angle of acquisition of 2D observations.

Different filter parameterizations have been taken into account. Although all filter parameters combinations provide similar results (see Fig. 5.12), best performances have been achieved with filter parameters combination \mathcal{P}_0 , with an average 3D Hausdorff Distance of 0.81 ± 0.53 mm, a 3D mean distance at the segment of 0.37 ± 0.17 mm and a 3D tip error of 0.24 ± 0.13 mm.

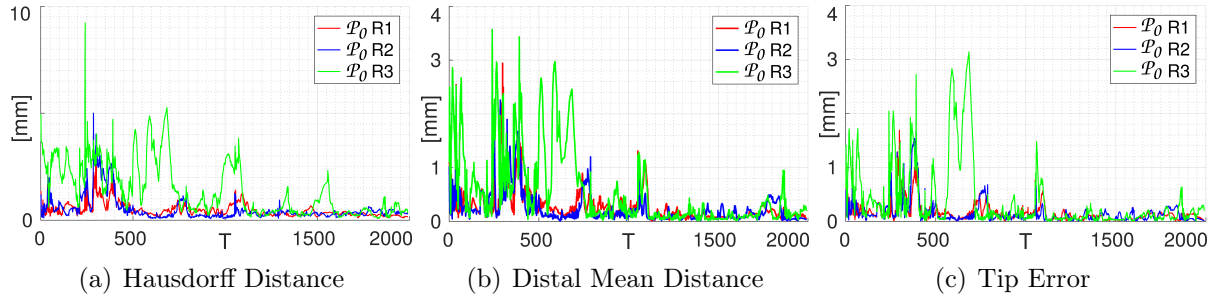


Figure 5.12: Reconstruction error between ground-truth and reconstructed shape. Metrics provided, with different colors, for filter parameters combinations $[\mathcal{P}_0, \mathbf{R}_1]$, $[\mathcal{P}_0, \mathbf{R}_2]$, $[\mathcal{P}_0, \mathbf{R}_3]$. For small \mathbf{R} (green graph), reconstruction appears less accurate due to the confidence given to observations which have an intrinsic uncertainty in depth direction.

5.2.4 Experiments on Real Data

5.2.4.1 Ground Truth Reference

The real data-set was acquired using the testbed described in [111]. A 1.7F micro-catheter (Headway TM 17, MicroVention Inc.) was inserted in a rigid phantom made of a silicone mould of an internal carotid artery (H+N-R-A-003 model, Elastrat). This navigation within the transparent phantom was captured at 198 frames per second by a pair of two high-speed cameras (TM-6740CL, JAI/Pulnix), synchronized using a trigger (C320 Machine Vision Trigger Timing Controller, Gardasoft). The stereovision camera set-up was calibrated using a chessboard target and OpenCV algorithms. One camera was placed above the phantom, to provide a top view, and the other one provided the side view. In particular, the calibration measured the projection matrices for each view (matrix \mathbf{C} in Eq. (5.8)). A sequence of 2130 images (640 x 480 pixels, with a pixel size of 0.13 mm), of a total duration of 10 s, was acquired: the catheter was automatically segmented and reconstructed in 3D by triangulation in each frame. This provided the ground-truth reconstruction. The reconstruction error was estimated to be below 0.05 mm on 1000 images of a motionless catheter. In the evaluated images sequence, a stick and slip transition occurred around frame number $T = 1300$ (see Fig. 5.15, (f)-(h)). The speed of the catheter tip was estimated to peak at 500 mm/s in the slip phase.

5.2.4.2 FE model parameterization and 2D Observations

The catheter length was 6 cm at the end of the insertion. Thereafter, we modeled the device as a series of 11 connected beams, of 5.5 mm each (12 nodes). Without further knowledge on the physical properties of the used materials (phantom silicone, catheter's properties, slippery liquid infused in the phantom, etc) the friction coefficient was set to $\mu = 0.1$, other mechanical properties such as mass, diameter, and Young's modulus have

been set according to manufacturers specifics (see Tab.5.3, ground-truth).

The insertion force has been set according to the velocity values provided for the catheter motion in [111] ($\mathbf{f}_1=0.8e-03$ N/timeStep). A second force intensity has been tested ($\mathbf{f}_2=2.5e-03$ N/timeStep), to simulate uncertainties occurring in reality.

Concerning 2D observations, as previously stated, the detection of markers is out of the scope of this thesis. Furthermore, the catheter did not carry any visible marker in the images. The 2D observations were therefore generated in a similar way as in the synthetic set-up: virtual markers were placed all along the length of the ground-truth shape and reprojected in each frame. Gaussian noise (with a standard deviation of 0.1 pixels) was added to their locations.

5.2.4.3 Stochastic Environment: Filter Parameter Tuning

As the synthetic vessel scenario, we considered the insertion force within the state vector, described through $\mathbf{f}_k = \mathbf{f}_{k-1} + \sigma_{\mathbf{f}_{mod}}$. Filter parameters have been initialized as the previous experiment. In particular, for $\mathbf{f}_1=0.8e-03$ N/timeStep the covariance was initialized with $\sigma_{\mathbf{f}_{1mod}} = 0.4e-03$, while for $\mathbf{f}_2=2.5e-03$ N/timeStep we set $\sigma_{\mathbf{f}_{2mod}} = 1e-03$.

5.2.4.4 Filter parameterization

Fig. 5.13 and 5.14 reports the evaluation metrics between the retrieved shape and the ground-truth when initializing the model with two different insertion forces.

We present the results for the filter parameters combination \mathcal{P}_{sup} , but all the three parameters configuration provided similar results. All the curves show a peak at around $T \sim 1300$. This is due to the filter response to the stick and slip transition, a phenomenon where the cumulative effect of the friction force causes an abrupt movement of the device. The filter was able to rapidly recover from such a sudden variation in positions and velocities.

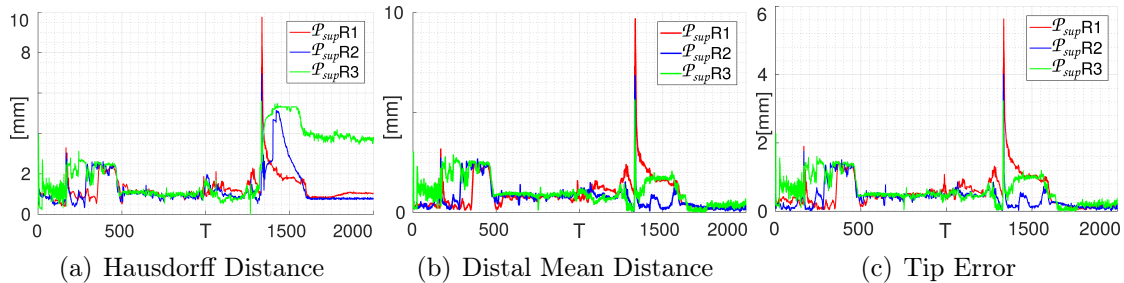


Figure 5.13: Reconstruction errors between ground-truth and reconstructed shape. Metrics provided, with different colors, for filter parameters combinations $[\mathcal{P}_{sup}, \mathbf{R}_1]$, $[\mathcal{P}_{sup}, \mathbf{R}_2]$, $[\mathcal{P}_{sup}, \mathbf{R}_3]$. In this case, the incorrect insertion force is: $\mathbf{f}_1=0.8e-03$ N/timeStep.

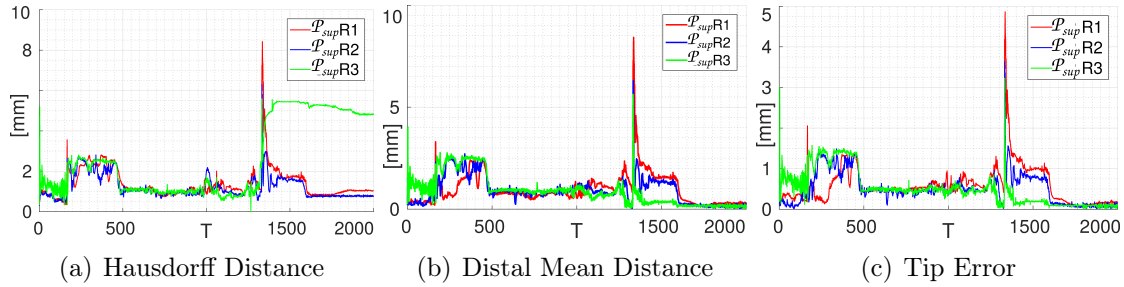


Figure 5.14: Reconstruction errors between ground-truth and reconstructed shape. Metrics provided, with different colors, for filter parameters combinations $[\mathcal{P}_{sup}, \mathbf{R}_1]$, $[\mathcal{P}_{sup}, \mathbf{R}_2]$, $[\mathcal{P}_{sup}, \mathbf{R}_3]$. In this case, the incorrect insertion force is: $\mathbf{f}_2 = 2.5 \times 10^{-3}$ N/timeStep

On average, we obtained a 3D Hausdorff distance of 1.74 ± 0.77 mm, a 3D mean distance at the distal segment of 0.91 ± 0.14 mm, a 3D error on the tip of 0.53 ± 0.09 mm. In Fig. 5.15, we present qualitative results: while the side view was used for the observations, the reconstructed catheter is here displayed under the orthogonal view.

The best results are provided for the parameters \mathcal{P}_{sup} and \mathbf{R}_2 , where the observation noise had to be underestimated by one order of magnitude.

The same testbed had been used in Chapter III under a deterministic approach. It is worth noticing how, in this scenario of stochastic approach, it is possible to reconstruct an accurate 3D shape even after the abrupt variation of configuration due to the stick and slip transition.

5.2.4.5 Reducing the number of markers

Our method relies on the presence of opaque markers placed along the catheter, but this is not the case for most of the current devices. Hence, we tested filter performances for different number of markers (respectively 3, 6, 12), equally distributed along the catheter length (see Fig. 5.16), while the state vector keeps the same size with $N = 12$.

Decreasing the number of observed markers globally degrades the quality of the reconstruction (see Fig. 5.16).

Reconstruction performed with 12 or 6 observed markers provide similar results (red and blue graph in Fig. 5.17). Instead, when using 3 markers the filter is no more able to handle the stick and slip transition occurring at $T \sim 1300$. Given the scarcity of observations, the filter cannot immediately retrieve the correct configuration and the error between the ground-truth shape and the reconstructed one increases.

In another experience, we kept the one to one mapping between the markers and nodes, iteratively reducing both of them ($M = N$, successively equal to 3, 6, 12). Indeed, reducing the number of nodes proportionally impacts the state vector and thereafter the filter

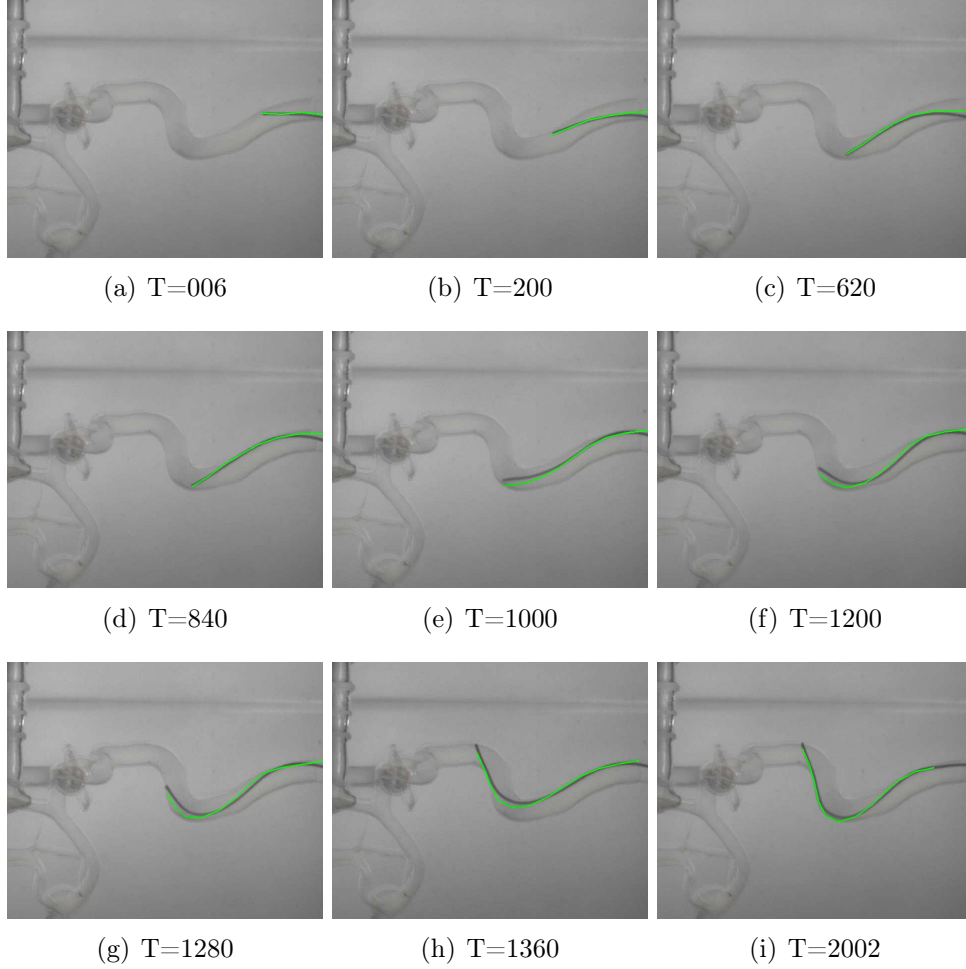


Figure 5.15: Reconstructed shape superimposed in the validation view. In Fig. (f), (g), (h) it is possible to observe the stick and slip transition where an abrupt movement happens within a short interval (for more details see [111]). Results are presented for $M = N = 12$ and for filter parameters \mathcal{P}_{sup} and \mathbf{R}_2 .

processing time performances. When the number of observations was divided by two (6 markers/nodes, see Fig. 5.18), the filter could reconstruct the catheter as long as its motion was smooth and gradual. However, a loss of accuracy was observed after the stick and slip transition. Indeed, fewer observations, especially along the distal segment, entails a loss of information on the curvature of the device, which is extremely flexible and may undergo significant deformations, like during the stick and slip transitions.

This was confirmed when further reducing the number of markers/nodes down to 3 (Fig. 5.19). The sparsity of the observations implies a lack of information about the bending of the device, which does not allow the filter to retrieve the correct 3D shape of the device.

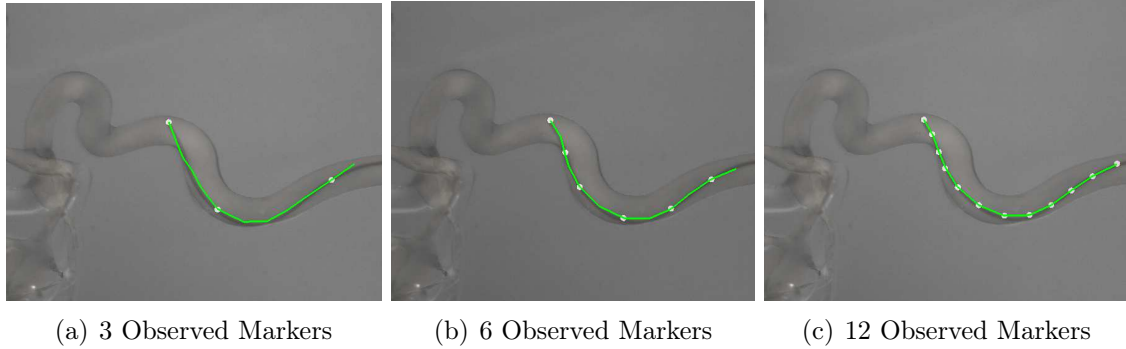


Figure 5.16: Visual results when having $N = 12$ model nodes and different number of available observations. Validation view at $T \sim 1300$

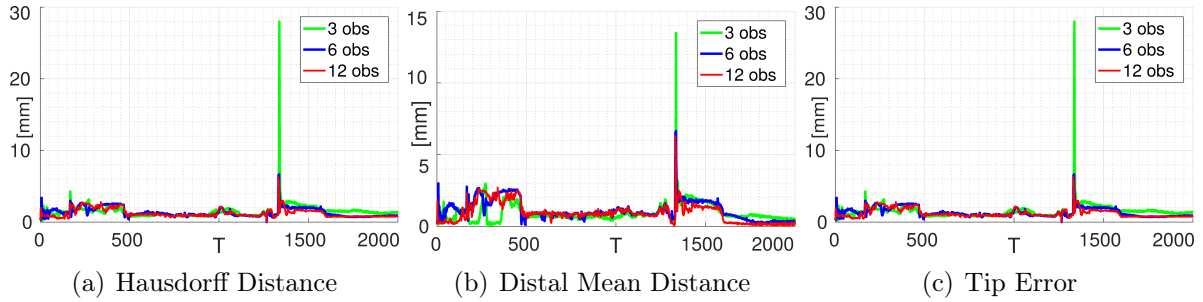


Figure 5.17: Reconstruction errors between ground-truth and estimated shape. Different colors correspond to different number of available observations (see legend). Best results (red graph) are provided when using $M = N$. Yet, similar performances are obtained for $M = 6$ (blue graph). Setting $M = 3$ entails a degradation, especially around $T \sim 1200$ where stick and slip transition occurs (green graph).

5.3 Conclusion

Within the proposed stochastic approach, we embedded a physics-based simulation in a Bayesian filtering framework where 2D observations on the catheter's current configuration are based on radio-opaque markers placed on the catheter detected in the fluoroscopic images. An Unscented Kalman Filter formulation was provided and experimented in both synthetic set-up and real phantom data. Both quantitative and qualitative results demonstrate the ability of our method to recover an accurate 3D shape, under a variety of filter parameterizations and challenging conditions: inaccurate friction coefficient and ambiguous views (synthetic scenario), complex non-linear contacts, and sudden stick and slip motions (real data set). The quality of the results depends on filter parameter tuning. The optimal filter parameterization could easily be deduced from practical considerations on the model uncertainty. This question is part of our current investigations, but we believe that an offline calibration step could provide adequate values, to be used during the clinical procedure. As presented in our results, including parameters in the state vector, notably the insertion force, allows us to improve the estimation globally. We also investi-

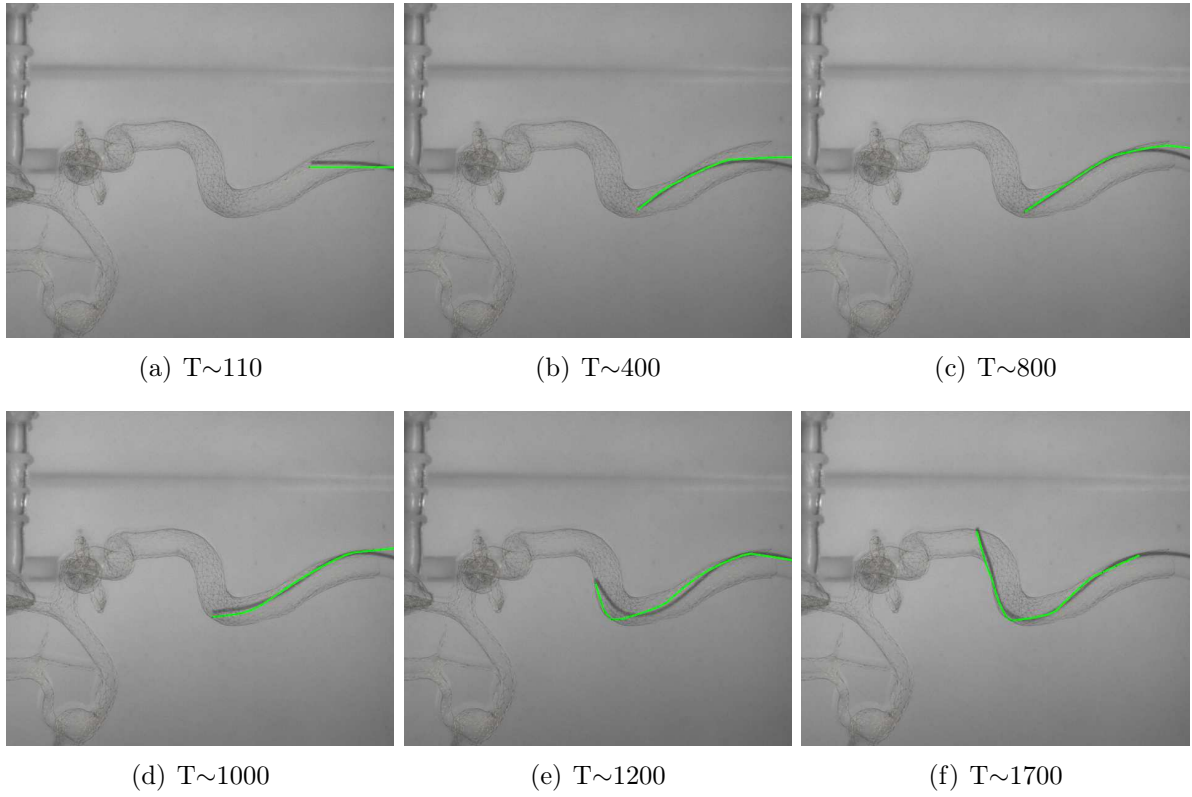


Figure 5.18: Results are presented for $M = N = 6$. Reconstruction appears less smooth compared to the background real image.

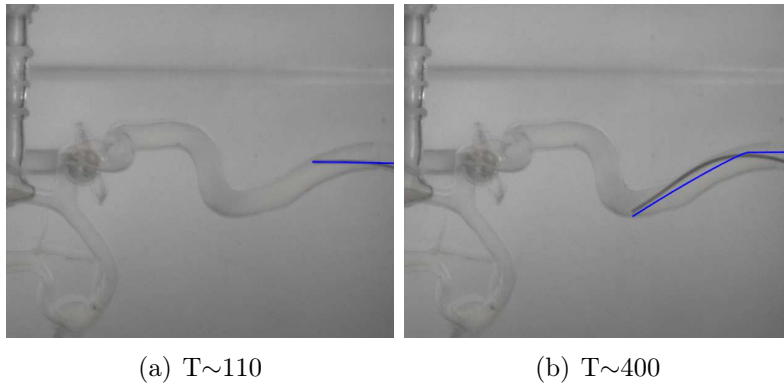


Figure 5.19: Results are presented for $M = N = 3$. Such configuration does not allow retrieving the correct curvature of the device.

gated the optimal markers/node configuration to reach the best compromise between the practical set-up, the accuracy of the reconstruction, and the simulation time. In conclusion, the optimal number of observed markers and model nodes depends on the rigidity of the device and the deformations it will undergo. More rigid devices, like needles, could

be reconstructed from a minimal number of observations. In the case of catheter-like devices, a good design would probably adapt the number of markers to both the flexibility and the accuracy required by the application. Also, markers could be positioned not uniform along the catheter length, for example: more markers on the distal segment, and only a few markers on the proximal portion. Such hypothetical configurations must be compatible with the device's design requirements.

Part VI

Conclusions and Perspectives

PROBLEMS AND SOLUTIONS FOR CLINICAL APPLICATION

Table of Contents

6.1	Introduction	139
6.2	Process Model	140
6.2.1	Vessel Geometry	141
6.2.2	Model Input	143
6.3	Observations Process	144
6.4	Computation Time	145
6.5	Method Validation	148
6.6	Future Applications	151
6.7	Conclusions	151

6.1 Introduction

In the introduction of this manuscript, we presented the clinical background and the scientific challenges of computer aided fluoroscopic procedures. Within this context, the main objective of this thesis has been to develop a method to enhance the visualization of fluoroscopic images, especially to overcome the lack of depth perception proper to X-ray images.

In Chapter II, we introduced and reviewed the most relevant approaches currently used to improve the visualization of fluoroscopic images. Several techniques aim at segmenting the 2D shape of the device (or other features) within the fluoroscopic images. This kind of solutions allow to highlight the shape of the device within a dense environment, but do not provide any further 3D insight. On the other hand, different approaches work by recreating a 3D model of the surgical scene (anatomy and/or interventional device), and registering it to fluoroscopic images. Such methods rely on different assumptions: the use of bi-plane or monocular systems, the use of external sensors embedded onto the device, along with different modeling choices (i.e. purely geometric, probabilistic approach, etc). In this clinical context, and after overviewing the state of the art, our main objective was to design and provide an accurate 3D simulation of device navigation. Indeed, a correct visualization of the device can significantly improve the global insight of the surgeon, who could have a precise knowledge of the location of the device. As previously stated, several methods exist to simulate the behavior of micro-devices in endovascular procedures. Generally speaking, in order to improve the accuracy of such models, the simulated results are compared to clinical data acquired in real-time. In case of interventional radiology, for example, the real-time clinical data consist of 2D fluoroscopic images. Different applications could have been contemplated. However, considering that losing one dimension would be a greater obstacle, our applicative objective was the monocular reconstruction of the simulated interventional device.

In Chapter III, we proposed a deterministic method. The device navigation is modeled through a physics-based approach and the 2D information is integrated to the simulation into the form of mechanical constraints. Retrieving a 3D shape solely from 2D features, is an ill-posed problem. In fact, several 3D configurations may correspond to the same projected shape. By including the surrounding vessel surface within the model, it is possible to reduce the number of possible solutions. Indeed, the vessel geometry defines a boundary volume of valid configurations. In our case, the approach is not purely geometric, but we took into account the non-linear interactions occurring between the instrument and the vessel when contacts occur. Further mechanical constraints might be defined in order to provide additional 3D information. For example, we defined an entry constraint, which imposes the orientation of the catheter at the insertion point. The results have shown good accuracy under restrictive hypotheses. In addition, the reconstruction method is not reliable whenever non-linear phenomena (such as stick-and-slip transitions) occur. A

more careful analysis reveals that uncertainty on model parameterization, as well as noise on external observations, must be taken into account in order to strengthen the robustness of the method.

For these reasons, we adopted a Bayesian approach. In particular, while in Chapter III the external information was integrated to the simulation as mechanical constraints, in the statistic approach, 2D information extracted from fluoroscopic images is integrated to the physics-based simulation through an Unscented Kalman Filter. In Chapter IV, we carried out preliminary studies aiming at defining which element of the model must be included into the state vector. Such studies were performed on simpler scenarios than the catheter navigation within blood vessels, in order to gather conclusions under simpler hypotheses. The results outlined that the state vector must include the positions and the velocities of the nodes of the device model. In the same chapter, we outlined the main sources of uncertainty of the process model and we demonstrated how data assimilation (i.e. taking into account an augmented state with incorrect parameters) may improve the final estimation of the 3D configuration.

In Chapter V, we eventually applied the method to a clinical scenario, where non-rigid interactions with the surrounding vessels are taken into account within the Bayesian framework. Such interactions occurring between the device and the surrounding vessel whenever they are in contact, represent a problem from the statistical point of view, which is known as *Constrained State Estimation*. We show how the collision response mechanism, used to model contacts, allows overcoming such issues. Results have shown how such a unified physics-based stochastic approach allows not only to compensate for a vast range model uncertainties, but also to retrieve a good estimate of the 3D shape of the device, in presence of non-linear phenomena such as stick-and-slip transitions.

In this last chapter, we want to provide an overview on the various topics affected by necessary simplifying assumptions, propose potential solutions and present some perspectives for future works and applications.

6.2 Process Model

The physics-based model used to describe the catheter navigation inside blood vessels (Sec. 3.4) has proven to be the best trade-off, in terms of description of the dynamic behavior of the surgical device and fast computation times. In our framework, we estimated that most of the uncertainties are due to an incorrect parameterization of the physic model of the catheter. In relation to that, we have shown that *Data Assimilation* (i.e. including the incorrect parameters within the state vector) may improve the final estimation of positions and velocities of the device.

Given the experimental set-up within which we validated our method, some simplifying assumptions have been done. For example, we considered the surrounding anatomy as

rigid, whereas real vessels may undergo different types of deformations. Similarly, another generalization has been done for the input of the model. In particular, we assumed the catheter to be inserted with a constant force, whereas, in reality, the surgeon's gesture is not continuous.

In the following sections, we will outline how these two aspects may be taken into account, in order to improve the predictive power of the process model.

6.2.1 Vessel Geometry

In clinical practice, for both pre-operative and intra-operative data set, the 3D acquisitions of the anatomy are performed with the patient holding his breath. The 3D acquisitions are usually registered to the 2D images, following different methods presented in Sec. 2.3. In our approach, the 3D geometry has been rigidly registered to the 2D fluoroscopic images. During the interactions between the interventional device and the surrounding vessel, solely the catheter is non-rigid.

In reality, blood vessels are deformable tissues that might undergo small deformations due to the action of the instrument (especially the tip) on the vessel wall. Therefore, a first improvement for the process model would be to take into account the deformability of the vessels. In case of two interacting objects that are both are deformable (i.e. the surgical device and the surrounding vessel), the Karush-Kuhn-Tucker system (KKT) presented in Eq. 3.18, is modified as follows:

$$\begin{cases} \mathbf{A}_c \mathbf{q}_c = \mathbf{b}_c + \mathbf{J}_c^T \boldsymbol{\lambda}_c \\ \mathbf{A}_v \mathbf{q}_v = \mathbf{b}_v + \mathbf{J}_v^T \boldsymbol{\lambda}_v \\ \mathbf{J}_c^T \mathbf{q}_c + \mathbf{J}_v^T \mathbf{q}_v = \boldsymbol{\delta} \end{cases} \quad (6.1)$$

where the indices c and v design the matrices of the two interacting objects. Taking into account the vessel deformability has a considerable impact on the computation time, given the size of matrices \mathbf{A}_v which depends on the discretization of the geometry of the vessel. Besides small deformations induced by the interactions with the interventional device, blood vessels may undergo quasi-rigid displacement due to the respiratory motion, the pulsations of the heart, which induce a periodical shift, and the interactions with adjacent internal organs. This kind of displacements may be taken into account into the model as a constant force, expressed through the term \mathbf{b}_v , mimicking the rigid movements of the vessel.

In general, under different assumptions, such deformations and motions can be neglected. Quasi-rigid motions may be ignored for small vessels far from the aorta, which is significantly impacted by the heart beat pulsing movement. In our case, no deformations nor movement were taken into account, given the experimental set-up we had available to

validate the method. Otherwise, the vessel and its behavior may be modeled through an FE approach, and its dynamics described through Eq. 6.1

Besides vessels' deformability and other occurring motions, the vessel model can be affected by errors and inaccuracies on its geometry. These errors may prevent a correct shape reconstruction, in particular with respect to the constrained state estimation, given that the vessel geometry represents a boundary condition for the catheter. As shown in Fig. 6.1, having a vessel model (red shape) that is incorrect with respect to the real geometry (blue shape), implies that the applied boundary condition is affected by a specific error. In practice, in case that the vessel model has a different configuration from the real one, the detected 2D shape of the real catheter may appear outside the projection of the vessel geometry (Fig. 6.1-(b)). Therefore, the reconstructed catheter, which bounded inside the vessel, could never match the 2D image information (appearing outside due to a misplacement of the vessel geometry, see Fig. 6.1-(c)).

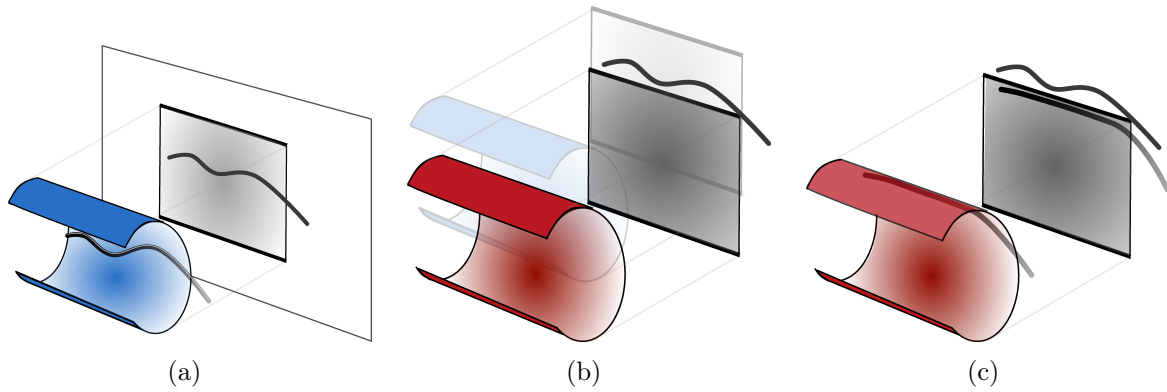


Figure 6.1: (a) Real configuration of the catheter inside the blood vessel. (b) The segmented vessel geometry does not match the current configuration of the anatomy. (c) The reconstructed catheter, bounded inside the simulated vessel, cannot fit the real 2D observations laying within the real geometry.

A Bayesian framework would allow us to take into account and compensate the existing errors and uncertainties. In particular, including the erroneous vessel geometry within the state estimation would allow us to release the surface constraint. Whereas inaccuracies on vessel deformability might be taken into account through data assimilation (i.e. augmenting the state vector with the incorrect mechanical parameters describing vessel properties), geometric errors deriving from segmentation of medical images are not so trivial to be taken into account. Indeed, a naive approach, where the nodes of the FE vessel model are included within the state vector, is faulty, due to the potential topology modifications that may occur, and computationally inefficient, due to the large number of instances that need be considered.

An efficient way to consider and compensate geometry errors, while remaining compatible with fast computations, would be to augment the state vector with the interpenetration δ_i (occurring when the constraint is violated) which is computed at the end of the *free-*

motion step (see Eq. 3.8). Perturbing these values, by generating several realizations of them (see Fig. 6.2), would be equivalent to mimicking different emplacements of the boundary surface. Besides the simplicity of the idea, the main challenge lies in an efficient implementation design, which has to be compatible with the current framework for contact resolution, along with a stochastic state vector of variable size (given that the number of occurring contacts is not constant through time).

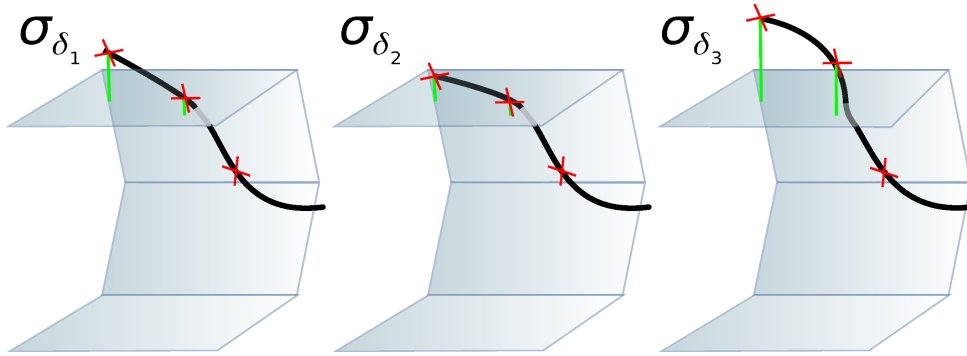


Figure 6.2: Estimating the computed interpenetrations occurring during collision response is equivalent to have different emplacements of the boundary surface, hence it allows us to take into account for potential uncertainties on it.

6.2.2 Model Input

Further improvement can be accomplished by providing a better definition of the input of the model. In this work, we assumed the interventional device to be inserted with a constant 6DoF force \mathbf{f} , applied at the bottom of the catheter.

In practice, this force is not constant. In fact, it depends on the surgical gesture of the clinician, which can variate in direction and intensity. To take into account the erroneous modeling, we included the insertion force within the state vector $\mathbf{f}_k = \mathbf{f}_{k-1} + \sigma_{\mathbf{f}_{mod}}$. A more precise approach could consist in using an external sensor providing some information about the insertion force applied at each time-step. In this context, a sensor would not modify the interventional device since it is positioned outside the patient, at the insertion valve (see Fig. 6.3-(c)).

This kind of device was used within the ER-REBOA project ¹, where the objective was to develop the physics-based models for catheter and guide-wire motion, blood flow and graphical rendering towards a novel simulator for REBOA procedures (Resuscitative Endovascular Balloon Occlusion of the Aorta). The aim was to design a device to track a catheter with translation, torque, and force feedback (see Fig. 6.3-(a)). The insertion of the catheter is obtained through a tracker composed of a sensor: ADNS-9800 Laser Motion

¹Collaboration among Inria Nancy, Harvard Medical School, Massachusetts General Hospital, CIMIT and MDSLAb. Funding Us Army. Duration 2017-2019.



Figure 6.3: (a) Set-Up of the ER-REBOA simulator. (b) Render of the external sensor for catheter insertion tracking.

Sensor and a controller: Adafruit Feather M0 WiFi - ATSAMD21 + ATWINC150. The laser sensor detects displacements of the advancing catheter and through this information, the insertion force is iteratively adapted.

6.3 Observations Process

Our proposed method solely relies on 2D features extracted and tracked from monocular fluoroscopic images. New contributions to fluoroscopic images processing were not the focus of this study. Instead, we made the initial assumption of using a catheter tagged with L radio-opaque markers. Consequently, we applied the best existing methods in literature to detect and track their projected coordinates within the fluoroscopic images. This choice allowed us to simplify the definition of the observation function h_k , which directly relates the external observations with the element of the state vector: $\mathbf{Z}_k = h_k(\mathbf{X}_k) + \boldsymbol{\nu}$. In particular, we assumed that the $\mathbf{m}_{j[j=1:L]}$ radio-opaque markers corresponded to the nodes of the FE model of the catheter $\mathbf{x}_{i[i=1:N]}$, through a known mapping \mathcal{M}_k so that, at every time-step: $\mathbf{m}_k = \mathcal{M}_k(\mathbf{x}_k)$. Given that the detected pixels coordinates $p_i = (u_i, v_i)$ are related to the corresponding 3D marker coordinates through the $[3 \times 4]$ projection matrix \mathbf{C} (such that $\mathbf{p}_i = \mathbf{C}\mathbf{m}_i$), the observation function will depend on both the mapping and the projection matrix: $h_k(\mathcal{M}_k, \mathbf{C})$.

In our case, we considered all markers as being visible within the image, and no occlusions nor detection errors were taken into account. In this case, the mapping \mathcal{M} is constant through time and well known, given the established discretization of the catheter FE model and the by-design spacing of the tagging markers on the real device.

In clinical practice, fluoroscopic images might be affected by noise and therefore be not clear. For that, even the detection of radio-opaque markers can become not trivial. In

this case, it is not possible to define a constant mapping, given that the number of observed features may change at each time step. A more practical solution, for these scenarios, would be to match the j^{th} detected 2D marker with the i^{th} closest point of the projected catheter model. In general, this binding operation might be affected by errors due to incorrect correspondences. In this case, where the tip of the catheter is always visible and the discretization of both the FE model and the radio-opaque tags, erroneous correspondences might be compensated by integrating this kind of information in the binding procedure.

In order to extend the method to a wider number of applications, where marker-less devices are used, a different observation function must be defined. In case of standard catheters or guide-wires, the extracted 2D features correspond with the projected shape of the device. In this case, one possible solution would be to parametrize the segmented curve as a B-spline function and discretize the spline in accordance with the catheter FE model discretization. Therefore, the obtained 2D landmarks could be binded with the nodes of the catheter model.

In this work, we started from the assumption that also the camera pose was constant. In practice, the view may change either due to the movement of the X-rays equipment or to displacements of the patient. Given that calibration markers are always visible during the procedure, it would be possible to correct the camera pose by including its parameters within the state vector. In [94], the authors include the camera pose within the state vector, where its motion is represented using a constant velocity model.

In general, any potential error affecting the observation function (from erroneous correspondences to the camera motion) , may be taken into account through the observations noise covariance matrix \mathbf{R} . Whenever a higher uncertainty is associated with the 2D-3D binding function, the value of \mathbf{R} can be incremented to take into account and compensate for the errors associated with it.

6.4 Computation Time

Fluoroscopic procedures are performed acquiring X-ray images at different rates of frame per second; the acquisition frequency is generally determined by the clinical requirements. Given that, the general goal of fluoroscopic procedures is to provide real-time images of moving objects (e.g., anatomic, contrast media, devices) that are the targets of the procedure at hand, typical acquisition rate values are: 7.5 frame-per-second, 15 FPS or 30 FPS.

For our method to be applicable in an operating room, the simulation must be performed in real-time. Hence, the computation time must be compatible with the fluoroscopic images acquisition rate. In general, the computation time of a numeric simulation depends on the size and the discretization of the FE models of the simulated object, as well as

the type of simulated behaviour (e.g. static, dynamic, rigid /non-rigid interactions between objects, etc.). Typically, a deterministic simulation of catheter navigation might run at 60 FPS. For our stochastic approach, computations are drastically impacted by the number of simulations performed within a single time-step. This number is related to the sigma-points propagations that must be computed in the prediction phase. For these first results, we reached an average computation time of 5 FPS, depending on the specific simulated scenario. The achievement of real-time computations was out of the scope of this first work. However, some solutions to speed up computation times are provided below. Fig. 6.4 shows an overview of the execution times of the different tasks, performed during a single time-step of a stochastic simulation. Two appears to be the most expensive tasks: within the *free motion*, the inversion of matrix \mathbf{A} to compute the free positions $\mathbf{q}^{free} = \mathbf{A}^{-1}\mathbf{b}$ (see Sec. 3.5); and within the *collision computation*, the computation of the Jacobian matrix \mathbf{J} .

Steps Duration Statistics (in ms) :									
LEVEL	START	NUM	MIN	MAX	MEAN	DEV	TOTAL	PERCENT	ID
0	0	1	502.97	502.97	502.97	0	502.97	100	TOTAL
-107	0.01	231	0	1.43	0.20	0.09	46.76	9.30	Simulation::animate
-107	0.10	231	0	0.41	0.01	0.03	2.90	0.58	KalmanFilterPrediction
-107	38.35	345	0	0.49	0.09	0.09	29.68	5.90	MechanicalVinitVisitor
-109	38.36	230	0	0.01	0	0	0.60	0.12	AnimateBeginEvent
-109	38.36	230	0	0.43	0.01	0.03	3.09	0.61	UpdatePosition
-111	38.36	115	0	0	0	0	0.26	0.05	updateInternalData
-111	38.38	115	0.09	0.14	0.09	0.01	10.70	2.13	Step2 FreeMotion
-110	38.38	115	0.09	0.14	0.09	0.01	10.44	2.08	Mechanical
-109	38.39	115	0.01	0.03	0.01	0	1.65	0.33	ComputeForce
-109	38.42	115	0.01	0.02	0.01	0	1.24	0.25	ComputeRHTerm
-109	38.44	115	0.02	0.04	0.02	0	2.71	0.54	MBKBuild
-109	38.48	115	0.03	0.04	0.03	0	3.30	0.66	MBKSolve
-109	38.51	115	0	0.01	0	0	0.42	0.08	UpdateVAndX
-111	38.55	115	3.52	3.79	3.60	0.06	413.72	82.26	Step3 ComputeCollision
-111	42.27	115	0.25	0.67	0.26	0.04	30.07	5.98	ConstraintSolver
-108	42.27	115	0.01	0.02	0.01	0	1.58	0.32	PrepareStates
-108	42.29	115	0.02	0.04	0.02	0	2.24	0.44	Accumulate Constraint
-108	42.33	115	0	0.01	0	0	0.35	0.07	Get Constraint Value
-108	42.33	115	0	0	0	0	0.28	0.06	Get Constraint Resolutions
-108	42.34	115	0.18	0.21	0.18	0.01	21.04	4.18	Get Compliance
-108	42.53	115	0	0	0	0	0.25	0.05	ConstraintsGaussSeidel
-108	42.54	115	0.01	0.02	0.01	0	1.19	0.24	Compute And Apply Motion Correction
-108	42.56	115	0.01	0.41	0.01	0.04	1.63	0.32	Store Constraint Lambdas
-112	42.59	117	0	0.01	0	0	0.54	0.11	UpdateMapping
-111	42.59	117	0	0	0	0	0.03	0	MappingVisitor - processMechanicalMapping: beamLinearMap1
-111	502.07	2	0	0	0	0	0	0	UpdateMappingEndEvent
-113	502.11	1	0.79	0.79	0.79	0	0.79	0.16	KalmanFilterCorrection
-114	502.91	1	0.01	0.01	0.01	0	0.01	0	Simulation::updateVisual
-113	502.91	1	0	0	0	0	0	0	
-113	502.91	1	0	0	0	0	0	0	
-113	502.92	1	0	0	0	0	0	0	

Figure 6.4: Computation times of single operations within a single time-step of a stochastic simulation.

Considering the structure of sigma-points, different solutions might be adopted to speed up the computation. For sake of simplicity, we will consider a 3DoFs beam composed of $N = 2$ nodes. The state vector including positions and velocities will have a size $r = 12$: $\mathbf{X}_{k-1} \in \mathbb{R}^{12}$. Therefore, $p = r + 1$ sigma-points will be generated according to: $\sigma_{jk} = \mathbf{X}_{k-1} \pm \sqrt{\mathbf{P}_{k-1}} \mathbf{I}^{(j)}$. Each sigma-point σ_j is generated so that a single element of the state vector is perturbed with respect to the initial state \mathbf{X}_{k-1} .

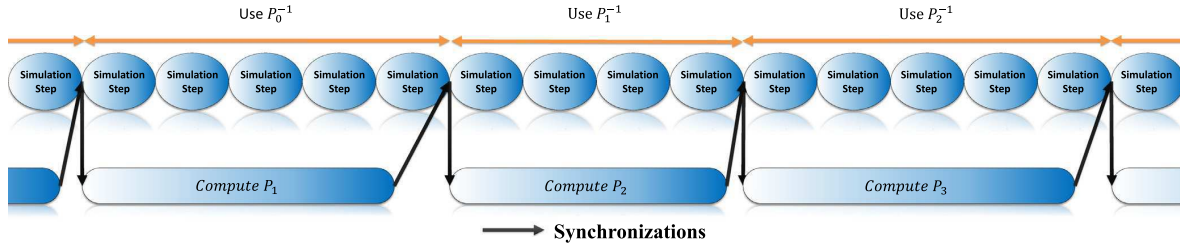
A first hardware solution would be to implement **Parallel Computing**. As the simulations performed for different sigma points are independent, they can be executed in parallel, thus accelerating the prediction phase. This approach has been adopted by [122], where they present a novel image-driven method for fast identification of boundary condi-

tions, modeled as stochastic parameters. In particular, while the deterministic simulation runs at 40 FPS, the stochastic simulation with parallelized prediction runs at 15 FPS.

Another design approach would be the **Preconditioning**. Solving Eq. 3.18 can be particularly expensive due to the inversion of the matrix \mathbf{A} . In addition, such matrix can be significantly ill-conditioned for specific scenarios (the condition number κ of a matrix, expresses the variation of the output, for a small change in the input argument). A standard solution is to use a preconditioner², which enables to rewrite the equation as:

$$\mathbf{P}^{-1}\mathbf{A}\mathbf{q} = \mathbf{P}^{-1}\mathbf{b} \quad \text{with} \quad \kappa(\mathbf{P}^{-1}\mathbf{A}) < \kappa(\mathbf{A}) \quad (6.2)$$

The more the preconditioner is similar to the source matrix, $\mathbf{P} \sim \mathbf{A}$, the most the computation of the preconditioner itself can be expensive. Assuming that \mathbf{A} undergoes small perturbations between two consecutive time steps, it is possible to presume that $\mathbf{P}_t = \mathbf{A}_t^{-1}$ might remain a good approximations for the following time-steps. Authors in [107] proposed to compute the preconditioner at low frequency, on a dedicated CPU thread, and use the last preconditioner available to advance the simulation (see Fig. 6.5). In case of a stochastic simulation, the preconditioner update frequency can be calculated according to the number of sigma-points. In practice, in the prediction phase, all the p predictions of the sigma-points σ_j are computed relying on the same \mathbf{P} .



(a) Asynchronous Preconditioning

Figure 6.5: Source [107]. The preconditioner is updated asynchronously within a dedicated CPU thread. The last preconditioner available is used to advance the simulation so that the simulation never needs to wait for the computation of the current preconditioner to be complete

After some preliminary tests carried out adopting this solution, we noticed that the computation time was not significantly improved. Indeed, as shown in Fig. 6.4, the *free motion* does not represent the most expensive computation of the simulation. The reason is that the matrix \mathbf{A} of the catheter model can be computed, or inverted, in real-time due to its BTD structure. Nevertheless, whenever considering two non-rigid interacting objects (see Eq. 6.1), such asynchronous precomputation might indeed fasten the computation time.

²a matrix \mathbf{P} is a preconditioner a matrix \mathbf{A} if the conditioning of $\mathbf{P}^{-1}\mathbf{A}$ is smaller than the conditioning of \mathbf{A} itself.

In our case, the most expensive task is represented by the Jacobian matrix computation during the collision response. Not only is this task generally costly, but with the prediction of p sigma-points, the same operation is repeated several times.

One possible solution to optimize this step would be to exploit the nature of the sigma-points. The Jacobian matrix \mathbf{J} is generally computed from the position at the beginning of the time step. Looking at all the generated sigma-points in Fig. 6.6, it is possible to notice that only a subset of the totality presents variations for the positions variables. Therefore, without any approximations or loss in accuracy, one possible solution would be to compute the Jacobian matrix only for the particles presenting actual perturbations of positions terms. (whereas for the others, we consider the one computed for the last valid positions).

x_0^*	x_0^*	x_0	x_0	x_0	x_0	x_0	x_0	x_0	x_0	x_0	x_0	x_0
y_0^*	y_0^*	y_0^*	y_0	y_0	y_0^*	y_0^*	y_0^*	y_0	y_0	y_0	y_0	y_0
z_0^*	z_0^*	z_0^*	z_0^*	z_0	z_0^*	z_0^*	z_0^*	z_0^*	z_0	z_0	z_0	z_0
x_1^*	x_1^*	x_1^*	x_1^*	x_1^*	x_1^*	x_1^*	x_1^*	x_1^*	x_1	x_1	x_1	x_1
y_1^*	y_1^*	y_1^*	y_1^*	y_1^*	y_1^*	y_1^*	y_1^*	y_1^*	y_1	y_1	y_1	y_1
z_1^*	z_1^*	z_1^*	z_1^*	z_1^*	z_1^*	z_1^*	z_1^*	z_1^*	z_1	z_1	z_1	z_1
$v_{x_0}^*$	$v_{x_0}^*$	$v_{x_0}^*$	$v_{x_0}^*$	$v_{x_0}^*$	$v_{x_0}^*$	$v_{x_0}^*$	$v_{x_0}^*$	v_{x_0}	v_{x_0}	v_{x_0}	v_{x_0}	v_{x_0}
$v_{y_0}^*$	$v_{y_0}^*$	$v_{y_0}^*$	$v_{y_0}^*$	$v_{y_0}^*$	$v_{y_0}^*$	$v_{y_0}^*$	$v_{y_0}^*$	$v_{y_0}^*$	$v_{y_0}^*$	v_{y_0}	v_{y_0}	v_{y_0}
$v_{z_0}^*$	$v_{z_0}^*$	$v_{z_0}^*$	$v_{z_0}^*$	$v_{z_0}^*$	$v_{z_0}^*$	$v_{z_0}^*$	$v_{z_0}^*$	$v_{z_0}^*$	$v_{z_0}^*$	$v_{z_0}^*$	v_{z_0}	v_{z_0}
$v_{x_1}^*$	$v_{x_1}^*$	$v_{x_1}^*$	$v_{x_1}^*$	$v_{x_1}^*$	$v_{x_1}^*$	$v_{x_1}^*$	$v_{x_1}^*$	$v_{x_1}^*$	$v_{x_1}^*$	$v_{x_1}^*$	v_{x_1}	v_{x_1}
$v_{y_1}^*$	$v_{y_1}^*$	$v_{y_1}^*$	$v_{y_1}^*$	$v_{y_1}^*$	$v_{y_1}^*$	$v_{y_1}^*$	$v_{y_1}^*$	$v_{y_1}^*$	$v_{y_1}^*$	$v_{y_1}^*$	$v_{y_1}^*$	v_{y_1}
$v_{z_1}^*$	$v_{z_1}^*$	$v_{z_1}^*$	$v_{z_1}^*$	$v_{z_1}^*$	$v_{z_1}^*$	$v_{z_1}^*$	$v_{z_1}^*$	$v_{z_1}^*$	$v_{z_1}^*$	$v_{z_1}^*$	$v_{z_1}^*$	$v_{z_1}^*$
σ_1	σ_2	σ_3	σ_4	σ_5	σ_6	σ_7	σ_8	σ_9	σ_{10}	σ_{11}	σ_{12}	σ_{13}

(a) Generated Sigma-Points Presenting Positions Perturbations

Figure 6.6:

Real-time computations were not a strict requirement within this first work, where our main objective was to define a general framework for the stochastic approach. Nevertheless, the above presented solutions, combined with further adjustments, must be taken into account in order to apply the method to a clinical context

6.5 Method Validation

Validation studies are primary to establish the reliability of a new proposed approach. In this section, we provide some considerations about the validation studies we carried

out, along with some potential improvements.

In the deterministic method presented in Chapter III, we proposed a purely geometric validation. At each time-step, we validated the reliability of the reconstructed 3D shape. Instead, with the Bayesian approach of Chapter V, we provided a further validation on the behavior of the reconstructed shape taking into account the velocity too. Nevertheless, positions and velocities are solely considered from a quantitative perspective. The validity of the applied forces, especially the computed contact forces, is not estimated. Such additional evaluations, about physical coherence of estimated values, could further strengthen the validation step.

Our studies have been mainly carried out on rigid phantoms. Further experiments must be performed onto real patient data, and eventually on in-vivo data within a intra-operative context. In this work, we carried out a series of experiences, in collaboration with IHU Strasbourg, aiming to retrieve animal data, that is useful for clinical validation. This part of the research presented several challenges. In general, animal experiences can be performed only under ethical approval of MSER (Ministre de l'Enseignement supérieur, de la Recherche et de l'Innovation). For that we submitted the Vision Project (*Validation par l'Image de Simulation Numérique*), which had as objective to collect medical images (such as MRI, CT, fluoroscopy and ultrasound) before, during and after minimally invasive surgery procedures whether percutaneous, laparoscopic or vascular. The aim was to create an anatomy image database, allowing the development and validation of numerical simulations for virtual reality in medicine. All surgical procedures were performed by surgeons who are experts in minimally invasive surgery, who know the anatomy of the animal and master the techniques of reduced suffering in animals. The approbation of our ethic protocol³ required several months and was only obtained in late 2018. In collaboration with surgeons, a strict protocol has been established to perform the procedures. The general idea behind the experiences was to perform a straightforward insertion under fluoroscopic guidance and acquire a 3D scan, at some critical points of the insertion, to be later used as comparison for the simulation. First, the animal was equipped with four devices, designed and printed by us (see Fig. 6.7-(a)), which are embedded with radio-opaque markers. These markers, both visible in fluoroscopy and under the CT scanner, allow performing the calibration of the 2D-3D system. Then, a contrast medium is injected for the surgeon to have a clear insight of the anatomy configuration and to identify the optimal path to insert the guide-wire towards the target location (see Fig. 6.7-(b)).

Performing the experiences turned out to be extremely challenging, even for expert surgeons. In particular, we noticed that performing the procedure straightforward (i.e. inserting the catheter from the insertion point to the target lesion, with no interruptions) is not practically feasible. The surgeon usually reaches the target lesion through multiple essays, which prevents from having a unique series of images for the insertion. However,

³Reference for the protocol: *APAFIS # 15433-2018060815283960*)

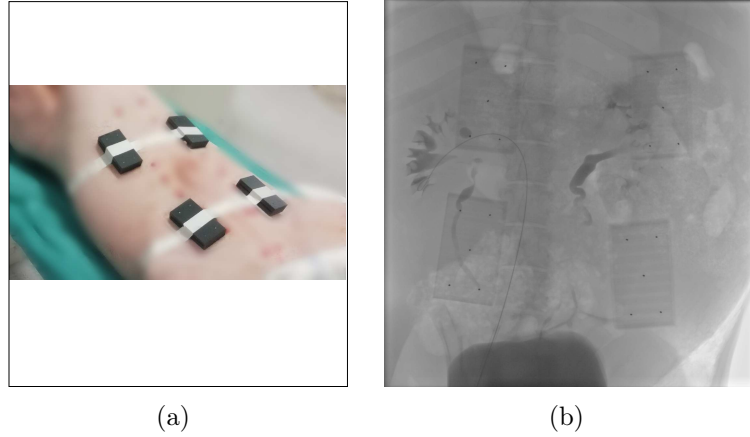


Figure 6.7: (a) The animal is embedded with calibration devices. (b) Fluoroscopic image of catheter insertion in renal artery. Both the guide-wire and the calibration markers appears visible in the image.

as long as no vascular branch needs to be accessed, it was possible to perform a straight insertion and acquire data coherent with our validation protocol. In Fig. 6.8, we show a fluoroscopic image of the catheter inserted in the aortic portion, and the relative 3D acquisition performed at the end of the insertion.

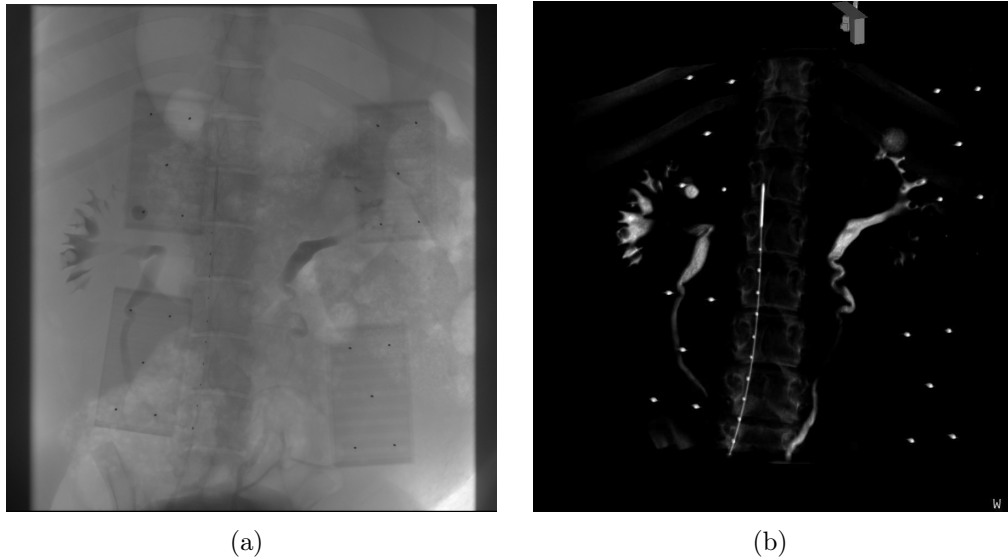


Figure 6.8: (a) Real configuration of the catheter inside the blood vessel. (b) The incorrect vessel geometry does not match the current configuration of the navigation. (c) The reconstructed catheter, enforcing the surface constraint, cannot fit the 2D observations.

The acquired data were not usable for a robust validation. A different validation protocol should be defined, like using a bi-plane system which allows recording a new series of images, providing an additional 2D validation view.

6.6 Future Applications

The research carried out within this thesis opens up different possibilities for computer-aided surgery. In particular, after overcoming the scientific challenges highlighted in the above sections, an intra-operative use of the method would be feasible, and even new applications could be defined.

Our preliminary works on data assimilation showed how estimating incorrect model parameters, enables to enhance the predictive power of the simulation. In this sense, data assimilation could open up new applications such as dose reduction.

In classic fluoroscopic, images are acquired and displayed at frame rates compatible and coherent with the temporal sensitivity and resolution of human vision. This results in X-ray emission (hence dose absorption) for every acquired image.

One possible solution to reduce the absorbed dose, would be to exploit the simulation to create virtual fluoroscopic images. The surgeon would rely on an augmented fluoroscopic guidance where two consecutive X-ray images would be interpolated by simulated ones (see Fig. 6.9). While all the images would be displayed at high frame rates, compatible with human vision, only a part of them would result in dose absorption.

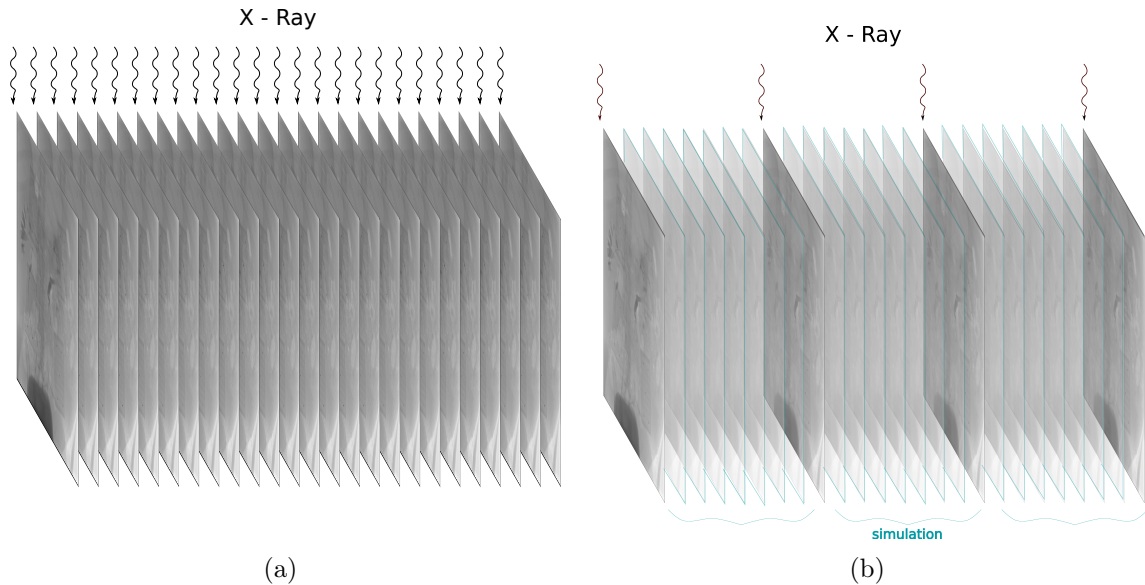


Figure 6.9: (a) Classic fluoroscopic: for every image there is emission of X-rays. (b) Augmented fluoroscopic: dose absorption is drastically reduced given that only few images are actually acquired thorough X-rays, while other are simply simulated.

Whenever a new X-ray image is available, 2D features are extracted and used to improve the predictive power and the accuracy of the simulation through state estimation and data assimilation. This way, the surgeon can rely on virtual images which are an accurate reproduction of the ongoing situation.

6.7 Conclusions

In this work, we mainly addressed the problem of monocular reconstruction of micro-devices for endovascular procedures. The core of our work was a new stochastic approach, where the physics-based simulation of the device navigation is combined with 2D image features extracted from fluoroscopic images, through an Unscented Kalman Filter. The use of such Bayesian formalism allows considering and tackling errors and uncertainties in model parameterization, and noise in external measurements (i.e. errors detection in fluoroscopic images). Also, it allows achieving accurate reconstructions in presence of non-linear phenomena such as slip and stick transitions. This kind of non-linearities could be handled by a deterministic method. Nevertheless, several scientific challenges exist to improve the method and generalize it before its use within an operative room.

We solely addressed the problem of 2D-3D catheter reconstruction, but other applicative fields are equally possible. Indeed, the same approach could be, for example, useful for robotic-assisted suture. The idea would be to use the estimated 3D reconstruction of the suture in order to control the robot, optimally computing the input controls through inverse simulations based on the estimated trajectory. In a deterministic context, a similar approach was presented by [123] for robotic needle insertion, where they calculate the robot's input commands from an optimization process based on iterative of inverse simulations needle insertion. We believe that, with appropriate development and improvements, our novel approach could bring significant benefits to several applications.

BIBLIOGRAPHY

- [1] R. Trivisonne, E. Kerrien, S. Cotin, Constrained Stochastic State Estimation of Deformable 1D Objects: Application to Single-view 3D Reconstruction of Catheters with Radio-opaque Markers, *Computerized Medical Imaging and Graphics* 81,(2020).
- [2] R. Trivisonne, E. Kerrien, S. Cotin, Augmented 3D Catheter Navigation using Constrained Shape from Template, *Hamlyn Symposium* (2017) 3–5.
- [3] R. Trivisonne, I. Peterlik, S. Cotin, H. Courtecuisse, 3D Physics-Based Registration of 2D Dynamic MRI Data, in: *MMVR - Medicine Meets Virtual Reality*, Los Angeles, United States, (2016).
- [4] Y. Adagolodjo, R. Trivisonne, N. Haouchine, S. Cotin, H. Courtecuisse, Silhouette-based pose estimation for deformable organs application to surgical augmented reality, in: *2017 IEEE/RSJ International Conference on Intelligent Robots and Systems (IROS)*, (2017), pp. 539–544.
- [5] V. S. Kashyap, S. S. Ahn, P. V. Petrik, W. S. Moore, Current training and practice of endovascular surgery: A survey, *Annals of Vascular Surgery* 15 (3) (2001) 294–305. [doi:10.1007/s100160010088](https://doi.org/10.1007/s100160010088).
- [6] D. L. Miller, Overview of contemporary interventional fluoroscopy procedures, *Health Physics* 95 (5) (2008) 638–644. [doi:10.1097/01.HP.0000326341.86359.0b](https://doi.org/10.1097/01.HP.0000326341.86359.0b).
- [7] R. Aufrichtig, X. Ping, C. W. Thomas, G. C. Gilmore, D. L. Wilson, Perceptual comparison of pulsed and continuous fluoroscopy, *Medical Physics* 21 (2) (1994) 245–256. [doi:10.1118/1.597285](https://doi.org/10.1118/1.597285).
- [8] S. Balter, Fluoroscopic Frame Rates: Not Only Dose, *American Journal of Roentgenology* 203 (3) (2014) W234–W236. [doi:10.2214/ajr.13.11041](https://doi.org/10.2214/ajr.13.11041).
- [9] C. J. Kotre, E. Guibelalde, Optimization of variable temporal averaging in digital fluoroscopy, *British Journal of Radiology* 77 (920) (2004) 675–678. [doi:10.1259/bjr/72726487](https://doi.org/10.1259/bjr/72726487).
- [10] S. Balter, R. C. Chan, T. B. a. Shope, Intravascular brachytherapy fluoroscopically guided interventions, *American Association of Physicists in Medicine*, 2002.
- [11] J. Ravenel, *The Essential Physics of Medical Imaging*, 2nd ed., *American Journal of Roentgenology* 180 (3) (2013) 596–596. [doi:10.2214/ajr.180.3.1800596](https://doi.org/10.2214/ajr.180.3.1800596).
- [12] P. Russo, *Handbook of X-ray Imaging : Physics and Technology*, Taylor & Francis

- Group, 2018.
- [13] J. S. Wambani, G. K. Korir, M. A. Tries, I. K. Korir, J. M. Sakwa, Patient radiation exposure during general fluoroscopy examinations., *Journal of applied clinical medical physics* 15 (2) (2014) 4555. [doi:10.1120/jacmp.v15i2.4555](https://doi.org/10.1120/jacmp.v15i2.4555).
 - [14] C. M. Stahl, Q. C. Meisinger, M. P. Andre, T. B. Kinney, I. G. Newton, Radiation risk to the fluoroscopy operator and staff (oct 2016). [doi:10.2214/AJR.16.16555](https://doi.org/10.2214/AJR.16.16555).
 - [15] Q. C. Meisinger, C. M. Stahl, M. P. Andre, T. B. Kinney, I. G. Newton, Radiation protection for the fluoroscopy operator and staff (oct 2016). [doi:10.2214/AJR.16.16556](https://doi.org/10.2214/AJR.16.16556).
 - [16] S. Balter, Reducing Unnecessary Radiation in Fluoroscopically Guided Interventional Procedures: Vigilance and Feedback Are Needed, *Radiology* 290 (3) (2019) 182738. [doi:10.1148/radiol.2019182738](https://doi.org/10.1148/radiol.2019182738).
 - [17] K. R. Beckett, A. K. Moriarity, J. M. Langer, Safe Use of Contrast Media: What the Radiologist Needs to Know, *RadioGraphics* 35 (6) (2015) 1738–1750. [doi:10.1148/rg.2015150033](https://doi.org/10.1148/rg.2015150033).
 - [18] P. R. DeLucia, R. D. Mather, J. A. Griswold, S. Mitra, Toward the Improvement of Image-Guided Interventions for Minimally Invasive Surgery: Three Factors That Affect Performance, *Human Factors: The Journal of the Human Factors and Ergonomics Society* 48 (1) (2006) 23–38. [doi:10.1518/001872006776412162](https://doi.org/10.1518/001872006776412162).
 - [19] A. Brost, R. Liao, N. Strobel, J. Hornegger, Respiratory motion compensation by model-based catheter tracking during EP procedures, *Medical Image Analysis* 14 (5) (2010) 695–706. [doi:10.1016/j.media.2010.05.006](https://doi.org/10.1016/j.media.2010.05.006).
 - [20] M. Hoffmann, A. Brost, C. Jakob, F. Bourier, M. Koch, K. Kurzidim, J. Hornegger, N. Strobel, Semi-Automatic Catheter Reconstruction from Two Views, in: *MICCAI*, 2012, pp. 584–591. [doi:10.1007/978-3-642-33418-4_72](https://doi.org/10.1007/978-3-642-33418-4_72).
 - [21] A. Vandini, C. Bergeles, F.-y. Lin, G.-z. Yang, Vision-Based Intraoperative Shape Sensing of Concentric Tube Robots, *International Conference on Intelligent Robots and Systems (IROS)* (2015) 2603–2610.
 - [22] A. Dore, G. Smoljkic, E. V. Poorten, M. Sette, J. V. Sloten, G. Z. Yang, Catheter navigation based on probabilistic fusion of electromagnetic tracking and physically-based simulation, in: *IEEE International Conference on Intelligent Robots and Systems*, 2012, pp. 3806–3811. [doi:10.1109/IRoS.2012.6386139](https://doi.org/10.1109/IRoS.2012.6386139).
 - [23] S. A. Baert, M. A. Viergever, W. J. Niessen, Guide-wire tracking during endovascular interventions, *IEEE Transactions on Medical Imaging* 22 (8) (2003) 965–972. [doi:10.1109/TMI.2003.815904](https://doi.org/10.1109/TMI.2003.815904).

- [24] C. Steger, Extraction of curved lines from images, in: Proceedings - International Conference on Pattern Recognition, Vol. 2, IEEE, 1996, pp. 251–255. [doi:10.1109/ICPR.1996.546827](#).
- [25] P. Wang, T. Chen, Y. Zhu, W. Zhang, S. K. Zhou, D. Comaniciu, Robust guidewire tracking in fluoroscopy, in: 2009 IEEE Computer Society Conference on Computer Vision and Pattern Recognition Workshops, CVPR Workshops 2009, Vol. 2009 IEEE, IEEE, 2009, pp. 691–698. [doi:10.1109/CVPRW.2009.5206692](#).
- [26] T. H. Heibel, B. Glocker, M. Groher, N. Paragios, N. Komodakis, N. Navab, Discrete tracking of parametrized curves, 2009 IEEE Computer Society Conference on Computer Vision and Pattern Recognition Workshops, CVPR Workshops 2009 2009 IEEE (2009) 1754–1761. [doi:10.1109/CVPRW.2009.5206714](#).
- [27] P.-L. Chang, A. Rolls, H. D. Praetere, E. V. Poorten, C. V. Riga, C. D. Bicknell, D. Stoyanov, Robust Catheter and Guidewire Tracking Using B-Spline Tube Model and Pixel-Wise Posteriors, IEEE Robotics and Automation Letters 1 (1) (2016) 303–308. [doi:10.1109/lra.2016.2517821](#).
- [28] N. Honnorat, R. Vaillant, N. Paragios, Guide-wire extraction through perceptual organization of local segments in fluoroscopic images, Lecture Notes in Computer Science (including subseries Lecture Notes in Artificial Intelligence and Lecture Notes in Bioinformatics) 6363 LNCS (PART 3) (2010) 440–448. [doi:10.1007/978-3-642-15711-0_55](#).
- [29] C. B. Baur, S. Albarqoun, S. Demirci, N. Navab, P. Fallavollita, CathNets: Detection and Single-View Depth Prediction of Catheter Electrodes, in: G. Zheng, H. Liao, P. Jannin, P. Cattin, S. Lee (Eds.), Medical Imaging and Augmented Reality. MIAR 2016., Springer, Cham, 2016, pp. 38–49. [doi:10.1007/978-3-319-43775-0_4](#).
- [30] A. Barbu, V. Athitsos, B. Georgescu, S. Boehm, P. Durlak, D. Comaniciu, Hierarchical learning of curves application to guidewire localization in fluoroscopy, in: Proceedings of the IEEE Computer Society Conference on Computer Vision and Pattern Recognition, IEEE, 2007, pp. 1–8. [doi:10.1109/CVPR.2007.383033](#).
- [31] P. Ambrosini, D. Ruijters, W. J. Niessen, A. Moelker, T. V. Walsum, Fully Automatic and Real-Time Catheter Segmentation in X-Ray Fluoroscopy, in: Medical Image Computing and Computer-Assisted Intervention – MICCAI 2013, Vol. 8150, 2017, pp. 577–585. [doi:10.1007/978-3-642-40763-5](#).
- [32] Y. Ma, R. Razavi, M. Cooklin, C. A. Rinaldi, J. Gill, K. S. Rhode, G. Gijssbers, R. J. Housden, P. Cathier, N. Gogin, M. O’Neill, Real-time x-ray fluoroscopy-based catheter detection and tracking for cardiac electrophysiology interventions, Medical Physics 40 (7) (2013) 071902. [doi:10.1118/1.4808114](#).

- [33] F. Milletari, V. Belagiannis, N. Navab, P. Fallavollita, Fully automatic catheter localization in C-arm images using ℓ_1 -sparse coding, in: *Lecture Notes in Computer Science (including subseries Lecture Notes in Artificial Intelligence and Lecture Notes in Bioinformatics)*, Vol. 8674 LNCS, Springer, Cham, 2014, pp. 570–577. [doi:10.1007/978-3-319-10470-6_71](https://doi.org/10.1007/978-3-319-10470-6_71).
- [34] S. Albarqouni, U. Konrad, L. Wang, N. Navab, S. Demirci, Single-view X-ray depth recovery: toward a novel concept for image-guided interventions, *International Journal of Computer Assisted Radiology and Surgery* 11 (6) (2016) 873–880. [doi:10.1007/s11548-016-1360-0](https://doi.org/10.1007/s11548-016-1360-0).
- [35] M. Kersten-Oertel, P. Jannin, D. L. Collins, The state of the art of visualization in mixed reality image guided surgery, *Computerized Medical Imaging and Graphics* 37 (2) (2013) 98–112. [doi:10.1016/j.compmedimag.2013.01.009](https://doi.org/10.1016/j.compmedimag.2013.01.009).
- [36] A. Sailer, M. de Haan, A. Peppelenbosch, M. Jacobs, J. Wildberger, G. Schurink, CTA with Fluoroscopy Image Fusion Guidance in Endovascular Complex Aortic Aneurysm Repair, *European Journal of Vascular and Endovascular Surgery* 47 (4) (2014) 349–356. [doi:10.1016/J.EJVS.2013.12.022](https://doi.org/10.1016/J.EJVS.2013.12.022).
- [37] D. Ruijters, B. M. ter Haar Romeny, P. Suetens, Vesselness-based 2D-3D registration of the coronary arteries, *International Journal of Computer Assisted Radiology and Surgery* 4 (4) (2009) 391–397. [doi:10.1007/s11548-009-0316-z](https://doi.org/10.1007/s11548-009-0316-z).
- [38] S. Gorges, E. Kerrien, M. Berger, Y. Troussset, J. Pescatore, R. Anxionnat, L. Picard, S. Bracard, 3D augmented fluoroscopy in interventional neuroradiology: Precision assessment and first evaluation on clinical cases, *Workshop on Augmented environments for Medical Imaging and Computer-aided Surgery-AMI-ARCS 2006* (August) (2006) 11–06.
- [39] W. Ahmad, H. C. Hasselmann, N. Galas, P. Majd, S. Brunkwall, J. S. Brunkwall, Image fusion using the two-dimensional-three-dimensional registration method helps reduce contrast medium volume, fluoroscopy time, and procedure time in hybrid thoracic endovascular aortic repairs, *Journal of Vascular Surgery* 69 (4) (2018) 1–8. [doi:10.1016/j.jvs.2018.07.043](https://doi.org/10.1016/j.jvs.2018.07.043).
- [40] A. Rougée, C. Picard, C. Ponchut, Y. Troussset, Geometrical calibration of x-ray imaging chains for three-dimensional reconstruction, *Computerized Medical Imaging and Graphics* 17 (4-5) (1993) 295–300. [doi:10.1016/0895-6111\(93\)90020-N](https://doi.org/10.1016/0895-6111(93)90020-N).
- [41] S. Gorges, E. Kerrien, M.-O. Berger, Y. Troussset, J. Pescatore, R. Anxionnat, L. Picard, An effective technique for calibrating the intrinsic parameters of a vascular C-arm from a planar target, in: K. R. Cleary, R. L. Galloway, Jr. (Eds.), *Medical Imaging 2006: Visualization, Image-Guided Procedures, and Display*, Vol. 6141, International Society for Optics and Photonics, 2006, p. 61411W. [doi:10.1117/](https://doi.org/10.1117/)

12.652118.

- [42] P. Markelj, D. Tomaževič, B. Likar, F. Pernuš, A review of 3D/2D registration methods for image-guided interventions, *Medical Image Analysis* 16 (3) (2012) 642–661. doi:[10.1016/j.media.2010.03.005](https://doi.org/10.1016/j.media.2010.03.005).
- [43] M. Groher, D. Zikic, N. Navab, Deformable 2D-3D registration of vascular structures in a one view scenario, *IEEE Transactions on Medical Imaging* 28 (6) (2009) 847–860. doi:[10.1109/TMI.2008.2011519](https://doi.org/10.1109/TMI.2008.2011519).
- [44] N. Baka, C. T. Metz, C. J. Schultz, R. J. Van Geuns, W. J. Niessen, T. Van Walsum, Oriented Gaussian mixture models for nonrigid 2D/3D coronary artery registration, *IEEE Transactions on Medical Imaging* 33 (5) (2014) 1023–1034. doi:[10.1109/TMI.2014.2300117](https://doi.org/10.1109/TMI.2014.2300117).
- [45] G. Turini, S. Condino, M. Postorino, Augmented Reality, Virtual Reality, and Computer Graphics, *Journal of Vascular Surgery* 2 (2018) 82–91. doi:[10.1177/019263656304728122](https://doi.org/10.1177/019263656304728122).
- [46] P. Ambrosini, D. Ruijters, W. J. Niessen, A. Moelker, T. van Walsum, Continuous roadmapping in liver TACE procedures using 2D–3D catheter-based registration, *International Journal of Computer Assisted Radiology and Surgery* 10 (9) (2015) 1357–1370. doi:[10.1007/s11548-015-1218-x](https://doi.org/10.1007/s11548-015-1218-x).
- [47] J. Lenoir, P. Meseure, L. Grisoni, SURGICAL THREAD SIMULATION, in: *ESAIM: Control, Optimisation and Calculus of Variations*, Vol. 12, 2003, pp. 102–107.
- [48] S. Baert, E. van de Kraats, T. van Walsum, M. Viergever, W. Niessen, Three-dimensional guide-wire reconstruction from biplane image sequences for integrated display in 3-d vasculature, *IEEE Transactions on Medical Imaging* 22 (10) (2003) 1252–1258. doi:[10.1109/TMI.2003.817791](https://doi.org/10.1109/TMI.2003.817791).
- [49] M. Schenderlein, S. Stierlin, R. Manzke, V. Rasche, K. Dietmayer, Catheter tracking in asynchronous biplane fluoroscopy images by 3D B-snakes, *Medical Imaging 2010: Visualization, Image-Guided Procedures, and Modeling* 7625 (2010) 76251U. doi:[10.1117/12.844158](https://doi.org/10.1117/12.844158).
- [50] C. Delmas, M.-O. Berger, E. Kerrien, C. Riddell, Y. Troussel, R. Anxionnat, S. Bracard, Three-dimensional curvilinear device reconstruction from two fluoroscopic views, *Medical Imaging 2015: Image-Guided Procedures, Robotic Interventions, and Modeling* 9415 (2015) 94150F. doi:[10.1117/12.2081885](https://doi.org/10.1117/12.2081885).
- [51] C. Shi, S. Giannarou, S. L. Lee, G. Z. Yang, Simultaneous catheter and environment modeling for Trans-catheter Aortic Valve Implantation (sep 2014). doi:[10.1109/IRO5.2014.6942832](https://doi.org/10.1109/IRO5.2014.6942832).

- [52] P. T. Tran, P.-L. Chang, H. De Praetere, J. Maes, D. Reynaerts, J. V. Sloten, D. Stoyanov, E. V. Poorten, 3D Catheter Shape Reconstruction Using Electromagnetic and Image Sensors, *Journal of Medical Robotics Research* 02 (03) (2017) 1740009. doi:[10.1142/S2424905X17400098](https://doi.org/10.1142/S2424905X17400098).
- [53] T. Van Walsum, S. A. Baert, W. J. Niessen, Guide wire reconstruction and visualization in 3DRA using monoplane fluoroscopic imaging, *IEEE Transactions on Medical Imaging* 24 (5) (2005) 612–623. doi:[10.1109/TMI.2005.844073](https://doi.org/10.1109/TMI.2005.844073).
- [54] M. Brückner, F. Deinzer, J. Denzler, Temporal estimation of the 3d guide-wire position using 2d X-ray images, *Lecture Notes in Computer Science (including subseries Lecture Notes in Artificial Intelligence and Lecture Notes in Bioinformatics)* 5761 LNCS (PART 1) (2009) 386–393. doi:[10.1007/978-3-642-04268-3_48](https://doi.org/10.1007/978-3-642-04268-3_48).
- [55] M. K. Konings, E. B. van de Kraats, T. Alderliesten, W. J. Niessen, Analytical guide wire motion algorithm for simulation of endovascular interventions, *Medical and Biological Engineering and Computing* 41 (6) (2003) 689–700. doi:[10.1007/BF02349977](https://doi.org/10.1007/BF02349977).
- [56] K. Ikuta, K. Iritani, J. Fukuyama, Mobile virtual endoscope system with haptic and visual information for non-invasive inspection training, *Proceedings 2001 ICRA. IEEE International Conference on Robotics and Automation (Cat. No.01CH37164)* 2 (2002) 2037–2044. doi:[10.1109/robot.2001.932907](https://doi.org/10.1109/robot.2001.932907).
- [57] M. Kukuk, B. Geiger, A Real-Time Deformable Model for Flexible Instruments Inserted into Tubular Structures, in: *MICCAI, 2002*, pp. 331–338. doi:[10.1007/3-540-45787-9_42](https://doi.org/10.1007/3-540-45787-9_42).
- [58] S. L. Dawson, S. Cotin, D. Meglan, D. W. Shaffer, M. A. Ferrell, Designing a computer based simulator for interventional cardiology training (dec 2002).
- [59] T. Alderliesten, M. K. Konings, W. J. Niessen, Modeling friction, intrinsic curvature, and rotation of guide wires for simulation of minimally invasive vascular interventions, *IEEE Transactions on Biomedical Engineering* 54 (1) (2007) 29–38. doi:[10.1109/TBME.2006.886659](https://doi.org/10.1109/TBME.2006.886659).
- [60] V. Luboz, R. Blazewski, D. Gould, F. Bello, Real-time guidewire simulation in complex vascular models, in: *Visual Computer*, Vol. 25, Springer-Verlag, 2009, pp. 827–834. doi:[10.1007/s00371-009-0312-x](https://doi.org/10.1007/s00371-009-0312-x).
- [61] P. Chiang, Y. Cai, K. H. Mak, E. M. Soe, C. K. Chui, J. Zheng, A geometric approach to the modeling of the catheterheart interaction for VR simulation of intracardiac intervention, *Computers and Graphics (Pergamon)* 35 (5) (2011) 1013–1022. doi:[10.1016/j.cag.2011.07.007](https://doi.org/10.1016/j.cag.2011.07.007).
- [62] H. Wang, J. Wu, M. Wei, X. Ma, A robust and fast approach to simulating the

- behavior of guidewire in vascular interventional radiology, *Computerized Medical Imaging and Graphics* 40 (2015) 160–169. doi:[10.1016/j.compmedimag.2014.10.006](https://doi.org/10.1016/j.compmedimag.2014.10.006).
- [63] J. Burgner-Kahrs, D. C. Rucker, Howie Choset, Continuum Robots for Medical Applications: A Survey, *IEEE TRANSACTIONS ON ROBOTICS* (2015) 111–140doi:[10.1109/TR0.2015.2489500](https://doi.org/10.1109/TR0.2015.2489500).
- [64] D. K. Pai, STRANDS: Interactive simulation of thin solids using cosserat models, *Computer Graphics Forum* 21 (3) (2002) 347–352. doi:[10.1111/1467-8659.00594](https://doi.org/10.1111/1467-8659.00594).
- [65] J. Spillmann, M. Teschner, CORDE : cosserat rod elements for the dynamic simulation of one-dimensional elastic objects, *Eurographics Symposium on Computer Animation* (2007) 1–10.
- [66] W. Tang, T. R. Wan, D. A. Gould, T. How, N. W. John, A stable and real-time nonlinear elastic approach to simulating guidewire and catheter insertions based on cosserat rod, *IEEE Transactions on Biomedical Engineering* 59 (8) (2012) 2211–2218. doi:[10.1109/TBME.2012.2199319](https://doi.org/10.1109/TBME.2012.2199319).
- [67] I. Tunay, Distributed parameter statics of magnetic catheters, *Proceedings of the Annual International Conference of the IEEE Engineering in Medicine and Biology Society, EMBS* (2011) 8344–8347doi:[10.1109/IEMBS.2011.6092058](https://doi.org/10.1109/IEMBS.2011.6092058).
- [68] C. Duriez, S. Cotin, J. Lenoir, P. Neumann, S. Dawson, C. Duriez, J. Lenoir, P. Neumann, S. Dawson, New Approaches to Catheter Navigation for, *Heart* 11 (2) (2005) 534–542.
- [69] J. Lenoir, S. Cotin, C. Duriez, P. Neumann, Interactive physically-based simulation of catheter and guidewire, *Computers and Graphics (Pergamon)* 30 (3) (2006) 416–422. doi:[10.1016/j.cag.2006.02.013](https://doi.org/10.1016/j.cag.2006.02.013).
- [70] J. Dequidt, M. Marchal, C. Duriez, E. Kerien, S. Cotin, Interactive simulation of embolization coils: Modeling and experimental validation, in: *Lecture Notes in Computer Science (including subseries Lecture Notes in Artificial Intelligence and Lecture Notes in Bioinformatics)*, Vol. 5241 LNCS, Springer, Berlin, Heidelberg, 2008, pp. 695–702. doi:[10.1007/978-3-540-85988-8_83](https://doi.org/10.1007/978-3-540-85988-8_83).
- [71] Y. Ganji, F. Janabi-Sharifi, Catheter kinematics for intracardiac navigation., *IEEE transactions on bio-medical engineering* 56 (3) (2009) 621–32. doi:[10.1109/TBME.2009.2013134](https://doi.org/10.1109/TBME.2009.2013134).
- [72] M. Khoshnam, M. Azizian, R. V. Patel, Modeling of a steerable catheter based on beam theory, *Proceedings - IEEE International Conference on Robotics and Automation* (2012) 4681–4686doi:[10.1109/ICRA.2012.6224784](https://doi.org/10.1109/ICRA.2012.6224784).
- [73] H. J. Bender, R. Männer, C. Poliwoda, S. Roth, M. Walz, R. Männer, C. Poliwoda,

- S. Roth, Reconstruction of 3D Catheter Paths from 2D X-ray Projections, in: MIC-CAI, Springer, Berlin, Heidelberg, 1999, pp. 981–989. [doi:10.1007/10704282_107](https://doi.org/10.1007/10704282_107).
- [74] T. Petković, S. Lončarić, T. Devčić, R. Homan, Non-iterative Guidewire Reconstruction From Multiple Projective Views (2011).
- [75] C. Delmas, C. Delmas, R. De, C. Delmas, C. Riddell, Reconstruction 3D de micro-outils curvilignes en neuroradiologie interventionnelle par, Ph.D. thesis, Université de Lorraine (Nancy) (2017).
- [76] V. Bismuth, Image processing algorithms for the visualization of interventional devices in X-ray fluoroscopy Image processing algorithms for the visualization of interventional devices in X-ray fluoroscopy par, Ph.D. thesis, Université Paris-Est (2013).
- [77] J. Esthappan, K. R. Hoffmann, Estimation of catheter orientations from single—plane x-ray images, in: Proceedings of SPIE - The International Society for Optical Engineering, Vol. 3976, SPIE Press, 2000, pp. 28–36. [doi:10.1117/12.383047](https://doi.org/10.1117/12.383047).
- [78] T. Petković, R. Homan, S. Lončarić, Real-time 3D position reconstruction of guidewire for monoplane X-ray, Computerized Medical Imaging and Graphics 38 (3) (2014) 211–223. [doi:10.1016/j.compmedimag.2013.12.006](https://doi.org/10.1016/j.compmedimag.2013.12.006).
- [79] P. Ambrosini, I. Smal, D. Ruijters, W. J. Niessen, A. Moelker, T. Van Walsum, A Hidden Markov Model for 3D Catheter Tip Tracking with 2D X-ray Catheterization Sequence and 3D Rotational Angiography, IEEE Transactions on Medical Imaging 36 (3) (2017) 757–768. [doi:10.1109/TMI.2016.2625811](https://doi.org/10.1109/TMI.2016.2625811).
- [80] N. Robert, G. G. Polack, B. Sethi, J. A. Rowlands, E. Crystal, 3D localization of electrophysiology catheters from a single x-ray cone-beam projection, Medical Physics [doi:10.1118/1.4931452](https://doi.org/10.1118/1.4931452).
- [81] E. J. Lobaton, J. Fu, L. G. Torres, R. Alterovitz, Continuous shape estimation of continuum robots using X-ray images, Proceedings - IEEE International Conference on Robotics and Automation (2013) 725–732 [doi:10.1109/ICRA.2013.6630653](https://doi.org/10.1109/ICRA.2013.6630653).
- [82] A. Vandini, S. Giannarou, S. L. Lee, G. Z. Yang, 3D robotic catheter shape reconstruction and localisation using appearance priors and adaptive C-arm positioning, Lecture Notes in Computer Science (including subseries Lecture Notes in Artificial Intelligence and Lecture Notes in Bioinformatics) 8090 LNCS (2013) 172–181. [doi:10.1007/978-3-642-40843-4_19](https://doi.org/10.1007/978-3-642-40843-4_19).
- [83] C. Papalazarou, P. M. J. Rongen, P. H. N. de With, 3D catheter reconstruction using non-rigid structure-from-motion and robotics modeling, Medical Imaging 2012: Image-Guided Procedures, Robotic Interventions, and Modeling 8316 (2012) 831620. [doi:10.1117/12.911046](https://doi.org/10.1117/12.911046).

- [84] M. S. Heiden, K. R. Henken, L. K. Chen, B. G. van den Bosch, R. van den Braber, J. Dankelman, J. van den Dobbelsteen, Accurate and efficient fiber optical shape sensor for MRI compatible minimally invasive instruments, in: *Optical Systems Design 2012*, Vol. 8550, 2012, p. 85500L. [doi:10.1117/12.981141](https://doi.org/10.1117/12.981141).
- [85] R. J. Roesthuis, M. Kemp, J. J. Van Den Dobbelsteen, S. Misra, Three-dimensional needle shape reconstruction using an array of fiber bragg grating sensors, *IEEE/ASME Transactions on Mechatronics* 19 (4) (2014) 1115–1126. [doi:10.1109/TMECH.2013.2269836](https://doi.org/10.1109/TMECH.2013.2269836).
- [86] F. Parent, S. Loranger, K. K. Mandal, V. L. Iezzi, J. Lapointe, J.-S. Boisvert, M. D. Baiad, S. Kadoury, R. Kashyap, Enhancement of accuracy in shape sensing of surgical needles using optical frequency domain reflectometry in optical fibers, *Biomedical Optics Express* 8 (4) (2017) 2210. [doi:10.1364/boe.8.002210](https://doi.org/10.1364/boe.8.002210).
- [87] A. M. Franz, T. Haidegger, W. Birkfellner, K. Cleary, T. M. Peters, L. Maier-Hein, Electromagnetic tracking in medicine -A review of technology, validation, and applications, *IEEE Transactions on Medical Imaging* 33 (8) (2014) 1702–1725. [doi:10.1109/TMI.2014.2321777](https://doi.org/10.1109/TMI.2014.2321777).
- [88] R. Xu, A. Yurkewich, R. V. Patel, Curvature, Torsion, and Force Sensing in Continuum Robots Using Helically Wrapped FBG Sensors, *IEEE Robotics and Automation Letters* 1 (2) (2016) 1052–1059. [doi:10.1109/lra.2016.2530867](https://doi.org/10.1109/lra.2016.2530867).
- [89] Z. Yaniv, E. Wilson, D. Lindisch, K. Cleary, Electromagnetic tracking in the clinical environment., *Medical physics* 36 (3) (2009) 876–92.
- [90] S. Condino, V. Ferrari, C. Freschi, A. Alberti, R. Berchiolli, F. Mosca, M. Ferrari, Electromagnetic navigation platform for endovascular surgery: How to develop sensorized catheters and guidewires, *International Journal of Medical Robotics and Computer Assisted Surgery* 8 (3) (2012) 300–310. [doi:10.1002/rcs.1417](https://doi.org/10.1002/rcs.1417).
- [91] A. Schwein, B. Kramer, P. Chinnadurai, S. Walker, M. O'Malley, A. Lumsden, J. Bismuth, Flexible robotics with electromagnetic tracking improves safety and efficiency during in vitro endovascular navigation, *Journal of Vascular Surgery* 65 (2) (2017) 530–537. [doi:10.1016/j.jvs.2016.01.045](https://doi.org/10.1016/j.jvs.2016.01.045).
- [92] A. Malti, R. Hartley, A. Bartoli, J. H. Kim, Monocular template-based 3d reconstruction of extensible surfaces with local linear elasticity, *Proceedings of the IEEE Computer Society Conference on Computer Vision and Pattern Recognition* (2013) 1522–1529. [doi:10.1109/CVPR.2013.200](https://doi.org/10.1109/CVPR.2013.200).
- [93] N. Haouchine, J. Dequidt, M. O. Berger, S. Cotin, Monocular 3D Reconstruction and Augmentation of Elastic Surfaces with Self-Occlusion Handling, *IEEE Transactions on Visualization and Computer Graphics* 21 (12) (2015) 1363–1376. [doi:10.1109/TVCG.2015.2452905](https://doi.org/10.1109/TVCG.2015.2452905).

- [94] A. Agudo, F. Moreno-Noguer, B. Calvo, J. M. Montiel, Real-time 3D reconstruction of non-rigid shapes with a single moving camera, *Computer Vision and Image Understanding* 153 (2016) 37–54. doi:10.1016/j.cviu.2016.05.004.
- [95] S. J. Julier, J. K. Uhlmann, New extension of the Kalman filter to nonlinear systems, in: *Int. Symp. Aerospace/Defense Sensing, Simul. and Controls*, 1997, pp. 182–193.
- [96] C. Duriez, S. Cotin, J. Lenoir, P. Neumann, New approaches to catheter navigation for interventional radiology simulation, *Computer Aided Surgery* 11 (6) (2006) 300–308. doi:10.1080/10929080601090623.
- [97] J. S. Przemieniecki, *Theory of matrix structural analysis*, Vol. 10, McGraw-Hill, 2003. doi:10.1016/0022-460x(69)90212-0.
- [98] S. Cotin, H. Delingette, N. Ayache, Real-time elastic deformations of soft tissues for surgery simulation, *IEEE Transactions on Visualization and Computer Graphics* 5 (1) (1999) 62–73. doi:10.1109/2945.764872.
- [99] D. L. James, D. K. Pai, ArtDefo Accurate Real Time Deformable Objects, in: *26th International Conference on Computer Graphics and Interactive Techniques, Proceedings of SIGGRAPH*, 1999, pp. 65–72.
- [100] W. L. Nowinski, C. K. Chui, Simulation of interventional neuroradiology procedures, in: *Proceedings - International Workshop on Medical Imaging and Augmented Reality, MIAR 2001*, IEEE Computer. Soc, 2001, pp. 87–94. doi:10.1109/MIAR.2001.930269.
- [101] S. Marchesseau, T. Heimann, S. Chatelin, R. Willinger, H. Delingette, Multiplicative Jacobian energy decomposition method for fast porous visco-hyperelastic soft tissue model, in: *Lecture Notes in Computer Science (including subseries Lecture Notes in Artificial Intelligence and Lecture Notes in Bioinformatics)*, Vol. 6361 LNCS, 2010, pp. 235–242. doi:10.1007/978-3-642-15705-9_29.
- [102] C. Felippa, A systematic approach to the element-independent corotational dynamics of finite elements, *Tech. Rep.* January, University of Colorado (2000).
- [103] M. Matthias, G. Markus, Interactive Virtual Materials, in: *Proceedings of Graphics Interface 2004*, Canadian Human-Computer Communications Society, 2004, p. 239–246.
- [104] M. Nesme, Y. Payan, F. Faure, Efficient, physically plausible finite elements (Corotational FEM - suppl. reference), in: *Eurographics Symposium on Computer Animation*, 2005, pp. 2–5.
- [105] C. Duriez, C. Guébert, M. Marchal, S. Cotin, L. Grisoni, Interactive simulation of flexible needle insertions based on constraint models, in: *Lecture Notes in Computer Science (including subseries Lecture Notes in Artificial Intelligence and Lecture*

- Notes in Bioinformatics), Vol. 5762 LNCS, Springer, Berlin, Heidelberg, 2009, pp. 291–299. [doi:10.1007/978-3-642-04271-3_36](https://doi.org/10.1007/978-3-642-04271-3_36).
- [106] C. Duriez, F. Dubois, A. Kheddar, C. Andriot, Realistic haptic rendering of interacting deformable objects in virtual environments, *IEEE Transactions on Visualization and Computer Graphics* 12 (1) (2006) 36–47. [doi:10.1109/TVCG.2006.13](https://doi.org/10.1109/TVCG.2006.13).
- [107] H. Courtecuisse, J. Allard, P. Kerfriden, S. P. Bordas, S. Cotin, C. Duriez, Real-time simulation of contact and cutting of heterogeneous soft-tissues, *Medical Image Analysis* 18 (2) (2014) 394–410. [doi:10.1016/j.media.2013.11.001](https://doi.org/10.1016/j.media.2013.11.001).
- [108] D. Baraff, A. Witkin, Large steps in cloth simulation, *Proceedings of the 25th annual conference on Computer graphics and interactive techniques - SIGGRAPH '98* (1998) 43–54. [doi:10.1145/280814.280821](https://doi.org/10.1145/280814.280821).
- [109] O. D. Faugeras, G. Toscani, The Calibration Problem for Stereoscopic Vision, in: *Sensor Devices and Systems for Robotics*, Springer Berlin Heidelberg, Berlin, Heidelberg, 1989, pp. 195–213. [doi:10.1007/978-3-642-74567-6_15](https://doi.org/10.1007/978-3-642-74567-6_15).
- [110] R. I. Hartley, A. Zisserman, *Multiple View Geometry in Computer Vision*, 2nd Edition, Cambridge University Press, ISBN: 0521540518, 2004.
- [111] M. Sanz-Lopez, J. Dequidt, E. Kerrien, C. Duriez, M.-O. Berger, S. Cotin, Testbed for assessing the accuracy of interventional radiology simulations, in: *ISBMS - 6th International Symposium on Biomedical Simulation*, LNCS, Springer, Strasbourg, France, 2014, pp. 155–159.
- [112] R. Van Der Merwe, A. Doucet, N. De Freitas, E. Wan, The unscented particle filter, *Advances in Neural Information Processing Systems*, (2001).
- [113] A. Agudo, F. Moreno-Noguer, B. Calvo, J. M. Montiel, Sequential Non-Rigid Structure from Motion Using Physical Priors, *IEEE Transactions on Pattern Analysis and Machine Intelligence* 38 (5) (2016) 979–994. [doi:10.1109/TPAMI.2015.2469293](https://doi.org/10.1109/TPAMI.2015.2469293).
- [114] B. Ristic, S. Arulampalam, N. Gordon, Beyond the kalman filter, *IEEE Aerospace and Electronics Systems Magazine* 19 (2004) 37–38.
- [115] R. E. Kalman, A new approach to linear filtering and prediction problems, *Journal of basic Engineering* 82 (1) (1960) 35–45.
- [116] R. Brown, P. Hwang, *Introduction to Random Signals and Applied Kalman Filtering with MatLab Exercises Fourth Edition*, Wiley, 2011.
- [117] P. Moireau, D. Chapelle, Reduced-order Unscented Kalman Filtering with application to parameter identification in large-dimensional systems, *ESAIM: Control, Optimisation and Calculus of Variations* 17 (2) (2011) 380–405. [doi:10.1051/cocv/2010006](https://doi.org/10.1051/cocv/2010006).

- [118] S. E. Cohn, An introduction to estimation theory, *Journal of the Meteorological Society of Japan* 75 (1 B) (1997) 257–288. [doi:10.2151/jmsj1965.75.1B_257](https://doi.org/10.2151/jmsj1965.75.1B_257).
- [119] F. Bouttier, P. Courtier, Data assimilation concepts and methods, *Meteorological Training Course Lecture Series* 4 (3) (1999) 80–81.
- [120] R. Kandepu, L. Imsland, B. A. Foss, Constrained state estimation using the unscented kalman filter, *2008 Mediterranean Conference on Control and Automation - Conference Proceedings, MED’08* (2008) 1453–1458.
- [121] K. Takashima, R. Shimomura, T. Kitou, H. Terada, K. Yoshinaka, K. Ikeuchi, Contact and friction between catheter and blood vessel, *Tribology International* 40 (2) (2007) 319–328.
- [122] I. Peterlik, N. Haouchine, L. Ručka, S. Cotin, Image-driven Stochastic Identification of Boundary Conditions for Predictive Simulation, in: *20th International Conference on Medical Image Computing and Computer Assisted Intervention*, Québec, Canada, 2017.
- [123] Y. Adagolodjo, Coupling rObotics aNd mEdical simulations for automatiC percutaneous procedures (CONNECT), Theses, Université de Strasbourg (Sep. 2018).

List of Figures

1.1	Fluoroscopic C-arm acquisition system	5
1.2	Outline of typical endovascular procedures	6
1.3	Examples of endovascular procedures	7
1.4	Catheter Design	8
1.5	C-arm Fluoroscopic Equipment	9
1.6	Fluoroscopic imaging modes	11
1.7	Fluoroscopic image porcine abdomen.	12
2.1	Examples of Device Segmentation in X-ray Images	20
2.2	Static 3D Model Registration	21
2.3	Enhanced Fluoroscopic Image	22
2.4	Interventional Device Model (1)	24
2.5	Interventional Device Model (2)	25
2.6	Interventional Device Model (3)	26
2.7	Scheme of Bi-plane Reconstruction	27
2.8	2D-3D Reconstruction of Curves	29

2.9	Interventional Device Extraction in Fluoroscopic Images	29
2.10	Examples of Monocular Reconstruction (1)	30
2.11	Examples of Monocular Reconstruction (2)	31
2.12	Advanced Navigation Model	32
2.13	External Sensors	34
2.14	FOS-based Sensing	35
2.15	EM Tracking	36
3.1	Beam FE Model	48
3.2	Holonomic Constraints	50
3.3	Object Interactions	52
3.4	Free Motion	54
3.5	Normals Identification	55
3.6	Constraint Resolution	56
3.7	Projective Constraint	59
3.8	Entry Constraint	60
3.9	Projective Views of Synthetic Data Set	63
3.10	Overview Synthetic Experiments Surface Constraint	64
3.11	Synthetic Experiments Surface Constraint - Case 1	65
3.12	Synthetic Experiments Overview - Case 2	65
3.13	Synthetic Experiments Surface Constraint - Case 2	66
3.14	Synthetic Experiments Overview - Case 3	66
3.15	Synthetic Experiments Surface Constraint - Case 3	67
3.16	Overview Synthetic Experiments Entry Constraint	68
3.17	Synthetic Experiments Entry Constraint - Case 1	69
3.18	Entry Constraint with Side Observations	69
3.19	Synthetic Experiments Surface Constraint - Case 2	70
3.20	Error on Entry Constraint	70
3.21	Synthetic Experiments Surface Constraint - Case 3	70
3.22	Real Data Validation Views	71
3.23	Real Data Experiments Surface Constraint	73
3.24	Qualitative Evaluation Real Data	73
3.25	Qualitative Evaluation Real Data	74
3.26	Calibration Markers on Rigid Phantom	75
3.27	Fluoroscopic Images Processing	76
3.28	Real Data Experiments Entry Constraint	77
3.29	Real Data Augmented View	78
4.1	Unscented Transform	86
4.2	State Vector Study: Acceleration Uncertainty	89
4.3	State Vector: 3DoFs point $\mathbf{X}=[\mathbf{x},\mathbf{v}]$	91
4.4	State Vector: 3DoFs point $\mathbf{X}=[\mathbf{x}]$	92

4.5	State Vector: 3DoFs point $\mathbf{X}=[\mathbf{x}]$ (2)	93
4.6	State Vector: 3DoFs point $\mathbf{X}=[\mathbf{v}]$	94
4.7	State Vector: 3DoFs point $\mathbf{X}=[\mathbf{x}, \mathbf{v}, \mathbf{c}]$	97
4.8	State Vector: 3DoFs point $\mathbf{X}=[\mathbf{x}, \mathbf{c}]$	97
4.9	3DoFs Beam Dynamics	98
4.10	State Vector: 3DoFs beam $\mathbf{X}=[\mathbf{x}, \mathbf{v}]$	99
4.11	State Vector: 3DoFs beam $\mathbf{X}=[\mathbf{x}]$	100
4.12	State Vector: 3DoFs beam $\mathbf{X}=[\mathbf{x}, \mathbf{v}]$ Orientation Estimation	101
4.13	3D Beam Augmented State	101
4.14	3D Beam Augmented State. Parameter Estimation	102
4.15	State Vector: 3DoFs beam with 2D observations	103
4.16	State Vector: 3DoFs beam $\mathbf{X}=[\mathbf{x}, \mathbf{v}]$ and 2D observations	104
4.17	State Vector: 3DoFs beam $\mathbf{X}=[\mathbf{x}, \mathbf{v}, \mathbf{c}]$ and 2D observations	104
4.18	State Vector: 3DoFs beam $\mathbf{X}=[\mathbf{x}, \mathbf{v}, \mathbf{c}]$ and 2D observations (2)	105
4.19	Beam FE Model Validation	106
4.20	Beam FE Model Discretization	107
5.1	Computation Overview	117
5.2	Constrained State Estimation	117
5.3	Standard Deviation of Tip Position	118
5.4	Observations Views	120
5.5	Filter Parameters Tuning	121
5.6	Sensitivity to Model Uncertainty	123
5.7	Synthetic Experiments Case 1	125
5.8	Synthetic Experiments Case 2	126
5.9	Synthetic Experiments Case 3	126
5.10	Synthetic Experiments Case 3-(2)	127
5.11	Projective View for Synthetic Vessel Geometry	128
5.12	Evaluation Metrics for Synthetic Vessel Geometry	129
5.13	Evaluation Metrics for $\mathbf{f}_1=0.8\text{e-}03$ N/timeStep	130
5.14	Evaluation Metrics for $\mathbf{f}_2=2.5\text{e-}03$ N/timeStep	131
5.15	Qualitative Validation Real Data	132
5.16	Number of Observed Markers	133
5.17	Evaluation Metrics for Different Numbers of Observed Markers	133
5.18	Validation view using 6 observations and 6 nodes	134
5.19	Validation view using 3 observations and 3 nodes	134
6.1	Error on Vessel Geometry	142
6.2	Sigma Points on Computed Interpenetrations	143
6.3	REBOA Force Sensor	144
6.4	Simulation Timer Export	146
6.5	Asynchronous Preconditioning	147

6.6	Generated Sigma-Points Presenting Positions Perturbations	148
6.7	Animal Validation Image Data (1)	150
6.8	Animal Validation Image Data (2)	150
6.9	Perspective Applications: Dose Reduction through Data Assimilation . . .	151

Résumé :

La chirurgie assistée par ordinateur (ou CAO) regroupe tous les types de procédures médicales planifiées ou réalisées avec le soutien des technologies informatiques.

Le travail de cette thèse se déploie dans ce contexte, en particulier autour de la chirurgie endovasculaire mini-invasive, où l'objectif principal est d'améliorer, à travers une simulation numérique, la visualisation des images fluoroscopiques utilisées comme guidage durant les procédures endovasculaires.

En général, les procédures endovasculaires mini-invasives sont basées sur l'utilisation de données d'imagerie en temps réel, grâce auxquelles il est possible de réaliser un geste diagnostique ou thérapeutique. Ce geste consiste principalement à guider des dispositifs médicaux (tels que cathéters, aiguilles, etc) à travers les vaisseaux sanguins. En particulier, la chirurgie endovasculaire est principalement basée sur le guidage de type fluoroscopique.

Comme toute procédure basée sur les rayons X, la fluoroscopie comporte certains risques liés à l'exposition aux radiations ionisantes. Ces risques peuvent inclure des effets biologiques, tels que des blessures cutanées et touchant les tissus sous-jacents, ou le cancer radio-induit. Ces effets peuvent affecter à la fois le patient et les opérateurs, et des études approfondies ont été menées afin d'évaluer l'exposition aux rayonnements ([13], [14]). Les risques liés à l'exposition aux radiations ionisantes sont principalement dus à la capacité de la fluoroscopie à afficher des processus dynamiques (une vidéo fluoroscopique est en effet obtenue comme une séquence d'images acquises à une fréquence maximale de 30 images par seconde). Alors que l'exposition nécessaire pour générer une seule image fluoroscopique est faible, des expositions plus élevées peuvent résulter de la durée globale de la procédure, compte tenu de la grande séquence d'images acquises. Ainsi, le temps fluoroscopique total est l'un des principaux facteurs qui détermine la dose absorbée. Un autre inconvénient mineur est lié au besoin d'agents de contraste néphrotoxiques, utilisés pour mettre en évidence les structures internes par rapport aux structures naturellement denses en arrière-plan des images fluoroscopiques. En dépit du fait que ces médicaments sont sûrs, une réaction allergique indésirable peut se produire. Dans leur travail, [17] résument les connaissances actuelles pour une utilisation sûre des produits de contraste.

Le deuxième inconvénient principal, lié aux propriétés intrinsèques des images radiographiques, est le manque d'informations spatiales. En particulier, les images fluoroscopiques, qui sont des images 2D projectives, ne permettent pas d'avoir de l'information sur la profondeur. Ce manque de perception de profondeur, qui est ultérieurement complexifié par l'environnement anatomique où de multiples organes et structures se superposent, a été identifié comme l'un des facteurs les plus importants affectant les performances cliniques [18]. En effet, en ne s'appuyant que sur des images bidimensionnelles, il est difficile pour les cliniciens de reconstruire mentalement la configuration spatiale 3D du dispositif d'intervention, ainsi que des anatomies des vaisseaux, des bifurcations ou la

localisation précise de la lésion cible. Par conséquent, les cliniciens exploitent généralement des techniques d'imagerie supplémentaires (par exemple l'échographie) ou acquièrent d'autres images fluoroscopiques, selon différents angles de vue, pour mieux reconstruire la configuration tridimensionnelle. Cela implique une augmentation du temps de procédure, et par là même une augmentation conséquente de l'exposition aux radiations.

L'objectif principal de notre travail est d'améliorer le feedback visuel des procédures basées sur des images fluoroscopiques. Par conséquent nous proposons de reconstruire la forme 3D du dispositif interventionnel à partir d'une vue fluoroscopique monoculaire et de combiner une telle reconstruction 3D avec les images fluoroscopiques 2D. Une meilleure visualisation 3D du dispositif, avec l'anatomie du patient, permettrait à terme de réduire le risque d'erreur, favoriser la réussite des opérations et diminuer le temps global de la procédure.

Les images fluoroscopiques 2D ne fournissent qu'une information partielle sur la configuration actuelle du dispositif médical. Cependant, ces informations projectives peuvent être combinées avec un modèle du dispositif, afin de trouver une estimation optimale de la forme 3D réelle du cathéter. Malheureusement, la reconstruction d'une forme 3D à partir d'informations 2D n'est pas triviale. En général, la reconstruction 2D / 3D est un problème mal posé: étant données les informations manquantes dans la direction de la profondeur, plusieurs configurations 3D peuvent correspondre à la même projection, et une solution unique n'existe pas. Afin de réduire les ambiguïtés résultant de l'absence d'informations détaillées, certaines contraintes supplémentaires doivent être appliquées. De telles contraintes peuvent être de natures différentes, parmi elles: des critères de régularisation appliqués au modèle 3D (propriétés géométriques ou physiques), un volume limite défini par l'anatomie du vaisseau environnant ou encore l'utilisation d'images multiples acquises sous différents angles de vue.

Par rapport aux méthodes existantes, ce travail propose une nouvelle approche stochastique qui combine un modèle de navigation 3D de l'instrument chirurgicale, avec des informations 2D extraites à partir d'images fluoroscopiques à travers un filtre de Kalman Unscented (UKF). Nous avons concentré nos recherches sur la reconstruction de dispositifs flexibles et extensibles comme les cathéters et les guides.

La méthode est basée sur un modèle de navigation avancé, où le dispositif interventionnel est décrit à travers un modèle à éléments finis (FE) basé physique. En effet, la prise en compte des propriétés physiques de l'outil permet de mieux décrire son comportement dynamique. La navigation du dispositif à l'intérieur du système vasculaire est modélisée à travers un modèle de collision non-linéaire, qui prend en compte des phénomènes complexes comme les contacts non-glissants non-rigides, fournissant ainsi une description plus réaliste des interactions entre le cathéter et l'anatomie environnante. Une implémentation optimisée permet de réaliser des calculs en temps réel et d'effectuer la simulation FE à des fréquences d'images compatibles avec celles de la fluoroscopie.

Bien que le modèle avancé fournisse une description réaliste de la dynamique du cathéter,

une caractérisation mécanique parfaite du modèle de navigation n'est en pratique pas possible. En effet, certaines erreurs peuvent affecter la paramétrisation mécanique du modèle du cathéter, tout comme peut apparaître une certaine incertitude liée au modèle d'interaction (coefficient de frottement de la surface des vaisseaux, géométrie du vaisseau, etc.).

Un filtre de Kalman Unscented est utilisé pour fusionner le modèle de navigation avec des features 2D détectées dans les images. En pratique: nous corrigeons la forme 3D prédite de l'instrument (fournie par le modèle de navigation) grâce aux informations fournies par des mesures externes sur son état actuel (la forme projetée du cathéter dans les images fluoroscopiques). L'utilisation d'un tel formalisme bayésien permet de prendre en compte et de traiter les erreurs et incertitudes dans le paramétrage du modèle ainsi que le bruit dans les mesures externes (c'est-à-dire les erreurs de détection dans les images fluoroscopiques).

En conclusion, nous proposons une nouvelle méthode pour reconstruire la forme 3D d'un dispositif interventionnel, capable de gérer et de résoudre de nombreux défis scientifiques complexes. Le type de mesures externes: nous utilisons des observations projectives, obtenues à partir d'une vue monoculaire. Ces observations ne fournissent qu'une information partielle sur l'état actuel de l'objet estimé. La nature de la forme à reconstruire: le cathéter est un objet mono-dimensionnel (filiforme), différent à reconstruire d'une surface entière (bi-dimensionnelle). L'interaction entre le dispositif médical et le vaisseau environnant: d'un point de vue Bayésien, ce problème consiste en une estimation d'état sous contraintes. Le calcul en temps réel à réaliser: le but est d'être compatible avec les fréquences d'acquisition d'images typiques de la fluoroscopie.

Le manuscrit s'articule en six chapitres.

- Le chapitre I présente le contexte clinique, les problèmes et les limites actuelles, ainsi que notre solution proposée.
- Le chapitre II comprend l'état de l'art des œuvres connexes. Outre une revue plus détaillée des méthodes de reconstruction 2D/ 3D, nous présentons également de la littérature sur les différents sujets scientifiques couverts par notre méthode. Nous fournissons une description des différents modèles utilisés pour la modélisation des dispositifs interventionnels, ainsi qu'un bref état de l'art sur les méthodes de segmentation d'image (bien que ce sujet soit hors des objectifs de notre travail, et qu'aucune recherche n'ait été menée dans ce domaine).
- Le chapitre III présente une première approche déterministe, pour la reconstruction d'un cathéter 3D à partir d'images monoculaires 2D. La méthode peut être définie comme un Shape-from-template sous contraintes, où les informations extraites des images fluoroscopiques sont prises en compte dans la simulation en tant que contraintes lagrangiennes. Ce travail a fait l'objet de la publication [2].

- Le chapitre IV présente la simulation stochastique, en introduisant d'abord une étude préliminaire sur le vecteur d'état et l'identification des incertitudes du modèle.
- Le chapitre V, cœur de notre travail, détaille la simulation stochastique pour la navigation de cathéter, également définie comme une approche contrainte du filtre de Kalman Unscented. Le modèle de cathéter basé physique et les features 2D des images fluoroscopiques sont définis dans le cadre bayésien d'un UKF. Ce travail a fait l'objet de la publication [1].
- Le chapitre VI présente un aperçu final de notre travail, mettant en évidence les solutions possibles pour améliorer et généraliser notre approche ainsi que les perspectives pour des travaux futurs.

Mots clés :

Chirurgie Assistée par Ordinateur, Chirurgie Cardiovasculaire, Reconstruction Monoculaire, Simulation basée-physique, Méthode Stochastique, Filtre de Kalman Unscented sous Contrainte